DRUG DEVELOPMENT FOR TUBERCULOSIS: DESIGN AND SYNTHESIS OF CYTOCHROME *BD* OXIDASE INHIBITORS

by

Sarah Marie Hopfner

A dissertation submitted in partial fulfillment

of the requirements for the degree

of

Doctor of Philosophy

in

Chemistry

MONTANA STATE UNIVERSITY
Bozeman, Montana

May 2022

DEDICATION

In loving memory of Rita Jacobson

ACKNOWLEDGEMENTS

First, I would like to thank my advisor, Prof. Mary Cloninger, for guidance and patience. The lessons you taught me did not end in lab. I would also like to thank my committee members, Garrett Moraski, Prof. Tom Livinghouse, Prof. Robert Walker, and Prof. Sharon Neufeldt for being an integral part of my education. My heartfelt thanks to all. Prof. Steve Holmgren, thank you for helping me grow as an instructor and person. I appreciate your grounding advice and for helping me navigate the tides of students that at times feel like their proverbial kayak is sinking. Thank you, Dr. Doreen Brown. Graduate school is stressful and challenging, I appreciate all you do to make it better. Graduate Dean Dr. Craig Ogilvie, thank you for improving life at MSU for graduate students. Your tireless advocacy does not go unnoticed.

The 342 crew (& Co.) thank you for listening and sharing sage advice, especially on this campaign. Sam and Harrison, thank you for making me feel welcome in the tiny office, I am fortunate to have such great company in the workplace and you as friends. Nick, thank you for being my summer sanity buddy when life got a little too exciting. Dr. Kate Marshall, kindness comes from the heart, but also comes from you. Thank you for all you've taught me and for cheering me on. Supportive family and friends, thank you. Elias, although I cannot thank you enough for your support and encouragement, I *can* keep on loving you for the rest of my life.

TABLE OF CONTENTS

TABLE OF CONTENTS CONTINUED

TABLE OF CONTENTS CONTINUED

LIST OF TABLES

LIST OF FIGURES

LIST OF FIGURES CONTINUED

Figure Page

LIST OF FIGURES CONTINUED

Figure Page

LIST OF FIGURES CONTINUED

LIST OF FIGURES CONTINUED

Figure Page

LIST OF FIGURES CONTINUED

Figure Page

LIST OF FIGURES CONTINUED

Figure Page

LIST OF FIGURES CONTINUED

Figure Page

LIST OF FIGURES CONTINUED

Figure Page

ABSTRACT

In 2019, more than 10 million people worldwide became ill with Tuberculosis (TB) according to the World Health Organization 2020 Global Tuberculosis Report. More disturbing is the continued rise in cases of drug resistant TB. Thus, there is an immediate need for the development of new antimicrobials and treatment options that can quickly eliminate resistant variants of *Mycobacterium tuberculosis* (Mtb) infection. The oxidative phosphorylation pathway in Mtb is an attractive target for drug development because only two terminal oxidases are present: cytochrome *bcc* : aa_3 (cyt-*bcc*:aa_3) and cytochrome *bd* (cyt-*bd*). Q203, a small-molecule inhibitor, targets cyt-*bcc*:aa_3 in the oxidative phosphorylation pathway. However, Q203 is bacteriostatic and does not inhibit respiration in Mtb. Thus, innovative drugs and effective drug combinations which target the oxidative phosphorylation pathway are still needed. In this dissertation, I report the synthesis and characterization of new cytochrome *bd* inhibitors that can be used in conjunction with a cytochrome *bcc* : aa_3 inhibitor such as Q203 to rapidly kill mycobacterium tuberculosis. This combination of drugs is expected to shut down oxidative phosphorylation in Mtb, thereby removing both the primary (cyt-*bcc* : aa_3) and the backup (cyt-*bd*) power sources of energy for Mtb. Additionally, the syntheses of molecules with a thieno[3,2-*d*]pyrimidine-4-amine core and substituted phenylethyl substituents are described. IC_{50} values of these compounds against three mycobacterial strains are presented using *M. bovis* BCG, *M. tuberculosis* H37Rv, and *M. tuberculosis* clinical isolate N0145 strains. Since the structure of the Mtb cyt-*bd* oxidase has only very recently been reported, these molecules are important targets not only to study the efficacy of a dual drug therapy but also to study membrane association of thienopyrimidine molecules. Therefore, the membrane partitioning of thienopyrmidine molecules into 1,2-dipalmitoyl-*sn*-glycero-3-phosphocholine was studied using time-correlated single photon counting and correlated with activity against Mtb. Finally, the syntheses of molecules with substitutions on a quinazoline core and substituted phenylethyl substituents are described. Through focused structure-activity relationships, activity against all 3 bacterial strains was improved with 2 compounds showing greater activity than the naturally derived cyt-*bd* inhibitor aurachin D.

CHAPTER ONE

INTRODUCTION

Tuberculosis

Tuberculosis (TB) is a public health threat. According to the World Health Organization (WHO) 2020 Global Tuberculosis report, over 10 million people became ill and 1.4 million died from TB in 2019.[1] Comparing to 2019 statistics, in 2020 only a little more than 150,000 people were provided care for drug-resistant TB, meaning 1 in 3 people with drug-resistant TB were not provided treatment.[2] Both the 2020 and 2021 WHO Global Tuberculosis reports show shortfalls in reporting and treatment because of the pandemic. Before the COVID-19 pandemic, TB was the leading cause of death from a single infectious agent. *Mycobacterium tuberculosis* (Mtb), the bacterium that causes TB, spreads by the aerosols of an infected individual's cough or sneeze. Approximately one quarter of the world's population is infected with Mtb, and infected individuals have a 5-10% lifetime risk of developing TB disease. Thus, this ancient disease[3-4] that was first isolated by Robert Koch[5-6] affects billions of people. TB is a multifaceted issue whose effects are amplified in poverty-stricken nations that face healthcare inequality; the poorest pay the highest cost.[7-9] Even after a cleared TB infection, many suffer from lung and other organ damage that results in a diminished quality of life.[7, 10-11]

Pathophysiology

A person first becomes infected with Mtb when they inhale aerosols from an infected person. The size of the infectious particles may range from 0.65 µM to >7.0 µM.[12] Larger particles are trapped in the oropharynx, where they can cause TB of the upper airway and cervical lymph nodes.[12] The smaller droplets travel to the nasopharyngeal or tracheobronchial region in the lower respiratory tract. From there, Mtb is phagocytosed by macrophages and dendritic cells.[13] Only particles smaller than 0.5 µM evade phagocytosis and are able to reach the alveoli.[14] Mtb dodges death in macrophages through a number of mechanisms.[15] Normally, the function of the macrophage is to ingest and degrade pathogenic invaders; however Mtb not only inhabits macrophages but also uses them to spread within the host.[13, 15-17]

Factors that influence disease severity include the level of viral exposure and the condition of the person's immune system.[12, 18] A well-functioning immune system is sufficient to stall disease progression such that exposure to Mtb results in a latent infection. It is estimated that 1.7 billion people have a latent infection of Mtb. These people are asymptomatic and are not infectious but have a 5-10% chance of developing active TB at some point during their lifetime. Any condition that compromises a person's immune system such as receiving treatment for cancer, suffering from diabetes or rheumatoid arthritis, or coinfection with HIV increases the chances of a more severe TB infection.[18-21]

Mtb's membrane is complex

Clinical determination of TB infection requires the detection of bacilli on a sputum smear. Ordinarily, organisms can be quickly screened by Gram staining and placed into two categories. Gram staining allows for quick determination of cell wall components. An organism that holds the primary stain possesses a thick peptidoglycan cell wall and is said to be Gram-positive, whereas an organism that allows the stain to be washed out with ethanol has a thinner peptidoglycan layer and is said to be Gram-negative. The cell wall of Mtb is unique and does not tolerate Gram staining. Bacteria that resist decolorization by acids during staining procedures are termed acid-fast. Since Koch first isolated the bacilli in year 1882, the complexity of the cell wall of Mtb has proven difficult to visualize as evidenced by the need for evolution of staining techniques.[22] Although much success has been made towards visualizing bacilli, the interaction between the bacilli and the stain is not yet fully elucidated. Furthermore, the composition of the mycobacterial outer membrane changes during phases of infection.[23] It is known that the cell envelope and complex lipids that comprise the outer membrane contribute to virulence.[24]

Vaccine

Bacille Calmette-Guerin (BCG) is a vaccine for tuberculosis. In the United States, the vaccine is not recommended due to the low risk of infection and interference with the Mantoux screening test. While the tuberculin skin test is not

contraindicated for people who have received the BCG vaccine, the vaccine may cause the test to afford a false-positive result. However, in parts of the world with high prevalence of TB, the BCG vaccine is given in childhood as a measure to prevent TB. Unfortunately, the BCG vaccine and efforts to eliminate TB have many limitations.[25-26] BCG varies widely in its ability to protect against pulmonary disease and has a reported range of effectiveness from 0-80% protection against TB.[27] Reasons why there is not an effective vaccine to protect against TB are numerous.[28] Vaccine development for TB is further complicated by the fact that TB disease can be reactivated under circumstances of immune dysfunction.[20-21, 29-34] Another strategy is the development of a new vaccine or one that increases the effectiveness of BCG,[25, 35-36] but results from clinical trials of a vaccine booster being developed have been disappointing.[37] Fortunately, there are diverse candidates including live attenuated, inactive, and subunit vaccines in various phases of clinical development.[36, 38-39]

Treatment for Tuberculosis

Persons with TB disease are treated with several medications that are taken simultaneously for 6-9 months. Both a lack of access to care and prolonged treatment regimens have made it difficult for patients to comply with treatment regimens. Furthermore, lengthy treatment prolongs adverse drug effects. Continued exposure to aggressive therapeutics carries risks including optic neuritis, anemia, QT prologation, flu-like symptoms, rash, headaches, gastrointestinal and neurological dysfunction, and liver toxicity.[40-44] Treatment is

complex, and patients may be hospitalized or even die from adverse drug reactions.[45-48] Moreover, complications to treatment can include an insufficient treatment regimen, drug intolerances and unacceptable side effects[42-50] In addition, lack of access to drugs and prohibitive patient costs restricts care and leads to poor adherence to adequate treatment.[40, 51-56] Thus, treatment schedules that are much more abbreviated are urgently needed.

Resistant forms of Mtb can be selected for when inappropriate treatment such as poor drug selection is employed,[57] and Mtb has developed resistance to many chemotherapies. The susceptibility of its strains to chemotherapies has been classified into four main categories: drug-susceptible (DS), multi-drug resistant (MDR), extensively-drug resistant (XDR) and totally-drug resistant (TDR). MDR-TB is resistant to both isoniazid and rifampicin, while XDR-TB is resistant to MDR chemotherapies and also fluoroquinolones and one of the second-line injectable drugs (capreomycin, kanamycin and amikacin). Another category is rifampicin-resistant (RR) TB. Rifampicin is one of the four first-line drugs used to treat TB.[1]

Treatment for TB is complex. The WHO classifies anti-TB drugs by groups (Table 1.1) where fluoroquinolones are Group A and are considered first-line anti-TB drugs, Group B consists of second-line injectable agents, and other second-line oral drugs are in Group C. Group D drugs are not part of the core treatment regimen and are used to augment therapy.

Group	Drugs	
A. Fluoroquinolones	Levofloxacin Moxifloxacin Gatifloxacin	
B. Injectable drugs	Amikacin Capreomycin Kanamycin Streptomycin	
C. Second-line drugs	Ethionamide/protionamide Cycloserine/terizidone Linezolid Clofazimine	
D. (Additional anti-TB)	D1	Pyrazinamide Ethambutol High doses of isoniazid
	D2	Bedaquiline Delamanid
	D3	Para-Aminosalicylic acid Meropenem Amoxycillin-clavulanate thioacetazone

Table 1.1 Drugs recommended by WHO for treating RR-TB and MDR-TB[58]

Poor patient compliance was a key cause of the development of resistant strains prior to the implementation of directly-observed-short-course-therapy (DOTS) treatment, which was implemented in the 1970's[59]. DOTS made an effort to encourage patient compliance and accountability through careful patient monitoring. The WHO has established treatment guidelines that include many combinations of drugs to best suit a particular strain and patient tolerances, but

drug resistance continues to increase. World-wide MDR/RR-TB increased 10% from 2018 to 2019 with 206,030 people with MDR/RR-TB detected in 2019.[57] Clearly, comprehensive drug combinations and new treatments are needed to thwart drug resistant TB.[60]

Modern drugs and their limitations

Since rifampicin was discovered in 1965, very few drugs have been discovered and even less have been approved to treat TB. In 2012, the US Food and drug Administration (FDA) approved Johnson and Johnson's Mtb ATP synthase inhibitor Bedaquiline (BDQ) (Sirturo®) for treatment of MDR and XDR-TB. Unfortunately within the first three years of clinical use, resistance to BDQ was indicated.[61] Two years later in 2014, the European Union (EU) approved the nitroimidazo-oxazole derivative delamanid (Deltyba®) which destabilizes the bacterial cell wall by inhibiting the synthesis of mycolic acids for MDR-TB. Pretomanid, another inhibitor of mycolic acid synthesis, was approved by the United States Food and Drug Administration (US FDA) in 2019 and in the EU in 2020 for MDR and XDR-TB.

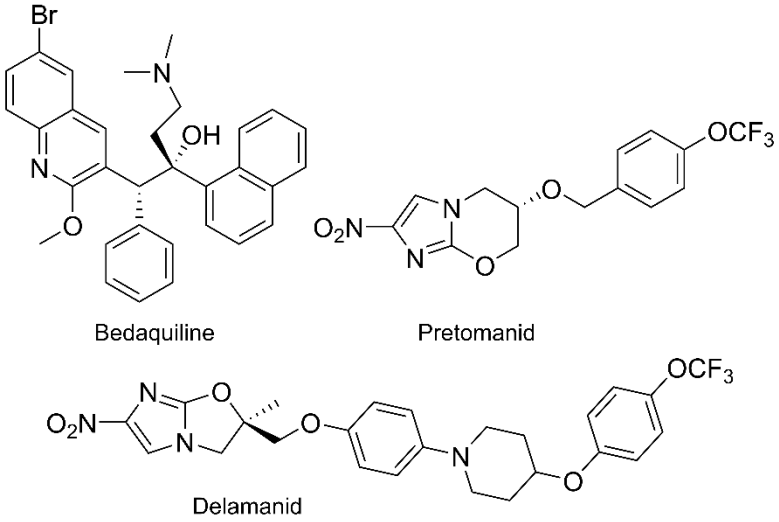

Figure 1.1 Anti-tuberculosis drugs approved after 2012 for MDR and XDR-TB: Bedaquiline, Pretomanid, and Delamanid.

Studying the mechanisms of action of these drugs provides insight regarding how a cure for TB might be reached.[62] Isoniazid inhibits the synthesis of mycolic acids necessary for the construction of a cell wall. Ethambutol and cycloserine disrupts cell wall biosynthesis. An analog of ethambutol, SQ109 is undergoing clinical trials.[63-65] Pyrazinamide, although used since the 1950s has puzzled researchers attempting to reveal the mechanism of action.[66-68] It has been recently reported that the panthothenate pathway is a target of this enigmatic drug.[69]

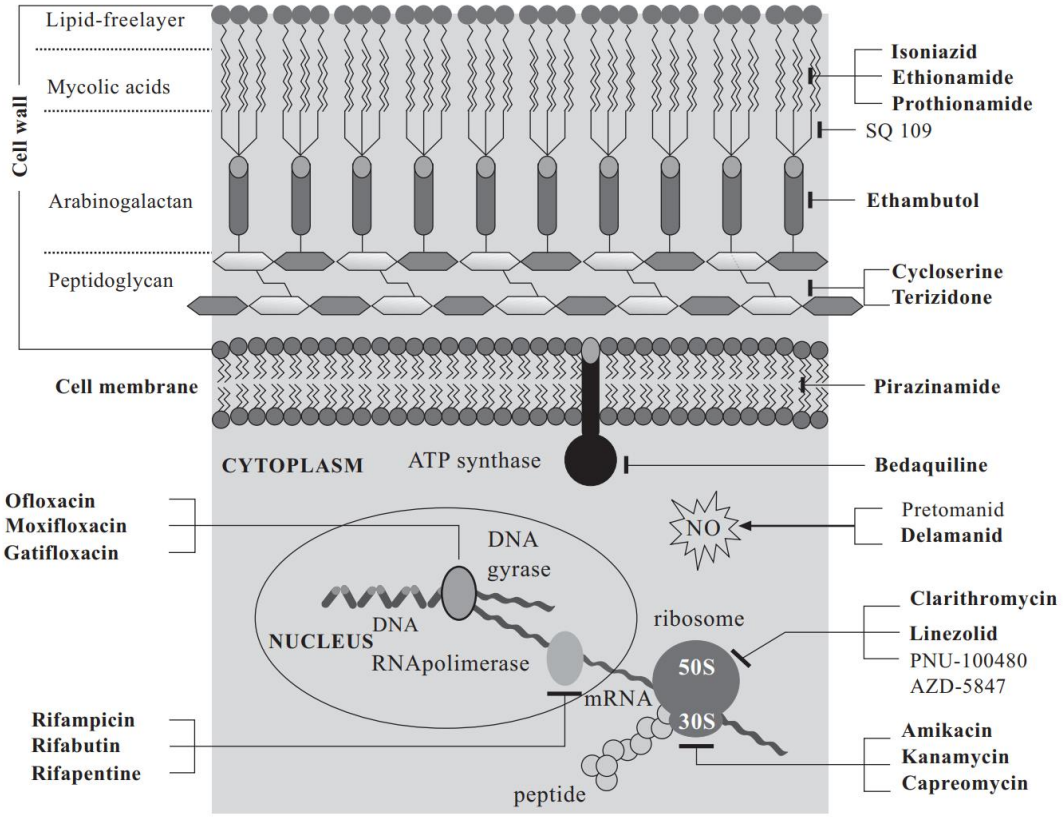

Figure 1.2 Anti-tuberculosis therapeutics and their targets.[70]

Anti-TB drugs and their cellular targets are shown schematically in Figure 1.2. Most therapeutics that have been developed against TB target the cell wall or cell wall component synthesis or aspects of DNA replication. However, a drug that targets cell wall synthesis is not beneficial if Mtb is not actively replicating. The membrane of Mtb is composed of many complex lipids,[71] which confer extreme hydrophobicity to the outer surface of the membrane.[72-73] Mtb deceives the immune system using cell-surface-associated lipids to prevent being recognized by microbicidal macrophages, protecting itself against destruction.[74-75] Instead of evading macrophages completely, Mtb recruits permissive macrophages and hijacks the

immune system so that it can be transported to deeper tissues.[75-81] Since the cell wall provides safety against threats to the bacilli, efforts have been made to weaken this fortification.[82] These drugs and their cell wall targets are shown in Table 1.2.

Drug	Class	Target	Ref
Isoniazid	Pyridines and derivatives	Mycolic acid	(Banerjee 1994, Larsen 2002)[83-84]
Ethambutol	Organonitrogen compounds	Arabinogalactan biosynthesis	(Stehr 2014)[85]
Ethionamide	Pyridines and derivatives	Mycolic acid	(Banerjee 1994)[83]
D-cycloserine	Azolines	D-alanine:D-alanine	(Bruning 2011, Prosser 2013)[86-87]
Muramycin	Nucleoside-lipopeptide antibiotic	MurX	(Kurosu 2007, Dini 2005)[88-89]
Liposidomycin	Nucleoside-lipopeptide antibiotic	MurX	(Kurosu 2007, Dini 2005)[88-89]
Caprazamycin	Nucleoside-lipopeptide antibiotic	MurX	(Kurosu 2007, Dini 2005)[88-89]

Table 1.2 Drugs targeting mycobacterial cell wall/lipids. Table adapted from[90]

Table 1.2 CONTINUED

Drug	Class	Target	Ref
Capuramycin	Nucleoside-lipopeptide antibiotic	MurX	(Kurosu 2007, Dini 2005)[88-89]
Vancomycin	Carboxylic acids and derivatives	Peptidoglycan biosynthesis	(Reynolds 1989)[91]
Teicoplanin	Glycopeptide	Peptidoglycan biosynthesis	(Reynolds 1989)[91]
Nisin	Lantibiotic	Peptidoglycan biosynthesis	(Wiedemann 2001)[92]
Ramoplanin	Lipoglycodepsipeptide	Peptidoglycan biosynthesis	(Lo 2000)[93]
Amphomycin	Lipopeptide	Peptidoglycan biosynthesis	(Banerjee 1981)[94]
Thiophene	Benzothiophenes	Pks13	(Wilson 2013)[95]
CCA34	4,6-Diaryl-5,7-dimethyl coumarins	FadD32	(Stanley 2013)[96]
OPC-67683	Nitroimidazooxazoles	Mycolic acid	(Zhang 2013)[97]
PA-824	Nitroimidazopyran	Mycolic acid	(Stover 2000)[98]
TBA-354	Nitroimidazole	Mycolic acid	(Mdluli 2015)[99]

Table 1.2 CONTINUED

Drug	Class	Target	Ref
SQ109	Ethylenediamine	MmpL3	(Nobre 2014, Sacksteder 2012)[63-64]
BM212	diphenyl pyrrole	MmpL3	(La Rosa 2012)[100]
Au1235	Adamantyl urea	MmpL3	(Grzegorzewicz 2012, Stanley 2012)[101-102]
C215	Benzimidazole	MmpL3	(Grzegorzewicz 2012, Stanley 2012)[101-102]
NITD-304	Indolcarboxamides	MmpL3	(Li 2017)[103]
NITD-349	Indolcarboxamides	MmpL3	(Li 2017)[103]
I3-AG85	Benzothiophene	Ag85C	(Warrier 2012, Favrot 2012)[104-105]
DNB1	Dinitrobenzamide	DprE1	(Mdluli 2015)[99]
BTZ043	Benzothiazinones	DprE1	(Lechartier 2012)[106]

In addition to drugs that target the cell wall or DNA replication, energy metabolism is a promising area of investigation: targets within the oxidative phosphorylation pathway are especially attractive.

Aerobic vs anerobic

Mtb is a primarily aerobic bacterium. Interestingly, this characteristic was exemplified in the 1920s when it was observed that patients infected with TB improved through high altitude treatment.[107-108] Under low oxygen conditions, tuberculosis transitions to an anaerobic state where bacterial replication and DNA synthesis stops.[109] Although less efficiently, ATP is still produced by functional cyt-*bd*, facilitating Mtb survival. Transmembrane enzymes that play an important role in anaerobic oxidative phosphorylation are shown schematically in Figure 1.3.

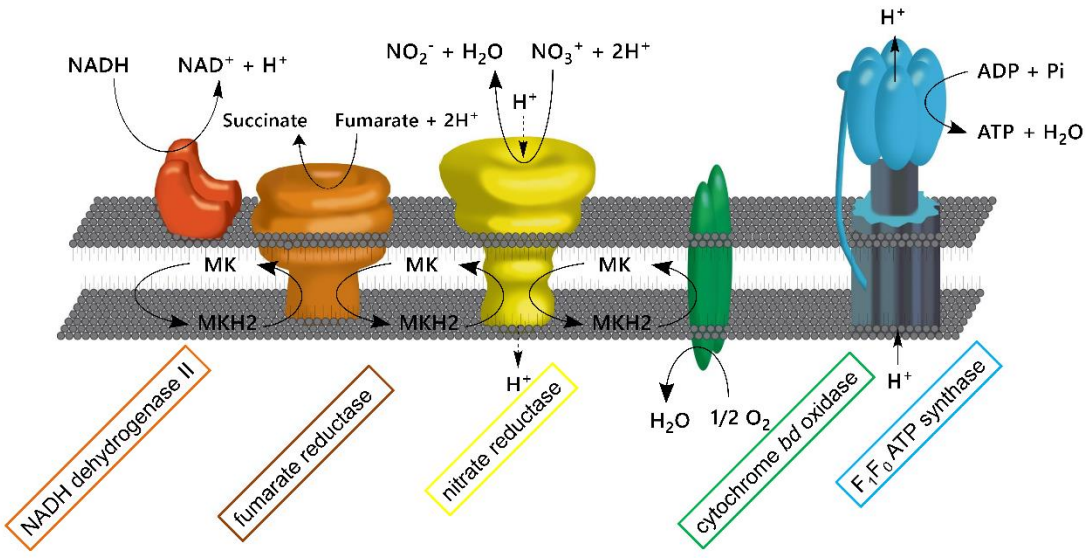

Figure 1.3 Oxidative phosphorylation under anaerobic conditions. The terminal oxidase cyt-*bd* is active.Figure adapted from Ref. 111.

Interactions between Mtb and the host prompt this non-replicating, latent phase. Upon increased oxygenation, the bacteria can be reactivated and can resume a replicating state as shown schematically in Figure 1.4.[110]

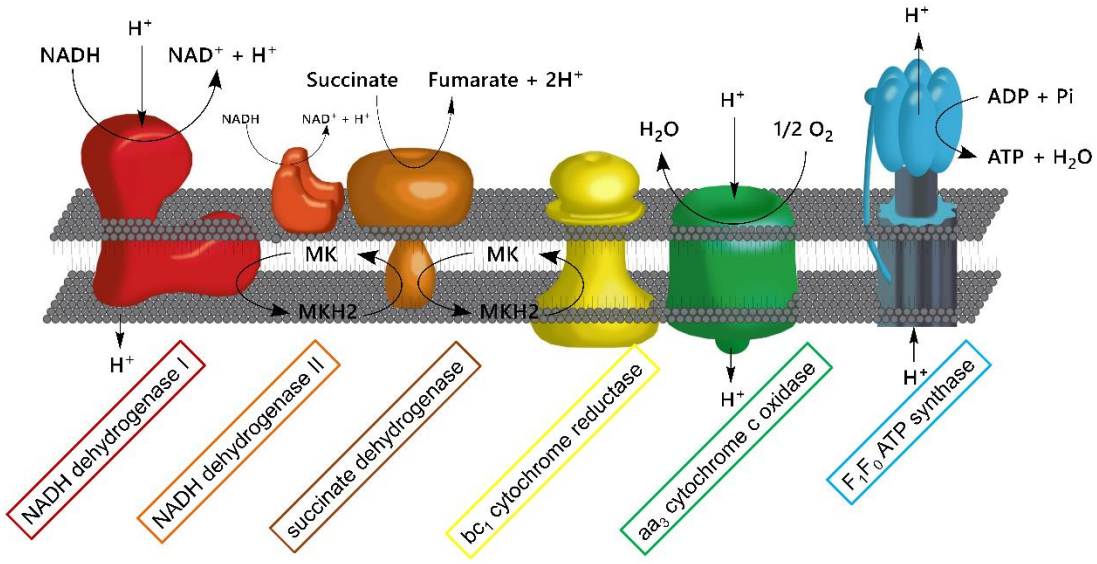

Figure 1.4 Oxidative phosphorylation under aerobic conditions. Q203 (Telacebec®) inhibits the terminal oxidase cyt-bcc:aa$_3$ and bedaquiline inhibits ATP synthase. Figure adapted from Ref. 111.

Various bacteria can make adenosine triphosphate (ATP) by two methods: substrate-level phosphorylation of fermentable carbon sources or oxidative phosphorylation.[111] During infection, TB demonstrates remarkable competence in its ability to adapt to environmental stresses. Of the investigated attributes, the mechanism of adapting to oxygen levels has been appreciably studied. High-density mutagenesis and deletion studies have shown that Mtb cannot produce sufficient ATP by substrate-level phosphorylation alone, and oxidative phosphorylation is required for growth.[112-113] There are two terminal oxidases in

this pathway; cytochrome *bcc:aa$_3$* (cyt-*bcc:aa$_3$*) is the aerobic oxidase while cytochrome *bd* (cyt-*bd*) serves as the oxidase under anaerobic conditions.

Disrupting energy metabolism

Clofazimine, a repurposed anti-leprosy drug, targets NDH-2 and probably additional respiratory cytochromes.[114-115] The diarylquinoline Bedaquiline targets ATP synthase[116-117] whereas Q203 (Telacebec®) inhibits the cytochrome *bcc:aa$_3$* complex (Figure 1.5).[118]

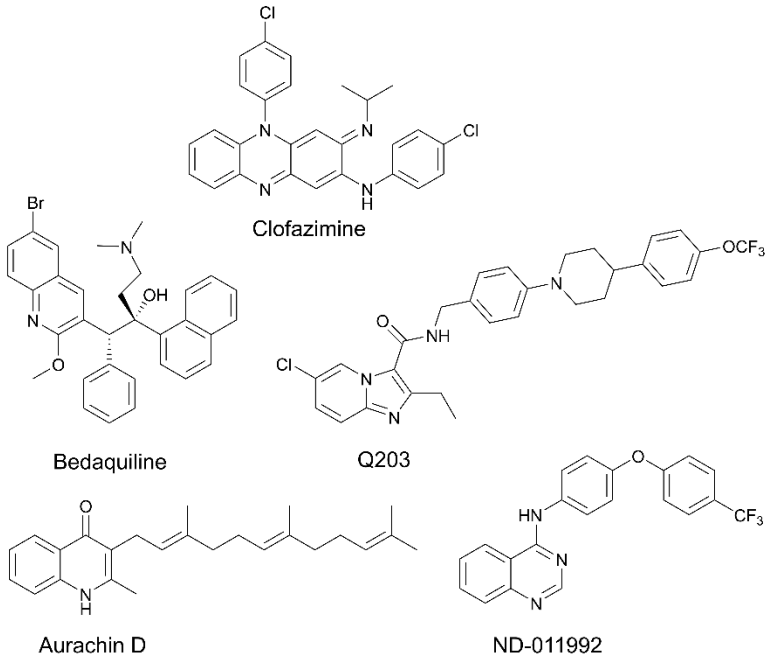

Figure 1.5 . Inhibitors of oxidative phosphorylation pathway within *M. tuberculosis*: Clofazimine, Bedaquiline, Q203, Aurachin D, ND-011992.

Q203 belongs to the imidazopyridine class of compounds and entered phase 2 clinical trials in July of 2018.[119-120] We have demonstrated that a potential clinical limitation of Q203 is that the compound is unable to inhibit oxygen respiration and

is bacteriostatic due to the functional redundancy between the cyt-*bcc:aa*$_3$ and the cytochrome *bd* oxidase (Cyt-*bd*).[118]

Interrupting oxidative phosphorylation in Mtb has shown to be a promising strategy.[112, 118, 121] The compound Q203 (Telacebec®) binds to the QcrB subunit of cytochrome *bcc*, inhibiting the function of the cytochrome *bcc:aa*$_3$ super complex.[119] An important limitation of Q203 is that it has been shown to be bacteriostatic and not bactericidal. This is because it is not able to completely shut down respiration due to a redundancy between the terminal oxidases cytochrome *bcc:aa*$_3$ (cyt-*bcc:aa*$_3$) and cytochrome *bd* (cyt-*bd*).[115] It has been shown that when cyt-*bcc:aa*$_3$ is inactive, cyt-*bd* is upregulated.[122] Cyt-*bd* allows for the continued production of sufficient ATP for Mtb to survive in a non-replicating state[109-110]. In this way, Mtb is protected against cyt-*bcc:aa*$_3$ inhibitors such as Q203, oxidative stress, and other chemotherapies.[123]

There are only two published Mtb cyt-*bd* inhibitors, menaquinone analogue Aurachin D[121] and ND-011992[124] (Figure 1.5). Issues with Aurachin D include not being able to permeate the TB cell wall effectively and having toxic off-target effects.[121] However, Aurachin D co-administered with Q203 shows almost identical bactericidal activity as that of Q203 within cyt-*bd* knockout strains.[121] This result indicates that cytochrome *bd* oxidase is an attractive Mtb drug target when used in combination with cyt-*bcc:aa*$_3$ inhibitors, as demonstrated by the bactericidal efficacy of the Q203/ ND-011992 combination against replicating and antibiotic-tolerant non-replicating mycobacteria.[124]

Bd oxidase assay general information

In order to reveal the activity of *bd* oxidase compounds, samples needed to be incubated with an excess amount of cyt-*bcc:aa*$_3$ inhibitor Q203. With the supercomplex inactive, production of ATP by cyt-*bd* can be quantified. Varying concentrations of the cyt-*bd* inhibitors are added to the wells of a 96-well plate. A luminescent reagent (BacTiter-Glo™) is added. In the presence of ATP, Mg^{2+} and O_2, luciferin is oxidized to oxyluciferin. When oxyluciferin reaches the ground state, light which can be read by the plate-reader is released. Luminescence is read and quantified by a cell imaging reader, allowing for ATP curves to be generated. Figure 1.6 shows the increased inhibition of ATP production of tested compounds when Q203 is coadministered.

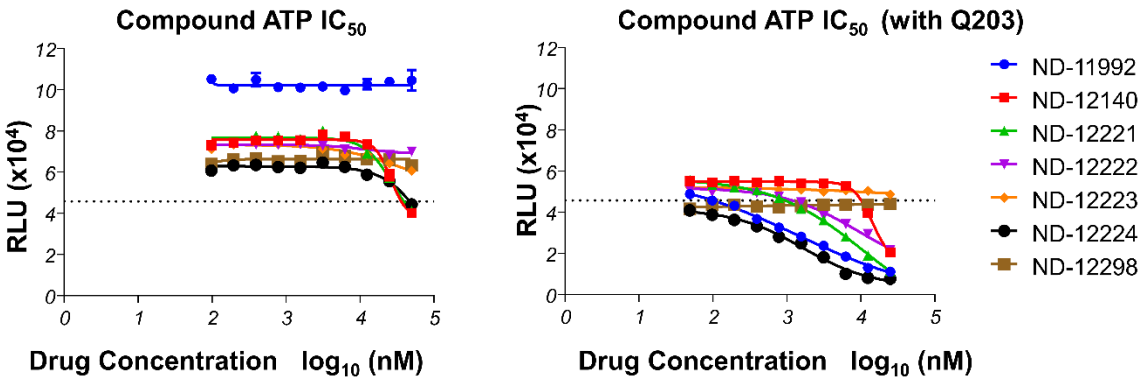

Figure 1.6 Kill curves from ATP depletion assay. Relative light units (RLU) correspond to presence of ATP.

From this example assay, performed by collaborators at Nanyang Technological University, we can see that ND-11992, which is an internal identifier for compounds

synthesized for this project, is the most potent, ND-12140 and ND-12221 inhibit both cyt-*bcc:aa*$_3$ and cyt-*bd*, and ND-12298 was inactive.

Structure-activity relationships

The relationships between chemical structure and biological activity are known as structure-activity relationships (SAR). Biological activity is often a response such as the death of an organism. SAR is used to design, predict, and optimize effective drug compounds. Additionally, SAR can be used to study selectivity, toxicity, and toxic pharmacophores. Analogs are prepared, and their activity is evaluated through a quantitative measurement such as a 50% inhibitory concentration (IC_{50}). An IC_{50} value indicates the minimum concentration of a compound required to inhibit a biological function. Thus, smaller IC_{50} values indicate greater biological activity. From analysis of IC_{50} values, incremental structural improvements are made, and the effects of these alterations are studied so that ideal drug candidates can be optimized.

Topliss Tree

What structural changes should be made to the core scaffold? Numerous compounds could show great biological activity, or none at all. The abundant options for structural modifications can be overwhelming, and the task of synthesizing these analogs can be quite daunting. Although SAR can inform medicinal chemists regarding which positions on a molecule should be modified to improve a desired characteristic, the number of possible modifications adds an

inordinate challenge. To design and synthesize the most potent analogs as efficiently as possible, a Topliss decision tree can be followed. In 1972, John Topliss devised a logical scheme for quickly discovering the most potent lead compound. The schematic was enabled by the 1963 method for structure-activity correlations developed by Hansch.[125] Hansch was able to rationalize the substituent effect of antibiotics on bacteria using the Hammett equation and a hydrophobicity constant (π). Using Hansch's hydrophobicity constant, and the Hammet variable (σ), a logical tree was formulated (Figure 1.7).

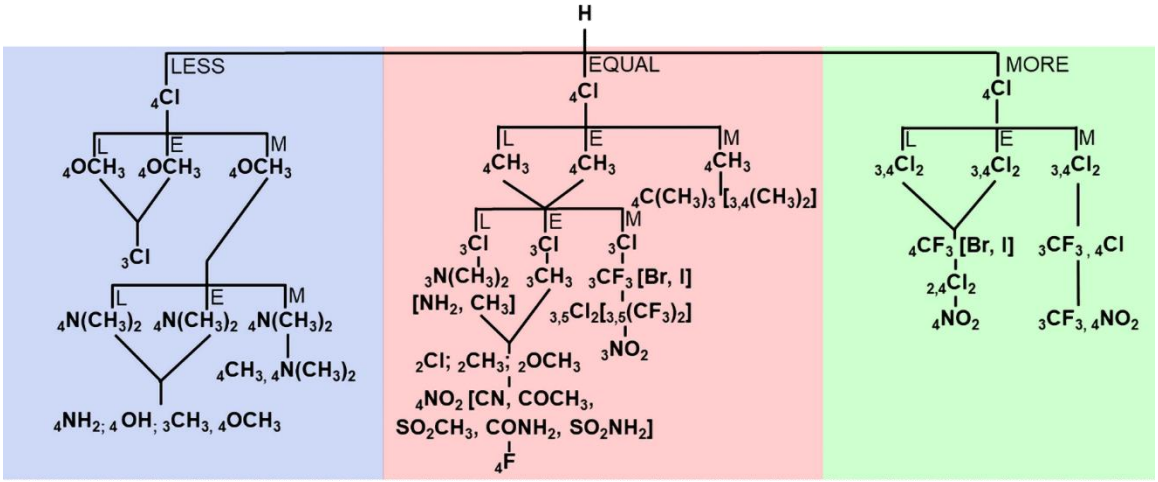

Figure 1.7 Topliss aromatic substitution schematic.[125]

The starting compound incorporates the unsubstituted phenyl. Next, the 4-chloro analog is prepared, and the biological activity of the chloride is compared to that of the unsubstituted phenyl. Comparing the 4-chloro analog to the unsubstituted aryl group can result in 3 outcomes; more potent (M), less potent (L), or equipotent (E). The 4-chloro analog is lipophilic (+π) and electron withdrawing (+σ). An increase in potency in the 4-chloro compound can be attributed to either or both of

these effects. If it is found that the 4-chloro analog is more potent, then the 3,4-dichloro analog would be prepared next since the (+π) and (+σ) effects would be larger for the dichloride. The 4-methyl analog would be made if the initial pairing of the unsubstituted phenyl and 4-chloro resulted in equipotency. The 4-methyl substituent is lipophilic (+π), and electron donating (-σ). Finally, if it was found that the 4-chloro analog was less potent than the unsubstituted phenyl, the 4-methoxy analogue would be prepared as it is electron donating (-σ) and affords a minimal lipophilic contribution (π). By comparing potency at each branch point, the next analogs to be synthesized can be systematically determined.

Drug partitioning

Drug design involves the multiparameter optimization of many physiochemical properties for each therapeutic molecule.[126-127] A significant challenge arises when the target enzyme structure is unknown. Therefore, knowing the partitioning behavior of the drug compound in biological membranes is imperative. The work described in this thesis was completed prior to the report of the structure of cyt-*bd* within Mtb.[128] Going forward, the details of the structure of cyt-*bd* within Mtb will be of enormous benefit to the design of highly specific cyt-*bd* inhibitors. The target cyt-*bd* is a transmembrane protein. One point worth noting is that even before a compound can interact with a binding site, it must first reach the desired destination. It is possible that a compound that binds well to the target will never reach it. Therefore, an investigation of drug-membrane interactions is imperative. The dynamic nature of cellular membranes presents a challenge in the

characterization of the interactions of therapeutic compounds with membranes.[129-131] Biological membranes are comprised primarily of lipids that provide a wide variety of characteristics because of their structural variations and amphipathic nature. Phospholipids, for example, generally have a polar headgroup that interacts with the aqueous environment as well as two hydrophobic acyl chains (Figure 1.8).

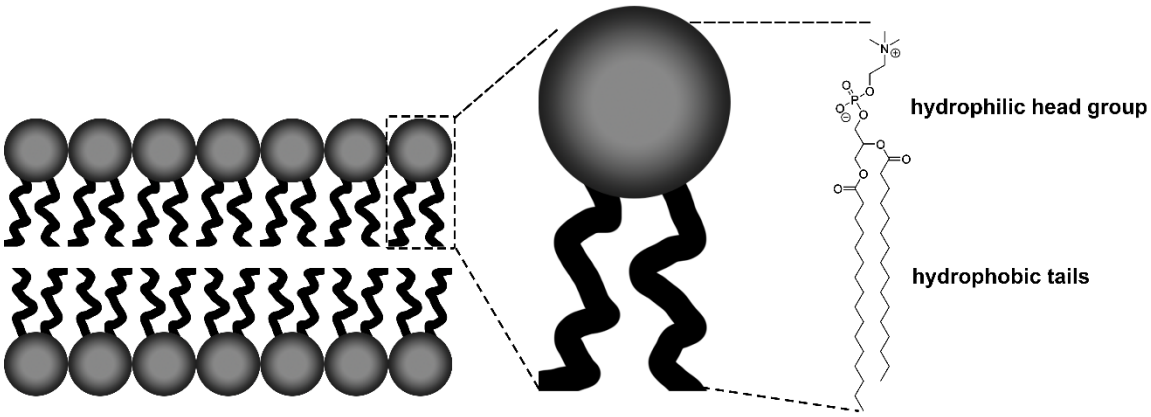

Figure 1.8 Phospholipid bilayer with hydrophilic head group and hydrophobic tails. Shown with model lipid 1,2-dipalmitoyl-*sn*-glycero-3-phosphocholine (DPPC) used in this work.

The assembly of lipids is motivated by the hydrophobicity or hydrophilicity of the environment. In aqueous media, the polar headgroups come together to face the aqueous region, while the hydrophobic acyl tails are sandwiched between the headgroups and are hidden from the water. The shape that the phospholipids form is determined by external factors such as pH, temperature, or ionic strength.[132]

The lipophilicity of a molecule can be defined as how a molecule partitions between an aqueous and an organic phase. The partition coefficient P is the ratio of the concentration of the solute in octanol and water (Equation 1). Log *P* can be measured experimentally or determined computationally through structural information.[133-134] Log *P* describes the partitioning behavior and continues to be widely used in drug development.[135-138]

$$\log P = \log \left(\frac{[solute]_{octanol}}{[solute]_{water}}\right) \quad (1)$$

The lipid shown in Figure 1.9 is 1,2-dipalmitoyl-*sn*-glycero-3-phosphocholine (DPPC), and this lipid is frequently used in model studies to mimic the biological membrane. For example, DPPC has been used as a model membrane to study the interactions of aspirin[139], methotrexate[140], and doxorubicin[141]. Generally, DPPC is a good model system of a biological membrane.

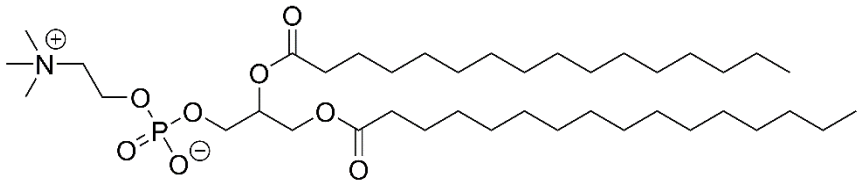

Figure 1.9 Skeletal structure of 1,2-dipalmitoyl-sn-glycero-3-phosphocholine, monomer of model biological membrane.

Most biological molecules take shape based on their interactions with water. These molecules have both polar and nonpolar portions and are termed amphipathic. The hydrophilic portion of the molecule interacts with water and the hydrophobic region repels it. Amphiphilic molecules tend to form aggregates with the nonpolar portions of the molecule coming together and the polar portion facing outwards towards the water. The aggregate is supported through the hydrophobic effect. DPPC can

mimic a biological membrane because it has a zwitterionic phosphate group, a polar region that can mimic the polar headgroups of a biological membrane and be solvated by water and nonpolar acyl chains that imitate the hydrophobic portion of the membrane. Just like a native biological membrane, DPPC can form micelles and bilayers. It is expected that charged molecules would interact with the DPPC polar headgroup like they would with the polar region of a biological membrane. Similarly, it is expected that the more hydrophobic compounds partition between the bilayers in the nonpolar region. Therefore, it is important to know the charge state of the solute at physiological pH. Fortunately, the charge state can be ascertained through the measurement of pKa values.

Summary and Organization

In summary, TB is a global health threat that affects billions of people. Modern medicine regimes are not comprehensive, and the search for powerful antimycobacterial agents continues. Targets within the oxidative phosphorylation pathway of Mtb have shown great promise. Specifically, simultaneously inhibiting cyt-*bcc:aa*$_3$ and cyt-*bd* has been demonstrated to remove avenues of ATP synthesis, resulting in total destruction of Mtb. Inhibition of cyt-*bcc:aa*$_3$ by Q203 is not enough. Therefore, designing effective compounds that inhibit cyt-*bd* are of utmost importance for the eradication of TB disease. Through the use of structure-activity relationship analysis and membrane interaction studies, optimized cyt-*bd* inhibitors can be elucidated. It is expected that the resultant cyt-*bd* inhibitor will

stop ATP production and accordingly obliterate the bacterium that causes this devastating disease, Mtb.

Research described in this dissertation is organized as follows:

Chapter 2 introduces the syntheses and structure-activity relationships as well as the activity of thieno[3,2-*d*]pyrimidin-4-amine *Mycobacterium tuberculosis bd* oxidase inhibitors. Biological activity against *Mycobacterium bovis* BCG, *Mycobacterium tuberculosis* H37Rv, and *Mycobacterium tuberculosis* clinical isolate N0145 was explored.

Chapter 3 builds on Chapter 2 by describing the quantitative investigation of membrane partitioning behavior of thieno[3,2-*d*]pyrimidin-4-amines in 1,2-dipalmitoyl-*sn*-glycero-3-phosphocholine (DPPC). The thieno[3,2-*d*]pyrimidin-4-amine derivatives reported in this chapter are cyt-*bd* oxidase inhibitors. The comparable partitioning within the DPPC model membrane system for all compounds studied indicates that differences in activity against cyt-*bd* oxidase arise from relative effectiveness at binding to the target enzyme rather than from membrane uptake or transport. The methods reported here for studying membrane partitioning are especially important for molecules that bind to transmembrane targets with unknown structures.

Chapter 4 also builds upon Chapter 2, reporting the syntheses and structure activity relationships of *N*-phenethyl-quinazolin-4-yl-amines as potent inhibitors of cytochrome *bd* oxidase in *Mycobacterium tuberculosis*. Biological activity against *Mycobacterium bovis* BCG, *Mycobacterium tuberculosis* H37Rv, and *Mycobacterium tuberculosis* clinical isolate N0145 was assessed. Two compounds

were more active against all three strains than aurachin D, the naturally derived cyt-*bd* inhibitor.

Chapters 2 and 4 are published manuscripts. Chapter 3 has been submitted. Because of their status as published manuscripts or manuscripts submitted for publication, information in the introductions and methods sections of these chapters appears several times in this dissertation.

CHAPTER TWO

STRUCTURE GUIDED GENERATION OF THIENO[3,2-*d*]PYRIMIDIN-4-AMINE MYCOBACTERIUM TUBERCULOSIS BD OXIDASE INHIBITORS

Contribution of Authors and Co-Authors

Manuscript in Chapter 2

Author: Sarah M. Hopfner

Contributions: Prepared and characterized compounds, co-wrote initial draft of the manuscript.

Co-Author: Bei Shi Lee

Contributions: Performed biological assays, assisted in drafting and editing the manuscript.

Co-Author: Nitin P. Kalia

Contributions: Performed biological assays.

Co-Author: Marvin J. Miller

Contributions: Provided data interpretation and scientific direction, assisted in editing the manuscript.

Co-Author: Kevin Pethe

Contributions: Assisted in editing the manuscript.

Co-Author: Garrett C. Moraski

Contributions: Designed compounds, assisted in compound preparation, co-wrote initial draft of the manuscript.

Manuscript Information

Sarah M. Hopfner, Bei Shi Lee, Nitin P. Kalia, Marvin J. Miller, Kevin Pethe, and Garrett C. Moraski

RSC Medicinal Chemistry

Status of Manuscript:

____ Prepared for submission to a peer-reviewed journal

____ Officially submitted to a peer-reviewed journal

____ Accepted by a peer-reviewed journal

_X__ Published in a peer-reviewed journal

Royal Society of Chemistry

RSC Med. Chem., 2021, 12, 73.

DOI: 10.1039/d0md00398k

STRUCTURE GUIDED GENERATION OF THIENO[3,2-*d*]PYRIMIDIN-4-AMINE *MYCOBACTERIUM TUBERCULOSIS BD* OXIDASE INHIBITORS

Sarah M. Hopfner,[a] Bei Shi Lee,[b] Nitin P. Kalia,[c] Marvin J. Miller,*[d] Kevin Pethe*[b] and Garrett C. Moraski*[a]

[a] *Department of Chemistry and Biochemistry, Montana State University, 103 Chemistry and Biochemistry Building, Bozeman, Montana 59717, USA*

[b] *Lee Kong Chian School of Medicine, Nanyang Technological University, Experimental Medicine Building, 59 Nanyang Drive, 636921, Singapore*

[c] *School of Biological Sciences, Nanyang Technological University, Experimental Medicine Building, 59 Nanyang Drive, 636921, Singapore*

[d] *Department of Chemistry and Biochemistry, University of Notre Dame, 251 Nieuwland Science Hall, Notre Dame, Indiana 46556, USA*

Abstract

Cytochrome *bd* oxidase (Cyt-*bd*) is an attractive drug target in *Mycobacterium tuberculosis*, especially in the context of developing a drug combination targeting energy metabolism. However, currently few synthetically assessable scaffolds target Cyt-*bd*. Herein, we report that thieno[3,2-*d*]pyrimidin-4-amines inhibit Cyt-*bd*, and report an initial structure–activity-relationship (SAR) of 13 compounds in three mycobacterial strains: *Mycobacterium bovis* BCG, *Mycobacterium tuberculosis* H37Rv and *Mycobacterium tuberculosis* clinical isolate N0145 in an established ATP depletion assay with or without the cytochrome *bcc : aa*$_3$ (QcrB) inhibitor Q203. All compounds displayed activity against *M. bovis* BCG and the *M.*

tuberculosis clinical isolate strain N0145 with ATP IC_{50} values from 6 to 54 μM in the presence of Q203 only, as expected from a Cyt-*bd* inhibitor. All derivatives were much less potent against *M. tuberculosis* H37Rv compared to N0145 (IC_{50}'s from 24 to >100 μM and 9–52 μM, respectively), an observation that may be attributed to the higher expression of the Cyt-*bd*-encoding genes in the laboratory-adapted *M. tuberculosis* H37Rv strain. *N*-(4-(*tert*-butyl)phenethyl)thieno[3,2-*d*]pyrimidin-4-amine (19) was the most active compound with ATP IC_{50} values from 6 to 18 μM against all strains in the presence of Q203, making it a good chemical probe for interrogation the function of the mycobacterial Cyt-*bd* under various physiological conditions.

Introduction

Tuberculosis (TB) is a public health crisis. According to the 2018 World Health Organization (WHO) report, 10 million people became ill with TB, and 1.3 million died in 2017.[59] TB is one of the top 10 causes of death worldwide.[59] TB infection is caused by *Mycobacterium tuberculosis* (Mtb), a primarily aerobic bacterium. Infection is spread from person to person by aerosol transmission, usually via an infected individual's cough or sneeze. Initial symptoms are mild and often go unnoticed. Most troubling is the continued rise in drug resistant TB. It is estimated that between 483,000 and 639,000 people have developed TB that was resistant to rifampicin.[59] Thus, there is an urgent need for the development of antimicrobials and treatment options that can swiftly eliminate Mtb infections.

Various bacteria can make adenosine triphosphate (ATP) by two methods: substrate-level phosphorylation of fermentable carbon sources or oxidative phosphorylation.[142] During infection, TB demonstrates remarkable competence in its ability to adapt to environmental stresses. Of the investigated attributes, the mechanism of adapting to oxygen levels has been appreciably studied. High-density mutagenesis and deletion studies have shown that Mtb cannot sufficiently produce ATP by substrate-level phosphorylation alone, and oxidative phosphorylation is strictly required for growth.[112-113]

Small-molecule inhibitors have been synthesized that have various targets in the oxidative phosphorylation pathway. Clofazimine **1** (Figure 2.1), a repurposed anti-leprosy drug, targets NDH-2 and probably additional respiratory cytochromes.[114-115] The first line TB drug pyrazinamide incapacitates the proton motive force that maintains an electrochemical gradient across the membrane (Figure 2.1).[67] The diarylquinoline Bedaquiline **2** targets ATP synthase[116-117] whereas Q203 (**3**) inhibits the cytochrome *bcc:aa*$_3$ complex (Figure 2.1).[118] Q203 belongs to the imidazopyridine class of compounds and entered phase 2 clinical trials in July of 2018.[119-120] We have demonstrated that a potential clinical limitation of Q203 is that the compound is unable to inhibit oxygen respiration and is bacteriostatic due to a functional redundancy between the cyt-*bcc:aa*$_3$ and the cytochrome *bd* oxidase (Cyt-*bd*).[118]

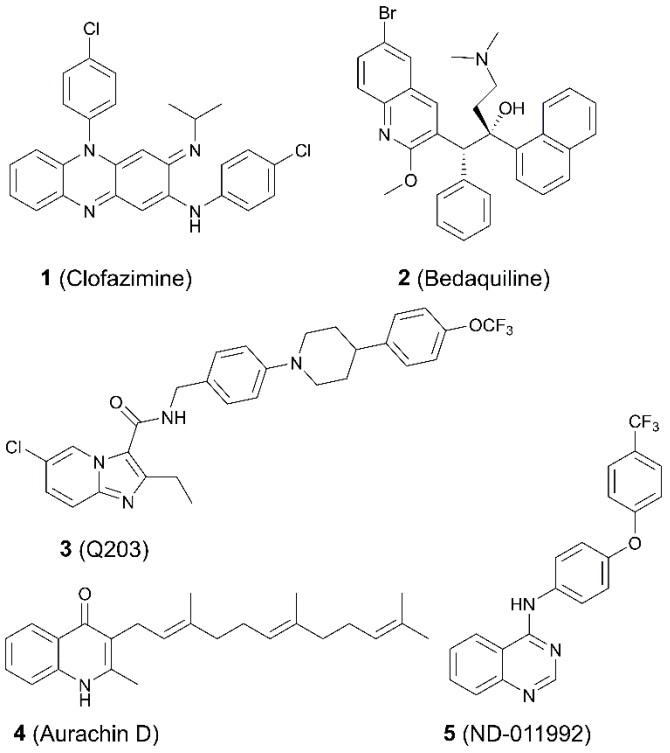

Figure 2.1 Inhibitors of *M. tuberculosis* oxidative phosphorylation pathway.

Bactericidal agents are strongly desired. A neglected target in the oxidative phosphorylation pathway is the Cyt-*bd*, an oxidoreductase that is important for viability when the function of the cyt-*bcc:aa*$_3$ is compromised.[142] The cyt-*bd* is over-expressed under low oxygen conditions that coincide with the entry into a reversible non-replicating, antibiotic tolerant state.[109-110]

Knockouts and mutations of the cytochrome *bcc:aa*$_3$ complex (Cyt-*bcc:aa*$_3$) show an upregulation of Cyt-*bd*,[122] making Cyt-*bcc:aa*$_3$ inhibitors themselves less effective. Although non-essential, the Cyt-*bd* is still required to maintain oxygen respiration and ATP homeostasis in concert with the cyt-*bcc:aa*$_3$.[143] In this manner, mycobacteria are protected against drug treatments by rerouting the electron flow

to the Cyt-*bd*. Therefore, targeting cytochrome *bd* and adding a Cyt-*bd* inhibitor to a TB treatment regimen may be an effective means to kill replicating and non-replicating mycobacteria more effectively.

There are only two published Mtb Cyt-*bd* inhibitors, menaquinone analogue Aurachin D[121] (**4**) and ND-011992[124] (**5**) (Figure 2.1). Issues with Aurachin D include not being able to permeate the TB cell wall effectively and having toxic off-target effects.[121] However, Aurachin D co-administered with Q203 shows almost identical bactericidal activity as that of Q203 within Cyt-*bd* knockout strains.[121] As such, cytochrome *bd* oxidase is an attractive Mtb drug target particularly when used in combination with Cyt-*bcc:aa*$_3$ inhibitors, as demonstrated by the bactericidal efficacy of the Q203/ ND-011992 combination against replicating and antibiotic-tolerant non-replicating mycobacteria.[124]

Results and Discussion

To discover new Cyt-*bd* oxidase inhibitors, we made use of a whole cell assay in *Mycobacterium bovis* BCG (BCG), followed by validation in *M. tuberculosis* H37Rv (H37Rv-Mtb) and *M. tuberculosis* clinical isolate N0145 (N0145-Mtb). This assay exploits the conditional essentiality of the Cyt-*bd* to maintain ATP homeostasis once cyt-*bcc:aa*$_3$ is selectively inhibited by Q203.[124] Measurement of ATP depletion in the presence and absence of Q203 reveals whether a compound inhibits alone or synergizes with Q203**.** Compounds that deplete ATP in the presence of Q203 but not in its absence are putative Cyt-*bd* inhibitors. Next, we screened a small but diverse set of around 50 compounds selected from our long-

standing antibacterial programs against *M. bovis* BCG to reveal active compounds like ND-011992.[124] When screened in the presence of Q203, our screening revealed two thienopyrimidines—compound **6** (a thieno[2,3-*d*]pyrimidine-4-amine) and compound **7** (a thieno[3,2-*d*]pyrimidine-4-amine)—displaying divergent potency with IC_{50} > 50 µM and 26 µM, respectively (Figure 2.2). Both **6** and **7** were inactive against BCG (IC_{50} > 50 µM when tested the absence of Q203), suggesting that these compounds work by inhibition of Cyt-*bd*.

When searching literature around the thienopyrimidine scaffold, we discovered an abundance of references including patent applications for use as pesticides,[144] anti-cancer compounds,[145-146] worm infections[147] and autoimmune diseases[148]. Interestingly, only one group has published on thienopyridines as anti-TB agents.[149-150] This group identified a thieno[2,3-*d*]pyrimidine-4-amine, CWHM-728 (**8**, Figure 2.3), through iterative screening of commercially available compounds against *Mycobacterium smegmatis*. CWHM-728 (**8**) was found to have an IC_{50} value of 3.2 µM against *M. tuberculosis* Erdman strain. Through diligent SAR studies, they developed a much more potent analogue, CWHM-1023 (**9**, Figure 2.3), possessing an IC_{50} value of 0.083 µM against *M. tuberculosis* Erdman strain. They also determined that mutations within the QcrB gene confer resistance, suggesting Cyt-*bcc:aa*$_3$ as the primarily target of these compounds.

The precedence of “hit to lead” development of the thieno[2,3-*d*]pyrimidine-4-amines combined with the structural simplicity of compound **7** makes this core an attractive scaffold to explore structure-activity-relationship (SAR) studies. Herein, we report our initial findings on thieno[3,2-*d*]pyrimidine-4-amines that

inhibit mycobacteria Cyt-*bd* over Cyt-*bcc:aa*$_3$ within replicating BCG, replicating Mtb-H37Rv and clinical N0145-Mtb strains.

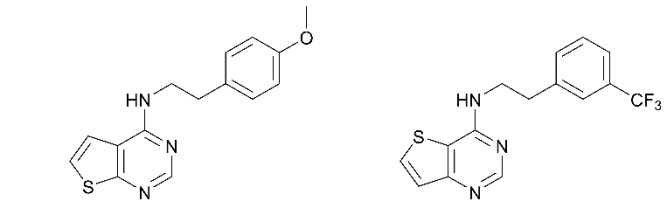

Figure 2.2 Thienopyrimidines **6** and hit **7** were identified by ATP depletion within *Mycobacterium bovis* BCG.

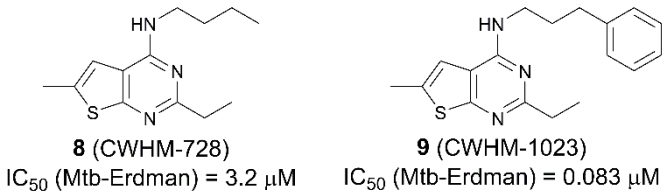

Figure 2.3 Thieno[2,3-d]pyrimidin-4-amines **8** and **9** identified as novel Cyt-*bc*$_1$:*aa*$_3$ inhibitors.

Our SAR efforts focused on probing three structural elements of hit **7**: 1) positioning of aryl substitution (2', 3' and 4' positions), 2) alteration of the pendant 2-(3-(trifluoromethyl)phenyl)ethan-1-amino moiety with other substitutions (i.e. H, halogen, CH_3, OCF_3, etc), and 3) changing of the aliphatic chain length (i.e. anilino, benzyl, ethanyl).

Compounds were prepared in one step by classical S_NAr reactions of 4-chlorothieno[3,2-*d*]pyrimidine, desired amines and potassium carbonate at elevated temperature (Scheme 1).[151] Yields varied from 22 to 70 %, after purification by recrystallization (see supporting information). We prepared thirteen

analogues (**10** – **22**) that were screened in a whole-cell ATP Cyt-*bd* assay —in BCG with subsequent validation in H37Rv-Mtb and the clinical isolate N0145-Mtb—under replicating conditions with and without added Q203. The BCG strain was used to identify any general Cyt-*bd* inhibitor (when Q203 was added, "+Q203"). The laboratory adapted *M. tuberculosis* H37Rv strain over expresses Cyt-*bd* compared to clinical isolates.[117]

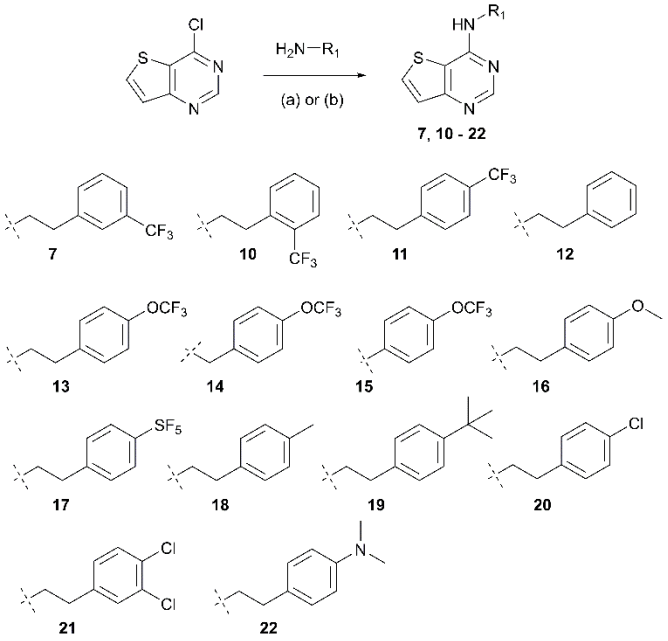

Figure 2.4 Syntheses of target thieno[3,2-*d*]pyrimidin-4-amines (**7**, **10**-**22**). Reagents and conditions: (a) K_2CO_3, DMSO, 100 °C, 12 h, or (b) HCl, THF : IPA (3 : 1), 70 °C, 12 h, yield: 22-70%.

As such, strains H37Rv and N0145 were used to identify and rank compounds that target *M. tuberculosis* Cyt-*bd* (when Q203 was added). Compounds that inhibited intracellular ATP level in mycobacteria ("-Q203") but did not show better activity when Cyt-*bcc:aa*$_3$ was inhibited ("+Q203") were presumed to not be targeting Cyt-*bd*, an example being the F_OF_1 ATP synthase inhibitor Bedaquiline (BDQ)[117] which

is equipotent in the presence or absence of Q203. All screening data along with compound molecular mass and calculated cLog*P* are listed in Table 2.1.

Separate placement of a trifluoromethyl group at the *ortho, meta*, *or para* positions of the peripheral phenyl group (compounds **10**, **7** and **11**, respectively) revealed that the *ortho*-CF_3 analogue (**10**) had good potency against BCG and N0145- Mtb (IC_{50} values of 12.4 and 15.5 µM, respectively; when Q203 was added). The *ortho*-CF_3 (**10**) was slightly more potent than the screening hit *meta*-CF_3 (**7**) and *para*-CF_3 (**11**) compounds against those two Mtb strains. The *para*-CF_3 compound (**11**) had slightly improved potency against H37Rv-Mtb but the IC_{50} value was high at 63 µM. Despite the slightly better potency at the *ortho*-position, there is greater availability of *para*-substituted phenyl analogues with which to probe the effect of substituents on SAR.

Considering the phenylethyl analogue (**12**) as electronically and sterically "neutral" we found this benchmark compound to have weak potency against the three strains (IC_{50} from 51 to >100 µM, when Q203 added). However, functionalization at the *para* position of the phenyl group significantly improved potency as the para-OCF_3 compound (**13**) had lower IC_{50} values than the para-CF_3 compound (**11**) (IC_{50} from 11 to 25 µM, in three strains when Q203 was added). In general, all electron withdrawing groups (SF_5, Cl, di-Cl) improved potency as compared to the unsubstituted phenylethyl (**12**) but none were more potent than the *para*-OCF_3 analogue (**13**). Electron donating groups gave diverse results as the *para*-methoxy (**16**) and *para*-dimethylamine (**22**) compounds had (weak) potency akin to the unsubstituted phenylethyl compound (**12**). The *para*-methyl

analogue (**18**) had slightly better potency than **12** (IC_{50} from 41 to >100 μM, in the presence of Q203) but not nearly as potent as the compounds with electron withdrawing groups (**7**, **10**, **11**, **13**, **17**, **20**, and **21**). Interestingly, the most potent compound was the 4-*para*-$C(CH_3)_3$ analogue (**19**) having IC_{50} values of 6 to 18 μM against all three stains (with Q203 added). Structurally, **19** is most like the *para*-SF_5 analogue (**17**) based upon volume[152] but more lipophilic (cLogP of 5.85 for **19** compared to 5.26 for **17**). The scope of active substituents suggests a pocket that can accommodate larger groups (SF_5, *t*-butyl, Cl) and these larger substituents had good potency. Conformational flexibility was probed through the synthesis and screening of the 4-(trifluoromethoxy)phenylethyl (**13**), 4-(trifluoromethoxy)benzyl (**14**) and 4-(trifluoromethoxy)aniline (**15**) analogues. The effect of the linker between the thienopyrimidine core and peripheral phenyl group was interesting in that the compound with the rotatable benzyl sidechain (**14**) was less active than that with aniline (**15**) and nearly 3-fold less active than the phenylethyl compound (**13**) (IC_{50} values of 33 to 96 μM in all three strains, when Q203 was added).

Cpd	Mol wt	cLog *P*	Replicating ATP IC_{50} (μM)					
			BCG		H37Rv		N0145	
			-Q203	+Q203	-Q203	+Q203	-Q203	+Q203
7	323.34	4.91	>50	25.6 ± 4.59	>100	61.7 ± 7.85	>50	23.4 ± 0.39
10	323.34	4.91	>50	12.4 ± 3.36	>100	68.3 ± 10.47	>50	17.4 ± 2.10
11	323.34	4.91	>50	33.1 ± 4.50	>100	63.2 ± 1.55	>50	24.9 ± 0.16
12	255.34	4.02	>50	43.3 ± 9.44	>100	>100	>50	51.5 ± 4.30
13	339.34	5.05	>50	12.6 ± 1.10	>100	24.4 ± 1.52	>50	10.6 ± 0.30
14	325.31	4.40	>50	38.1 ± 7.43	>100	99.8 ± 19.06	>50	36.1 ± 3.80
15	311.28	4.79	>50	22.9 ± 3.55	>100	66.7 ± 1.79	>50	22.8 ± 4.34
16	285.36	3.94	>50	42.8 ± 10.34	>100	>100	>50	45.0 ± 14.63
17	381.39	5.26	>50	27.1 ± 6.38	>100	>100	>50	18.9 ± 2.88
18	269.36	4.52	>50	40.4 ± 11.29	>100	108.3 ± 7.80	>50	37.4 ± 10.23
19	311.44	5.85	>50	5.8 ± 1.06	>100	18.9 ± 9.03	>50	8.5 ± 2.38
20	289.78	4.74	>50	30.4 ± 9.27	>100	83.5 ± 0.97	>50	31.8 ± 9.98
21	324.23	5.33	>50	25.6 ± 8.35	>100	109.3 ± *	>50	35.3 ± 9.49
22	298.41	4.20	>50	38.9 ± 9.08	>100	>100	>50	41.5 ± 15.31
3	555.52	7.25	0.17*	0.09*	0.04*	0.07 ± 0.01	0.01*	0.03*
5	381.36	6.69	>50	0.80 ± 0.07	>100	5.8 ± 1.18	>50	1.6 ± 0.69

Table 2.1 In vitro activity of thieno[3,2-*d*]pyrimidin-4-amines (**7**, **10**-**22**) and control compounds **3** and **5** against three mycobacterial strains (*M. bovis* BCG, *M. tuberculosis* H37Rv, *M. tuberculosis* clinical isolate N0145) IC_{50} values were determined by ATP depletion in the presence and absence of Q203 (see, ESI† for assay details). clog *P* was calculated by PerkinElmer ChemDraw Professional 16.0. Bedaquiline (BDQ) and ND-011992 were used as positive control compounds. IC_{50} values were determined using GraphPad Prism 9. The values reflected in the table represent the average and standard deviation, which were calculated from the IC_{50} values of replicates from two experimental repeats.

Since the increased level of Cyt-*bd* expression in H37Rv-Mtb implied a lower potency of the inhibitors, the extra effort of screening the clinical strain in tandem with more commonly used H37Rv-Mtb strain was justified. While it was possible that strain selectively (either BCG or Mtb) could have been revealed, instead, there was strong activity correlation between the BCG and N0145-Mtb strains for all the compounds screened. Finally, none of the compounds alone inhibited ATP, strongly suggesting that these compounds do target Cyt-*bd* since potency was only revealed when cyt-*bcc:aa*$_3$ was selectively inhibited by Q203. The lack of ATP inhibition against Mtb (or BCG) greatly increases the challenge to discover Cyt-*bd* inhibitors and establishes combination drug therapy as a viable treatment option to use with such inhibitors.

General procedure for base promoted S_NAr for synthesis of compounds 7, 11, 13, 17, 19 22

In a sealed vial, 4-chlorothieno[3,2-*d*]pyrimidine (100 mg, 0.57 mmol), desired amine (0.57 mmol) and K_2CO_3 (79 mg, 0.57 mmol) were dissolved in DMSO (4 mL). The reaction was heated to 100^{o}C for 12 h. The reaction mixture was concentrated to dryness and the residue was dissolved in CH_2Cl_2 and washed with 5% aqueous acetic acid solution (2x), water and brine. The organic phase was collected, dried over sodium sulfate, filtered, and concentrated *in vacuo*. Crude material obtained was purified by either silica gel column chromatography with a gradient of CH_2Cl_2 : ethyl acetate : solvent system (0 to 80%) or recrystallized from hot isopropanol or acetonitrile to afford the product.

General procedure for acid catalyzed S_NAr for synthesis of compounds 12, 14-16, 18, 20, 21

In a sealed vial, 4-chlorothieno[3,2-*d*]pyrimidine (100 mg, 0.57 mmol) and desired amine (0.57 mmol) were dissolved in a 3:1 tetrahydrofuran: 2-propanol solution (8 mL). Next, a drop of 12 M HCl (~0.05 mL) was added and the solution was heated at 70°C for 24 h. The reaction mixture was concentrated to dryness and the residue was dissolved in CH_2Cl_2 and washed with saturated aqueous $NaHCO_3$ solution, water, and brine. The organic phase was collected, dried over sodium sulfate, filtered, and concentrated *in vacuo*. Crude material obtained was purified by either silica gel column chromatography with a gradient of CH_2Cl_2 : ethyl acetate solvent system (0 to 80%) or recrystallized from hot isopropanol or acetonitrile to afford the product.

Conclusions

Herein we described our preliminary SAR assessment of the thieno[3,2-*d*]pyrimidin-4-amines as Cyt-bd inhibitors. This is one of a few published examples of synthetically accessible compounds that can inhibit Cyt-*bd* in mycobacteria. While, the IC_{50} values of the most potent compound (19) are merely good (6.2 µM vs. BCG and 7.3 µM vs. N0145-Mtb, when Q203 was added) this class of compounds can be used as a new tool to probe the mycobacterial oxidative phosphorylation pathway. Based upon this exploratory work, we will endeavor to design new thieno[3,2-*d*]pyrimidin-4-amines with improved potency and acceptable pharmacokinetics to warrant *in vivo* evaluation.

Conflicts of interest

Hsiri Therapeutics has licensed this technology. M.J.M. and G.C.M. own equity in Hsiri. M.J.M. is CSO of Hsiri. G.C.M. and K.P. are consultants to Hsiri. Hsiri Therapeutics did not fund this study and was not involved in study design or interpretation.

Acknowledgements

M.J.M. and G.C.M. acknowledge funding from the NIH R37AI054193. K.P. and G.C.M. acknowledge funding from the NIH R01AI139465. This work was supported in part by the National Research Foundation (NRF) Singapore under its NRF Competitive Research Programme (Project Award Number NRF-CRP18-CRP18-2017-0).

CHAPTER THREE

TESTING THE MEMBRANE AFFINITY OF THIENOPYRIMIDINE DRUG CANDIDATES WITH TIME RESOLVED FLUORESCENCE EMISSION

Contribution of Authors and Co-Authors

Manuscript in Chapter 3

Author: Sarah M. Hopfner

Contributions: Data collection and analysis, co-wrote initial draft of the manuscript

Co-Author: Katelyn M. Duncan

Contributions: Data collection and analysis, co-wrote initial draft of the manuscript

Co-Author: Rhys C. Trousdale

Contributions: Data collection

Co-Author: Mary J. Cloninger

Contributions: Supervision, funding acquisition, writing review & editing

Co-Author: Robert A. Walker

Contributions: Supervision, funding acquisition, writing review & editing

Manuscript Information

Sarah M. Hopfner, Katelyn M. Duncan, Rhys C. Trousdale, Mary J. Cloninger, Robert A. Walker

ACS Molecular Pharmaceutics

Status of Manuscript:

____Prepared for submission to a peer-reviewed journal

_X__ Officially submitted to a peer-reviewed journal

____ Accepted by a peer-reviewed journal

____ Published in a peer-reviewed journal

ACS Molecular Pharmaceutics

Mol. Pharmaceutics., 2022, xx, xx.

DOI: 10.1021/acs.molpharmaceut.xxxxxxxx

TESTING THE MEMBRANE AFFINITY OF THIENOPYRIMIDINE DRUG CANDIDATES WITH TIME RESOLVED FLUORESCENCE EMISSION

Sarah M. Hopfner‡[1], Katelyn M. Duncan‡[1], Rhys C. Trousdale+, Mary J. Cloninger[1,*], Robert A. Walker[1,2,*]

[1]Department of Chemistry and Biochemistry, Montana State University, 103 Chemistry and Biochemistry Building, Bozeman, Montana 59717, United States

[2]Montana Materials Science Program, Montana State University, Bozeman, Montana, 59717, United States

‡Both authors contributed equally to this work.

KEYWORDS: Drug design, drug partitioning, lipid permeability, Log *P*, thienopyrimidines, partition coefficient, cytochrome *bd* oxidase, drug development

Abstract:

Time resolved fluorescence emission spectroscopy was used to study the affinity of structurally related thienopyrimidines for model biological membranes. The thienopyrimidines were chosen due to their potential to block activity in cytochrome-*bd* oxidase, an important protein in *Mycobacterium tuberculosis*. Experiments tested the hypothesis that a large lipophilic log *P* value and a high IC_{50} activity should correlate with bioaccumulation within a lipid vesicle bilayer. Experiments reported herein did not confirm the hypothesis. The thieno[3,2-*d*]pyrimidin-4-amines bearing aryl methyl and *tert*-butyl substituents exhibited evidence of a non-radiative decay pathway induced by association with the model

biological membrane with the methyl substituted species having the strongest membrane affinity. The methyl-substituted thienopyrimidine also displayed a conformationally restricted local solvation environment despite having an intermediate log *P* value and IC_{50} value. These results strongly suggest that targeted protein specificity by these drug candidates is primarily responsible for the observed differences in IC_{50} values across the series of compounds rather than membrane accumulation.

Introduction:

Drug design involves the multiparameter optimization of many physiochemical properties for each therapeutic molecule.[126] For example, compounds having poor bioavailability or off-target toxicity will not move forward in development. One way to enhance the efficacy of a therapeutic is to design it in such a way so that its local concentration in or near its intended target is higher than in the general periplasm. Therefore, knowing the affinity of a drug compound for biological membranes is an important structural consideration.[153-155] A common prediction tool for partitioning behavior is the partitioning coefficient (log *P*), a tool that has been employed since the late 1800's and is still widely used today in drug development.[127, 135-137, 156-157] Log *P* is a helpful, zeroth order measure of solute affinity for biological membranes, but the log *P* scale is also based on a simple equilibrium constant description and fails to account for the specific chemical interactions that occur when a solute is introduced to a biological membrane. In effort to identify the specific chemical interactions that occur when a solute associates with a biological membrane, time-

resolved fluorescence spectroscopy can be a valuable tool for quantifying relative populations and specific interaction mechanisms.

Experiments described in this study use time correlated single photon counting (TCSPC) spectroscopy to measure the lifetimes of different thienopyrimidine solutes in solutions containing vesicles composed of 1,2-dipalmitoyl-*sn*-glycero-3-phosphocholine (16:0 DPPC). This family of solutes are promising drugs to combat *Mycobacterium tuberculosis* (Mtb). While there are many ways of disabling Mtb, whether through interruption of cell wall synthesis[158] or inhibition of DNA replication,[159] one of the most promising methods of sterilizing Mtb is through cessation of energy metabolism.[112] Mtb is an obligate aerobe, meaning that it requires oxygen in order to grow. Under low oxygen conditions Mtb persists in a non-replicating state[160], [109] and requires oxidative phosphorylation to make ATP.[112-113] There are two terminal oxidases in this pathway; cytochrome *bcc:aa*$_3$ (cyt-*bcc:aa*$_3$) and cytochrome *bd* (cyt-*bd*). Cyt-*bcc:aa*$_3$ functions as the main oxidase, and cyt-*bd* is upregulated only when cyt-*bcc:aa*$_3$ is inactivated.[122] Thus, Cyt-*bd* protects Mtb against oxidative stress and, more importantly, against chemotherapies.[123]

The thienopyrimidine scaffold is of interest to medicinal chemists, and thienopyrimidine derivatives have been studied for use as anti-bacterial agents[161] including those that target Mtb.[149-150, 162] Various thienopyrimidine derivatives have also shown promising activity against cancer,[146, 163-165] autoimmune diseases,[148] and malaria.[166] Because of their noteworthy biological activity, assessing the membrane partitioning properties of the thienopyrimidine derivatives is an

important consideration when developing mechanisms to describe thienopyrimidine activity. We hypothesized that partitioning into a biological membrane will correlate with anti Mtb activity; thienopyrimidine derivatives that partition into the DPPC membrane should exhibit better IC_{50} values for a transmembrane target protein such as the respiratory oxidase cytochrome *bd* (cyt-*bd*) in *Mycobacterium tuberculosis* (vide infra). To test this hypothesis, our studies focused on three specific thienopyrimidine solutes having different log *P* values and very different IC_{50} values (Figure 3.1).

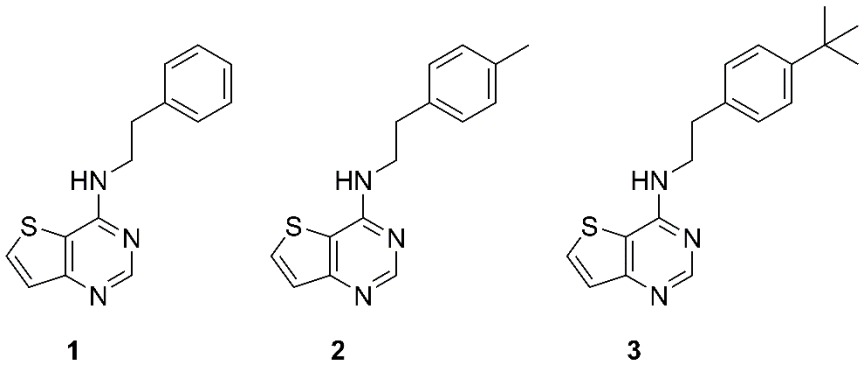

1 **2** **3**

Figure 3.1 Thieno[3,2-d]pyrimidin-4-amines **1**–**3**.

All three compounds share a phenethylamine attached to the same thieno[3,2-*d*]pyrimidine heterocyclic ring. These three solutes are distinguished by the substitution in the 4' position of the aryl ring. Compound **1** is the most hydrophilic, having a log *P* value of 4.0. Compound **3** with its tert-butyl group is the most hydrophobic solute and has a log *P* value of 5.9. With its methyl group at the para position, Compound **2** is intermediate in its hydrophobicity and log *P* value (4.5). Of these three solutes, Compound **3** is predicted to be the most promising

candidate for further development as an anti-TB agent with an IC_{50} of 9 μM against N0145-Mtb in the presence of Q203.[119] Compounds **1** and **2** have weaker activity against N0145-Mtb (IC_{50} values of 52 and 37 μM, respectively when Q203 was added).

Compounds that simultaneously inhibit cyt-*bcc:aa*$_3$ and cyt-*bd* have proven lethal to replicating and non-replicating Mtb.[124] For this reason, the IC_{50} values of compounds **1**–**3** were studied previously with coadministration of the cyt-*bcc:aa*$_3$ inhibitor Q203. Although the structure of cytochromes *bd* have been reported in *Escherichia coli (E. coli),*[167-168] *Geobacillus thermodenitrificans (G. th),*[169] and *Mycobacterium smegmatis (M. smegmatis),*[170] significant structural differences between the cytochromes *bd* of these three organisms were noted, indicating that the existing structures cannot serve as useful comparisons for cyt-*bd* in Mtb.[170] Compounds that effectively inhibit cyt-*bd* activity have the potential to dramatically improve the destruction of Mtb, making the recently reported structure of cyt-*bd* in Mtb[128] a spectacular benefit to the design of drugs to inhibit cyt-*bd*.[167-168] Since the structures of cyt-*bd* are unknown in other prokaryotes, having additional methods of predicting potency is important for the development of antimicrobial agents.

Experiments were carried out with several structurally related compounds to assess whether the calculated log *P* values tracked with measured membrane affinity. DPPC vesicle bilayers were chosen because DPPC is often the dominant lipid in eukaryotic cell membranes. Real biological membranes are, of course, more complex than a single component lipid bilayer systems as biological membranes also contain proteins, carbohydrates, and cholesterol as described by

the fluid mosaic model.[129-130] Nevertheless, single-component lipid vesicle bilayers have proven useful in determining the physiological partitioning tendencies of aspirin,[139] methotrexate,[140] and doxorubicin.[141] Furthermore, as one criterion in the Lipinski Rule of 5 guidelines used to assess whether or not a given pharmaceutical is a candidate for further development, a solute's log *P* value is assumed to be an important indicator of whether or not it will bioaccumulate.[134, 171] Recent reports suggest that adding heterogeneity to lipid membranes (in the form of other constituents) can change quantitative (but not qualitative) solute partitioning behavior.[172]

For those solutes that fluoresce, TCSPC has proven an invaluable tool for identifying solute partitioning tendencies. Reported studies have found that small structural changes to the solute alter partitioning behavior drastically.[173-176] In addition, chemical complexity in the form of other biologically relevant, available solutes change a solute's partitioning tendencies and local solvation environment. In the studies discussed below, a suite of independent methods was used to assess the properties and structures of thienopyrimidines in aqueous buffer and the tendencies of these structurally related solutes to accumulate in DPPC membranes. TCSPC data provide important evidence not only of membrane association, but also where in the membrane the solutes partition.

While only weakly fluorescent, the thienopyrimidine compounds (Figure 3.1) do have measurable time dependent fluorescence that depends on the local solvation environment. This fluorescence behavior allows us to employ TCSPC for analysis of each compound's partitioning behavior in 1,2-dipalmitoyl-*sn*-glycero-3-

phosphocholine (DPPC) vesicles. The data show that despite having only an intermediate IC_{50} value, Compound **2** showed the strongest affinity for DPPC bilayers. Specifically, Compound **2** displayed a conformationally restricted local solvation environment and evidence of membrane assisted aggregation predicted to be due to association with the DPPC charged headgroup in concentrations of 40% and 4%, respectively. In contrast, neither Compound **1** nor Compound **3** showed any detected membrane affinity. Taken together, these findings imply that the efficacy of this next generation of anti TB drugs likely operate through direct association with the cytochrome *bd* oxidase protein in the cell membrane, rather than through enrichment in/near the membrane followed by less specific binding.

Materials & methods:

Synthesis Materials.

ACS grade sodium hydroxide (97%), ACS plus grade hydrochloric acid (37%), ACS grade potassium hydrogen phthalate (99% purity) were purchased from Sigma-Aldrich Chemical Co. (Milwaukee, WI). All working solutions for pKa determination were prepared with degassed Aquafina water. The titrant solution of NaOH was prepared at 0.01 M and standardized with potassium hydrogen phthalate. The exact concentration was determined to be 0.009 ± 0.001 M. This solution was stored in a capped plastic bottle. The standardized NaOH solution was then used to standardize the hydrochloric acid solution. The hydrochloric acid solution was found to be 0.014 ± 0.0005 M. The PASCO Scientific pH probe was connected to a Model 270 Denver Instrument pH meter. The pH meter was

calibrated with standard buffers at pH 4.01 ± 0.01 (0.05 M potassium biphthalate), pH 6.86 ± 0.01 (0.05 M potassium phosphate monobasic – sodium hydroxide), pH 10.01 ± 0.02 (0.05 M potassium carbonate – potassium borate – potassium hydroxide) Buffers were purchased from Fisher Scientific, Pittsburgh, PA.

Synthesis

The thieno[3,2-*d*]pyrimidin-4-amines were prepared as reported previously.[162]

1D Selective Gradient Nuclear Overhauser Effect (NOE) spectra were recorded at 300 K on a Bruker 600 MHz Avance III NMR Spectrometer using standard acquisition parameters: spectral width 12,019 Hz, acquisition time 2.73 seconds, pulse width 8 µs, relaxation delay 2 s, mixing time 0.3 seconds, number of scans 128. Peaks were selected for excitation in each experiment.

Sample Preparation for pKa Measurements

Compounds were dissolved in 2 mL of DMSO, diluted with water, sonicated, heated, and allowed to stir for 1 week. The solution was continuously mixed with a magnetic stirrer. Titrations were performed in triplicate at ambient temperature (20 °C). A Hamilton syringe was used to incrementally add sodium hydroxide or hydrochloric acid, and the solution was equilibrated to reach a stable pH reading prior to the next acid or base addition. After each experiment, the pH probe was thoroughly washed with Aquafina water and recalibrated.

Time-Resolved Fluorescence Measurement

Materials. Solvents were purchased from Sigma-Aldrich and used as received. Millipore water (18.2 MΩ) was used to make 10 mM carbonate buffer (pH = 7). 1,2-Dipalmitoyl-*sn*-glycero-3-phosphocholine (16:0 DPPC) was purchased from Avanti Polar Lipids (Alabaster, AL). All bulk solvent solutions were made at a 45 μM concentration and lipid vesicles used for fluorescence experiments were made at 1.5 mM concentration.

Lipid Bilayer Vesicle Preparation.

Lipid vesicles were prepared by dissolving DPPC in chloroform and subsequently removed via rotary evaporation, resulting in a thin lipid film. The resulting lipid film was rehydrated with 45 μM solution of **1**, **2**, or **3** in 10 mM carbonate buffer to form a lipid vesicle solution. The solution was sonicated for 30 minutes at ~50 °C. The solution was then passed through a PTFE syringe filter (450 nm) to remove giant unilamellar vesicles. The solution was then subsequently heated to 50 °C and passed through an Avanti Mini Extruder 11 times with a membrane pore size of 200 nm.

Time-Correlated Single-Photon Counting (TCSPC).

Fluorescence lifetimes were measured using a Ti:sapphire oscillator (Coherent Chameleon, 80 MHz, 85 fs pulse duration, 680-1040 nm wavelength range) coupled with an APE autotracker capable of frequency tripling the fundamental to select solute specific excitation wavelengths. A Conoptics model 350-80 modulator

was used to reduce the repetition rate to 4 MHz. Picoquant PicoHarp 300 and FluoTime 200 software were used for data collection. Samples were equilibrated at reported temperatures for 5 minutes using a Quantum Northwest TC125 control (Seattle, WA). A long pass filter (90% transmission >300 nm) was placed after the sample to reduce scattering from the vesicles. Photon emission was collected at 370 nm, a wavelength that overlapped all solutes in each of the bulk solvents. Excitation wavelength was 260 nm for all solutes, a wavelength that overlapped all solutes in each of the bulk solvents.

Time-resolved emission data were collected for each compound in bulk solvents chosen to mimic the unique environments a solute could solvate within lipid bilayer vesicle: carbonate buffer to model the compound not integrating into the lipid bilayer, acetonitrile to model the polar aprotic headgroup, and methanol to model the polar protic headgroup when water has integrated into the membrane. Such an approach has been used previously to approximate small molecule partitioning into lipid bilayer membranes.[177-178] The fluorescence behavior of each compound was measured in cyclohexane used to model the nonpolar tails, however, were excluded from this work due to low solubility. Next, the fluorescence behavior was analyzed in vesicle-containing solutions. The corresponding lifetimes and amplitude parameters were independently calculated and adjusted to optimize $\chi 2$. When possible, a linear combination of lifetimes found in the bulk solvents (mentioned above) was created to assign local solvation environments of the compound in a lipid bilayer vesicle. The fluorescence decay and amplitude expressions are shown in Eq. 1 where Ai and τi are the amplitude and lifetime of

the ith component, respectively, and IRF is the instrument response function allowing for reconvolution of the histogram.

$$I(t) = \int_0^t IRF\ (t') \sum_{i=1}^{n} A_i e^{-\frac{t-t'}{\tau_i}}\, dt' \qquad (1)$$

Each trace was fit independently, without any constraints, for the lifetimes or amplitudes with a typical χ2 between 0.9 and 1.1 when accounting for, at most, four lifetimes. Reported data represent averaged lifetimes from three experiments with independently prepared, equivalent samples. Lifetime uncertainties are reported as ± 0.2 ns because and typical uncertainties in amplitudes are ± 0.03. Error bars presented in this work are a result of 3 trials averaged together with a single standard deviation reported for the 3 averaged trials. The averaged lifetimes and amplitudes are reported for each temperature.

Results:

As noted above, thienopyrimidines have been studied for a variety of biological applications. One particularly compelling application is their development as anti-*Mycobacterium tuberculosis* (Mtb) compounds. Previously, Moraski and co-workers have reported that thieno[3,2-*d*]pyrimidin-4-amines **1**–**3** (shown in Figure 3.1) have encouraging activity against *Mycobacterium bovis* BCG, *Mycobacterium tuberculosis* H37Rv, and *Mycobacterium tuberculosis* clinical isolate N0145.[162] As summarized in Table 2.1, the phenethyl analog **1** was found to have weak potency when co-administered with Q203. Additional experiments demonstrated that Mtb requires oxidative phosphorylation for growth.[112-113] Mtb has two terminal oxidases

within the oxidative phosphorylation pathway, cytochrome *bcc:aa*$_3$ (cyt-*bcc:aa*$_3$) serving as the main aerobic oxidase and cyt-*bd* helping in a less-efficient, redundant manner. Q203 binds to the cytochrome b subunit on cyt-*bcc:aa*$_3$, deactivating its function.[119] When this occurs, cyt-*bd* activity is upregulated[122] and sustains ATP production sufficiently for Mtb to survive in a non-replicating state.[109], [110] In this way, Mtb is shielded from complete shutdown of the oxidative phosphorylation pathway from cyt-*bcc:aa*$_3$ inhibitors such as Q203. We have shown that inhibition of both cyt-*bcc:aa*$_3$ and cyt-*bd* is bactericidal against Mtb.[124] The 4-methylphenethyl analog **2** had better potency than **1**, and the most potent derivative was found to be the 4-*tert*-butylphenethyl analog **3** (in the presence of Q203; none of the described compounds displayed significant activity in the absence of Q203). Interestingly, compound **3** showed the greatest potency against all three bacterial strains (BCG, H37Rv, and N0145) and has the highest log *P* value. The partitioning coefficients for **1**–**3** all indicate a strong preference for solubility in the organic phase and, by inference, a strong tendency to partition into membranes.

Compound	Log *P*	BCG IC_{50} (μM) (+Q203)[a]	H37Rv IC_{50} (μM) (+Q203)[a]	N0145 IC_{50} (μM) (+Q203)[a]
1	4.0	43 ± 9	>100	52 ± 4
2	4.5	40 ± 11	108 ± 8	37 ± 10
3	5.9	6 ± 1	19 ± 9	9 ± 2

Table 3.1. [a]In vitro activity of thieno[3,2-*d*]pyrimidin-4-amines against three Mycobacterial strains (*M. bovis* BCG, *M. tuberculosis* H37Rv, *M. tuberculosis* clinical isolate N0145) – previously reported values.[162]

In this work, we examine how each thieno[3,2-*d*]pyrimidin-4-amine compound interacts with a lipid bilayer vesicle using time-resolved fluorescence spectroscopy. Prior to the solutes being introduced to lipid vesicle-containing solutions, the compounds were first modeled in bulk solvents. The bulk solvents were chosen to mimic the various solvation environments of a lipid bilayer vesicle: acetonitrile for the polar aprotic headgroup region, cyclohexane for the nonpolar tails, and methanol for a polar protic headgroup region that has water percolated into the membrane. Due to the low solubility limit of these compounds in cyclohexane, the behavior of compounds **1**–**3** in a nonpolar environment is omitted from this work. The vesicles in this study are prepared in a 10 mM carbonate buffer (pH 7) and therefore represent the solute remaining in aqueous solution and not integrating with the bilayer. The steady-state excitation and emission peak wavelengths as well as the fluorescence lifetimes of compounds **1**, **2**, and **3** in carbonate buffer, methanol, and acetonitrile are shown in Table 2.2. The time-resolved fluorescence decay of **1**–**3** is shown in Figure 3.2 and steady-state excitation and emission spectra are found in the Supporting Information (Figures S19 – S20, respectively).

Solvent	Compound 1			Compound 2			Compound 3		
	λ_{exc} (nm)	λ_{em} (nm)	τ_f (ns)	λ_{exc} (nm)	λ_{em} (nm)	τ_f (ns)	λ_{exc} (nm)	λ_{em} (nm)	τ_f (ns)
Carbonate Buffer	246/298	360	0.27 (0.97), 1.45 (0.03)	270	395	0.29 (0.69), 1.48 (0.31)	253/298	360	0.28 (0.94), 1.44 (0.06)
Methanol	245/295	350	0.22	245/295	350	0.22 (0.99), 1.60 (0.01)	270	350	0.21 (0.97), 0.54 (0.03)
Acetonitrile	245/295	350	0.18	245/295	350	0.18 (0.98), 2.05 (0.02)	245/290	350	0.18 (0.99), 2.00 (0.01)

Table 3.2 Fluorescence properties of **1**–**3** in each of the bulk solvents. Absorbance spectra along with fluorescence excitation and emission spectra are provided in the Supporting Information (Figures S19-S20). Uncertainties in reported lifetimes are ± 0.2 ns. Numbers in parentheses next to lifetimes are amplitudes of that lifetime. In the case of a biexponential fluorescence decay, the lifetime with the largest amplitude will be used as an indicator for that local solvation environment.

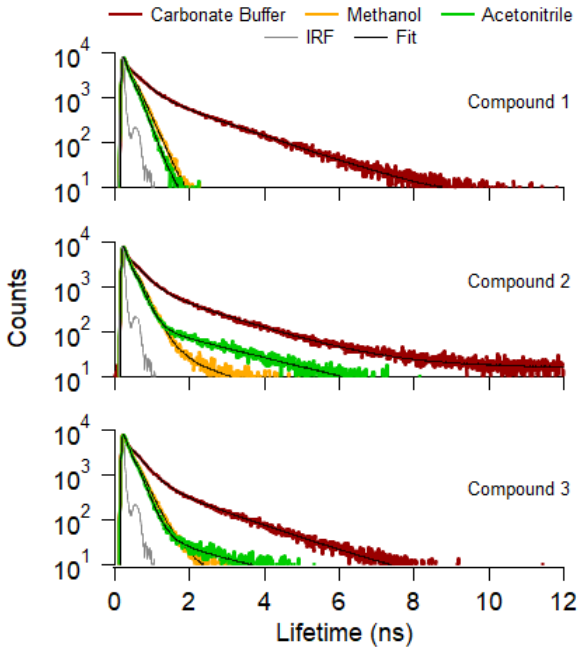

Figure 3.2 TCSPC spectra of 45 µM solutions of **1**, **2**, or **3** in each of the bulk solvents at 20 °C. Results from fitting these emission traces to Eq. 1 are reported in Table 3.2. Gray trace is instrument response function (IRF).

The lifetimes of each compound differ very little between each of the bulk solvents, with the major lifetime being 0.18 – 0.29 ns (Table 3.2). Compound **1** only displays

a dual lifetime in carbonate buffer, while **2** and **3** display dual lifetimes in all three solvents, albeit with one of those lifetimes typically having very small amplitudes. For amplitudes ≤ 3%, the lifetime is not considered significant and is reported solely for fitting purposes.

Once the fluorescence behavior of each compound was characterized, each compound, separately, was introduced to a solution of lipid bilayer vesicles and was analyzed as a function of temperature in 10 °C increments from 10 °C to 70 °C and then back to 10 °C (Figure 3.3). The variable temperature protocol was used to analyze the effect of the compounds on the vesicle as it transitions from the gel phase through the transition temperature into the liquid crystalline phase ($T_{gel\text{-}lc}$: 41 °C) and to evaluate each compound's membrane affinity as a function of membrane phase. Each trace was fit using Eq. 1. Lifetimes and corresponding amplitudes for selected temperatures are reported in Table 3.3. The full list of lifetimes at all temperatures studied is provided in the Supporting Information (Table B.1).

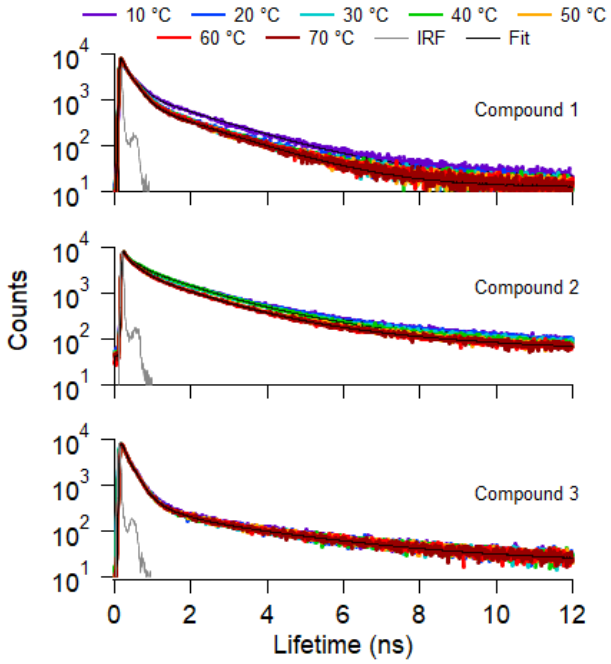

Figure 3.3 TCSPC spectra of 45 µM solutions of **1**, **2**, or **3** in a DPPC lipid vesicle solution as a function of temperature. Top panel: **1**; middle panel: **2**; bottom panel: **3**. Results from fitting these emission traces to Eq. 1 at selected temperatures are reported in Table 3.3. A full summary of data taken at all temperatures is in the Supporting Information (Table B.1). Gray trace is instrument response function (IRF).

temp. (°C)	Compound 1		Compound 2				Compound 3		
	buffer τ_1 (A_1)	buffer τ_2 (A_2)	buffer τ_1 (A_1)	buffer τ_2 (A_2)	New K_{rad} τ_3 (A_3)	Conf. Restricted τ_4 (A_4)	buffer τ_1 (A_1)	buffer τ_2 (A_2)	New K_{rad} τ_3 (A_3)
10	0.25 (0.89)	1.71 (0.11)	0.31 (0.38)	1.40 (0.19)	3.89 (0.04)	0.06 (0.39)	0.19 (0.93)	0.84 (0.05)	3.60 (0.02)
30	0.23 (0.92)	1.69 (0.08)	0.28 (0.44)	1.35 (0.21)	3.94 (0.04)	0.05 (0.32)	0.18 (0.92)	0.70 (0.06)	3.22 (0.02)
50	0.23 (0.92)	1.63 (0.08)	0.25 (0.48)	1.37 (0.19)	4.22 (0.03)	0.08 (0.30)	0.17 (0.93)	0.80 (0.05)	3.49 (0.02)
70	0.22 (0.93)	1.61 (0.07)	0.24 (0.54)	1.39 (0.22)	5.05 (0.02)	0.10 (0.22)	0.17 (0.91)	0.68 (0.08)	3.03 (0.02)
50	0.23 (0.92)	1.64 (0.08)	0.24 (0.41)	1.30 (0.20)	3.96 (0.03)	0.09 (0.36)	0.17 (0.91)	0.81 (0.07)	3.23 (0.03)
30	0.25 (0.90)	1.67 (0.10)	0.27 (0.42)	1.30 (0.26)	3.36 (0.05)	0.07 (0.28)	0.18 (0.87)	0.79 (0.09)	3.06 (0.04)
10	0.25 (0.89)	1.70 (0.11)	0.31 (0.34)	1.36 (0.23)	3.58 (0.06)	0.09 (0.37)	0.18 (0.85)	0.90 (0.10)	3.22 (0.05)

Table 3.3 Selected fluorescent lifetimes (in ns) and amplitudes (in parentheses) for 1–3 in solutions of DPPC vesicles obtained between 10 and 70 °C and back down to 10 °C in 10 °C increments. Uncertainties in lifetimes are ± 0.2 ns; uncertainties in amplitudes are ± 0.03.

Figures 4 and 5 provide a visual representation of the lifetimes and lifetime contributions listed in Table 3.3 as a function of temperature and bilayer phase. Compound **2** was best fit to 4 lifetimes (at 20˚C) with τ1 (0.30 ns) and τ2 (1.40 ns) matching **2**'s behavior in carbonate buffer. The third long lifetime (τ3: ~3.90 ns) does not match any behavior observed in bulk solvents and indicates a new radiative decay pathway (new K_{rad}). An origin of this new emission is proposed in the Discussion section below. The fourth lifetime is extremely short (τ4: 0.06 ns). We propose that this lifetime originates from compound **2** in a conformationally restricted environment where it interacts with the bilayer below the $T_{gel\text{-}lc}$. The basis for this assignment is also considered in the Discussion section. Compound **3** was best fit to 3 lifetimes with τ1 and τ2 that match **3** in bulk carbonate buffer, and a long (~3.60 ns) lifetime that again does not match any observed behavior in bulk

solvents. The low amplitude of the fluorescence decay for the third lifetime suggests that **3** remains largely in the carbonate buffer rather than partitioning into the vesicle. This result stands in contrast to the anticipated behavior based on the large log *P* value for **3**. As seen in Figures 4 and 5, solute fluorescence shows no strong dependence on temperature or bilayer phase for any of the compounds in a lipid vesicle solution. There is a slight variation at higher temperatures above the $T_{gel\text{-}lc}$ for **2** (τ3: 5.05 ns); however, the amplitude for the third lifetime approaches zero (2%) at these elevated temperatures and therefore is present strictly for fitting purposes. An important point to note is that the number of lifetimes chosen to fit a fluorescence decay is based on the χ2 parameter for a value between 0.9-1.1 using the lowest number of exponentials required to do so. These fits are carried out independent of any results measured for the bulk solvents.

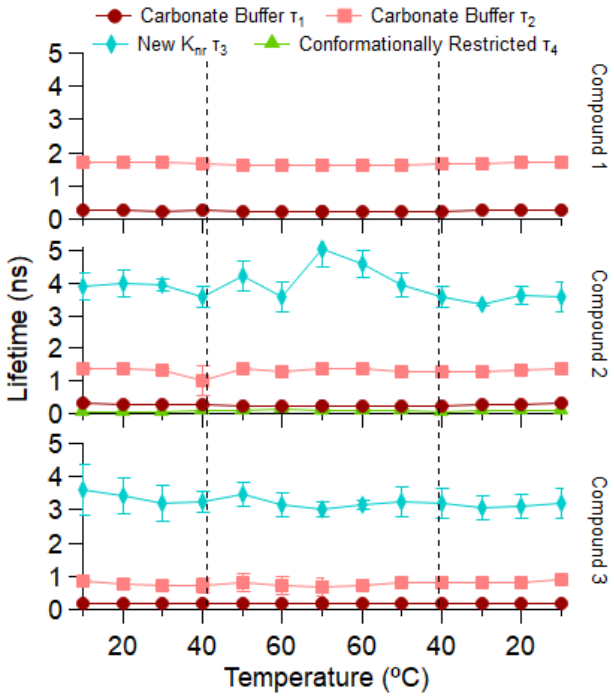

Figure 3.4 Fluorescence lifetimes of each compound in solutions of DPPC vesicles as a function of temperature: carbonate buffer (τ1, burgundy circles; τ2, pink squares), possible new non-radiative decay (K_{nr}) pathway (τ3, teal diamonds), conformationally restricted environment (τ4, green triangles). Dashed lines show the temperature (41 °C) at which the vesicle transitions between the gel phase and the liquid-crystalline phase. Note that the x-axis follows an experiment as the temperature is raised (to 70˚C) and then lowered (to 10˚C). Error bars on each point reflect one standard deviation of uncertainty from 3 measurements averaged together. In some cases, the uncertainty is smaller than the symbols used to represent the data.

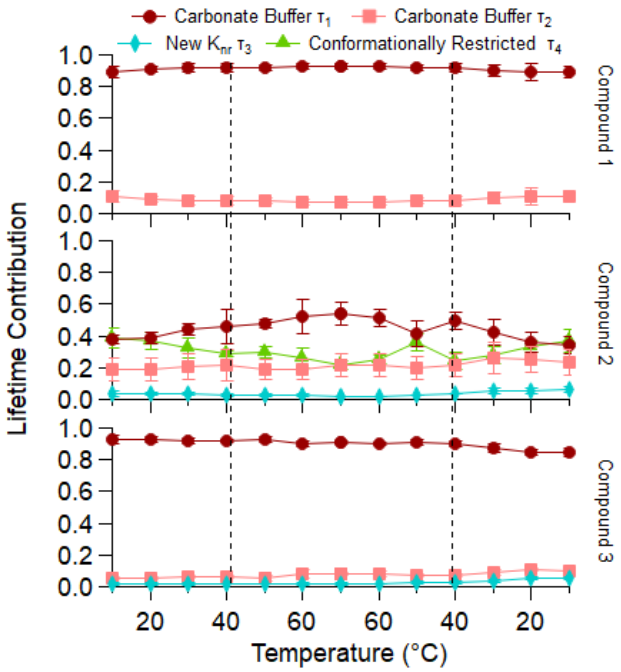

Figure 3.5 Lifetime contributions of **1**–**3** in solutions of DPPC vesicles as a function of temperature: carbonate buffer (τ1, burgundy circles; τ2, pink squares), possible new non-radiative decay (K_{nr}) pathway (τ3, teal diamonds), conformationally restricted environment (τ4, green triangles), Dashed lines show the temperature (41 °C) at which the vesicle transitions between the gel phase and the liquid-crystalline phase. Note that the x-axis follows an experiment as the temperature is raised (to 70˚C) and then lowered (to 10˚C). Error bars on each point reflect one standard deviation of uncertainty from 3 measurements averaged together. In some cases, the uncertainty is smaller than the symbols used to represent the data.

Compound **2** with a log *P* value of 4.5 displayed the largest change in fluorescence lifetime in the presence of DPPC vesicles, although the nature of this interaction is mysterious given that neither the long new lifetime (τ3: ~3.90 ns) nor extremely short new lifetime (τ4: 0.06 ns) matches results from the bulk solvent experiments. To understand these lifetimes and assign significance to the third and fourth lifetime, **2** was frozen in carbonate buffer to observe its fluorescence behavior in a conformationally restricted environment (Figure 3.6 and Table 3.4). A similar

analysis has been carried out recently to simulate the effects of conformational restriction in confining environments.[179]

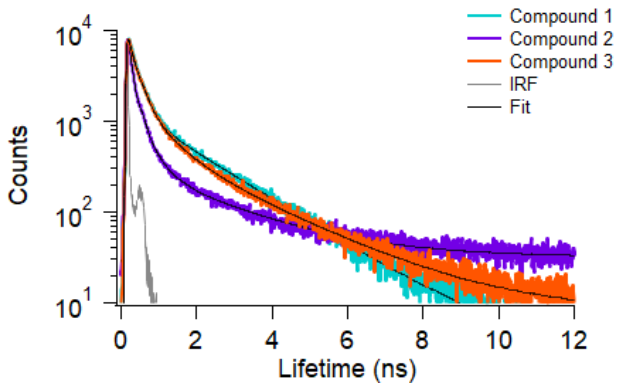

Figure 3.6 TCSPC spectra of 45 µM solutions of **1**, **2**, or **3** in a frozen carbonate buffer. Results from fitting these emission traces to Eq. 1 are reported in Table 3.4. Gray trace is instrument response function (IRF).

Compound	τ_1 (A_1)	τ_2 (A_2)	τ_3 (A_3)
1	0.21 (0.89)	1.68 (0.11)	
2	0.10 (0.88)	0.37 (0.10)	2.23 (0.02)
3	0.18 (0.82)	0.66 (0.12)	2.18 (0.05)

Table 3.4 Fluorescent lifetimes (in ns) and amplitudes (in parentheses) of **1**–**3** in frozen carbonate buffer solutions. Uncertainties in lifetimes are ± 0.2 ns; uncertainties in amplitudes are ± 0.03.

The results found in Table 3.4 from fitting the fluorescence decays in Figure 3.6 display a short lifetime that accounts for the majority of the fluorescence decay for all three compounds. This short lifetime also matches closely with the dominant lifetime for compounds **1**, **2**, and **3** in bulk aqueous buffer. Compound **1** emission decay also displays the second lifetime generally associated with solvation in the carbonate buffer (1.68 ns, 0.11). From this result, we conclude that the frozen

aqueous matrix does not force compound **1** to experience solvation forces that are any different than the liquid carbonate buffer. Compounds **2** and **3** each show a second lifetime on the order of 0.6 ns with small but measurable amplitudes (~0.1). The long, 2.2 ns lifetimes in the **2** and **3** emission traces are longer than long aqueous lifetime (1.5 ns) lifetime and relatively close to the long, small amplitude lifetimes shown by **2** and **3** in polar, aprotic solvents like acetonitrile.

Discussion:

The studies described above were motivated by the hypothesis that membrane affinity and resulting bioconcentration could be causing differences in efficacy, as characterized by the differences in IC_{50} values for **1**–**3**. While our findings do not support the original hypothesis, they do highlight some very unusual photophysical behavior of this class of compounds. Differences in membrane affinity inferred from the TCSPC measurements also strongly suggest that simple log *P* considerations are not sufficient to predict anti-Mtb activity for this family of compounds. Compounds **1**-**3** are neutral at physiological pH (pKa measurements are found in the Supporting Information, Figures S1 – S18, respectively), which suggest alternative mechanisms – specifically direct compound-protein binding – are responsible for deactivating these bacteria. The balance of this section will consider several surprising discoveries made about how compounds **1**–**3** behave in bulk buffer and in the presence of simple lipid vesicle membranes. These discoveries include: 1) preferential association of compound **2** with membranes

relative to compounds **1** and **3**; 2) the origin of the very short lifetime of **2** in vesicle solutions; and 3) the origin of the long (≥ 3ns) lifetime in solutions containing DPPC vesicles shown by compounds **2** and **3**.

Unique membrane affinity of compound **2** –
a breakdown in log *P*

Time-resolved fluorescence measurements of compounds **1**, **2**, and **3** introduced to lipid bilayer vesicle solutions display unique and distinctive partitioning behavior. As shown in Figures 4 and 5, compound **1** displays two fluorescence lifetimes that closely match the lifetimes found for **1** in bulk carbonate buffer. This result strongly suggests that **1** does not partition into the bilayer despite its log *P* value of 4.0 and instead remains in aqueous solution (Figures 3-5 and Table 3.3). From these results, we conclude that if compound **1** associates with the DPPC lipid bilayer, it does so at concentrations below the detection limits of our instrumentation.

Compound **2** displays four unique fluorescence lifetimes all with significant amplitudes (Figures 4-5 and Table 3.3). The first and second lifetime match that of **2** in a bulk carbonate buffer and retain the 65/35% amplitude ratio. The third and fourth lifetimes, 3.89 ns (4%) and 0.06 ns (39%), respectively, do not match any lifetimes found in any bulk solvent tested. Given that these lifetimes are present in the DPPC-vesicle containing solutions but not in the simple buffer itself, we attribute these two new lifetimes to compound **2** associating with the lipid bilayer. Compound **2** has a calculated log *P* value of 4.5, meaning that the solute is expected to have a strong tendency to partition into biological membranes. Despite

the fact that compound 1 with its log *P* of 4.0 does not appear to associate with DPPC vesicles, the behavior of compound **2** is consistent with membrane affinity. For Compound **3**, the shortest lifetime found in DPPC vesicles, τ1: 0.19 ns (93%), matches that in bulk carbonate buffer. Compound **3** in DPPC vesicle containing solutions also shows an intermediate lifetime at τ2: 0.84 ns (5%) that is similar to the 0.6 ns lifetime observed from compound **3** emission in the frozen carbonate buffer. Finally, compound **3**, like compound **2**, shows a third, longer fluorescence lifetime, 3.60 ns, albeit with very low amplitude (2%). The intermediate lifetime may be consistent with **3** associating with the bilayer in a way that restricts conformational freedom (as is the case in frozen carbonate buffer), but the amplitude of this contribution to the decay trace does not scale with anticipated behavior based on log *P*.

Origin of short lifetime in DPPC-Compound **2** system

Perhaps the most dramatic change for any of the compounds studied in carbonate buffer and carbonate buffer with DPPC vesicles was the emergence of a very short decay (≤ 0.1 ns) component for compound **2** that accounted for ~33% of the decay trace total amplitude. Typically, a lifetime this short points to very efficient non-radiative decay. Subsequent experiments carried out with compound **2** in a frozen carbonate buffer (with no vesicles) also showed an extremely short fluorescence lifetime, 0.10 ns (88%), and a third long fluorescence lifetime (2.23 ns). Based on this frozen-buffer result, we propose that if compound **2** is integrating into the bilayer, the extremely short lifetime (τ4: 0.06 ns) reflects a geometrically restricted

local solvation environment. Similar effects have been reported for solutes adsorbed to strongly associating solid-liquid interfaces where close registry between an aqueous solvent and a hydrophilic silica substrate creates a cage-like structure around adsorbates. This cage-like structure restricts isomerization after photoexcitation and markedly shortens the adsorbate's fluorescence lifetime relative to bulk solution limits.[179-180] Drawing on the findings from these earlier studies, we propose that the sub 0.2 ns lifetime observed for compound **2** in the DPPC solutions results from the solute associating with the membrane in such a way so as to restrict its conformational mobility following photoexcitation. While the excited state photophysical behavior of compounds **1**–**3** remains unknown, the behavior exhibited by compound **2** is consistent with a photoexcited solute that is unable to be stabilized by its surrounding solvation environment and therefore relaxes back to the ground state through a non-radiative decay pathway.

Origin of long lifetime in DPPC-Compound **2** and **3** systems

A lifetime common to the emission decay from both compounds **2** and **3** in DPPC solutions is longer than all other observed lifetimes. Although this lifetime always shows a small amplitude, the effects of this ≥3 ns lifetime are readily evident in the decay traces of DPPC containing solutions (Figure 3.3) and is completely absent in simple carbonate buffer solutions. A longer lifetime implies greater stabilization of a solute's excited state electronic structure.[181-183] Given that this long lifetime appears only in vesicle containing solutions, we assign this radiative decay pathway to a small population of compounds **2** and **3** that interact with a part of the

lipid membrane in a way that still allows either the solute or the membrane to reorganize itself following photoexcitation.

We explored the possibility that this new lifetime resulted from a small population of compounds **2** and **3** having a different conformation within or near the DPPC bilayer by measuring the NOE spectra of these species in different solvents. However, these experiments showed no obvious intramolecular conformational signatures denoting a folded or otherwise contorted structure (NOE spectra are presented in Supporting Information). We also considered that the long lifetime may result from excited state isomerization as related families of solutes are known to incorporate multiple rotamer and twisted conformations of the aromatic rings.[184-185] Furthermore, thienopyrimidines are known to aggregate in solution leading to a phenomenon described as aggregate induced emission.[186]

While our results cannot identify specific conformations, and the corresponding amplitudes associated with this long lifetime are very small, the observed behavior is consistent with compounds **2** and **3** aggregating through some sort of lipid-membrane assisted mechanism. Evidence supporting this hypothesis comes in part from thienopyrimidines known tendency to aggregate in solution,[186] and in part from our observation that this long lifetime (that would coincide with significant enhancement in emission intensity from solute aggregate formation) becomes statistically insignificant at higher temperatures where thermal energy would be expected to keep aggregates from forming.

Overall, the fluorescence lifetimes obtained from the TCSPC studies reported herein indicate that none of the studied thienopyrimidines **1**–**3** were found to

accumulate in measurable amounts in the DPPC vesicles. These results suggest that membrane partitioning is not the most important factor in determining the activity of the thienopyrimidines against Mtb. This insight suggests that the IC_{50} values of compounds **1**–**3** likely correlate to specific binding mechanisms of cyt-*bd* rather than to differences in concentrations in biological membranes due to differences in bioaccumulation.

Conclusion:

Time-resolved fluorescence spectroscopy was employed to study the membrane affinity of three thieno[3,2-*d*]pyrimidin-4-amines compounds all having a phenethylamine substituent attached to the same heterocyclic core. Compounds **1**–**3** differ only in the substituent at the para-position on their phenethyl group. It was hypothesized that the compounds' membrane affinities would correlate with their activity as measured by their IC_{50} values. Therefore, if a compound displays significant IC_{50} values for intended target proteins, those same compounds are expected to display appreciable partitioning behavior into DPPC lipid membranes. All three thienopyrimidine compounds displayed log *P* values indicating a strong membrane preference, with log *P* values of 4.0, 4.5, and 5.9 for **1**, **2**, and **3**, respectively. Compound 3 displayed the most promising IC50, has the highest log *P* value, and was hypothesized to show largest partitioning behavior.

Results showed that Compound **1**, when introduced into a lipid bilayer vesicle, did not show indication of partitioning behavior; the measured lifetimes corresponded to those of **1** in bulk carbonate buffer. On the other hand, upon integration into a

lipid bilayer vesicle solution, compound **2** displayed four unique lifetimes. The first two lifetimes were that of **2** in bulk carbonate buffer. The third lifetime is suggestive of an alternate non-radiative decay pathway induced and stabilized by lipid bilayer vesicles. The fourth lifetime of **2** in lipid vesicles was predicted to be that of **2** in a conformationally restricted environment, enhancing its non-radiative decay pathway and resulting in an extremely short radiative decay. Compound **3** displayed three lifetimes when integrated into a lipid vesicle solution. The first two lifetimes are suggestive of **3** that remains in bulk carbonate buffer. The third lifetime has a very small contribution to the time resolved emission and is not considered to be significant. Overall, the results presented here argue against a hypothesis that correlates membrane affinity with a solute's toxicological efficacy, and instead indicate that differences in activity for the studied thienopyrimidines should be attributed to differences in direct association with their target membrane proteins rather than to changes in membrane uptake and transport. Moreover, the studies reported here describe methodology that should prove useful for predicting the activity of compounds in cases where membrane uptake (rather than receptor binding) is the limiting factor for activity.

Associated content:

Supporting Information.

The supporting information contains spectra specifications for pKa measurements; steady-state fluorescence spectra of all compounds in bulk solvents; the full table including all fluorescence lifetime and amplitudes from 10-70 °C and back to 10

°C; the 1D selective gradient NOESY spectra of compound **3** can also be found in supporting information.

Author information:

Corresponding Authors

*Mary J. Cloninger – email: mcloninger@montana.edu. Phone: 406-994-3051

*Robert A. Walker – email: rawalker@montana.edu. Phone: 406-994-7928

Author Contributions

The manuscript was written through contributions of all authors. All authors have given approval to the final version of the manuscript. ‡These authors contributed equally.

Funding Sources

S.M.H. is supported by a Ph.D. Completion Grant from Montana State University. This material is based upon work supported in part by the National Science Foundation EPSCoR Cooperative Agreement OIA-1757351.

Any opinions, findings, and conclusions or recommendations expressed in this material are those of the author(s) and do not necessarily reflect the views of the National Science Foundation.

Notes

The authors declare no competing financial interest.

Acknowledgment:

The authors would like to thank Garrett Moraski for his support and subject matter expertise. Support for Montana State University's NMR Center and the 600 MHz NMR spectrometer used in this research has been provided by the NIH Shared Instrumentation Grant (1S10RR13878 and 1S10RR026659), the NSF MRI program (DBI-1532078), the Murdock Charitable Trust, and MSU's Vice President for Research and Economics Development office.

Abbreviations:

log *P*, partitioning coefficient; TCSPC, time-correlated single-photon counting spectroscopy; IRF, instrument response function; $T_{gel\text{-}lc}$, Transition temperature where lipid bilayer transitions from rigid, gel-phase to fluid liquid-crystalline phase; New K_{nr}, predicted new non-radiative decay pathway.

CHAPTER FOUR

SYNTHESES AND STRUCTURE-ACTIVITY RELATIONSHIPS OF *N*-PHENETHYL-QUINAZOLIN-4-YL-AMINES AS POTENT INHIBITORS OF CYTOCHROME *BD* OXIDASE IN *MYCOBACTERIUM TUBERCULOSIS*

Contribution of Authors and Co-Authors

Manuscript in Chapter 4

Author: Sarah M. Hopfner

Contributions: Prepared and characterized compounds, co-wrote initial draft of the manuscript.

Co-Author: Bei Shi Lee

Contributions: Performed biological assays, assisted in drafting and editing the manuscript.

Co-Author: Nitin P. Kalia

Contributions: Performed biological assays.

Co-Author: Marvin J. Miller

Contributions: Provided data interpretation and scientific direction, assisted in editing the manuscript.

Co-Author: Kevin Pethe

Contributions: Assisted in editing the manuscript.

Co-Author: Garrett C. Moraski

Contributions: Designed compounds, assisted in compound preparation, co-wrote initial draft of the manuscript.

Manuscript Information

Sarah M. Hopfner, Bei Shi Lee, Nitin P. Kalia, Marvin J. Miller, Kevin Pethe, and Garrett C. Moraski

RSC Medicinal Chemistry

Status of Manuscript:

____ Prepared for submission to a peer-reviewed journal

____ Officially submitted to a peer-reviewed journal

____ Accepted by a peer-reviewed journal

_X__ Published in a peer-reviewed journal

MDPI

Appl.Sci., 2021, 11, 9092.

DOI: 10.3390/app11199092

SYNTHESES AND STRUCTURE-ACTIVITY RELATIONSHIPS OF *N*-PHENETHYL-QUINAZOLIN-4-YL-AMINES AS POTENT INHIBITORS OF CYTOCHROME *BD* OXIDASE IN MYCOBACTERIUM TUBERCULOSIS

Sarah M. Hopfner[1], Bei Shi Lee[2], Nitin P. Kalia[3], Marvin J. Miller[4], Kevin Pethe[2,5] and Garrett C. Moraski[1,*]

[1] Department of Chemistry and Biochemistry, Montana State University, 103 Chemistry and Biochemistry Building, Bozeman, Montana 59717, USA; sarah.hopfner@student.montana.edu

[2] School of Biological Sciences, Nanyang Technological University, Singapore 637551, Singapore; beishi001@e.ntu.edu.sg (B.S.L.); kevin.pethe@ntu.edu.sg (K.P.)Experimental Medicine Building, 59 Nanyang Drive, 636921, Singapore

[3] Department of Biological Sciences, National Institute of Pharmaceutical Education and Research, Hyderabad, Telangana 500037, India; kalianpk@gmail.com

[4] Department of Chemistry and Biochemistry, University of Notre Dame, 251 Nieuwland Science Hall, Notre Dame, Indiana, IN 46556, USA; mmiler1@nd.edu

[5] Lee Kong Chian School of Medicine, Nanyang Technological University, Experimental Medicine Building, 59 Nanyang Drive, Singapore 636921, Singapore

[*]Correspondence: garrett.moraski@montana.edu

Abstract

The development of cytochrome *bd* oxidase (cyt-*bd*) inhibitors are needed for comprehensive termination of energy production in *Mycobacterium tuberculosis* (Mtb) to treat tuberculosis infections. Herein, we report on the structure-activity-relationships (SAR) of 22 new *N*-phenethyl-quinazolin-4-yl-amines that target cyt-*bd*. Our focused set of compounds was synthesized and screened against three mycobacterial strains: *Mycobacterium bovis* BCG, *Mycobacterium tuberculosis* H37Rv and the clinical isolate *Mycobacterium tuberculosis* N0145 with and without the cytochrome *bcc:aa*$_3$ inhibitor Q203 in an ATP depletion assay. Two compounds, **12a** and **19a**, had better potency against all three strains than the naturally derived cyt-*bd* inhibitor Aurachin D.

Keywords: tuberculosis; drug development; structure activity relationships; quinazoline; energy metabolism; cytochrome *bd* oxidase

Introduction

Tuberculosis (TB) is still a leading cause of death from an infectious agent and according to the World Health Organization's 2020 Global Tuberculosis Report, over 10 million people became ill with the disease in 2019 [1]. Action must be taken to combat this continuing public health threat. TB infection is caused by the bacterium *Mycobacterium tuberculosis* (Mtb) and spread by aerosols of an infected person through a cough or sneeze. Treatment of individuals infected with TB consists of several medications that are taken together for 6-9 months. First-line

drugs include isoniazid (INH), rifampin (RIF), ethambutol (EMB) and pyrazinamide (PZA) [1]. Other barriers such as lengthy treatment regimens and access to care have made adherence to treatment challenging. Shorter treatment schedules are strongly desired. Despite the advances in drug therapies and modern medications such as bedaquiline, delamanid and pretomanid, there is a need for comprehensive drug combinations and new treatment regimens to combat drug resistant TB [60]. Consideration of how Mtb survives onslaughts of chemotherapies gives insight into more effective treatment. Investigating the mechanism of action of antibiotics provides critical information that can be used to ultimately cure TB infections [62]. Targets within energy metabolism processes, specifically those involved in the oxidative phosphorylation pathway, have become increasingly important. Mtb can persist in a hypoxic, non-replicating, drug-tolerant state [160]. It has been demonstrated that interrupting oxidative phosphorylation in Mtb is an encouraging strategy [112, 118, 121]. While compounds have been made to inhibit various targets within the oxidative phosphorylation pathway, limitations have been observed including the inability to inhibit oxygen respiration and clear Mtb infection due to a redundancy between the oxidases cytochrome *bcc:aa$_3$* (cyt-*bcc:aa$_3$*) and cytochrome *bd* (cyt-*bd*) [115]. Cytochrome *bcc:aa$_3$* is the main aerobic terminal oxidase in Mtb [187]. The compound Q203 (Telacebec®) inhibits cytochrome *bcc* by binding to the QcrB sub-unit, thereby inhibiting the function of the cytochrome *bcc:aa$_3$* super-complex [119]. When cytochrome *bcc:aa$_3$* is inactive, cyt-*bd* is upregulated [122]. This adaptation provides protection against cytochrome *bcc:aa$_3$* inhibitors such as Q203. We have shown that targeting cyt-*bd* in combination with

Q203 is bactericidal against replicating and non-replicating Mtb [124]. This makes cyt-*bd* an enticing target for the development of antituberculosis agents to effectively eliminate infection.

Interested in the inhibition of this target, we screened a small set (56) of antibacterial compounds that originated from our decades old antibacterial program. This led to the identification of cyt-*bd* compounds like the thieno[3,2-*d*]pyrimidin-4-amines in which (**1**) is an example, the *in vivo* active optimized inhibitor ND-11992 (**2**) and hit compound **3** (Figure 4.1) [162].

The *N*-phenethylquinazolin-4-amine class, exemplified by compound **3** (Figure 4.1), had an IC_{50} of 11 μM against *Mycobacterium bovis* BCG and an IC_{50} of 27 μM against *Mycobacterium tuberculosis* H37Rv as determined by our published ATP depletion assay [162]. This assay is purposefully run in the presence and absence of Q203 (**4**, a selective cyt- *bcc:aa*$_3$ inhibitor) to indicate whether a compound inhibits alone or synergizes with cyt-*bd* inhibitors due to the conditional essentiality of the cyt-*bd* to maintain ATP homeostasis once cyt-*bcc:aa*$_3$ is selectively inhibited by Q203. Compound **3** was inactive (IC_{50} >25 μM) in the absence of Q203 which is an indication of on target potency based upon assay design. Similarly, compound **3** was amenable to chemical modifications and structure activity relationship (SAR) development. Herein we report our initial design, synthesis, and activity assessment of various quinazoline compounds for potency against cyt-*bd* of *Mycobacterium bovis* BCG and *Mycobacterium tuberculosis*.

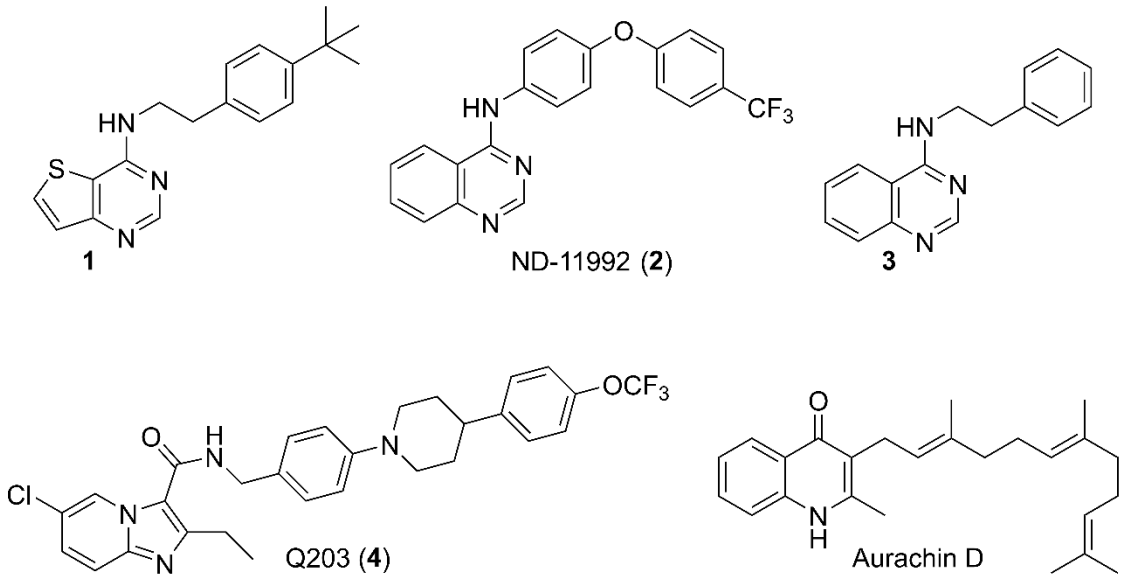

Figure 4.1 Known synthetically accessible small molecule cyt-*bd* inhibitors: thieno[3,2-*d*]pyrimidin-4-amine (**1**),[162] ND-11992 (**2**),[124] and *N*-phenethylquinazolin-4-amine (**3**) screening hit. The selective cyt-*bcc:aa*$_3$ inhibitor Q203 (**4**)[119] and natural cyt-*bd* inhibitor Aurachin D.[121]

Materials and Methods

Chemistry

General. All anhydrous solvents, reagent grade solvents for chromatography and starting materials were purchased from either Aldrich Chemical Co. (Milwaulkee, WI) or Fisher Scientific (Suwanee, GA) unless otherwise noted. Water was distilled and purified through a Milli-Q water system (Millipore Corp., Bedford, MA). General methods of purification of compounds involved the use of silica cartridges purchased from Practichem, LLC. (www.practicachem.com) and/or recrystallization. The reactions were monitored by TLC on precoated Merck 60

F254 silica gel plates and visualized using UV light (254 nm). All compounds were analyzed for purity by HPLC and characterized by ^{1}H and ^{13}C NMR using a Bruker Ascend Avance III HD Spectrometer (500 MHz). Chemical shifts are reported in ppm (δ) relative to the residual solvent peak in the corresponding spectra; chloroform δ 7.27 and δ 77.23, methanol δ 3.31 and δ 49.00 and coupling constants (*J*) are reported in hertz (Hz) (where, s = singlet, bs = broad singlet, d = doublet, dd = double doublet, bd = broad doublet, ddd = double doublet of doublet, t = triplet, tt – triple triplet, q = quartet, m = multiplet) and analyzed using MestreNova NMR data processing. ^{19}F NMR were run without a standard and are uncorrected. Mass spectra values are reported as m/z. Melting points were measured on a Büchi B-545 melting point instrument and are uncorrected, measured against benzoic acid 118.8-120.2°C. Compounds **3**, **6a** – **26a** appear within US Provisional Patent Application No. 62/783,984. The quinazolines (**5**, **16** – **26**) and amines (**6** – **15**) used in synthesis are all commercially available. LC-MS method: Liquid Chromatography-Mass Spectrometry method was performed on an Agilent 1290 infinity coupled to Agilent 6538 Ultra High-Definition Quadrupole Time of Flight (UHD-QTOF) instrument. A separation was achieved by using reverse phase Waters Acuity UPLC HSS T3 1.8µm (2.1 X 100mm) column from Waters (Milford, USA). All solvents were purchased from Fischer Scientific LCMS Optima grade solvents. Water containing 0.1% formic acid was used as mobile phase A and acetonitrile containing 0.1% formic acid was used as mobile phase B. The injection volume was set at 1 µL. Samples were injected in a gradient of 95% mobile phase A and 5% mobile phase B in the initial condition to 5% mobile

phase A and 95% mobile phase B in 9 min. The eluent was held at that composition for an additional 3 min and switched back to the initial condition at 12 min.

The MS data acquisition was performed from 50-1000 m/z at 1.0 spectra/sec scan rate. The source gas temperature was set at 350°C with a flow of 8 l/min. The nebulizer gas was set at 55 psig. The capillary voltage was set at 3500 volts with fragmentor at 100, skimmer at 45 and octopole RF 500 volts. Prior to sample runs, the instrument was calibrated using Agilent low mass calibrant solution.

Data analysis: The data collected in Agilent LC-MS was analyzed using Agilent Mass Hunter software for HRMS calculation.

General syntheses of *N*-phenethylquinazolin-4-amine analogs General procedure A for base catalyzed S_NAr reaction for the preparation of compounds **6a, 7a**, **9a**, **12a**-**26a**. In a sealed vial, desired quinazoline core (**5**, 100 mg, 0.61 mmol, 1 equiv.), 2-[4-(trifluoromethoxy)phenyl]ethylamine (**7**, 125 mg, 0.61 mmol, 1 equiv.) and potassium carbonate (84 mg, 0.61 mmol, 1 equiv.) were dissolved in DMSO (4 mL). The reaction was heated to 100°C for 12 h. The reaction mixture was concentrated to dryness. The residue was dissolved in CH_2Cl_2 and washed with 5% aqueous acetic acid solution (2x), water and brine. The organic phase was collected, dried over sodium sulfate, filtered, and concentrated *in vacuo*. Crude material obtained was purified by either silica gel chromatography with a gradient of CH_2Cl_2: ethyl acetate: solvent system (0 to 80%) or recrystallized from hot isopropanol or acetonitrile to afford the product.

General procedure B for acid catalyzed S_NAr reaction for the preparation of compounds **3**, **8a**, **10a**, **11a**. In a sealed vial, desired quinazoline core (**16-26,** 1 equiv.), 2-[4-(trifluoromethoxy)phenyl]ethylamine (**7**, 1 equiv.) were dissolved in a 3:1 tetrahydrofuran: 2-propanol solution (4 mL). Next, was added 12 M HCl (~0.4 equiv.). The solution was heated at 70°C for 24 h. The reaction was concentrated to dryness. The residue was dissolved in CH_2Cl_2 and washed with saturated aqueous $NaHCO_3$ solution, water, and brine. The organic phase was collected, dried over sodium sulfate, filtered, and concentrated *in vacuo*. Crude material obtained was purified by either silica gel column chromatography with a gradient of CH_2Cl_2: ethyl acetate: solvent system (0-80%) or recrystallized from hot isopropanol or acetonitrile to afford the product.

N-Phenethylquinazolin-4-amine, **3** Following general procedure B, using 4-chloroquinazoline (100 mg, 0.59 mmol), 2-phenylethylamine (72 mg, 0.59 mmol), and 12 N HCl (11 µL, 0.14 mmol) gave **3** as pale-yellow crystals (43 mg, 28%). mp 171.5-171.9°C; ^{1}H (500 MHz, MeOD) δ ppm 8.47 (s, 1H), 8.06 (d, *J* = 8.3 Hz, 1H), 7.82-7.77 (m, 1H), 7.72 (d, *J* = 8.3 Hz, 1H), 7.55-7.50 (m, 1H), 7.31-7.26 (m, 4H), 7.23-7.17 (m, 1H), 3.86 (t, *J* = 7.4 Hz, 2H), 3.04(t, *J* = 7.4 Hz, 2H) ^{13}C (125 MHz, MeOD) δ ppm 160.0, 154.7, 148.2, 139.3, 132.7, 128.5, 128.1, 126.3, 126.0, 125.9, 121.9, 115.1, 42.5, 34.7. HRMS (EI), M + 1 calculated for $C_{16}H_{15}N_3$, 250.1339, found 250.1351. These experimental results are consistent with previous reports [188-190].

Quinazolin-4-yl{2-[4-(trifluoromethyl)phenyl]ethyl}amine, **6a** Following general procedure A, using 4-chloroquinazoline (100 mg, 0.59 mmol), 2-[4-(trifluoromethyl)phenyl]ethylamine (114 mg, 0.59 mmol) and potassium carbonate (81 mg, 0.59 mmol) gave **6a** as gold crystals (79 mg, 38%). mp 160.3-161.0°C; ^{1}H (500 MHz, $CDCl_3$) δ ppm 8.73 (s, 1H), 7.88 (d, *J* = 7.9 Hz, 1H), 7.77 (ddd, *J* = 8.4, 7.0, 1.3 Hz), 7.63-7.57 (m, 3H), 7.47 (ddd, *J* = 8.2, 7.0, 1.2 Hz), 7.40 (d, *J* = 8.0 Hz, 2H), 5.79 (br.s, 1H), 3.99 (dt, *J* = 6.9, 5.9 Hz, 2H), 3.14 (t, *J* = 6.9 Hz, 2H). ^{13}C (125 MHz, $CDCl_3$) δ ppm 159.6, 155.4, 149.5, 143.2 (d, *J* = 1.5 Hz), 132.7, 129.2, 129.1 (q, *J* = 32.4 Hz), 128.2, 126.1, 125.6 (q, *J* = 3.8 Hz), 124.7 (q, *J* = 271.9 Hz), 120.2, 114.9, 42.1, 35.2. ^{19}F (470 MHz, $CDCl_3$) δ ppm -62.4 (s, 3F). HRMS (EI), M + 1 calculated for $C_{17}H_{14}F_3N_3$, 318.1213, found 318.1229. This compound appears in referenced patent and fungicidal activity was reported [191].

Quinazolin-4-yl{2-[4-(trifluoromethoxy)phenyl]ethyl}amine, **7a** Following general procedure A, using 4-chloroquinazoline (100 mg, 0.59 mmol), 2-[4-(trifluoromethoxy)phenyl]ethylamine (125 mg, 0.59 mmol) and potassium carbonate (84 mg, 0.59 mmol) gave **7a** as white crystals (85 mg, 42%). mp 137.4-137.8°C; ^{1}H (500 MHz, $CDCl_3$) δ ppm 8.73 (s, 1H), 7.88 (d, *J* = 8.2 Hz, 1H), 7.77 (ddd, *J* = 8.4, 7.0, 1.3 Hz, 1H), 7.60-7.56 (m, 1H), 7.48 (ddd, *J* = 8.3, 7.0, 1.1 Hz), 7.33-7.26 (m, 2H), 7.20 (d, *J* = 8.0 Hz, 2H), 5.73 (br.s, 1H), 3.97 (dt, *J* = 7.0, 5.9 Hz, 2H), 3.08 (t, *J* = 7.0 Hz, 2H). ^{13}C (125 MHz, $CDCl_3$) δ ppm 159.3, 155.4, 149.5, 148.0 (d, *J* = 1.8 Hz), 137.7, 132.6, 130.2, 128.8, 126.1, 121.3, 120.6 (q, *J* = 235.0

Hz), 120.1, 114.9, 42.3, 34.6. ^{19}F (470 MHz, $CDCl_3$) δ ppm -59.9 (s, 3F). HRMS (EI), M + 1 calculated for $C_{17}H_{14}F_3N_3O$, 334.1162, found 334.1155.

[2-(4-Chlorophenyl)ethyl]quinazolin-4-ylamine, **8a** Following general procedure B, using 4-chloroquinazoline (100 mg, 0.59 mmol), 2-(4-chlorophenyl)ethylamine (94 mg, 0.59 mmol) and 12 N HCl (11 µL, 0.14 mmol) gave **8a** as yellow crystals (35 mg, 20%). mp 191.0-192.1°C; ^{1}H (500 MHz, MeOD) δ ppm 8.47 (s, 1H), 8.05 (dd, *J* = 8.3, 0.7 Hz, 1H), 7.80 (ddd, *J* = 8.3, 7.0, 1.3 Hz, 1H), 7.73-7.70 (m, 1H), 7.53 (ddd, *J* = 8.3, 7.0, 1.3 Hz, 1H), 7.30-7.25 (m, 2H), 3.88-3.83 (m, 2H), 3.03 (t, *J* = 7.3 Hz, 2H). ^{13}C (125 MHz, MeOD) δ ppm 160.0, 154.6, 148.2, 138.1, 132.8, 131.8, 130.2, 128.1, 126.3, 126.1, 121.9, 115.1, 42.2, 34.0. HRMS (EI), M + 1 calculated for $C_{16}H_{14}ClN_3$, 284.0949, found 284.0950. These experimental results are consistent with previous reports [192-194].

[2-(4-(Pentafluoro-(λ)^6-sulfaneyl]quinazolin-4-ylamine, **9a** Following general procedure A, using 4-chloroquinazoline (70 mg, 0.42 mmol) and 2-(4-(pentafluoro-(λ)^6-sulfaneyl)phenyl)ethan-1-amine (105 mg, 0.42 mmol) and potassium carbonate (59 mg, 0.42 mmol) gave **9a** as white crystals (97 mg, 61%). mp 169.2-170.7°C; ^{1}H (500 MHz, $CDCl_3$) δ ppm 8.73 (s, 1H), 7.89 (d, *J* = 8.3 Hz, 1H), 7.80-7.70 (m, 3H), 7.61 (d, *J* = 8.2 Hz, 1H), 7.51-7.46 (m, 1H), 7.37 (d, *J* = 8.3 Hz, 2H), 5.80 (br.s, 1H), 3.99 (q, *J* = 6.6 Hz, 2H), 3.14 (t, *J* = 6.9 Hz, 2H). ^{13}C (125 MHz, $CDCl_3$) δ ppm 159.3, 155.3, 152.5 (quintet, *J* = 17.6 Hz), 149.5, 143.2, 132.7, 129.1, 128.8, 126.3 (quintet, *J* = 4.5 Hz), 120.2, 114.9, 42.1, 34.9. ^{19}F (470 MHz,

$CDCl_3$) δ ppm 84.8 (pent, *J* = 150.0 Hz, 1F), 63.1 (d, *J* = 150.0 Hz, 4F). HRMS (EI), M + 1 calculated for $C_{16}H_{14}F_5N_3S$, 376.0901, found 376.0908.

[2-(4-Methylpheny)ethyl]quinazolin-4-ylamine, **10a** Following general procedure B, using 4-chloroquinazoline (100 mg, 0.59 mmol), 2-(4-methylphenyl)ethan-1-amine (82 mg, 0.59 mmol) and 12 N HCl (11 µL, 0.14 mmol) gave **10a** as white crystals (25 mg, 15%). mp 183.6-184.6°C; ^{1}H (500 MHz, $CDCl_3$) δ ppm 8.71 (s, 1H), 7.86 (d, *J* = 8.2 Hz, 1H), 7.74 (ddd, *J* = 8.3, 7.0, 1.3 Hz, 1H), 7.56 (d, *J* = 7.8 Hz, 1H), 7.44 (ddd, *J* = 8.2, 7.0, 1.1 Hz, 1H), 5.79 (br.s, 1H), 3.95 (dt, *J* = 6.7, 5.8 Hz, 2H), 3.02 (t, *J* = 6.8 Hz, 2H), 2.37 (s, 3H). ^{13}C (125 MHz, $CDCl_3$) δ ppm 159.3, 155.4, 149.3, 136.3, 135.7, 132.6, 129.5, 128.7, 128.6, 126.0, 120.3, 115.0, 42.3, 34.8, 21.1. HRMS (EI), M + 1 calculated for $C_{17}H_{17}N_3$, 264.1495, found 264.1496.

[2-(4-Methoxyphenyl)ethyl]quinazolin-4-ylamine, **11a** Following general procedure B, using 4-chloroquinazoline (100 mg, 0.59 mmol), 2-(4-methoxyphenyl)ethylamine (91 mg, 0.59 mmol) and 12 N HCl (11 µL, 0.14 mmol) gave **11a** as off-white crystals (74 mg, 43%). mp 172.3-172.9°C; ^{1}H (500 MHz, $CDCl_3$) δ ppm 8.71 (s, 1H), 7.86 (d, *J* = 8.3 Hz, 1H), 7.74 (ddd, *J* = 8.3, 7.0, 1.3 Hz, 1H), 7.56 (d, *J* = 8.3 Hz, 1H), 7.45 (ddd, *J* = 8.2, 7.0, 1.2 Hz, 1H), 7.20 (dt, *J* = 8.6, 2.9 Hz, 2H), 6.90 (dt, *J* = 8.6, 2.9 Hz, 2H), 5.78 (s, 1H), 3.93 (dt, *J* = 6.8, 5.7 Hz, 2H), 3.83 (s, 3H), 3.01 (t, *J* = 6.8 Hz, 2H). ^{13}C (125 MHz, $CDCl_3$) δ ppm 159.3, 158.4, 155.4, 149.4, 132.6, 130.8, 129.8, 128.6, 126.0, 120.3, 115.0, 114.2, 55.3, 42.4, 34.3. HRMS (EI), M + 1 calculated for $C_{17}H_{17}N_3O$, 280.1444, found 280.1458.

{2-[4-(*tert*-Butyl)phenyl]ethyl}quinazolin-4-ylamine, **12a** Following general procedure A, using 4-chloroquinazoline (100 mg, 0.59 mmol), 2-[4-(tert-butyl)phenyl]ethylamine (110 mg, 0.59 mmol) and potassium carbonate (81 mg, 0.59 mmol) gave **12a** as yellow crystals (58 mg, 29%). mp 149.5-151.3°C; ^{1}H (500 MHz, $CDCl_3$) δ ppm 8.71 (s, 1H), 7.86 (dd, *J* = 8.4, 0.6 Hz, 1H), 7.74 (ddd, *J* = 8.4, 7.0, 1.3 Hz, 1H), 7.57 (dd, *J* = 8.3, 0.8 Hz, 1H), 7.45 (ddd, *J* = 8.2, 7.0, 1.2 Hz, 1H), 7.39 (dt, *J* = 8.3, 2.3 Hz, 2H), 7.22 (dt, *J* = 8.3, 2.2 Hz, 2H), 5.81 (br.s, 1H), 3.96 (dt, *J* = 6.8, 5.7 Hz, 2H), 3.04 (t, *J* = 6.8 Hz, 2H), 1.35 (s, 3H). ^{13}C (125 MHz, $CDCl_3$) δ ppm 159.3, 155.5, 149.6, 149.5, 135.8, 132.5, 128.7, 128.5, 125.9, 125.7, 120.3, 115.0, 42.3, 34.7, 34.5, 31.4. HRMS (EI), M + 1 calculated for $C_{20}H_{23}N_3$, 306.1965, found 306.1967. These experimental results are consistent with previous report [195].

Quinazolin-4-yl{2-[3-(trifluoromethoxy)phenyl]ethyl}amine, **13a** Following general procedure A, using 4-chloroquinazoline (100 mg, 0.59 mmol), 3-(trifluoromethoxy)phenylamine (125 mg, 0.59 mmol) and potassium carbonate (84 mg, 0.59 mmol) gave **13a** as white crystals (136 mg, 67%). mp 144.0-144.9°C; ^{1}H (500 MHz, $CDCl_3$) δ ppm 8.72 (s, 1H), 7.87 (d, *J* = 7.8 Hz), 7.76 (ddd, *J* = 8.4, 7.0, 1.3 Hz, 1H), 7.60 (ddd, *J* = 8.2, 7.0, 1.2 Hz, 1H), 7.39-7.35 (m, 1H), 7.22-7.19 (m, 1H), 7.16-7.12 (m, 1H), 5.83 (br.s, 1H), 3.97 (dt, *J* = 6.9, 5.9 Hz, 2H), 3.09 (t, *J* = 6.9 Hz, 2H). ^{13}C (125 MHz, $CDCl_3$) δ ppm 159.3, 155.4, 149.5 (q, *J* = 1.8 Hz), 141.3, 132.6, 130.1, 128.7, 127.3, 126.1, 121.4, 120.5 (q, *J* = 257.2 Hz), 120.2,

119.1, 114.9, 42.1, 35.1. ^{19}F (470 MHz, $CDCl_3$) δ ppm -57.7 (s, 3F). HRMS (EI), M + 1 calculated for $C_{17}H_{14}F_3N_3O$, 306.1965, found 306.1967.

[2-(3-Ethoxyphenyl)ethyl]quinazolin-4-ylamine, **14a** Following general procedure A, using 4-chloroquinazoline (151 mg, 0.92 mmol), 3-ethoxyphenylethylamine (155 mg, 0.92 mmol) and potassium carbonate (127 mg, 0.92 mmol) gave **14a** as off-white crystals (211 mg, 78%). mp 148.5-148.8°C; ^{1}H (500 MHz, $CDCl_3$) δ ppm 8.71 (s, 1H), 7.86 (d, *J* = 8.3 Hz, 1H), 7.74 (ddd, *J* = 8.3, 7.0, 1.2 Hz, 1H), 7.56 (d, *J* = 8.0 Hz, 1H), 7.44 (ddd, *J* = 8.0, 7.0, 1.1 Hz, 1H), 6.86 (d, *J* = 7.5 Hz, 1H), 6.83-6.79 (m, 2H), 5.79 (br.s, 1H), 4.02 (q, *J* = 7.0 Hz, 2H), 3.96 (dt, *J* = 6.7, 5.8 Hz, 2H), 1.42 (t, *J* = 7.0 Hz, 3H). ^{13}C (125 MHz, $CDCl_3$) δ ppm 159.4, 159.3, 155.5, 149.5, 140.4, 132.5, 129.8, 128.7, 126.0, 121.0, 120.3, 115.1, 115.0, 112.6, 63.4, 42.1, 35.3, 14.8. HRMS (EI), M + 1 calculated for $C_{18}H_{19}N_3O$, 294.1601, found 294.1616.

Quinazolin-4-yl{2-[2-(trifluromethyl)phenyl]ethyl}amine, **15a** Following general procedure A outlined, using 4-chloroquinazoline (100 mg, 0.59 mmol), 2-(2-trifluoromethylphenyl)ethylamine (117 mg, 0.59 mmol) and potassium carbonate (81 mg, 0.59 mmol) gave **15a** as a yellow flaky solid (68 mg, 34%). mp 134.4-137.4°C; ^{1}H (500 MHz, $CDCl_3$) δ ppm 8.66 (s, 1H), 8.12-8.05 (m, 1H), 7.95 (d, *J* = 8.3 Hz, 1H), 7.80-7.74 (m, 1H), 7.66 (d, *J* = 7.8 Hz, 1H), 7.54-7.49 (m, 1H), 7.49-7.46 (m, 1H), 7.37-7.32 (m, 1H), 4.04 (dt, *J* = 6.9, 6.7 Hz, 2H), 3.30 (t, *J* = 7.2 Hz, 2H). ^{13}C (125 MHz, $CDCl_3$) δ ppm 159.9, 153.5, 145.7, 137.3, 133.6, 132.0, 131.7, 128.9 (q, *J* = 29.7 Hz), 126.9, 126.1 (q, *J* = 5.7 Hz), 126.8, 125.7, 124.5 (q, *J* =

254.0 Hz), 121.9, 114.4, 42.7, 31.8. ^{19}F (470 MHz, $CDCl_3$) δ ppm -59.2 (s, 3F). HRMS (EI), M + 1 calculated for $C_{17}H_{14}F_3N_3$, 318.1213, found 318.1220. This compound appears in referenced patent and fungicidal activity was reported [191].

(6-Fluoroquinazolin-4-yl){2-[4-(trifluormethoxy)phenyl]ethyl}amine, **16a** Following general procedure A, using 4-chloro-6-fluoroquinazoline (100 mg, 0.55 mmol), 2-[4-(trifluromethoxy)phenyl]ethylamine (112 mg, 0.55 mmol), and potassium carbonate (76 mg, 0.55 mmol) gave **16a** as a white solid (99 mg, 51%). mp 171.6-172.6°C; ^{1}H (500 MHz, $CDCl_3$) δ ppm 8.70 (s, 1H), 7.89 (dd, *J* = 9.1, 5.3 Hz, 1H), 7.52 (ddd, 9.1, 8.2, 2.7 Hz, 1H), 7.32-7.29 (m, 2H), 7.23-7.19 (m, 3H), 5.57 (br.s, 1H), 3.96 (dt, *J* = 7.0, 5.8 Hz, 2H), 3.08 (t, *J* = 7.0 Hz, 2H). ^{13}C (125 MHz, $CDCl_3$) δ ppm 160.0 (d, *J* = 248.9 Hz), 159.0, 148.1 (q, *J* = 1.9 Hz), 146.5, 137.5, 131.4 (d, *J* = 8.4 Hz), 130.1, 122.2 (d, *J* = 24.4 Hz), 121.5, 121.3, 120.5 (q, *J* = 255.5 Hz), 115.2 (d, *J* = 7.9 Hz), 104.7 (d, *J* = 22.7 Hz), 42.4, 34.6. ^{19}F (470 MHz, $CDCl_3$) δ ppm -57.9 (s, 3F), -112.3 (ddd, *J* = 5.4, 8.5, 8.5 Hz, 1F). HRMS (EI), M + 1 calculated for $C_{17}H_{13}F_4N_3O$, 352.1068, found 352.1078. This compound was shown to inhibit autophagy in referenced patent [196].

(6-Methylquinazolin-4-yl){2-[4-(trifluormethoxy)phenyl]ethyl}amine, **17a** Following general procedure A, using 4-chloro-4-methylquinazoline (100 mg, 0.56 mmol), 2-[4-(trifluoromethoxy)phenyl]ethylamine (115 mg, 0.56 mmol), and potassium carbonate (77 mg, 0.56 mmol) gave **17a** as an off-white solid (134 mg, 69%). mp 134.3-135.0°C; ^{1}H (500 MHz, $CDCl_3$) δ ppm 8.67 (s, 1H), 7.77 (d, *J* = 8.5 Hz, 1H), 7.58 (dd, *J* = 8.5, 1.6 Hz, 1H), 7.36 (s, 1H), 7.31-7.27 (m, 2H), 5.76 (br.s, 1H), 3.94

(dt, *J* = 6.9, 5.9 Hz, 2H), 3.08 (t, *J* = 7.0 Hz, 2H), 2.50 (s, 3H). ^{13}C (125 MHz, $CDCl_3$) δ ppm 158.9, 154.6, 148.0 (q, *J* = 1.8 Hz), 147.8, 137.8, 136.1, 134.5, 130.2, 128.5, 121.2, 120.5 (q, *J* = 256.9 Hz), 119.4, 114.8, 42.3, 34.7, 21.7. ^{19}F (470 MHz, $CDCl_3$) δ ppm -57.9 (s, 3F). HRMS (EI), M + 1 calculated for $C_{18}H_{16}F_3N_3O$, 348.1318, found 348.1336.

(6-Methoxyquinazolin-4-yl){2-[4-(trifluormethoxy)phenyl]ethyl}amine, **18a**

Following general procedure A, using 4-chloro-6-methoxyquinazoline (100 mg, 0.51 mmol), 2-[4-(trifluoromethoxy)phenyl]ethylamine (105 mg, 0.51 mmol), and potassium carbonate (71 mg, 0.51 mmol) gave **18a** as a white solid (93 mg, 50%). mp 144.7-145.2°C; ^1H (500 MHz, $CDCl_3$) δ ppm 8.64 (s, 1H), 7.81 (d, *J* = 9.1 Hz, 1H), 7.41 (dd, *J* = 9.1, 2.5 Hz, 1 Hz), 7.32-7.26 (m, 2H), 7.20 (d, *J* = 8.1 Hz, 2H), 6.82 (d, *J* = 2.5 Hz, 1H), 5.65 (br.s, 1H), 3.95 (dt, *J* = 6.8, 6.2 Hz, 2H), 3.87 (s, 3H), 3.08 (t, *J* = 7.0 Hz, 2H). ^{13}C (125 MHz, $CDCl_3$) δ ppm 158.6, 157.6, 153.4, 148.0 (q, *J* = 1.8 Hz), 144.9, 137.9, 130.3, 130.2, 123.6, 121.2, 120.5 (q, *J* = 258.4 Hz), 115.3, 99.8, 55.6, 42.3, 34.7. ^{19}F (470 MHz, $CDCl_3$) δ ppm -57.9 (s, 3F). HRMS (EI), M + 1 calculated for $C_{18}H_{16}F_3N_3O_2$, 364.1267, found 364.1276.

(7-Fluoroquinazolin-4-yl){2-[4-(trifluormethoxy)phenyl]ethyl}amine, **19a** Following general procedure A, using 4-chloro-7-fluoroquinazoline (100 mg, 0.55 mmol), 2-[4-(trifluoromethoxy)phenyl]ethylamine (112 mg, 0.55 mmol), and potassium carbonate (76 mg, 0.55 mol) gave **19a** as off-white crystals (107 mg, 56%). mp 128.9-129.7°C; ^1H (500 MHz, $CDCl_3$) δ ppm 8.69 (s, 1H), 7.60 (dd, *J* = 9.1, 5.6 Hz, 1H), 7.49 (dd, *J* = 9.8, 2.5 Hz, 1H), 7.32-7.26 (m, 2H), 7.24-7.17 (m, 3H), 5.74 (br.s,

1H), 3.96 (dt, *J* = 6.9, 5.9 Hz, 2H), 3.07 (t, *J* = 7.0 Hz, 2H). ^{13}C (125 MHz, $CDCl_3$) δ ppm 165.0 (d, *J* = 253.3 Hz), 159.1, 156.4, 151.6 (d, *J* = 13.1 Hz), 148.1 (q, *J* = 2.0 Hz), 137.6, 130.1, 122.8 (d, *J* = 10.4 Hz), 121.3, 120.5 (q, *J* = 256.9 Hz), 115.8 (d, *J* = 24.9 Hz), 112.9 (d, *J* = 20.4 Hz), 111.8, 42.3, 34.6. ^{19}F (470 MHz, $CDCl_3$) δ ppm -57.9 (s, 3F), -105.3 (ddd, *J* = 5.3, 9.2, 9.2 Hz, 1F). HRMS (EI), M + 1 calculated for $C_{17}H_{13}F_4N_3O$, 352.1068, found 352.1072.

(7-Chloroquinazolin-4-yl){2-[4-(trifluormethoxy)phenyl]ethyl}amine, **20a** Following general procedure A, using 4,7-dichloroquinazoline (100 mg, 0.51 mmol), 2-[4-(trifluoromethoxy)phenyl]ethylamine (105 mg, 0.51 mmol), and potassium carbonate (78 mg, 0.56 mol) gave **20a** as an off-white flaky crystals (72 mg, 50%). mp 153.0-153.4°C; ^{1}H (500 MHz, MeOD) δ ppm 8.47 (s, 1H), 8.03 (d, *J* = 8.6 Hz, 1H), 7.69 (d, *J* = 2.1 Hz, 1H), 7.49 (dd, *J* = 8.6, 2.1 Hz, 1H), 7.36 (dt, *J* = 8.6, 2.7 Hz, 2H), 7.21-7.16 (m, 2H), 3.86 (t, *J* = 7.3 Hz, 2H), 3.06 (t, *J* = 7.3 Hz, 2H). ^{13}C (125 MHz, MeOD) δ ppm 159.8, 155.8, 149.3, 147.7 (q, *J* = 1.7 Hz), 138.6, 130.1, 126.4, 125.4, 123.9, 120.7, 120.5 (q, *J* = 255.1 Hz), 113.6, 42.2, 33.9. ^{19}F (470 MHz, MeOD) δ ppm -59.6 (s, 3F). HRMS (EI), M + 1 calculated for $C_{17}H_{13}ClF_3N_3O$, 368.0772, found 368.0767.

(7-Bromoquinazolin-4-yl){2-[4-(trifluormethoxy)phenyl]ethyl}amine, **21a** Following general procedure A, using 4-chloro-7-bromoquinazoline (75 mg, 0.30 mmol), 2-[4-(trifluoromethoxy)phenyl]ethylamine (62 mg, 0.30 mmol), and potassium carbonate (41 mg, 0.30 mmol) gave **21a** as off-white crystals (52 mg, 42%). mp 151.8-152.8°C; ^{1}H (500 MHz, $CDCl_3$) δ ppm 8.68 (s, 1H), 8.06 (s, 1H), 7.56 (s,

2H), 7.32-7.26 (m, 2H), 7.20 (d, *J* = 8.0 Hz, 2H), 6.18 (br.s, 1H), 3.97 (dt, *J* = 6.9, 6.1 Hz, 2H), 3.09 (t, *J* = 7.0 Hz, 2H). ^{13}C (125 MHz, $CDCl_3$) δ ppm 159.4, 155.7, 149.4, 148.1 (q, *J* = 1.6 Hz), 137.4, 130.4, 130.1, 129.7, 127.4, 122.2, 121.3, 120.5 (q, *J* = 257.0 Hz), 113.4, 42.5, 34.5. ^{19}F (470 MHz, $CDCl_3$) δ ppm -57.9 (s, 3F). HRMS (EI), M + 1 calculated for $C_{17}H_{13}BrF_3N_3O$, 412.0267, found 412.0246.

{2-[4-(Trifluoromethoxy)phenyl]ethyl}[7-(trifluoromethyl)quinazolin-4-yl]amine, **22a**

Following general procedure A, using 7-(trifluoromethyl)-4-chloroquinazoline (100 mg, 0.45 mmol), 2-[4-(trifluoromethoxy)phenyl]ethylamine (93 mg, 0.45 mmol), and potassium carbonate (69 mg, 0.50 mol) gave **22a** as off-white crystals (82 mg, 55%). mp 149.7-152.3°C; ^{1}H (500 MHz, MeOD) δ ppm 8.44 (d, *J* = 8.4 Hz, 1H), 8.41-8.37 (m, 1H), 8.01 (s, 1H), 7.86 (dd, *J* = 8.4, 1.5 Hz, 1H), 7.42 (dt, *J* = 8.6, 2.8 Hz, 2H), 7.31-7.25 (m, 2H), 3.22 (t, *J* = 7.7 Hz, 2H), 3.02 (t, *J* = 7.7 Hz, 2H). ^{13}C (125 MHz, MeOD) δ ppm 160.4, 148.3 (q, *J* = 1.8 Hz), 147.3, 135.8, 135.8 (q, *J* = 32.9 Hz), 130.2, 127.7, 125.0, 123.4 (q, *J* = 272.4 Hz), 123.1 (q, *J* = 3.6 Hz), 122.8 (m), 121.2, 120.5 (q, *J* = 255.5 Hz), 119.5, 40.3, 32.4. ^{19}F (470 MHz, MeOD) δ ppm -59.6 (s, 3F), -64.8 (s, 3F). HRMS (EI), M + 1 calculated for $C_{18}H_{13}F_6N_3O$, 402.1036, found 402.1025.

(7-Methoxyquinazolin-4-yl){2-[4-(trifluormethoxy)phenyl]ethyl}amine, **23a**

Following general procedure A, using 7-(methoxy)-4-chloroquinazoline (100 mg, 0.54 mmol), 2-[4-(trifluoromethoxy)phenyl]ethylamine (110 mg, 0.54 mmol), and potassium carbonate (82 mg, 0.59 mol) gave **23a** as colorless crystals (68 mg, 51%). mp 158.0-159.0°C; ^{1}H (500 MHz, MeOD) δ ppm 8.40 (s, 1H), 7.94 (d, *J* =

9.1 Hz, 1H), 7.36 (dt, *J* = 8.7, 2.8 Hz, 2H), 7.21-7.16 (m, 2H), 7.11 (dd, *J* = 9.1, 2.6 Hz, 1H), 7.08 (d, *J* = 2.5 Hz, 1H), 3.93 (s, 3H), 3.83 (t, *J* = 7.4 Hz, 2H), 3.05 (t, *J* = 7.4 Hz, 2H). ^{13}C (125 MHz, MeOD) δ ppm 163.5, 159.6, 155.0, 150.6, 147.7 (q, *J* = 1.7 Hz), 138.7, 130.1, 123.5, 120.7, 120.6 (q, *J* = 255.1 Hz), 117.3, 109.1, 105.5, 54.7, 42.1, 34.1. ^{19}F (470 MHz, MeOD) δ ppm -59.5 (3F). HRMS (EI), M + 1 calculated for $C_{18}H_{16}F_3N_3O_2$, 364.1267, found 364.1259.

(2-Methylquinazolin-4-yl){2-[4-(trifluormethoxy)phenyl]ethyl}amine, **24a** Following general procedure A, using 4-chloro-2-methylquinazoline (100 mg, 0.56 mmol), 2-[4-(trifluoromethoxy)phenyl]ethylamine (115 mg, 0.56 mmol), and potassium carbonate (77 mg, 0.56 mmol) gave **24a** as a pale yellow solid (153 mg, 79%). mp 124.4-127.2°C; ^{1}H (500 MHz, $CDCl_3$) δ ppm 7.81 (d, *J* = 8.3 Hz, 1H), 7.74-7.68 (m, 1H), 7.60 (d, *J* = 8.1 Hz, H), 7.42-7.37 (m, 2H), 7.20 (d, *J* = 8.0 Hz, 2H), 5.91 (br.s, 1H), 3.96 (dt, *J* = 6.9, 6.0 Hz, 2H), 3.07 (t, *J* = 7.0 Hz, 2H), 2.69 (s, 3H). ^{13}C (125 MHz, $CDCl_3$) δ ppm 164.3, 159.3, 149.4, 148.0 (q, *J* = 1.7 Hz), 137.8, 132.7, 130.2, 127.5, 125.3, 121.2, 120.5 (q, *J* = 256.9 Hz), 120.3, 112.8, 42.2, 34.7, 26.5. ^{19}F (470 MHz, $CDCl_3$) δ ppm -57.9 (s, 3F). HRMS (EI), M + 1 calculated for $C_{18}H_{16}F_3N_3O$, 348.1318, found 348.1335.

(2-Cyclopropylquinazolin-4-yl){2-[4-(trifluoromethoxy)phenyl]ethyl}amine, **25a** Following general procedure A, using 4-chloro-2-methylquinazolne (100 mg, 0.49 mmol), 2-[4-(trifluoromethoxy)phenyl]ethylamine (100 mg, 0.49 mmol) and potassium carbonate (67 mg, 0.48 mmol) gave **25a** as a tan solid (119 mg, 65%). mp 205.1-205.5°C; ^{1}H (500 MHz, MeOD) δ ppm 8.24 (d, *J* = 8.5 Hz, 1H), 8.02-7.97

(m, 1H), 7.74-7.68 (m, 2H), 7.36 (dt, *J* = 8.6, 2.7 Hz, 2H), 7.20 (d, *J* = 7.8 Hz, 2H), 3.99 (t, *J* = 7.1 Hz, 2H), 3.08 (t, *J* = 7.1 Hz, 2H), 2.23-2.16 (m, 1H), 1.44-1.32 (m, 4H). ^{13}C (125 MHz, MeOD) δ ppm 166.5, 160.8, 147.9, 138.3, 137.9, 135.7, 130.2, 127.7, 123.3, 120.9, 120.5 (q, *J* = 255.2 Hz), 118.0, 111.9, 42.9, 33.8, 14.5, 11.2. ^{19}F (470 MHz, MeOD) δ ppm -59.6 (s, 3F). HRMS (EI), M + 1 calculated for $C_{20}H_{18}F_3N_3O$, 374.1475, found 374.1493.

(7-Fluoro-2-methylquinazolin-4-yl){2-[4-(trifluormethoxy)phenyl]ethyl}amine, **26a**

Following general procedure A, using 4-chloro-7-fluoro-2-methylquinazoline (75 mg, 0.37 mmol), 2-[4-(trifluoromethoxy)phenyl]ethylamine (77 mg, 0.37 mmol), and potassium carbonate (52 mg, 0.37 mmol) gave **26a** as a white solid (58 mg, 43%). mp 121.7-124.7°C; ^{1}H (500 MHz, $CDCl_3$) δ ppm 14.78 (s, 1H), 10.62 (s, 1H), 9.10 (dd, *J* = 9.1, 5.2 Hz, 1H), 7.84 (dd, *J* = 8.6, 2.4 Hz, 1H), 7.30-7.22 (m, 1H), 7.19-7.13 (m, 2H), 7.06-7.02 (m, 2H), 4.14 (q, *J* = 6.9 Hz, 2H), 3.22 (t, *J* = 7.4 Hz, 2H), 2.77 (s, 3H). ^{13}C (125 MHz, $CDCl_3$) δ ppm 166.1 (d, *J* = 259.4 Hz), 162.0, 160.0, 149.3 (q, *J* = 2.0 Hz), 140.7, 140.5 (d, *J* = 12.9 Hz), 129.8, 128.7 (d, *J* = 10.3 Hz), 127.4, 121.4, 120.4 (q, *J* = 257.1 Hz), 119.1, 116.9 (d, *J* = 23.9 Hz), 108.6, 104.7 (d, *J* = 25.6 Hz), 43.1, 34.6, 22.4. ^{19}F (470 MHz, $CDCl_3$) δ ppm -57.8 (s, 3F), -98.3 (ddd, *J* = 4.8, 8.1, 8.1 Hz, 1F). HRMS (EI), M + 1 calculated for $C_{18}H_{15}F_4N_3O$, 366.1224, found 366.1199.

Biological Assessments

Mycobacterium bovis BCG and *Mycobacterium tuberculosis* strains were routinely cultured in Middlebrook 7H9 medium (Becton Dickson and Company Limited,

USA) supplemented with 0.05 % tween 80, 0.5 % glycerol, bovine serum albumin fraction V, D-glucose, and NaCl. *M. tuberculosis* clinical isolate N0145 was a gift from Sebastien Gagneux (Swiss Tropical and Public Health Institute at the University of Basel). Prior to use, bacteria cells were pelleted and resuspended in medium without glycerol and adjusted to a cell density of circa 10^7 CFU/mL. The test compounds were tested in the presence or absence of Q203. Prior to the assay, Q203 or DMSO (solvent control) was added to the bacteria cultures. Q203 was used in excess (at 100 nM) to completely inhibit the function of the cytochrome *bcc:aa*$_3$, thereby revealing the activity of cyt-*bd* in the assay. The Q203 ATP IC_{50} for *M. bovis* BCG, *M. tuberculosis* H37Rv, and *M. tuberculosis* N0145 are 2.6, 1.0, and 2.5 nM, respectively (Suppl. Fig S61). The test compounds were tested in eight concentrations, starting at 25 µM, in two-fold dilutions (0.2 – 25.0 µM) in the presence or absence of 100 nM Q203. 1 µL of test compounds of varying concentrations was added to each well of 96-well white plates, and 100 µL of bacterial culture was subsequently added. The assay plates were incubated at 37°C for 15 h, after which the BacTiter-Glo™ (Promega, USA) reagent was added. Following a 12-min incubation, the luminescence of each plate was measured using a BioTek Cytation 3 Cell Imaging Multiple mode reader. IC_{50} values were determined using GraphPad Prism 9.

Results and Discussion

Our initial efforts were to probe the effect of alteration and modification of the phenethylaniline moiety around a fixed quinazoline core. This was done by

syntheses of 10 compounds and screening against *M. bovis* BCG and Mtb strains (H37Rv and N0145) to assess potency against mycobacterial cyt-*bd*. A representative compound from this set (**7a**) served as the foundation toward the design of a second set of 11 compounds that focused upon modification of the quinazoline core and subsequently screened for cyt-*bd* activity.

Chemical Syntheses of the first set of N-phenethylquinazolin-4-amines (**6a**-**15a**) and the second set of N-phenethylquinazolin-4-amines (**16a**-**26a**)

The first set of compounds (**6a** – **15a**) were prepared by coupling of 4-chlorquinazoline (**5**) with ten commercially available amines (**6** – **15**) using S_NAr conditions (basic or acidic, Scheme 1). These compounds were evaluated for their potency against cyt-*bd* in *M. bovis* BCG using an ATP readout (Table 4.1).

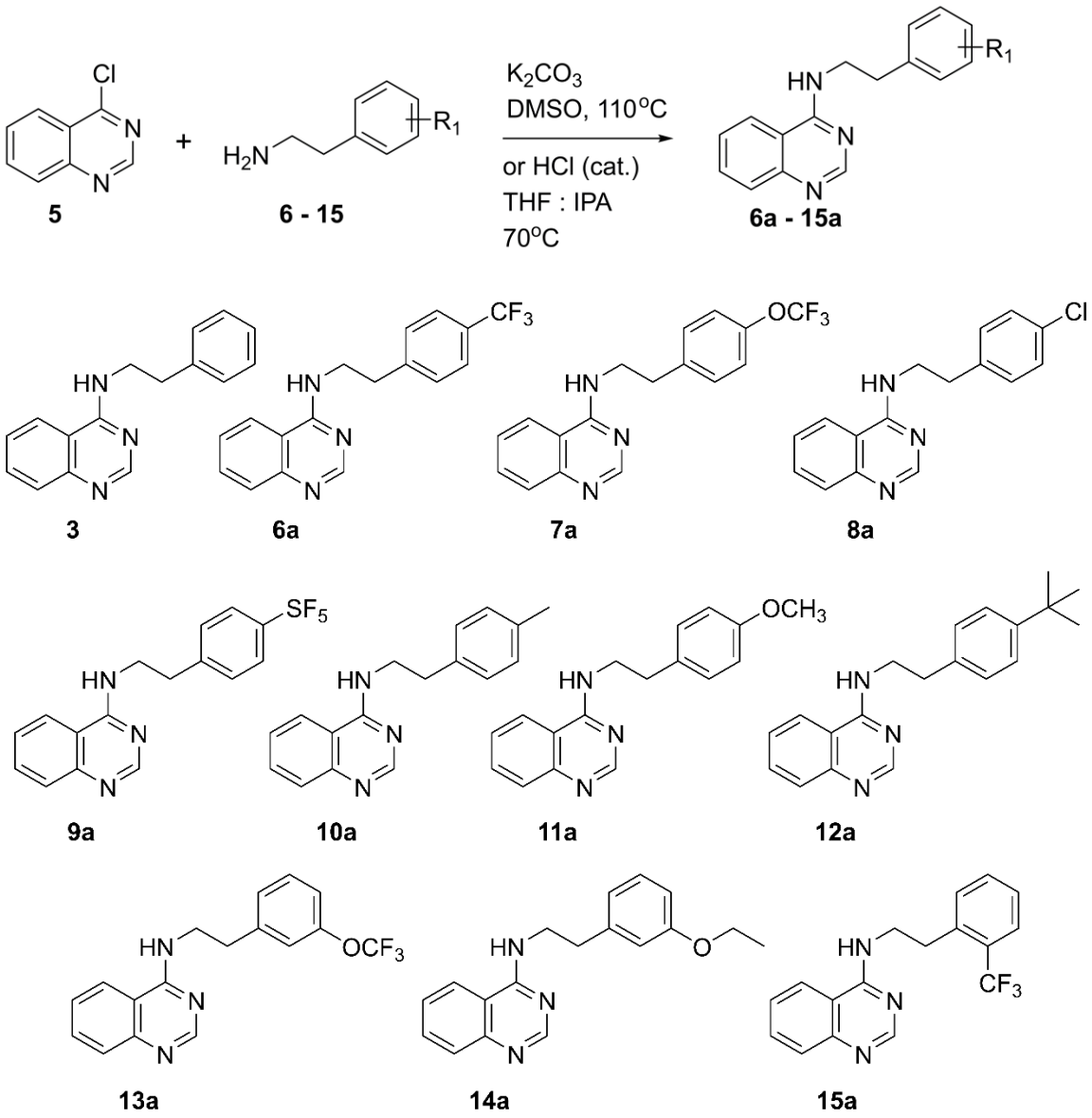

Figure 4.2 S_NAr conditions to prepare the first set of *N*-phenethylquinazolin-4-amines (**6a** – **15a**) for screening against cyt-*bd* of *M. bovis* BCG and *M. tuberculosis* H37Rv.

The second set of compounds (**16a** – **26a**) was prepared by coupling eight functionalized 4-chloroquinazolines (**16** – **26**) with 4-(trifluoromethoxy)benzylamine (**7**) using standard S_NAr conditions (Scheme 2). As

with the first set, the potency was determined against cyt-*bd* in *M. bovis* BCG and *M. tuberculosis* H37Rv by ATP readout (Table 4.2).

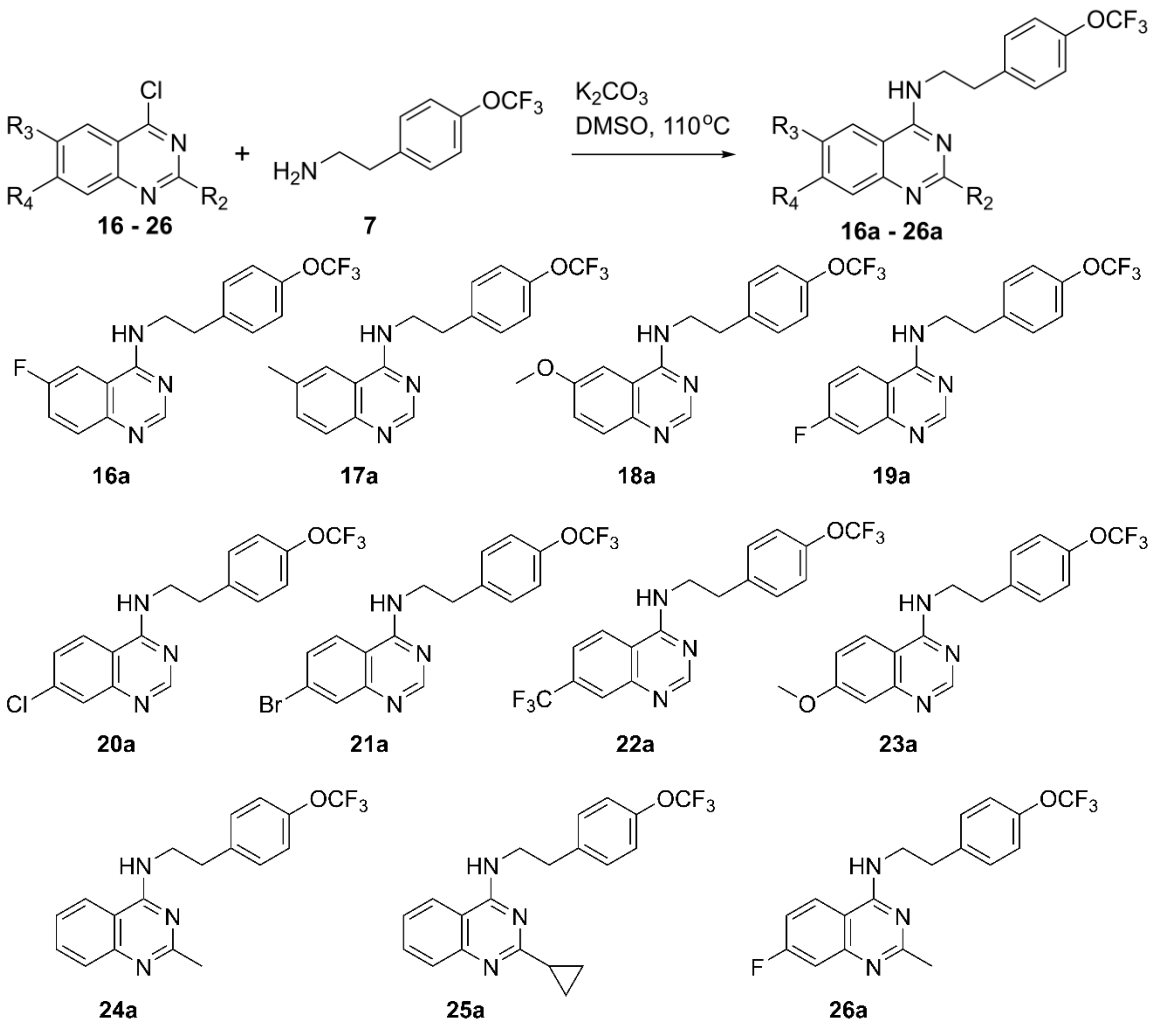

Figure 4.3 S_NAr conditions to prepare the second set of *N*-phenethylquinazolin-4-amines (**16a** – **26a**) for screening against cyt-*bd* of *M. bovis* BCG and *M. tuberculosis* H37Rv.

Structure-activity-Relationship Studies

The structure-activity-relationship (SAR) studies revealed that the cyt-*bd* of *M. bovis* BCG was more sensitive to inhibition than *M. tuberculosis* H37Rv (Table

4.1). This mirrors the trend observed previously and is indicative that there is a greater expression of cyt-*bd* within the lab adapted *M. tuberculosis* H37Rv strain as compared to *M. bovis* BCG or “fresh” Mtb clinical isolate N0145 [162]. This is further supported by the activity of Aurachin D [121], a known synergist cyt-*bd* inhibitor of Mtb, which had greater potency against *M. bovis* BCG in our ATP assay as compared to *M. tuberculosis* H37Rv (2.9 µM vs. 5.5 µM, respectively; Table 4.1). In addition, based on our assay, compounds **6a** – **15a** are all specific inhibitors of cyt-*bd* as they show no potency against wild-type (WT) *M. bovis* BCG or *M. tuberculosis* H37Rv (Mtb-H37Rv), whereas the positive control bedaquiline (BDQ), a selective ATP synthase inhibitor, remains very potent against both strains (Table 4.1). Interestingly, Aurachin D showed the expected synergy with Q203 against mycobacterial strains but was unexpectedly active against wild-type Mtb-H37Rv (Table 4.1).

Compound	clog *P*	Mol. Wt.	Replicating ATP IC_{50} (μM) BCG		H37Rv		N0145	
			–Q203	+Q203	–Q203	+Q203	–Q203	+Q203
3	3.98	249.31	>25	11.2 ± 1.574	>25	27.2 ± 4.613	>25	6.9 ± 0.752
6a	4.86	317.31	>25	5.1 ± 0.501	>25	16.9 ± 3.758	>25	2.6 ± 0.581
7a	5.01	333.31	>25	2.1 ± 0.205	>25	11.0 ± 2.081	>25	1.1 ± 0.719
8a	4.69	283.76	>25	12.5 ± 1.952	>25	29.7 ± 5.336	>25	8.2 ± 0.808
9a	5.21	375.36	>25	3.9 ± 0.490	>25	14.5 ± 2.691	>25	2.3 ± 0.853
10a	4.48	263.34	>25	6.7 ± 1.116	>25	20.7 ± 3.624	>25	3.8 ± 0.813
11a	3.9	279.34	>25	13.7 ± 2.107	>25	>25	>25	7.1 ± 0.653
12a	5.81	305.42	>25	0.8 ± 0.144	>25	5.8 ± 0.616	>25	0.1 ± 0.017
13a	5.01	333.31	>25	7.1 ± 0.849	>25	22.5 ± 3.912	>25	3.8 ± 0.733
14a	4.43	293.36	>25	5.8 ± 0.867	>25	19.3 ± 5.703	>25	3.2 ± 0.204
15a	4.86	317.31	>25	3.9 ± 0.311	>25	17.0 ± 2.945	>25	3.2 ± 0.795
1	5.85	313.44	>25	5.8 ± 1.06	>25	18.9 ± 9.03	>25	8.5 ± 2.38
2	6.69	381.36	>25	0.7 ± 0.103	>25	6.3 ± 0.349	>25	0.3 ± 0.049
BDQ	7.25	555.52	0.17 ± 0.019	0.11 ± 0.026	0.06 ± 0.019	0.04 ± 0.024	0.05 ± 0.003	0.03 ± 0.001
Aurachin D	6.79	363.55	>25	2.9 ± 0.317	5.5 ± 1.107	7.3 ± 1.973	>25	1.5 ± 0.065

Table 4.1 In vitro activity of phenethyl-quinazolin-4-yl-amines (**3**, **6a**-**15a**) and control compounds Bedaquiline (BDQ), ND-11992 (**2**), and Aurachin D against three mycobacterial strains (*M. bovis* BCG, *M. tuberculosis* H37Rv, and *M. tuberculosis* N0145). IC_{50} values were determined by ATP depletion in the presence and absence of Q203 (see 2.2 for details). IC_{50} values were determined using GraphPad Prism 9. The values reflected in the table represent the average and standard deviation, which were calculated from the IC_{50} values of replicates from two experimental repeats. cLog*P* was calculated by Perkin Elmer ChemDraw Professional 16.0. Bedaquiline (BDQ), ND-11992 (**2**) and Aurachin D were used as positive control compounds.

SAR trends revealed that the pendant aryl group can accommodate a variety of steric and electronic changes and retain good activity (Table 4.1). Evaluation of the compounds with electron withdrawing substituents **6a** (*p*-CF_3), **7a**, (*p*-OCF_3), **8a** (*p*-Cl), **9a** (*p*-SF_5), indicated that **7a** is the most potent compound with IC_{50} values of 2.1 μM against *M. bovis* BCG and 11 μM against Mtb H37Rv. We explored electron withdrawing groups at the meta- and ortho-positions of the

pendant aryl group by comparing compound sets **7a** (para-OCF_3) and **13a** (meta-OCF_3) and **6a** (para-CF_3) and **15a** (ortho-CF_3). We found that the meta-OCF_3 compound (**13a**) position was less potent compared to the para-OCF_3 (**17a**). Whereas incorporation of substituents in the ortho-position gave slightly improved potency against *M. bovis* but equal activity (within error) in Mtb-H37Rv as demonstrated by comparing **6a** and **15a**. When evaluating the compounds with electron donating substituents, **10a** (*p*-CH_3), **11a** (*p*-OCH_3), and **12a** (*p*-*tert*-butyl), **12a** was found to be significantly more potent with IC_{50} values of 0.8 µM against *M. bovis* BCG and 5.8 µM against Mtb H27Rv. That is a potency improvement over thieno[3,2-*d*]pyrimidine (**1**) and activity on par with the optimized quinazoline ND-11992 (**2**). This is particularly interesting as it follows the Topliss aromatic substitution decision tree pattern [125] where one would first evaluate the phenyl (**3**), then *para*-chloro (**8a**) and if equally potent (as it is in our assays) then prepare the *tert*-butyl (**12a**) to derive the most potent compound. While the Topliss approach can often lead to compounds with improved potency it also directs the syntheses of compounds which often have metabolic liabilities (CH_3, OCH_3, *t*-butyl) or toxic pharmacophores (NH_2, NO_2, I). For this reason, we chose **7a** which bears a *para*-trifluoromethoxy group (which is prevalent in various anti-TB drugs such as delamanid, pretomanid, and telacebec) as the basis for our second set of compounds (Table 4.2) because it possesses good potency (IC_{50}'s of 2.1 and 11 µM against BCG and Mtb-H37Rv, respectively).

Compound	clog *P*	Mol. Wt.	Replicating ATP IC_{50} (μM) BCG		H37Rv		N0145	
			–Q203	+Q203	–Q203	+Q203	–Q203	+Q203
16a	5.19	351.3	>25	13.1 ± 0.651	>25	28.8 ± 5.054	>25	7.1 ± 0.207
17a	5.51	347.33	>25	7.5 ± 0.580	>25	22.3 ± 5.796	>25	3.4 ± 0.559
18a	5.41	363.33	>25	26.9 ± 1.231	>25	>25	>25	17.1 ± 0.220
19a	5.19	351.3	>25	0.8 ± 0.077	>25	7.6 ± 1.079	>25	0.2 ± 0.057
20a	5.76	367.75	>25	>25	>25	>25	>25	>25
21a	5.91	412.21	>25	6.7 ± 0.591	>25	19.5 ± 2.356	>25	4.9 ± 0.226
22a	5.95	401.31	>25	>25	>25	>25	>25	>25
23a	5.41	363.33	>25	>25	>25	>25	>25	>25
24a	5.51	347.33	12.2 ± 0.737	3.1 ± 0.369	7.5 ± 1.025	11.7 ± 1.252	8.2 ± 0.654	2.9 ± 0.140
25a	5.95	373.37	8.5 ± 1.529	4.0 ± 0.604	7.6 ± 1.026	11.7 ± 1.036	7.3 ± 1.052	2.1 ± 0.347
26a	5.69	365.32	27.6 ± 9.513	6.5 ± 0.751	23.6 ± 7.807	16.9 ± 3.822	32.7 ± 2.700	4.6 ± 0.219
2	6.69	381.36	>25	0.7 ± 0.103	>25	6.3 ± 0.349	>25	0.3 ± 0.049
BDQ	7.25	555.52	0.17 ± 0.019	0.11 ± 0.026	0.06 ± 0.019	0.04 ± 0.024	0.05 ± 0.003	0.03 ± 0.001
Aurachin D	6.79	363.55	>25	2.9 ± 0.317	5.5 ± 1.107	7.3 ± 1.973	>25	1.5 ± 0.065

Table 4.2 Screening of the second set of *N*-phenethylquinazolin-4-amines **16a** – **26a** against cyt-*bd* of *M. bovis* BCG and *M. tuberculosis* H37Rv by ATP readout along with known inhibitors ND-11992 (**2**), Aurachin D and Bedaquiline (BDQ) as positive controls. IC_{50} values were determined by ATP depletion in the presence and absence of Q203 (see 2.2 for details). IC_{50} values were determined using GraphPad Prism 9. The values given in the table represent the average and standard deviation, which were calculated from the IC_{50} values of replicates from two experimental repeats. cLog*P* was calculated by Perkin Elmer ChemDraw Professional 16.0. Bedaquiline (BDQ), ND-11992 (**2**) and Aurachin D were used as positive control compounds.

The SAR trends for alteration of the quinazoline core suggest an interplay between both steric and electronic effects (Table 4.2). For instance, the 6-position was probed with three substituents – fluoro (**16a**), methyl (**17a**) and methoxy (**18a**) – which resulted in a wide spectrum of activity. The 6-methyl analog (**17a**) was the most active against *M. bovis* BCG (IC_{50} of 7.5 μM) but weakly active against Mtb H37Rv (IC_{50} of 22 μM). Whereas the fluoro (**16a**) and methoxy (**18a**) analogs had

diminished potency against *M. bovis* BCG (IC_{50} of 13 µM and 27 µM, respectively) and both were >25 µM against Mtb H37Rv. The 7-position was explored with five different substituents – fluoro (**19a**), chloro (**20a**), bromo (**21a**), trifluoromethoxy (**22a**) and methoxy (**23a**) – resulting in only two active compounds (**19a** and **21a**). The 7-fluoro analog (**19a**) displayed good potency against both mycobacterial strains (IC_{50} of 0.8 µM and 7.6 µM; respectively) and the 7-bromo (**21a**) showed much better potency against *M. bovis* BCG than Mtb H37Rv (IC_{50} of 7 µM and 20 µM; respectively). The most interesting SAR was observed with substitution of the quinazoline 2-position with methyl (**24a**) and cyclopropyl (**25a**) groups. Both compounds displayed good potency range (3 – 12 µM) against both the cyt-*bd* target strains and parental mycobacteria strains suggesting possible dual modes of action. Lastly, one compound (**26a**) bore both 7-fluoro and 2-methyl quinazoline substituents which biased potency back towards the cyt-*bd* strains (IC_{50} of 7 and 17 µM; respectively) over the wild-type strains (IC_{50} of 28 µM and 24 µM, respectively).

Our previous work had shown that the laboratory adapted Mtb H37Rv strain over expresses cyt-*bd* resulting in higher IC_{50} values than those observed using a clinical Mtb isolate [116]. These higher IC_{50} values render compound ranking more challenging. To gain greater insight on the potency of these compounds, they were re-screened against the clinical Mtb isolate N0145 strain. As observed previously with the thieno[3,2-*d*]pyrimidin-4-amine class of cyt-*bd* oxidase inhibitors [162], these compounds displayed greatly improved potency against the Mtb clinical isolate likely due to lower expression of cyt-*bd* within clinical isolates as compared to lab

adapted strains like H37Rv [124]. Two compounds, **7a** and **12a**, from the first set were more active than or comparable in activity to Aurachin D (0.1 and 1.1 µM vs. 1.5 µM, respectively). While six additional compounds (**6a**, **9a**, **10a**, **13a** – **15a**) had IC_{50} values below 5 µM against N0145-Mtb. In the second set of compounds, only **19a** had potency superior to Aurachin D (0.2 µM vs. 1.5 µM, respectively) and four additional compounds (**17a**, **21a**, **24a – 26a**) had potency below 5 µM. The two most potent compounds, **12a** and **19a**, had slightly improved potency relative to ND-11992 which was active in the murine infection model of tuberculosis. However, preliminary metabolic stability assessment of these compounds against human and rat microsomes indicate much more rapid metabolism than that of ND-11992 (data not shown).

Conclusions

The described *N*-phenethylquinazolin-4-amine class of compounds are mycobacterial cyt-*bd* inhibitors. Through focused SAR, the potency of the hit compound **3** (IC_{50} = 6.9 µM against Mtb N0145) was improved with 14 of the 22 analogs (64%) and two, **12a** and **19a**, had sub-micromolar potency (0.1 and 0.2 µM against Mtb N0145, respectively). Future work includes identification of more efficacious compounds through additional SAR around the quinazoline core. These results will be reported in due course.

Patents

US Provisional Application No. 62/783,984.

Supplementary Materials:

The following are available online at www.mdpi.com/article/10.3390/app11199092/s1, Figures C.1-C.60: ^{1}H NMR, ^{13}C NMR and ^{19}F NMR Spectra of all compounds; Figure C.61: ATP dose response curves of Q203 in *M. bovis* BCG, *M. tuberculosis* H37Rv, and *M. tuberculosis* N0145.

Author Contributions:

G.C.M. designed the compounds which were prepared and characterized by S.M.H. and G.C.M. K.P. designed all the biological assays which were carried out by B.S.L. and N.P.K. M.J.M. provided data interpretation and scientific direction. All authors assisted in the drafting and editing of the manuscript.

Funding:

M.J.M. and G.C.M. acknowledge funding from the NIH R37AI054193. K.P. and G.C.M. acknowledge funding from the NIH R01AI139465. This study was partially funded by the National Research Foundation (NRF) Singapore under its NRF Competitive Research Programme (Project Award Number NRF–CRP18–2017–01, to K.P.) and its NRF Investigatorship programme (Award Number NRF-I06-2020-0012, to K.P.). B.S.L. is supported by a Nanyang President's Graduate Scholarship from NTU.

Acknowledgments:

G.C.M. acknowledges Prof. Jennifer DuBois for persistent scientific discussions, Prof. Mary Cloninger for mentoring guidance and Dr. Kate Marshall for NMR assistance.

Conflicts of Interest:

Hsiri Therapeutics has licensed this technology. M.J.M. and G.C.M. own equity in Hsiri. M.J.M. is CSO of Hsiri. G.C.M. and K.P. are consultants to Hsiri. Hsiri Therapeutics did not fund this study and was not involved in study design or interpretation.

CHAPTER FIVE

CONCLUSIONS AND FUTURE DIRECTIONS

Conclusions

Chapter 2 introduced the syntheses and structure-activity relationships as well as the activity of thieno[3,2-*d*]pyrimidin-4-amine *Mycobacterium tuberculosis bd* oxidase inhibitors. Compounds were tested in an ATP depletion assay with and without the addition of cyt-*bcc:aa*$_3$ inhibitor Q203 against *Mycobacterium bovis* BCG, *Mycobacterium tuberculosis* H37Rv and *Mycobacterium tuberculosis* clinical isolate N0145. All compounds exhibited activity against the three mycobacterial strains used, exhibiting IC_{50} values from 6 to 54 µM when cyt-*bcc:aa*$_3$ inhibitor Q203 was added. Compared to the unsubstituted phenylethyl compound electron-withdrawing groups improved potency, with *para*-OCF_3 being the most potent of the subset displaying 10.6 µM potency against N0145. The subset with electron-donating substituents showed less than stellar activity apart from the *tert*-butyl. The most active compound was *N*-(4-(*tert*-butyl)phenethyl)thieno[3,2-*d*]pyrimidin-4-amine showing IC_{50} values from 6 to 18 µM. Although the activity of this collection of thienopyrimidine analogs is modest against mycobacterial strains, the lessons learned from these structure-activity relationships will guide the design of more potent cyt-*bd* inhibitors and provide tools to investigate targets of the oxidative phosphorylation pathway.

Chapter 3 builds on Chapter 2 by describing the quantitative investigation of membrane partitioning behavior of thieno[3,2-*d*]pyrimidin-4-amines in 1,2-dipalmitoyl-*sn*-glycero-3-phosphocholine (DPPC). The thieno[3,2-*d*]pyrimidin-4-amine derivatives reported in this chapter are cyt-*bd* oxidase inhibitors. The comparable partitioning within the DPPC model membrane system for all compounds studied indicates that differences in activity against cyt-*bd* oxidase arise from relative effectiveness at binding to the target enzyme rather than from membrane uptake or transport. The methods reported here for studying membrane partitioning are especially important for molecules that bind to transmembrane targets with unknown structures.

Chapter 4 builds upon Chapter 2, by reporting the syntheses and structure-activity relationships of *N*-phenethyl-quinazolin-4-yl-amines as potent inhibitors of cytochrome *bd* oxidase in *Mycobacterium tuberculosis*. Here, 22 compounds were screened for biological activity against *Mycobacterium bovis* BCG, *Mycobacterium tuberculosis* H37Rv and *Mycobacterium tuberculosis* clinical isolate N0145 in an ATP depletion assay. Two compounds; {2-[4-(*tert*-Butyl)phenyl]ethyl}quinazolin-4-ylamine and (7-Fluoroquinazolin-4-yl){2-[4-(trifluoromethoxy)phenyl]ethyl}amine were found to be more active against Mtb clinical strain N0145 (0.1 and 0.2 μM, respectively) than aurachin D (1.5 μM), the naturally derived cyt-*bd* inhibitor.

Future Directions

Multivalent scaffold

Cytochrome *bd* oxidase is a cell-surface protein that may be better inhibited by multivalent interactions. In biological systems, interactions between a ligand and receptor are fleeting and therefore weak. This issue can be overcome by multivalent interactions. Multivalent interactions can lengthen the duration of a binding event.[197] There are different classifications of multivalency. One is known as the statistical effect. This is when the binding partner presents multiple ligands that can interact with a receptor. Having multiple copies of the drug presented on the surface of a dendrimer can be more effective than having the same number of drug molecules free in solution. The local concentration of ligands at the receptor site is increased by having another adjacent ligand that can interact and bind with the receptor.[198] Polyamidoamine (PAMAM) dendrimers are tree-like branched polymers with repeating amidoamine subunits and terminal amine groups. The surface functional groups can be used for purposes including attaching a biologically active molecule such as a drug, antibody, sugar, or lipid,[199] or targeting agent for specific delivery and controlled release, or imaging applications[190]. These synthetic polymers have a well-defined structure and are nanometer scale in size[200]. In contrast, hyperbranched polymers are non-symmetrical, polydisperse, more easily prepared, and less expensive. Polymer choice is guided by the desired utility and takes advantage of different characteristics/physical properties.

For purposes of drug delivery, dendrimers have been demonstrated to be useful.[200-203] It is important that the drug-dendrimer conjugate be stable enough to reach the target site so that the drug may be delivered. This is a critical challenge associated with designing drug-dendrimer conjugates for effective drug delivery. Bonds commonly used to attach drugs to dendrimers include amide and ester bonds. The terminal endgroups of the dendrimer can be decorated with a biologically active molecule and later cleaved from the dendrimer to produce an active drug.

The PAMAM dendrimer has been used as a targeted carrier of the antitumor drug methotrexate.[204] Additionally, linkers can be made of varying lengths, flexibility, and aqueous solubility to optimize multivalent binding.[205]

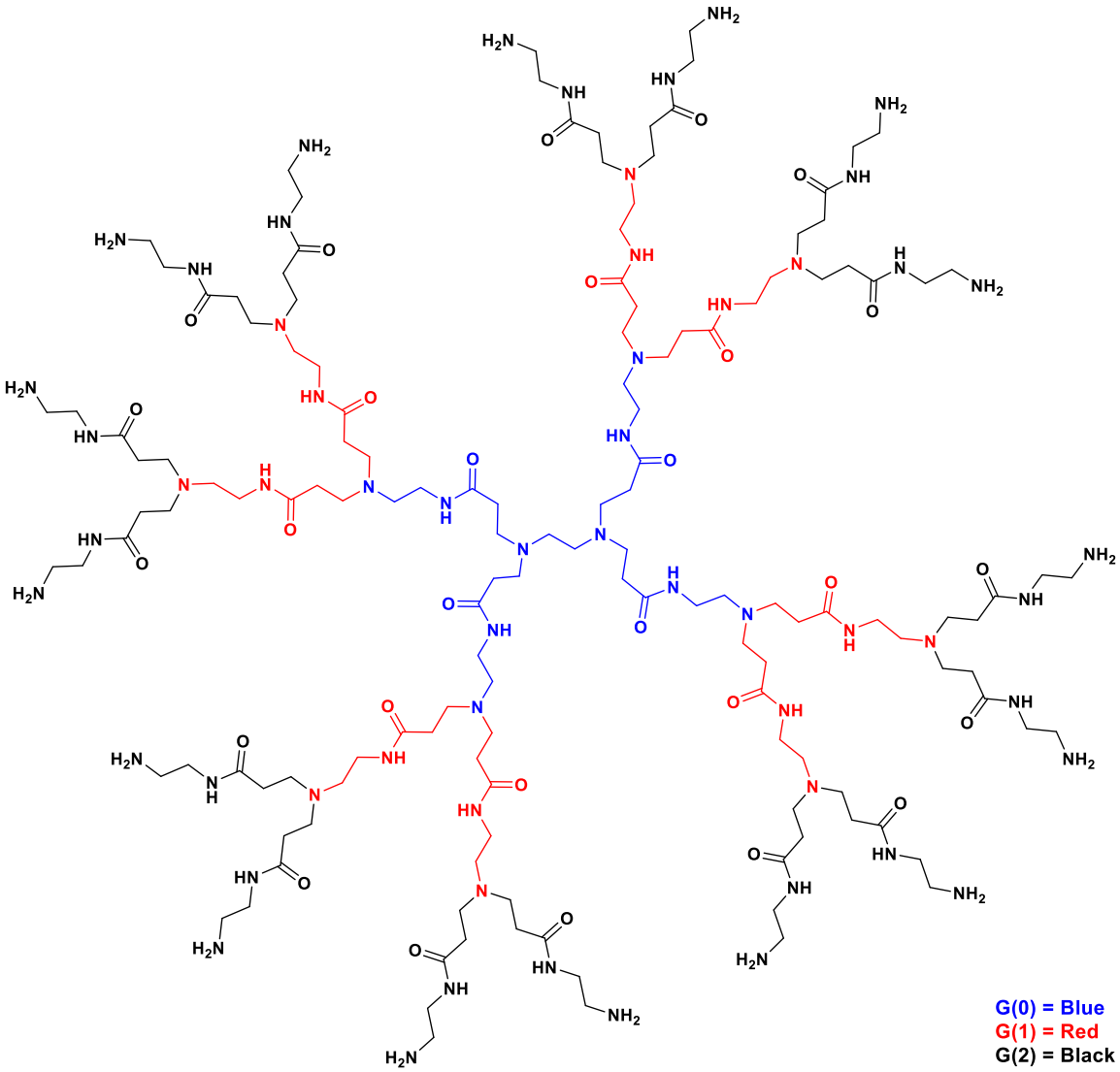

Figure 5.1 Poly(amidoamine)(PAMAM) dendrimer

Development of effective drugs and drug combinations for treatment of TB requires ample support from many disciplines. Structure-activity relationships, genetic studies and cell-based assays build a strong foundation on which to build and develop effective cyt-*bd* inhibitors, but until human clinical trials are undertaken there is no way of knowing which structures will be the most effective at eliminating Mtb. From the work described in this dissertation, a few themes are present in the

SAR of thienopyrimidine and quinazoline cores. Increasing the fluorine content through the addition of a CF_3, OCF_3, or SF_5 substituent generally increases activity of the cyt-*bd* inhibitor against Mtb. This is not surprising as metabolic advantages of fluorinated compounds are well-known.[206] Replacing H with F often affords molecules with similar or improved potency. In this work, substitution with a *tert*-butyl group resulted in high activity against Mtb in both the thienopyrimidine and quinazoline SAR. Replacement of the *tert*-butyl group with a bioisostere such as a trifluormethylcyclopropyl group may provide greater metabolic stability than the *tert*-butyl analog while simultaneously increasing fluorine content.

Targeting cyt-*bd* is vital for the swift elimination of drug-resistant strains of Mtb. Inhibition of both cyt-*bcc:aa*$_3$ and cyt-*bd* shows remarkable promise as an efficacious treatment strategy for TB disease. Inhibiting the oxidative phosphorylation pathway provides a means of abbreviating treatment duration and preventing activation of latent infection. Groundwork has been established for the design of cyt-*bd* inhibitors. It is important to evaluate partitioning behavior of drug compounds, especially when drug targets are embedded in the cellular membrane. Drug compounds must also be designed so that they reach the target. Through structural modifications of the drug compound core and substituents, the electronic and steric features can be tuned. These characteristics are critically important for membrane partitioning and target binding and must be considered when endeavoring to design the ideal cyt-*bd* inhibitor.

APPENDICES

APPENDIX A

SUPPORTING INFORMATION FOR CHAPTER 2

Experimental Section, Chemistry

All anhydrous solvents, reagent grade solvents for chromatography and starting materials were purchased from either Aldrich Chemical Co. (Milwaulkee, WI) or Fisher Scientific (Suwanee, GA) unless otherwise noted. The reactions were monitored by TLC on precoated Merck 60 F254 silica gel plates and visualized using UV light (254 nm). All compounds were analyzed for purity by a Bruker micrOTOF with Agilent 1290 UHPLC or Agilent 6520 Q-TOF with Agilent 1100 nano-HPLC and were characterized by ^{1}H and ^{13}C NMR using a Bruker DPX Avance I NMR Spectrometer (300 MHz) and/or a Bruker Ascend Avance III HD Spectrometer (500 MHz) and/or Bruker Avance III Spectrometer (600 MHz). Chemical shifts are reported in ppm (δ) relative to the residual solvent peak in the corresponding spectra; chloroform δ 7.27 and δ 77.23, methanol δ 3.31 and δ 49.00 and coupling constants (*J*) are reported in hertz (Hz) (where, s = singlet, br s = broad singlet, d = doublet, dd = double doublet, bd = broad doublet, ddd = double doublet of doublet, t = triplet, tt–triple triplet, q = quartet, m = multiplet) and analyzed using MestreNova NMR data processing. ^{19}F NMR were run without a standard and are uncorrected. Mass spectra values are reported as m/z. Melting points were measured on a Büchi B-545 melting point instrument and are uncorrected, measured against benzoic acid 118.8-120.2°C.

General procedure A for the preparation of **7**, **10**, **11**, **13**, **17**,**19**, **22**.

In a sealed vial, 4-chlorothieno[3,2-*d*]pyrimidine (100 mg, 0.57 mmol), desired amine (0.57 mmol) and K_2CO_3 (79 mg, 0.57 mmol) were dissolved in DMSO (4 mL). The reaction was heated to 100ºC for 12 h. The reaction mixture was concentrated to dryness and the residue was dissolved in CH_2Cl_2 and washed with 5% aqueous acetic acid solution (2x), water and brine. The organic phase was collected, dried over sodium sulfate, filtered, and concentrated in vacuo. Crude material obtained was purified by either silica gel column chromatography with a gradient of CH_2Cl_2 : ethyl acetate : solvent system (0 to 80%) or recrystallized from hot isopropanol or acetonitrile to afford the product.

General procedure B for the preparation of **12**, **14**-**16**, **18**, **20**, **21**.

In a sealed vial, 4-chlorothieno[3,2-*d*]pyrimidine (100 mg, 0.57 mmol, 1 equiv.) and amine (1 equiv.) were dissolved in a 3:1 tetrahydrofuran: 2-propanol solution (4 mL). Next, 12 M HCl (11 µL, “drop”, ~0.4 equiv.) was added. The solution heated to 70°C for 24 h. The reaction was concentrated to dryness and the residue was dissolved in CH_2Cl_2 and washed with saturated aqueous NaHCO3 solution, water, and brine. The organic phase was collected, dried over sodium sulfate, filtered, and concentrated *in vacuo*. Crude material obtained was purified by either silica gel column chromatography with a gradient of CH_2Cl_2 : ethyl acetate : solvent system (0-80%) or recrystallized from hot isopropanol or acetonitrile to afford the product.

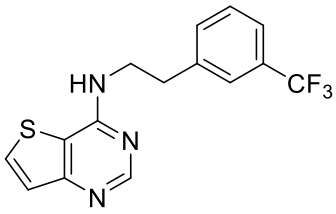

Figure A.1 *N*-(3-(Trifluoromethyl)phenethyl)thieno[3,2-*d*]pyrimidin-4-amine (**7**). The reaction was carried out according to the general procedure A using 4-chlorothieno[3,2-*d*]pyrimidine (50 mg, 0.28 mmol), 2-(3-(trifluoromethyl)phenyl)ethan-1-amine (55 mg, 0.38 mmol), potassium carbonate (39 mg, 0.28 mmol) to give **7** as a yellow flaky solid (32 mg, 33% yield). m.p. 109.8-111.4°C. ^{1}H NMR (500 MHz, $CDCl_3$) δ ppm 8.68 (s, 1H), 7.72 (d, *J* = 5.4 Hz, 1H), 7.55-7.51 (m, 2H), 7.47-7.43 (m, 3H), 5.06 (br s, 1H), 3.97 (dt, *J* = 6.9, 6.3 Hz, 2H), 3.11 (t, *J* = 7.0 Hz, 2H). ^{13}C NMR (125 MHz, $CDCl_3$) δ ppm 159.8, 157.2, 155.0, 139.7, 132.3, 130.9, 129.1, 125.5, 123.5, 115.2, 42.2, 35.6. ^{19}F (282 MHz, $CDCl_3$) δ ppm -62.56 (s, 3F). HRMS (EI), M + 1 calculated for $C_{15}H_{12}F_3N_3S$, 324.0777, found 324.0890; HPLC t_R = 5.9 min, >95% pure.

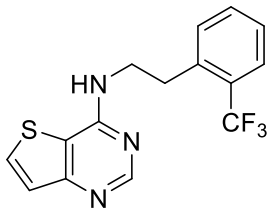

Figure A.2 *N*-(2-(Trifluoromethyl)phenethyl)thieno[3,2-*d*]pyrimidin-4-amine (**10**). The reaction was carried out according to the general procedure A using 4-chlorothieno[3,2-*d*]pyrimidine (100 mg, 0.57 mmol), 2-(2-(trifluoromethyl)phenyl)ethan-1-amine (0.09 mL, 0.57 mmol), potassium carbonate (79 mg, 0.57 mol) to give **10** as white, fluffy crystals (80.8 mg, 42%). m.p. 141.5-141.8°C. ^{1}H NMR (600 MHz, $CDCl_3$) δ ppm 8.68 (s, 1H), 7.72 (d, *J* = 5.3 Hz, 1H), 7.68 (d, *J* = 7.7 Hz, 1H), 7.51 (t, *J* = 7.4 Hz, 1 H), 7.46-7.42 (m, 2H), 7.36 (t, *J* = 7.4 Hz, 1H), 5.13 (s, 1H), 3.96 (dt, *J* = 7.3, 6.8 Hz, 2H), 3.24 (t, *J* = 6.9 Hz, 2H). ^{13}C NMR (150 MHz, $CDCl_3$) δ ppm 159.8, 157.2, 155.1,137.4, 131.9, 131.7, 130.8, 126.7, 125.5, 123.5, 121.3, 115.2, 42.2, 23.5. ^{19}F (470 MHz, $CDCl_3$) δ ppm -59.2 (s, 3F). HRMS (EI), M + 1 calculated for $C_{15}H_{12}F_3N_3S$, 324.0777, found 324.0786; HPLC t_R = 6.4 min, >95% pure.

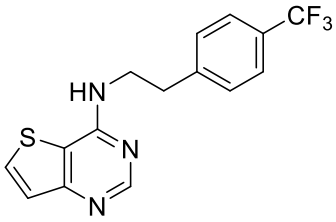

Figure A.3 *N*-(4-(Trifluoromethyl)phenethyl)thieno[3,2-*d*]pyrimidin-4-amine (**11**). The reaction was carried out according to the general procedure A using 4-chlorothieno[3,2-*d*]pyrimidine (100 mg, 0.57 mmol), 2-(4-(trifluoromethyl)phenyl)ethan-1-amine (108 mg, 0.57 mmol), and potassium carbonate (79 mg, 0.57 mmol) to give **11** as yellow crystals (75.1 mg, 39%). m.p. 171.0-171.5°C. ^{1}H NMR (500 MHz, $CDCl_3$) δ ppm 8.68 (s, 1H), 7.72 (d, *J* = 5.4 Hz, 1H), 7.60 (d, *J* = 8.1 Hz, 2H), 7.44 (d, *J* = 5.4 Hz, 1H), 7.38 (d, *J* = 8.0 Hz, 2H), 5.08 (s, 1H), 3.97 (dt, *J* = 6.9, 6.2 Hz, 2H), 3.11 (t, *J* = 7.0 Hz, 2H). ^{13}C NMR (125 MHz, $CDCl_3$) δ ppm 159.89, 157.16, 155.03, 142.98, 130.89, 129.23, 125.10 (q, *J* = 15.0 Hz), 125.52, 123.13, 120.97, 115.22, 42.13, 35.60. ^{19}F (470 MHz, $CDCl_3$) δ ppm -62.43 (s, 3F). HRMS (EI), M + 1 calculated for $C_{15}H_{12}F_3N_3S$, 324.0777, found 324.0780; HPLC t_R = 6.5 min, >95% pure.

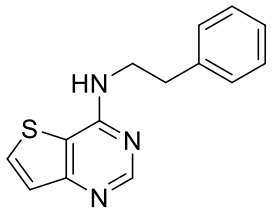

Figure A.4 *N*-Phenethylthieno[3,2-*d*]pyrimidin-4-amine amine (**12**). The reaction was carried out according to the general procedure B using 4-chlorothieno[3,2-*d*]pyrimidine (100 mg, 0.57 mmol), 2-phenylethan-1-amine (0.07 mL, 0.57 mmol) and 12 N HCl (11 µL, 0.13 mmol) to give **12** as yellow, sand-like crystals (35.1 mg, 24%). m.p. 173.0-173.5°C. ^{1}H NMR (500 MHz, DMSO) δ ppm 8.46 (s, 1H), 8.08 (d, *J* = 5.4 Hz, 1H), 7.94 (t, *J* = 5.3 Hz, 1H), 7.37 (d, *J* = 5.4 Hz, 1H), 7.32-7.24 (m, 4H), 7.20 (t, *J* = 7.0 Hz, 1H), 3.72 (dt, *J* = 6.6, 7.9 Hz, 2H), 2.94 (t, *J* = 7.5 Hz, 2H). ^{13}C NMR (125 MHz, DMSO) δ ppm 159.69, 157.30, 155.04, 139.99, 133.26, 129.15, 128.81, 126.56, 124.91, 115.15, 42.29, 35.34. HRMS (EI), M + 1 calculated for $C_{14}H_{13}N_3S$, 256.0903, found 256.0911; HPLC t_R = 5.6 min, >95% pure.

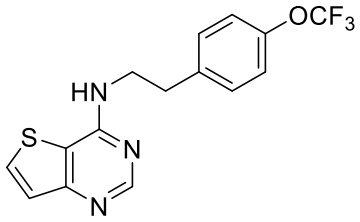

Figure A.5 *N*-(4-(Trifluoromethoxy)phenethyl)thieno[3,2-*d*]pyrimidin-4-amine (**13**). The reaction was carried out according to the general procedure A using 4-chlorothieno[3,2-*d*]pyrimidine (100 mg, 0.57 mmol), 2-(4-(trifluoromethoxy)phenyl)ethan-1-amine (120 mg, 0.57 mmol), and potassium carbonate (81 mg, 0.57 mmol) to give **13** as a white solid (39.2 mg, 20%). m.p. 129.0-130.8°C. ^{1}H NMR (600 MHz, DMSO) δ ppm 8.46 (s, 1H), 8.09 (d, *J* = 5.3 Hz, 1H), 7.95 (t, *J* = 5.5 Hz, 1H, NH), 7.40-7.36 (m, 3H), 7.28 (d, *J* = 7.9 Hz, 2H), 3.73 (dt, *J* = 6.5, 7.6 Hz, 2H), 2.98 (t, *J* = 7.4 Hz, 2H). ^{13}C NMR (150 MHz, DMSO) δ ppm 159.7, 157.3, 155.0, 147.3, 139.6, 133.3, 130.9, 124.9, 121.4, 119.7, 115.1, 42.0, 34.5. ^{19}F (282 MHz, DMSO) δ ppm -56.8 (s, 3F). HRMS (EI), M + 1 calculated for $C_{15}H_{12}F_3N_3OS$, 340.0726, found 340.0741; HPLC t_R = 5.5 min, >95% pure.

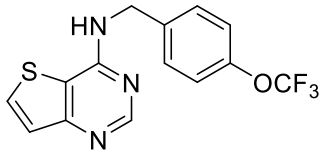

Figure A.6 *N*-(4-(Trifluoromethoxy)benzyl)thieno[3,2-*d*]pyrimidin-4-amine (**14**). The reaction was carried out according to the general procedure B using 4-chlorothieno[3,2-*d*]pyrimidine (50 mg, 0.29 mmol), 4-(trifluoromethoxy)benzylamine (56 mg, 0.29 mmol), and 12 M HCl (11 µL, 0.13 mmol). Crude material was purified through column chromatography (ethyl acetate) to give **14** as an orange solid (21.2 mg, 22%). m.p. 109.5-109.9°C. ^{1}H NMR (600 MHz, $CDCl_3$) δ ppm 8.60 (s, 1H), 7.67 (d, *J* = 5.3 Hz, 1H), 7.40 (d, *J* = 5.3 Hz, 1H), 7.31 (t, *J* = 7.9 Hz, 1H), 7.26 (d, *J* = 7.7 Hz, 1H), 7.20-7.17 (m, 1H), 7.09 (d, *J* = 8.1 Hz, 1H), 5.30 (br.s, 1H), 4.84 (d, *J* = 5.9 Hz, 2H). ^{13}C NMR (150 MHz, $CDCl_3$) δ ppm 157.1, 154.8, 149.6, 140.6, 131.3, 130.2, 126.0, 125.4, 120.3, 120.0, 115.2, 44.4. ^{19}F (282 MHz, $CDCl_3$) ppm -57.7 (s, 3F). HRMS (EI), M + 1 calculated for $C_{14}H_{10}F_3N_3OS$, 326.0569, found 326.0568; HPLC t_R = 6.5 min, >95% pure.

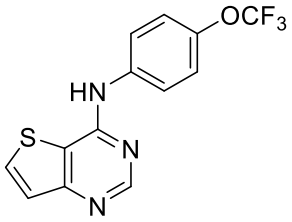

Figure A.7 *N*-(4-(Trifluoromethoxy)phenyl)thieno[3,2-*d*]pyrimidin-4-amine (**15**). The reaction was carried out according to the general procedure B using 4-chlorothieno[3,2-*d*]pyrimidine (60 mg, 0.35 mmol), 4-(trifluoromethoxy)aniline (62 mg, 0.35 mmol), and 12 M HCl (11 µL, 0.13 mmol) to give **15** as a yellow solid (49.6 mg, 45%). m.p. 151.2-151.8°C. ^{1}H NMR (600 MHz, $CDCl_3$) δ ppm 8.77 (s, 1H), 7.79 (d, *J* = 5.4 Hz, 1H), 7.70 (dt, *J* = 9.0, 3.3 Hz, 2H), 7.49 (d, *J* = 5.3 Hz, 1H), 7.31-7.26 (m, 3H). ^{13}C NMR (150 MHz, $CDCl_3$) δ ppm 161.2, 155.6, 154.6, 146.1, 136.4, 123.4, 125.4, 124.3, 121.8, 115.5. ^{19}F (282 MHz, DMSO) δ ppm -58.0 (s, 3F). HRMS (EI), M + 1 calculated for $C_{13}H_8F_3N_3OS$, 312.0413, found 312.0425; HPLC t_R = 5.8 min, >95% pure.

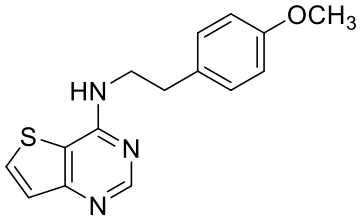

Figure A.8 *N*-(4-Methoxyphenethyl)thieno[3,2-*d*]pyrimidin-4-amine (**16**). The reaction was carried out according to the general procedure B using 4-chlorothieno[3,2-*d*]pyrimidine (100 mg, 0.57 mmol), 2-(4-methoxyphenyl)ethan-1-amine (0.09 mL, 0.57 mmol), and 12 M HCl (11 µL, 0.13 mmol) to give **16** as a shiny bronze solid (75.4 mg, 46%). m.p. 151.5-151.7°C. ^{1}H NMR (600 MHz, $CDCl_3$) δ ppm 8.67 (s, 1H), 7.71 (d, *J* = 5.3 Hz, 1H), 7.44 (d, *J* = 5.3 Hz, 1H), 7.18 (dt, *J* = 8.6, 3.0 Hz, 2H), 6.89 (dt, *J* = 8.6, 3.0 Hz, 2H), 3.92 (dt, *J* = 6.9, 5.9 Hz, 2H), 3.83 (s, 3H), 2.98 (t, *J* = 6.8 Hz, 2H). ^{13}C NMR (150 MHz, $CDCl_3$) δ ppm 159.7, 158.4, 157.3, 155.0, 130.8, 130.6, 129.8, 12525, 115.2, 114.2, 55.3, 42.6, 34.8. HRMS (EI), M + 1 calculated for $C_{15}H_{15}N_3OS$, 286.1009, found 286.0998; HPLC t_R = 5.6 min, >95% pure.

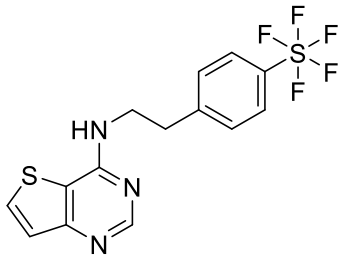

Figure A.9 *N*-(4-(Pentafluoro-λ^6-sulfaneyl)phenethyl)thieno[3,2-d]pyrimidin-4-amine (**17**). The reaction was carried out according to the general procedure A using 4-chlorothieno[3,2-*d*]pyrimidine (72 mg, 0.42 mmol), 2-(4-(pentafluoro-λ^6-sulfaneyl)phenyl)ethan-1-amine (105 mg, 0.42 mmol), and potassium carbonate (59 mg, 0.42 mmol) to give **17** as a white solid (59.3 mg, 36%). m.p. 288.1-288.2°C. ^{1}H NMR (500 MHz, DMSO) δ ppm 8.46 (s, 1H), 8.09 (d, *J* = 5.4 Hz, 1H), 7.94 (t, *J* = 5.4 Hz, 1H), 7.82 (d, *J* = 8.6 Hz, 2H), 7.48 (d, *J* = 8.6 Hz, 2H), 7.38 (d, *J* = 5.4 Hz, 3.76 (dt, *J* = 6.8, 6.2 Hz, 2H), 3.05 (t, *J* = 6.8 Hz, 2H). ^{13}C NMR (125 MHz, $CDCl_3$) δ ppm 159.7, 157.3, 155.0, 145.2, 133.4, 130.2, 126.2, 124.9, 115.2, 41.7, 34.7; ^{19}F NMR (282 MHz, DMSO) δ ppm 84.5 (penta, *J* = 150.0 Hz, 1F), 63.0 (d, *J* = 150.0 Hz, 4F); HRMS (EI), M + 1 calculated for $C_{14}H_{12}F_5N_3S_2$, 382.0466; found 382.0476; HPLC t_R = 6.8 min, >95% pure.

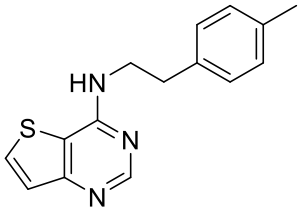

Figure A.10 *N*-(4-Methylphenethyl)thieno[3,2-*d*]pyrimidin-4-amine (**18**). The reaction was carried out according to the general procedure B using 4-chlorothieno[3,2-*d*]pyrimidine (100 mg, 0.57 mmol), 2-(*p*-tolyl)ethan-1-amine (79 mg, 0.57 mmol), and 12 M HCl (11 µL, 0.13 mmol) to give **18** as pale yellow crystals (75.1 mg, 47%). m.p. 186.8-190.0°C. ^{1}H NMR (500 MHz, $CDCl_3$) δ ppm 8.46 (s, 1H), 8.08 (d, *J* = 5.4 Hz, 1H), 7.91 (t, *J* = 5.4 Hz, 1H), 7.37 (d, *J* = 5.4 Hz, 1H), 7.15 (d, *J* = 7.9 Hz, 2H), 7.90 (d, *J* = 7.9 Hz, 2H), 3.69 (dt, *J* = 6.3, 8.4 Hz, 2H), 2.89 (t, *J* = 7.1 Hz, 2H), 2.27 (s, 3H). ^{13}C NMR (125 MHz, $CDCl_3$) δ ppm 159.7, 157.3, 155.0, 136.9, 135.5, 133.2, 129.4, 129.0, 124.9, 42.4, 34.9, 21.1. HRMS (EI), M + 1 calculated for $C_{15}H_{15}N_3S$, 270.1059, found 270.1051; HPLC t_R = 6.1 min, >95% pure.

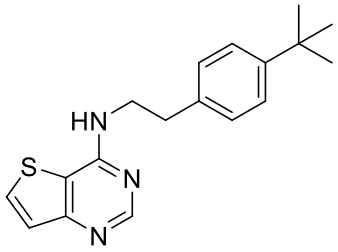

Figure A.11 *N*-(4-(*tert*-Butyl)phenethyl)thieno[3,2-*d*]pyrimidin-4-amine (**19**). The reaction was carried out according to the general procedure A using 4-chlorothieno[3,2-*d*]pyrimidine (100 mg, 0.57 mmol), 2-(4-(*tert*-butyl)phenyl)ethan-1-amine (106 mg, 0.57 mmol), and potassium carbonate (79 mg, 0.57 mmol) to give **19** as a yellow solid (103 mg, 55%). m.p. 133.8-134.5°C. ^{1}H NMR (500 MHz, $CDCl_3$) δ ppm 8.66 (s, 1H), 7.70 (d, *J* = 5.4 Hz, 1H), 7.44 (d, *J* = 5.4Hz, 1H), 7.38 (d, *J* = 8.2 Hz, 2H), 7.20 (d, *J* = 8.2 Hz, 2H), 5.03 (s, 1H), 3.95 (q, *J* = 6.8, 6.2 Hz, 2H), 3.01 (t, *J* = 6.7 Hz, 2H), 1.35 (s, 9H). ^{13}C NMR (125 MHz, $CDCl_3$) δ ppm 159.9, 157.3, 155.1, 149.6, 135.6, 130.7, 128.5, 125.6, 125.5, 115.2, 64.41, 42.4, 35.2, 34.5, 31.4. HRMS (EI), M + 1 calculated for $C_{18}H_{21}N_3S$, 312.1534 found, 312.1520; HPLC t_R = 5.8 min, >95% pure.

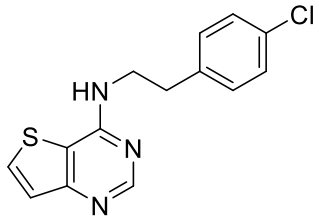

Figure A.12 *N*-(4-Chlorophenethyl)thieno[3,2-*d*]pyrimidin-4-amine (**20**). The reaction was carried out according to the general procedure B using 4-chlorothieno[3,2-*d*]pyrimidine (100 mg, 0.57 mmol), 2-(4-chlorophenyl)ethan-1-amine (0.08 mL, 0.57 mmol), and 12 M HCl (11 µL, 0.13 mmol) to give **20** as a pale yellow, flaky solid (34.7 mg, 20%). m.p. 174.2-175.0°C. ^{1}H NMR (500 MHz, $CDCl_3$) δ ppm 8.67 (s, 1H), 7.72 (d, *J* = 5.4 Hz, 1H), 7.45 (d, *J* = 5.4 Hz, 1H), 7.31 (dt, *J* = 8.4, 2.6 Hz, 2H), 7.21-7.16 (m, 2H), 5.00 (br.s, 1H), 3.92 (dt, *J* = 6.9, 6.1 Hz, 2H), 3.02 (t, *J* = 6.7 Hz, 2H). ^{13}C NMR (125 MHz, $CDCl_3$) δ ppm 159.7, 157.2, 154.9, 137.2, 132.5, 130.9, 130.2, 128.8, 125.5, 115.2, 42.3, 35.1. HRMS (EI), M + 1 calculated for $C_{14}H_{12}ClN_3S$, 290.0513 found, 290.0513; HPLC t_R = 6.2 min, >95% pure.

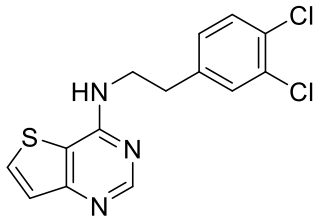

Figure A.13 *N*-(3,4-Dichlorophenethyl)thieno[3,2-*d*]pyrimidin-4-amine (**21**). The reaction was carried out according to the general procedure B using 4-chlorothieno[3,2-*d*]pyrimidine (100 mg, 0.57 mmol), 2-(3,4-dichlorophenyl)ethan-1-amine (0.09 mL, 0.57 mmol), and 12 M HCl (11 µL, 0.13 mmol) to give **21** as a yellow brown pebble-like solid (35.1 mg, 18%). m.p. 186.1-187.2°C. ^{1}H NMR (500 MHz, MeOD) δ ppm 8.45 (s, 1H), 7.97 (d, *J* = 5.4 Hz, 1H), 7.44 (d, *J* = 1.9 Hz, 1H), 7.41 (d, *J* = 8.2 Hz, 1H), 7.35 (d, J = 5.4 Hz, 1H), 7.18 (dd, *J* = 8.2, 1.9 Hz, 1H), 3.83 (t, *J* = 7.2 Hz, 2H), 3.00 (t, *J* = 7.2 Hz, 2H). ^{13}C NMR (125 MHz, MeOD) δ ppm 158.2, 157.4, 154.0, 140.2, 132.4, 131.7, 130.7,130.0, 129.7, 128.6, 123.4, 115.4, 41.5, 34.2. HRMS (EI), M + 1 calculated for $C_{14}H_{11}Cl_2N_3S$, 324.0124, found 324.0132; HPLC t_R = 6.7 min, >95% pure.

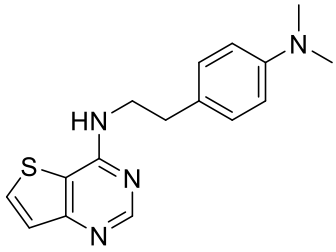

Figure A.14 *N*-(4-(Dimethylamino)phenethyl)thieno[3,2-*d*]pyrimidin-4-amine (**22**). The reaction was carried out according to the general procedure A using 4-chlorothieno[3,2-*d*]pyrimidine (100 mg, 0.57 mmol), 4-(2-aminoethyl)-*N,N*-dimethylaniline (0.10 mL, 0.57 mmol), and potassium carbonate (79 mg, 0.57 mmol) to give **22** as pale yellow crystals (88.3 mg, 49%). m.p. 169.5-171.7°C. ^{1}H NMR (600 MHz, $CDCl_3$) δ ppm 8.66 (s, 1H), 7.69 (d, *J* = 5.3 Hz, 1H), 7.43 (d, *J* = 5.3 Hz, 1H), 7.14 (d, *J* = 7.1 Hz, 1H), 6.74 (d, *J* = 7.1 Hz,), 5.02 (br.s, 1H), 3.90 (dt, *J* = 6.8, 6.7 Hz, 2H), 2.96 (s, 6H), 2.93 (t, *J* = 6.6 Hz, 2H). ^{13}C NMR (150 MHz, $CDCl_3$) δ ppm 162.26, 159.71, 157.33, 155.06, 149.57, 130.74, 129.51, 125.44, 113.10, 42.67, 40.77, 34.65. HRMS (EI), M + 1 calculated for $C_{16}H_{18}N_4S$ 299.1325 found, 299.1320; HPLC t_R = 4.2 min, >95% pure.

NMR spectra

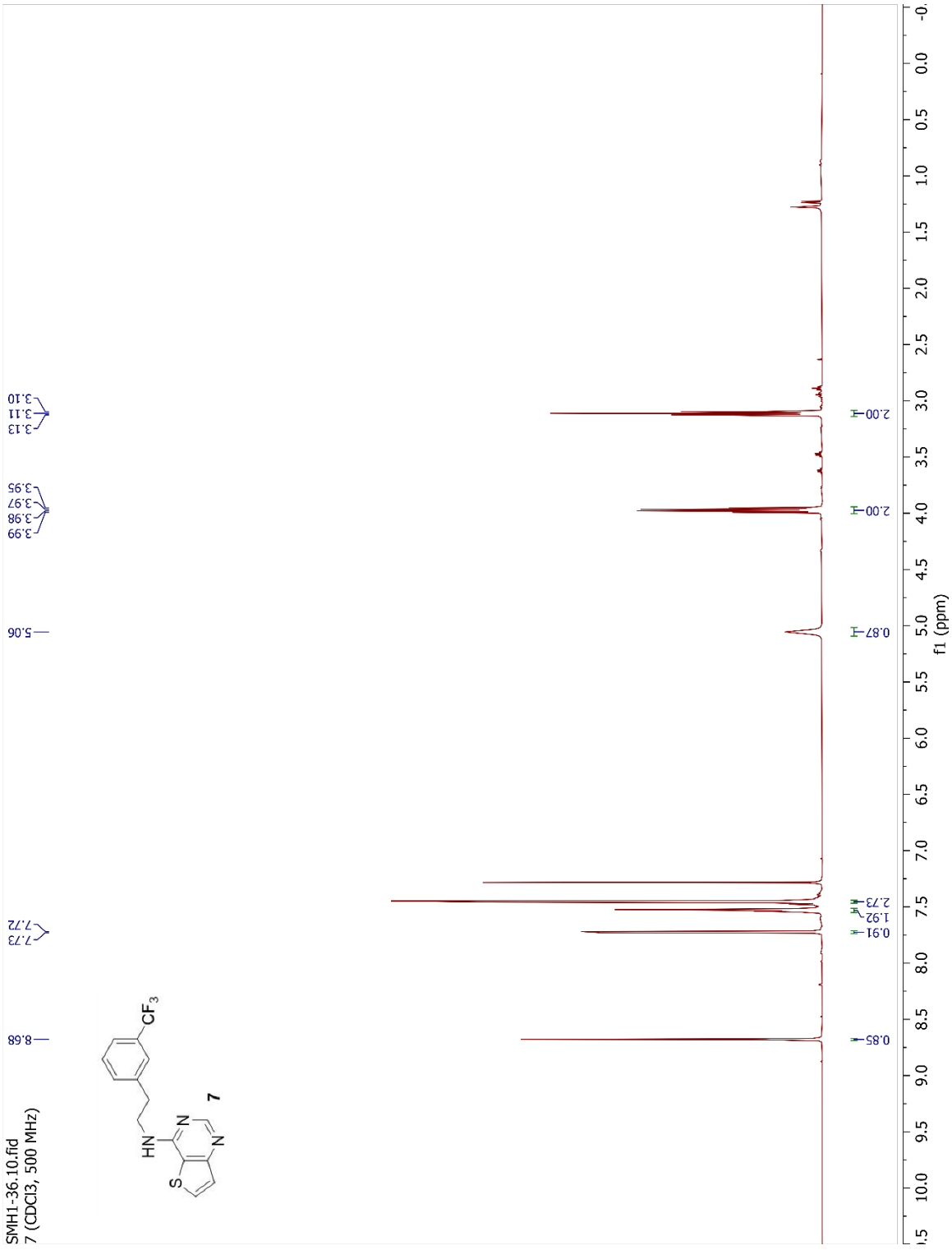

Figure A.15 ^{1}H NMR Spectrum ($CDCl_3$, 500 MHz) of **7**

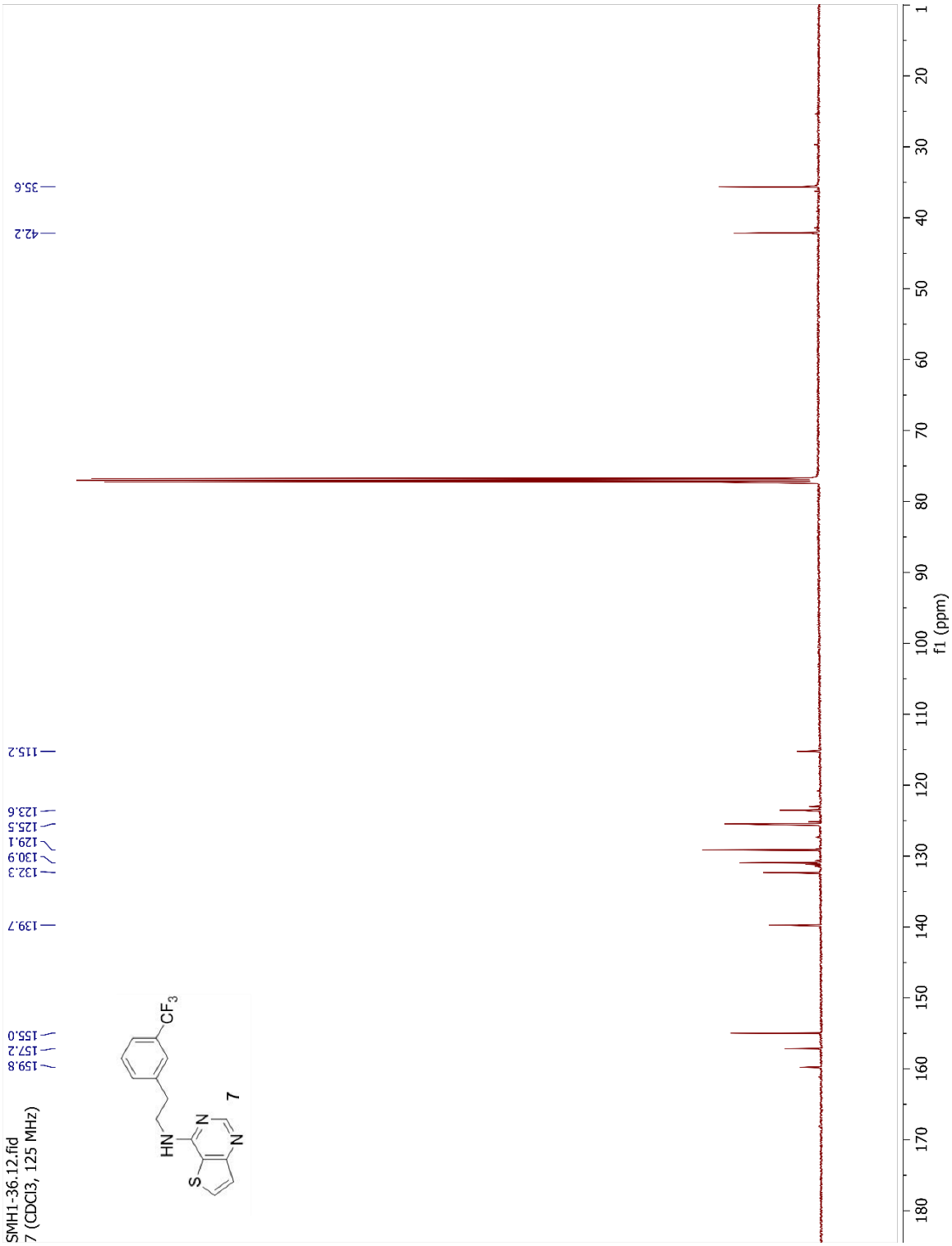

Figure A.16 ^{13}C NMR Spectrum ($CDCl_3$, 125 MHz) of **7**

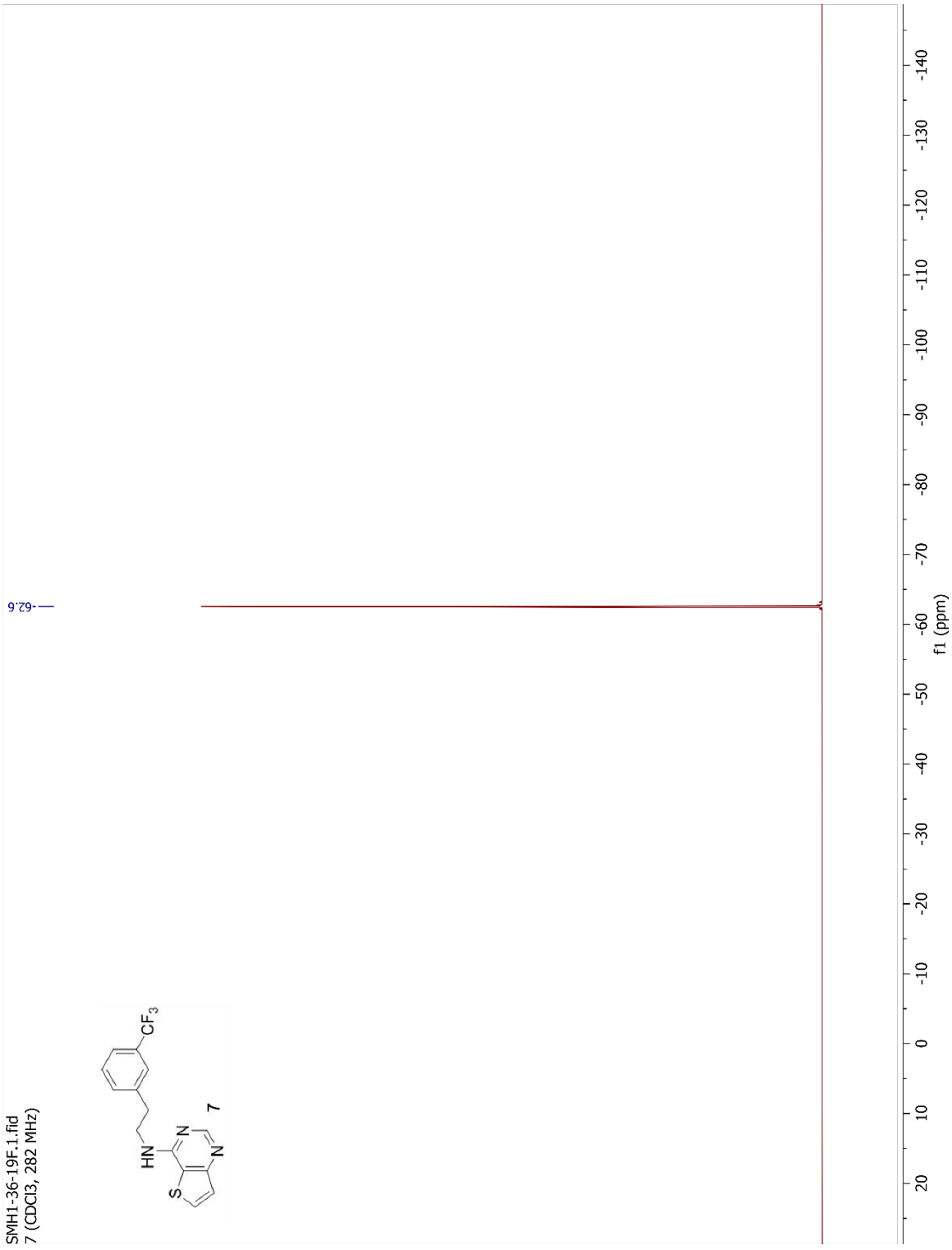

Figure A.17 ^{19}F NMR Spectrum ($CDCl_3$, 282 MHz) of **7**

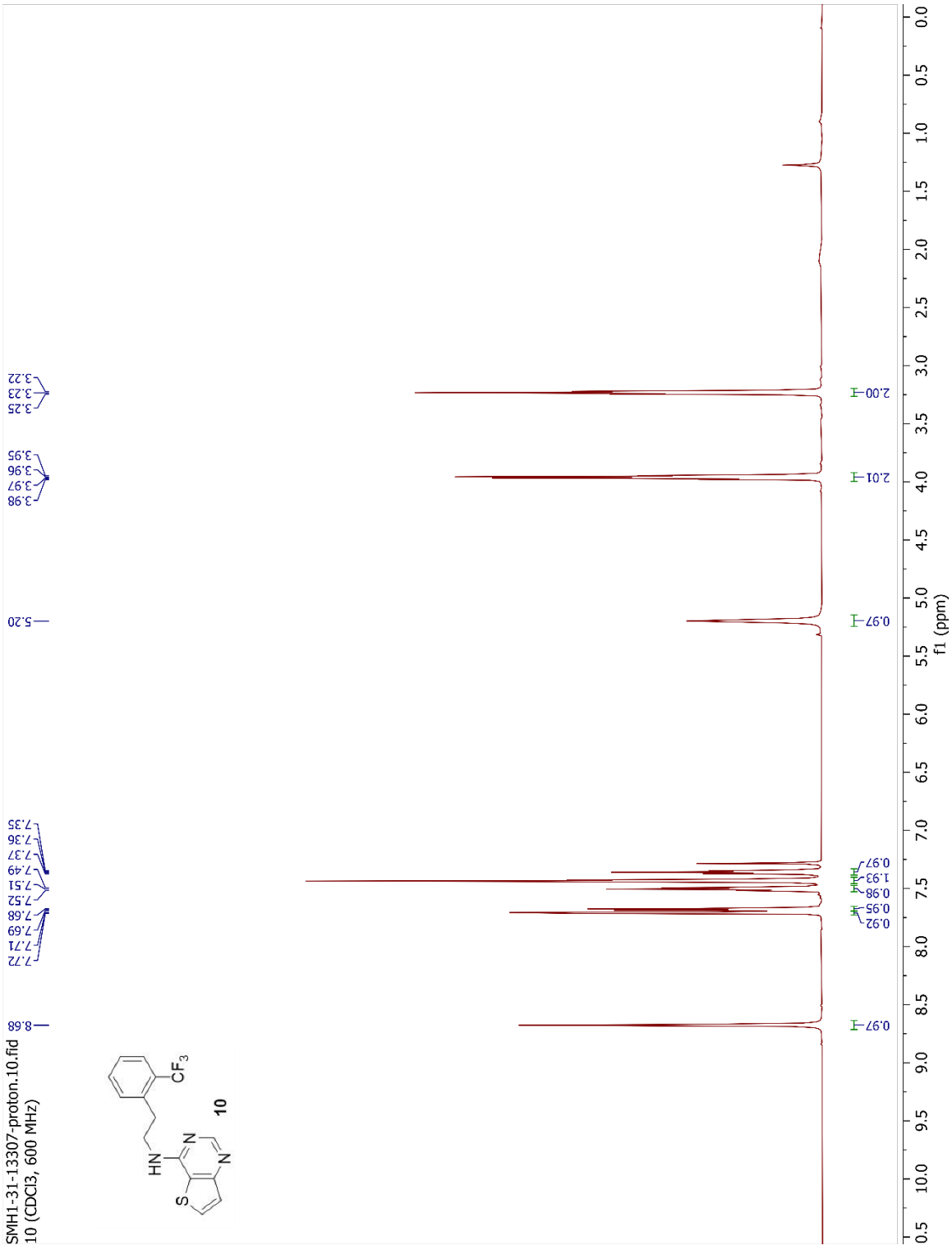

Figure A.18 ^{1}H NMR Spectrum ($CDCl_3$, 600 MHz) of **10**

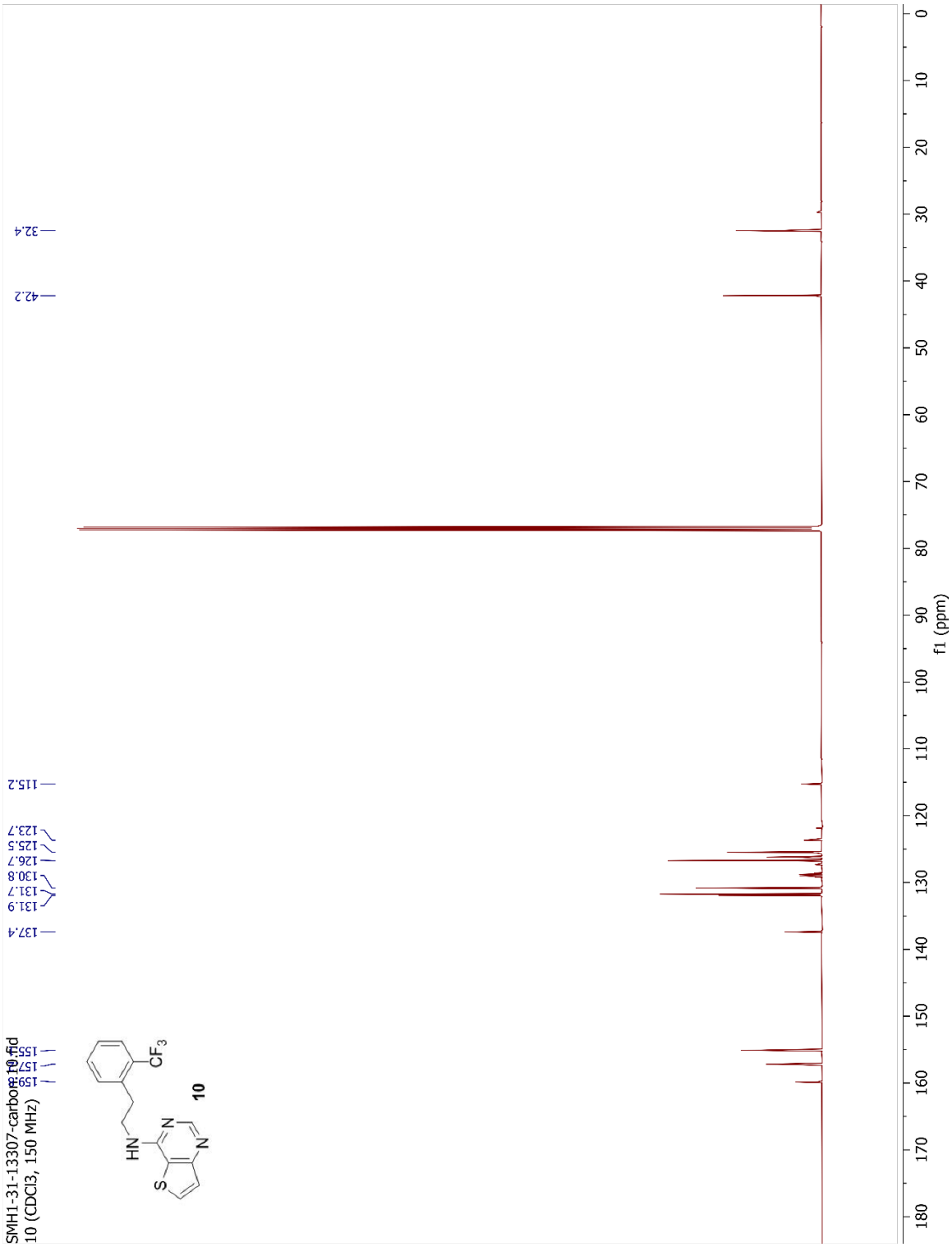

Figure A.19 ^{13}C NMR Spectrum ($CDCl_3$, 150 MHz) of **10**

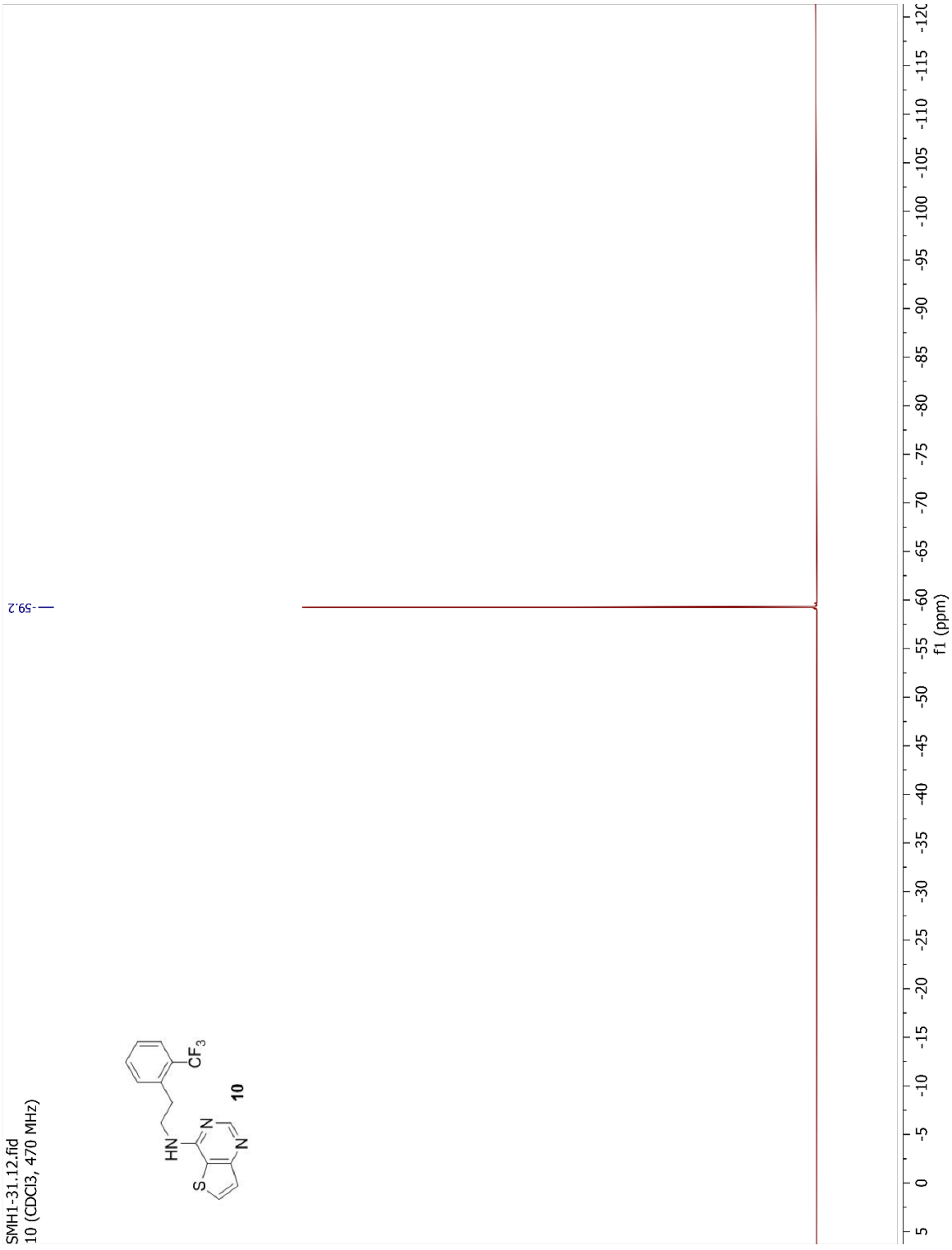

Figure A.20 ^{19}F NMR Spectrum ($CDCl_3$, 470 MHz) of **10**

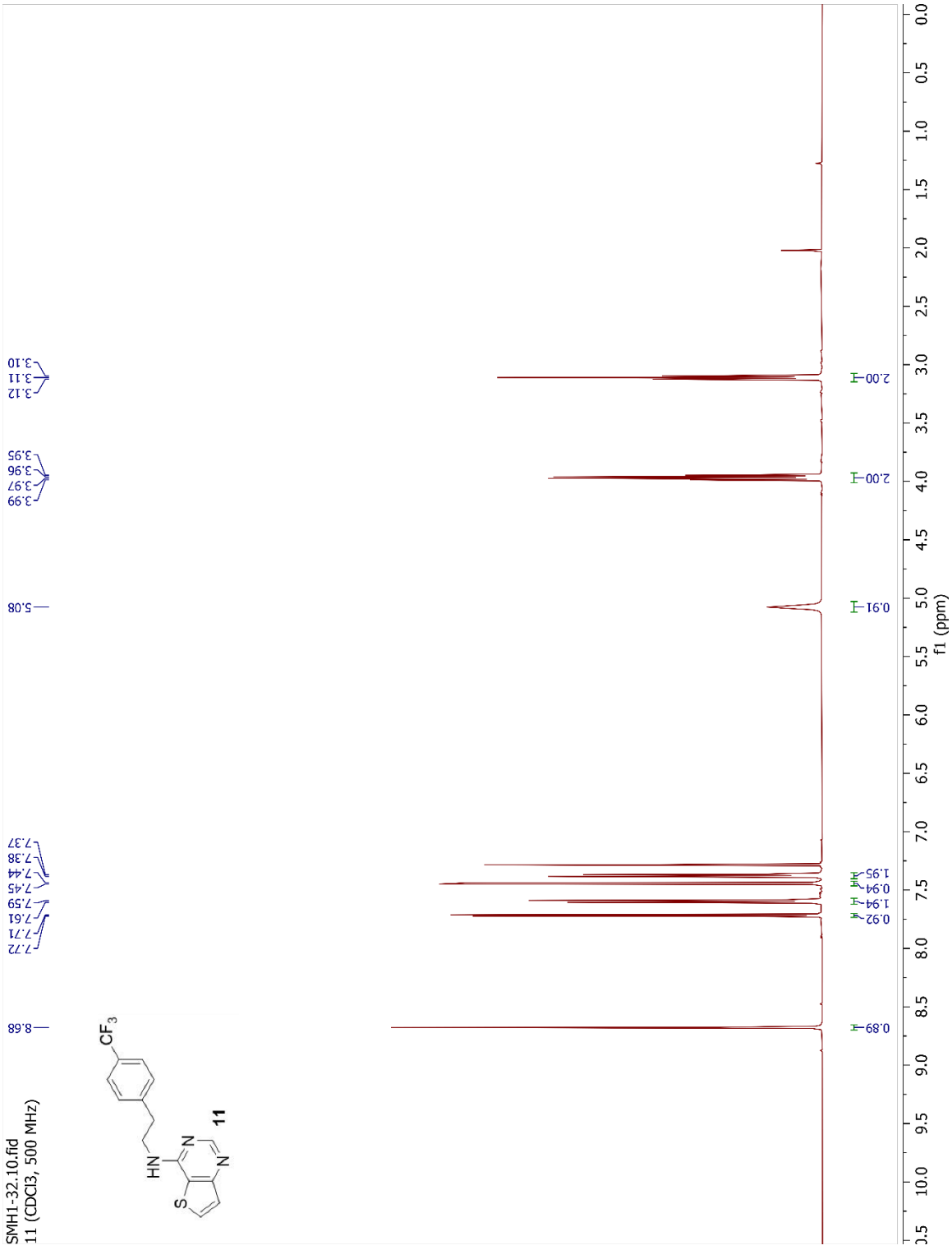

Figure A.21 ^{1}H NMR Spectrum ($CDCl_3$, 500 MHz) of **11**

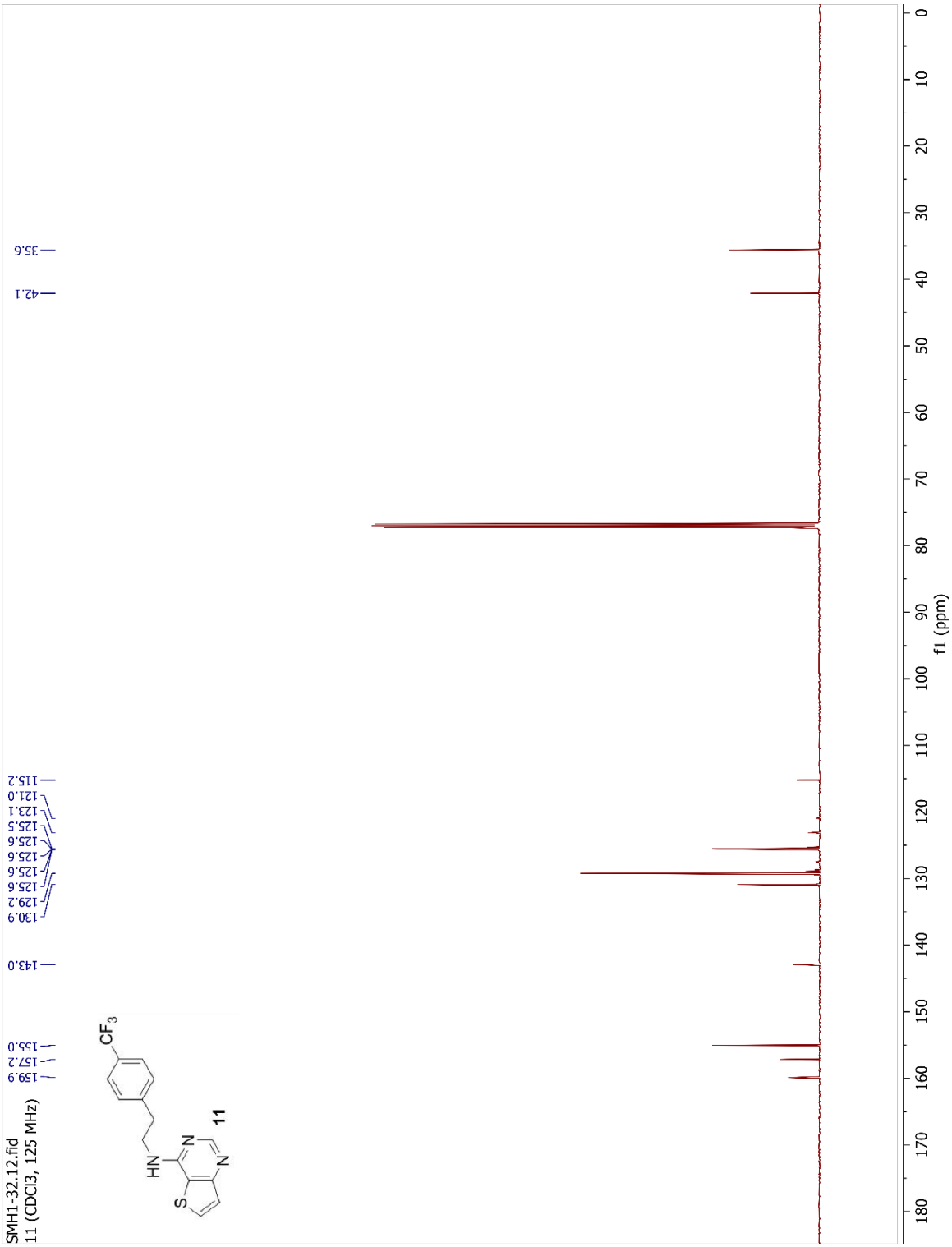

Figure A.22 ^{13}C NMR Spectrum ($CDCl_3$, 125 MHz) of **11**

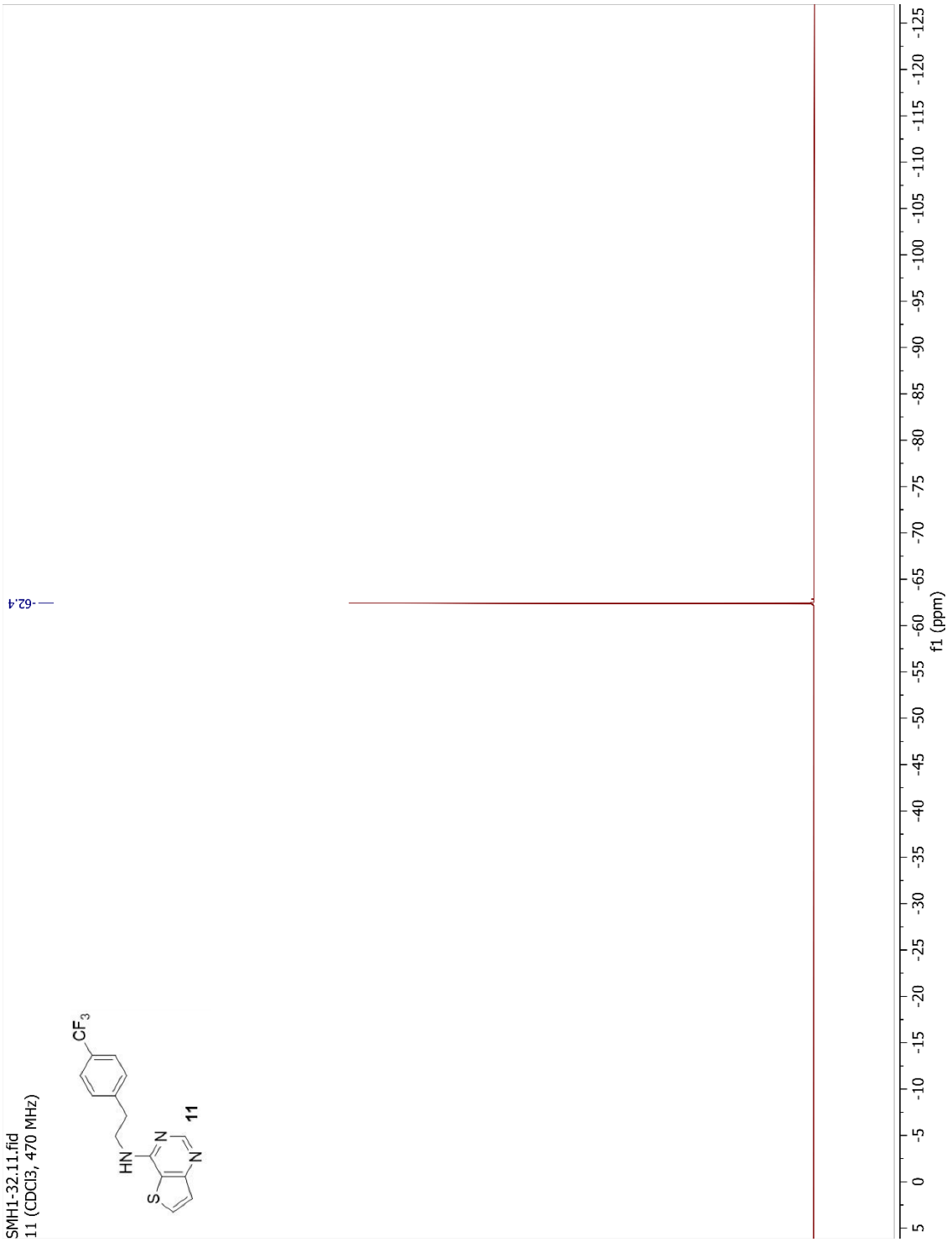

Figure A.23 ^{19}F NMR Spectrum ($CDCl_3$, 470 MHz) of **11**

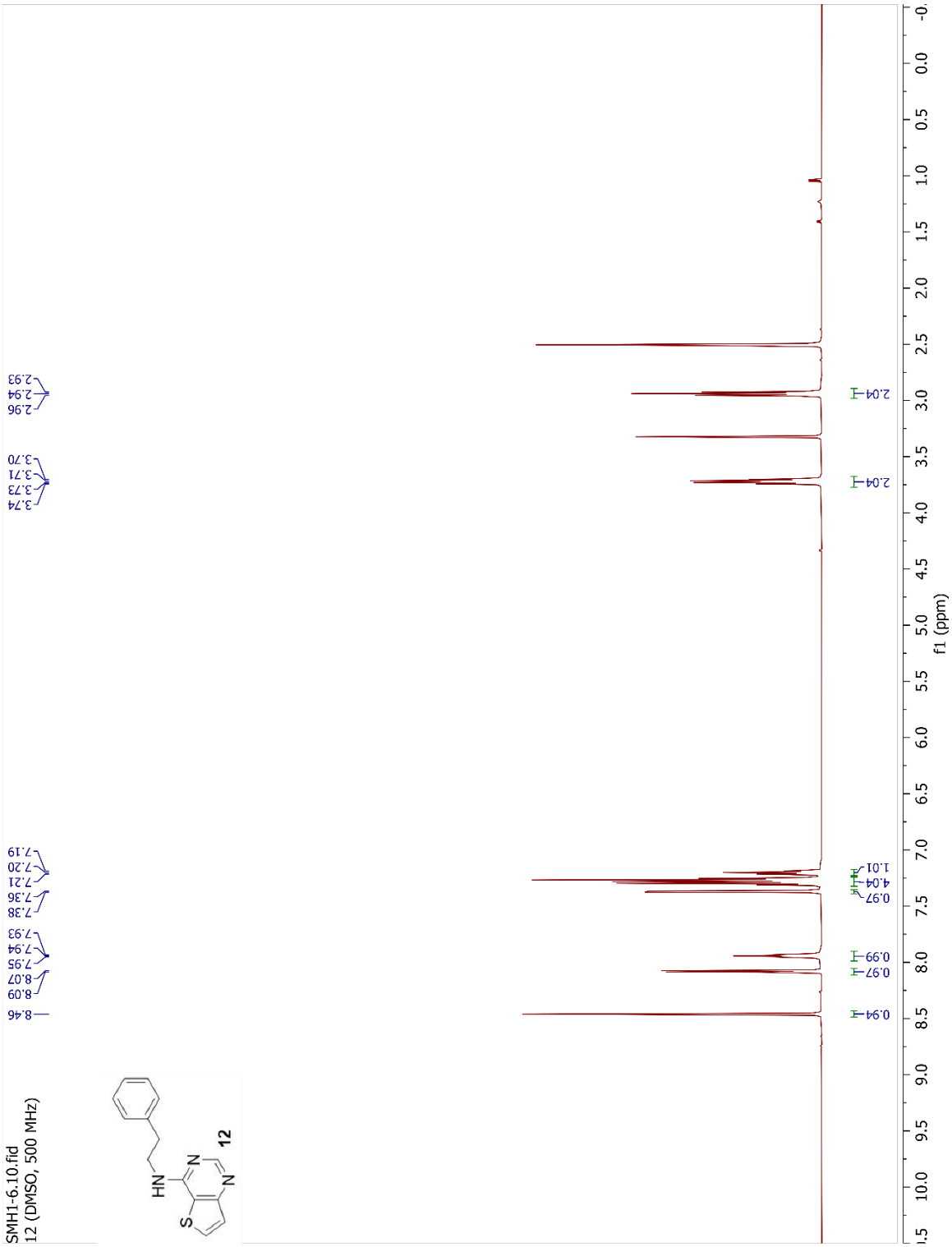

Figure A.24 ^{1}H NMR Spectrum (DMSO, 500 MHz) of **12**

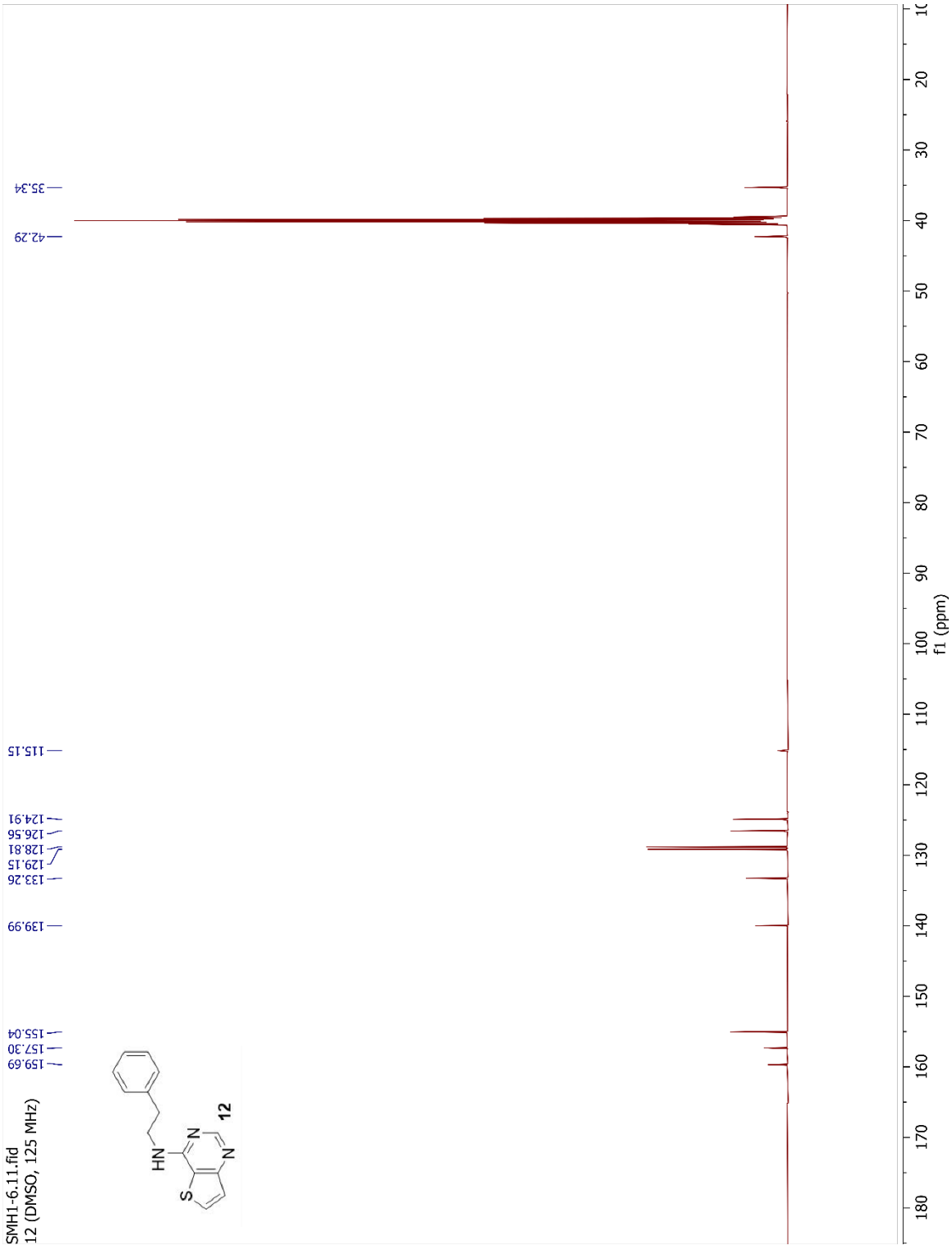

Figure A.25 ^{13}C NMR Spectrum (DMSO, 125 MHz) of **12**

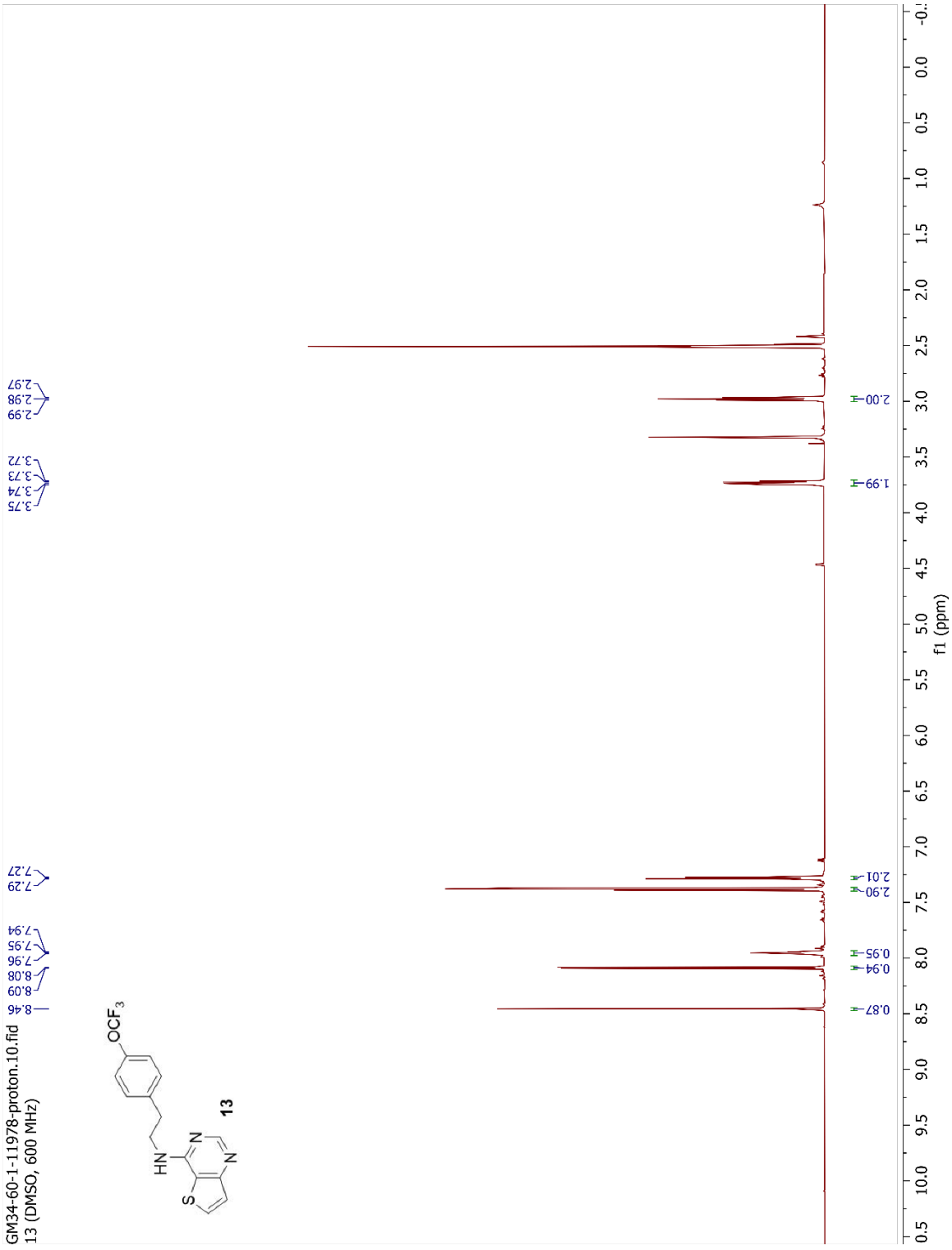

Figure A.26 ^{1}H NMR Spectrum (DMSO, 600 MHz) of **13**

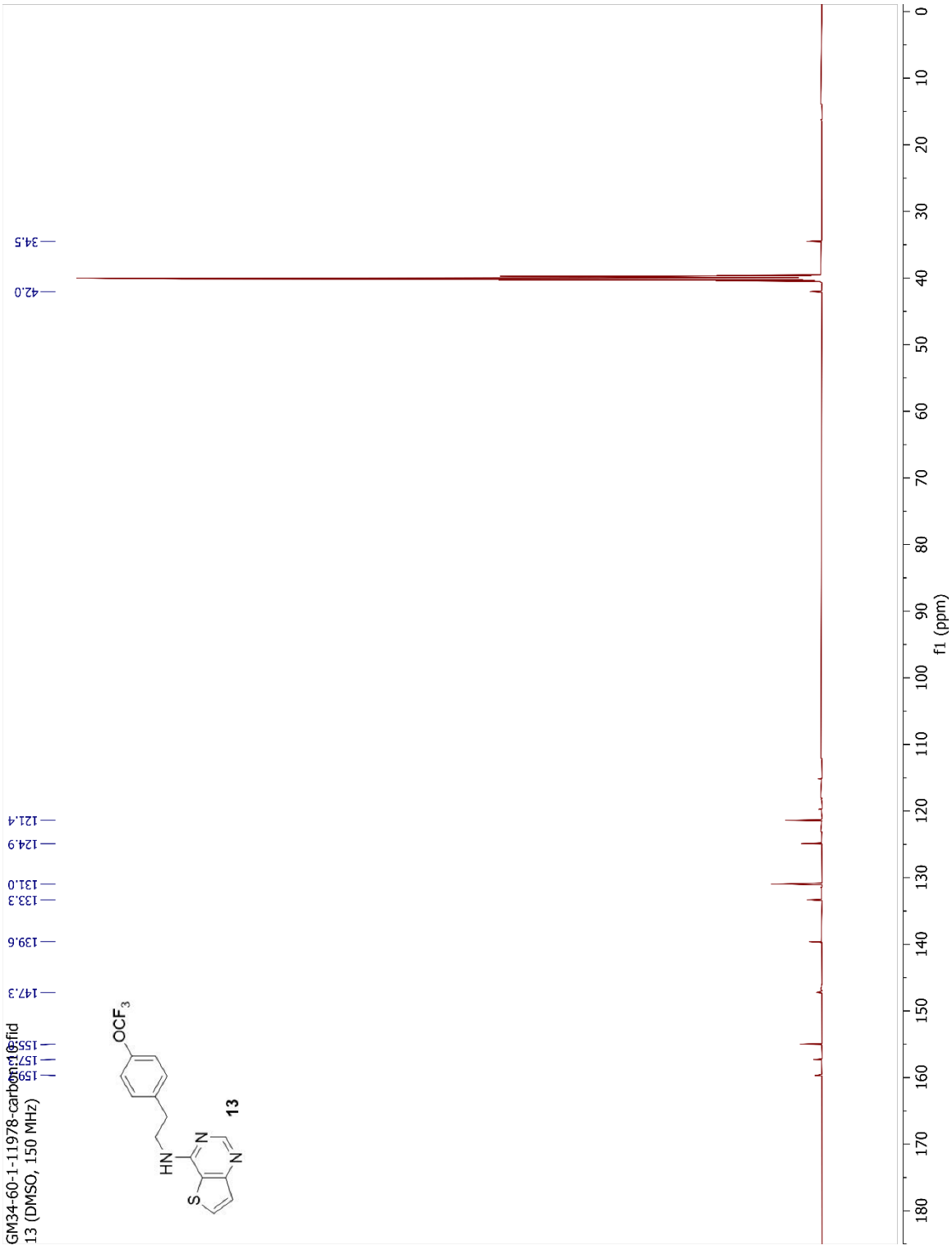

Figure A.27 ^{13}C NMR Spectrum (DMSO, 150 MHz) of **13**

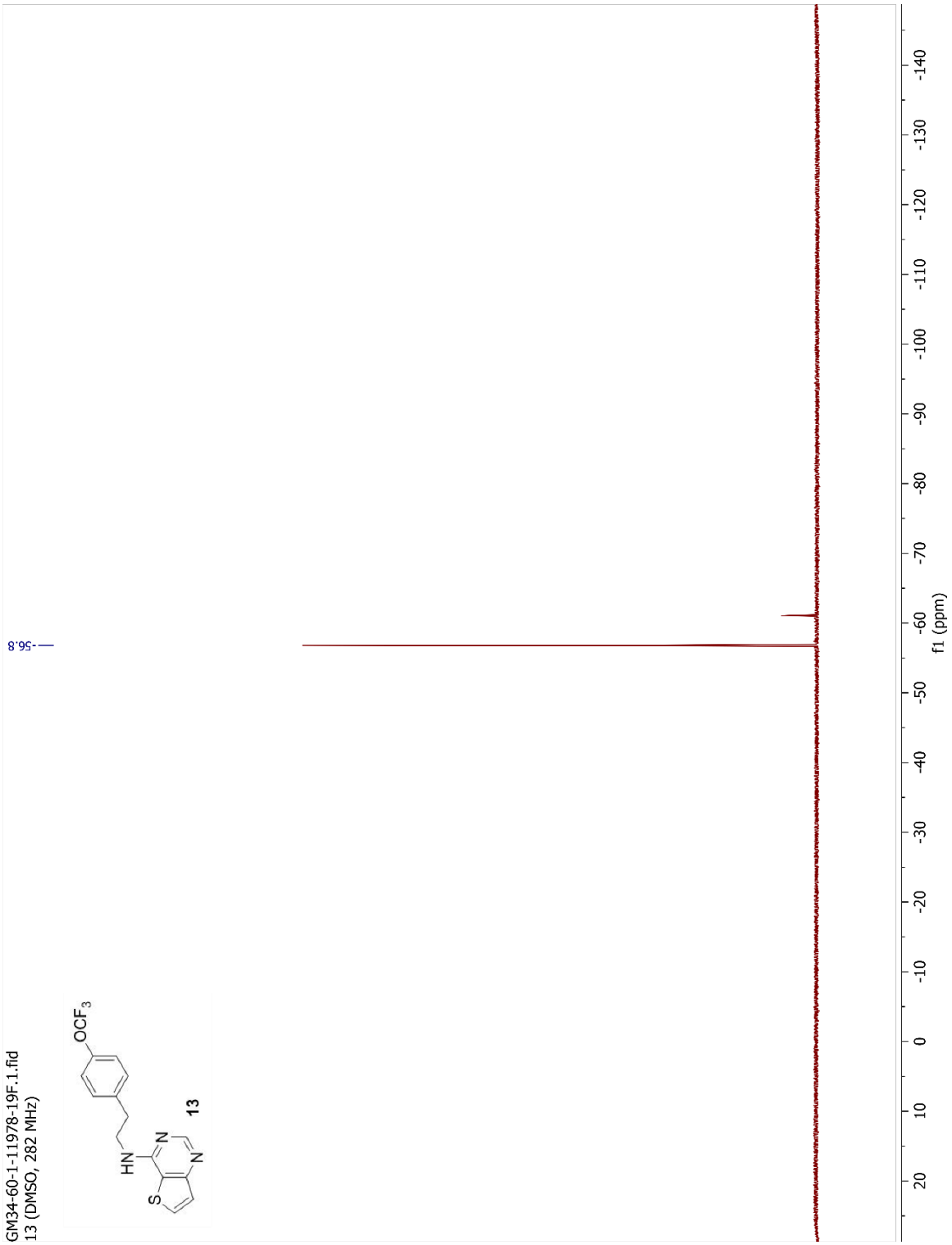

Figure A.28 ^{19}F NMR Spectrum (DMSO, 282 MHz) of **13**

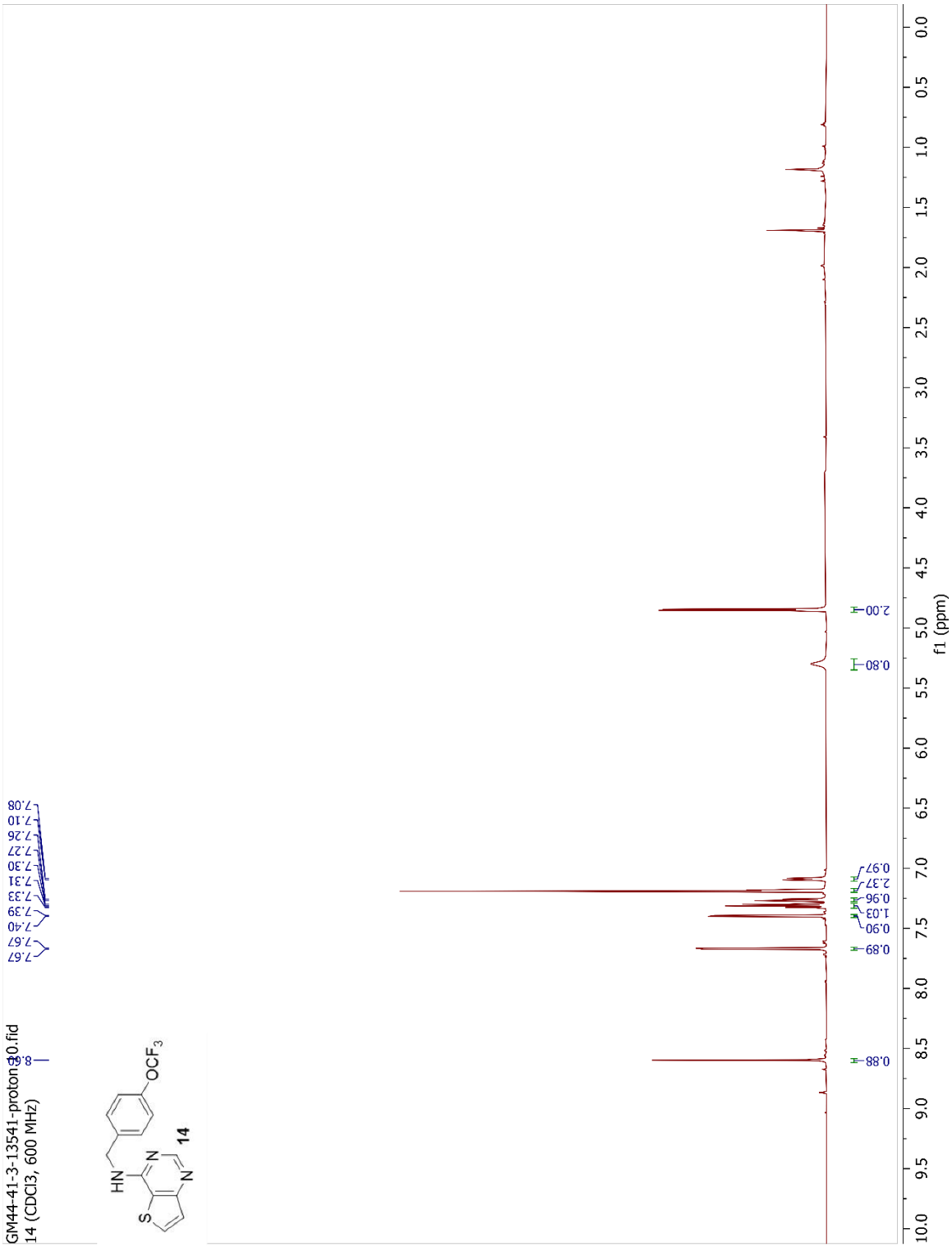

Figure A.29 ^{1}H NMR Spectrum ($CDCl_3$, 600 MHz) of **14**

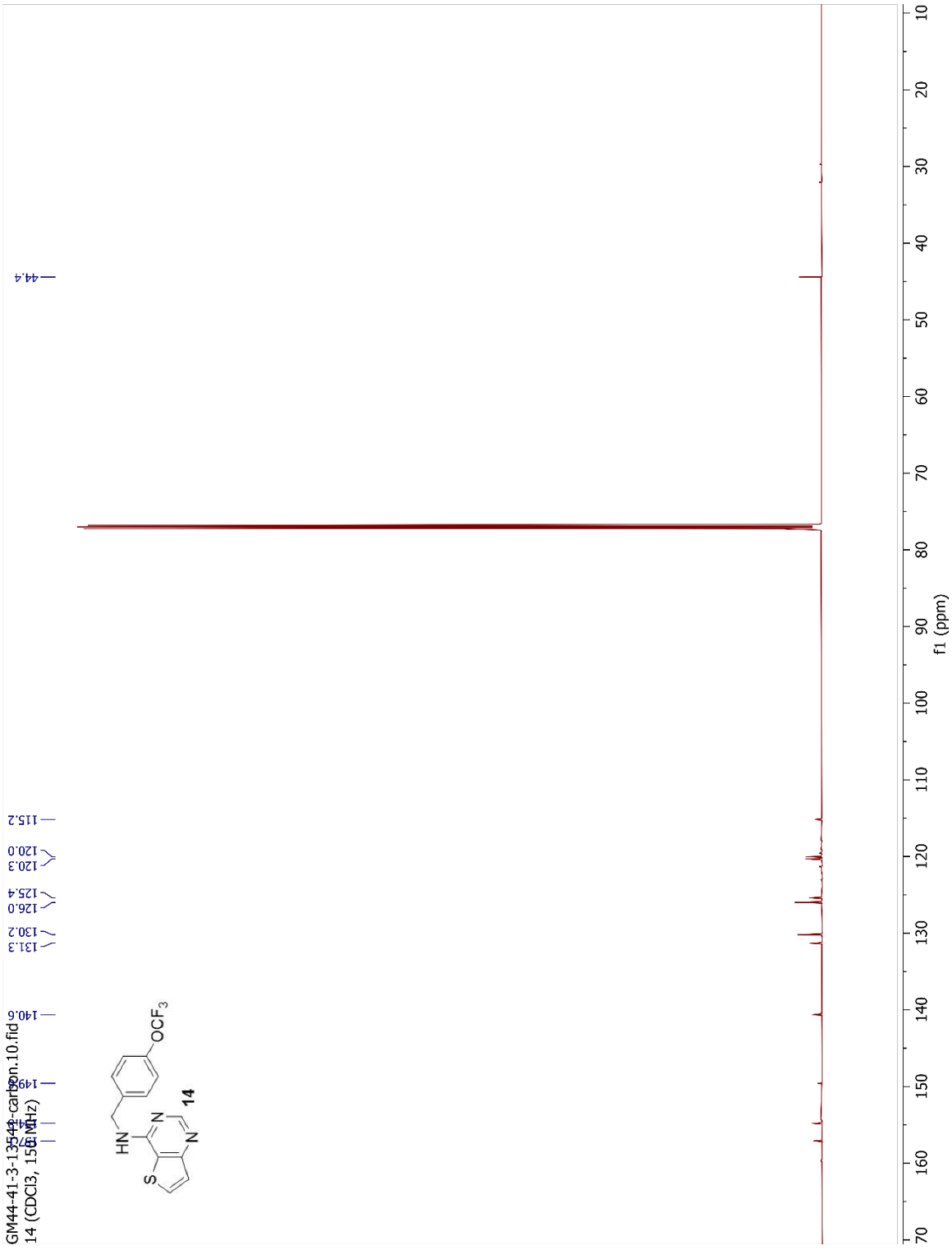

Figure A.30 ^{13}C NMR Spectrum ($CDCl_3$, 150 MHz) of **14**

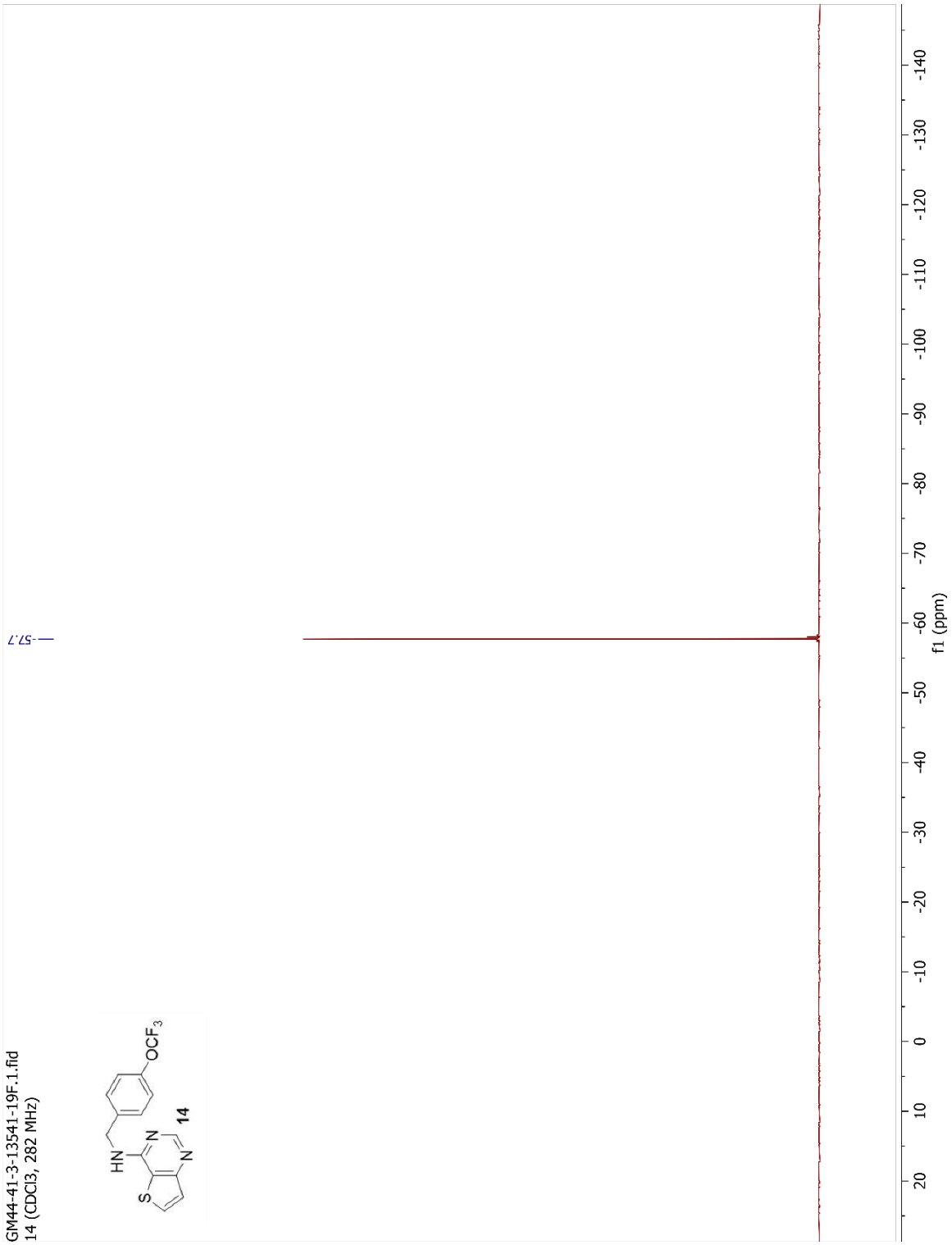

Figure A.31 ^{19}F NMR Spectrum ($CDCl_3$, 282 MHz) of **14**

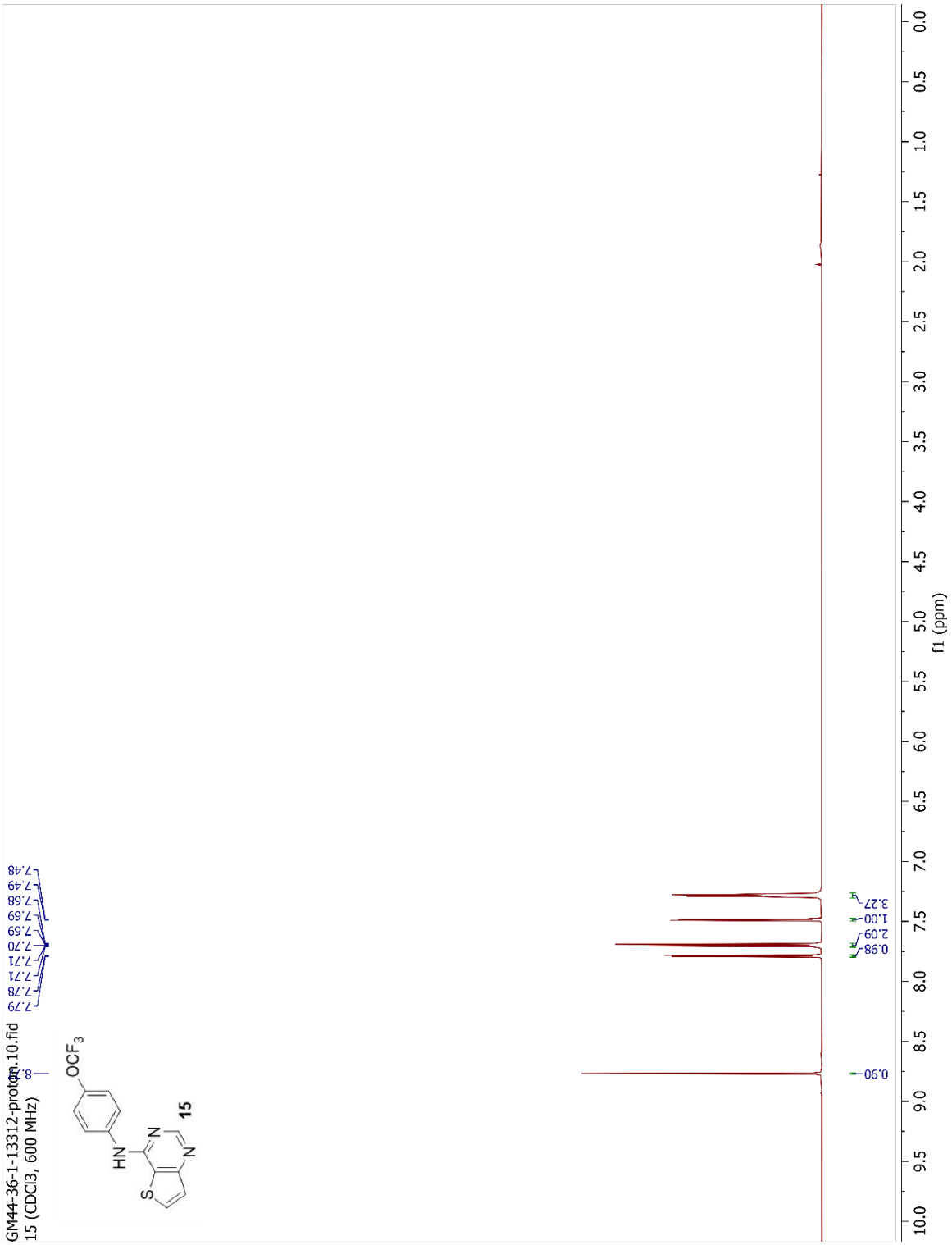

Figure A.32 ^{1}H NMR Spectrum ($CDCl_3$, 600 MHz) of **15**

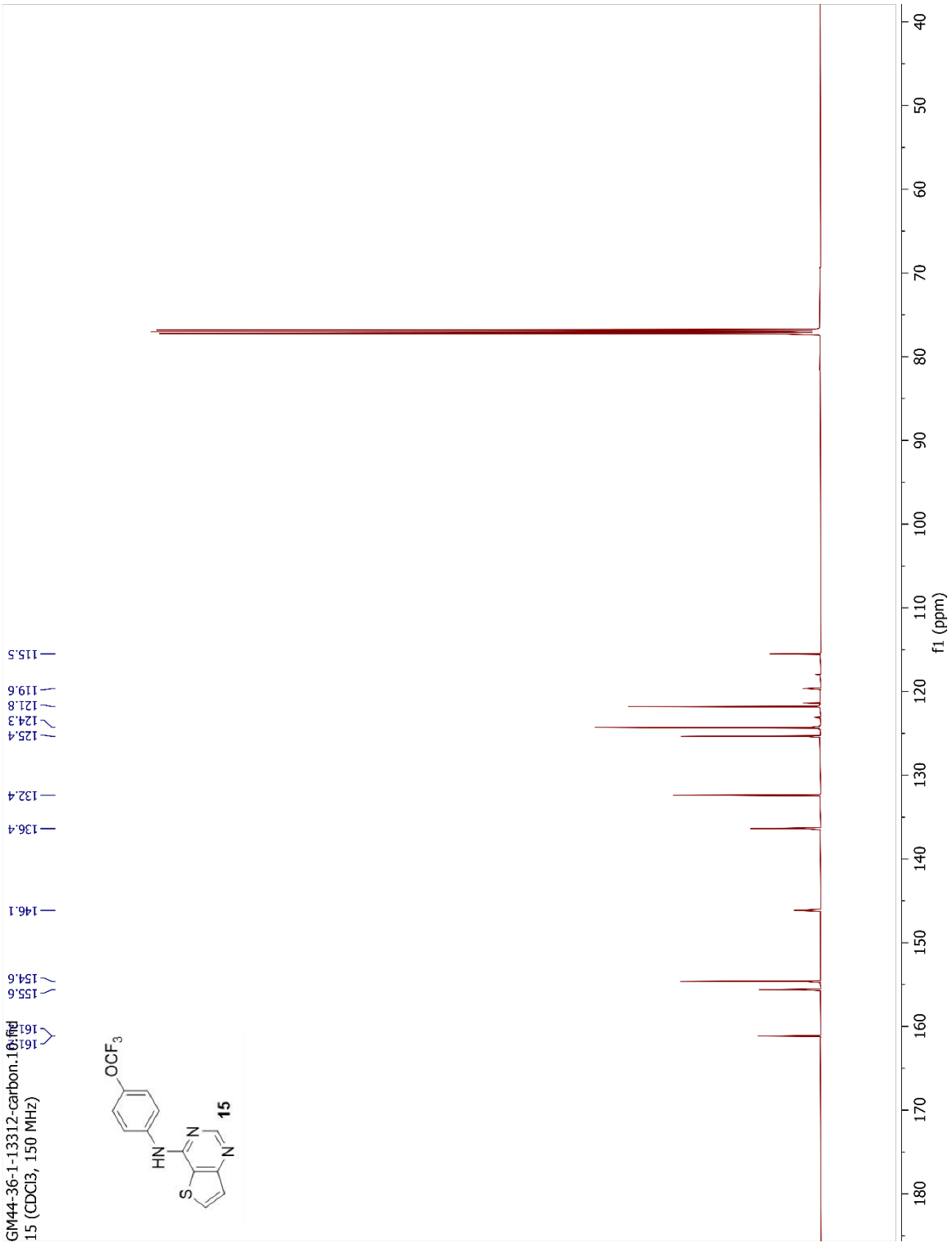

Figure A.33 ^{13}C NMR Spectrum ($CDCl_3$, 150 MHz) of **15**

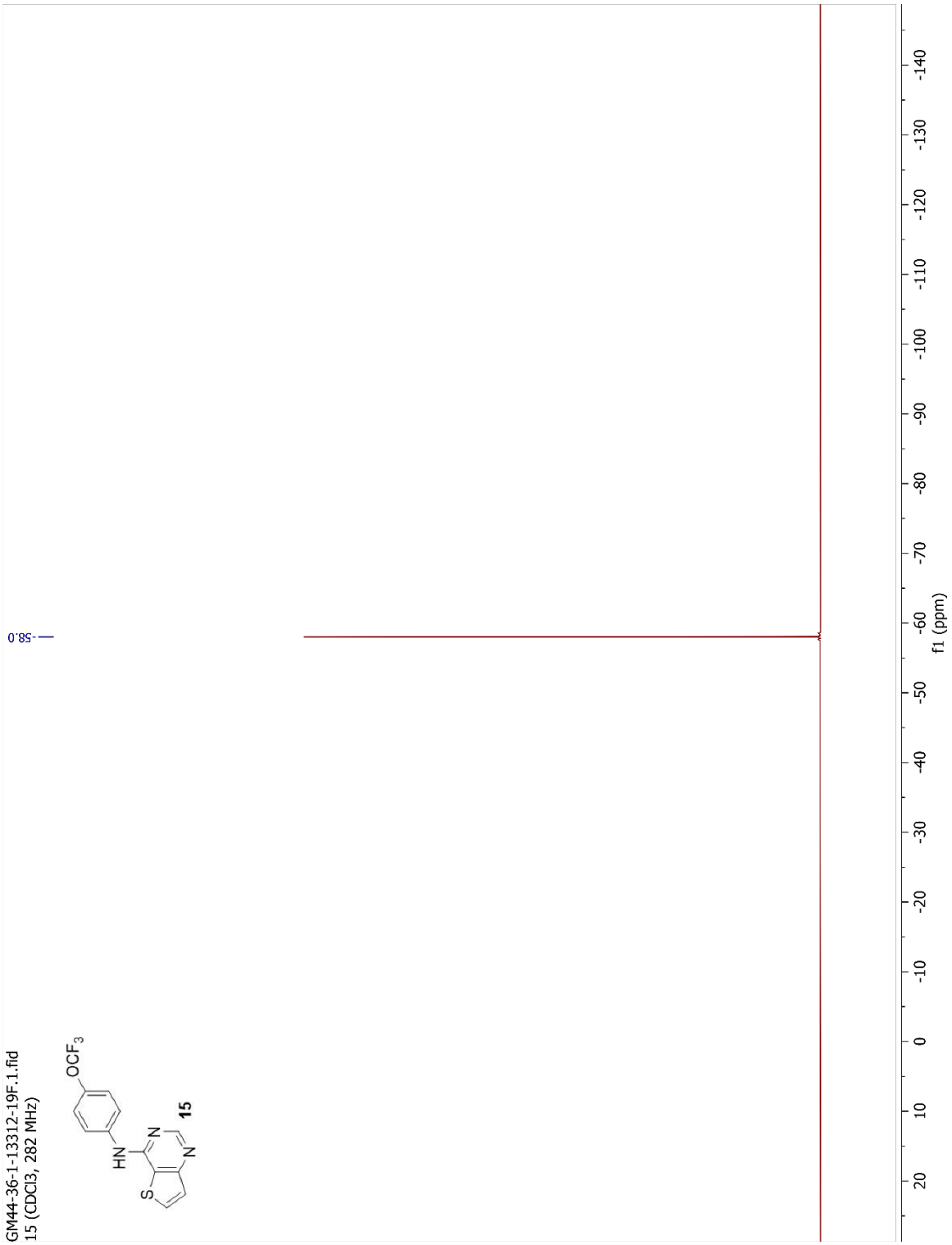

Figure A.34 ^{19}F NMR Spectrum ($CDCl_3$, 282 MHz) of **15**

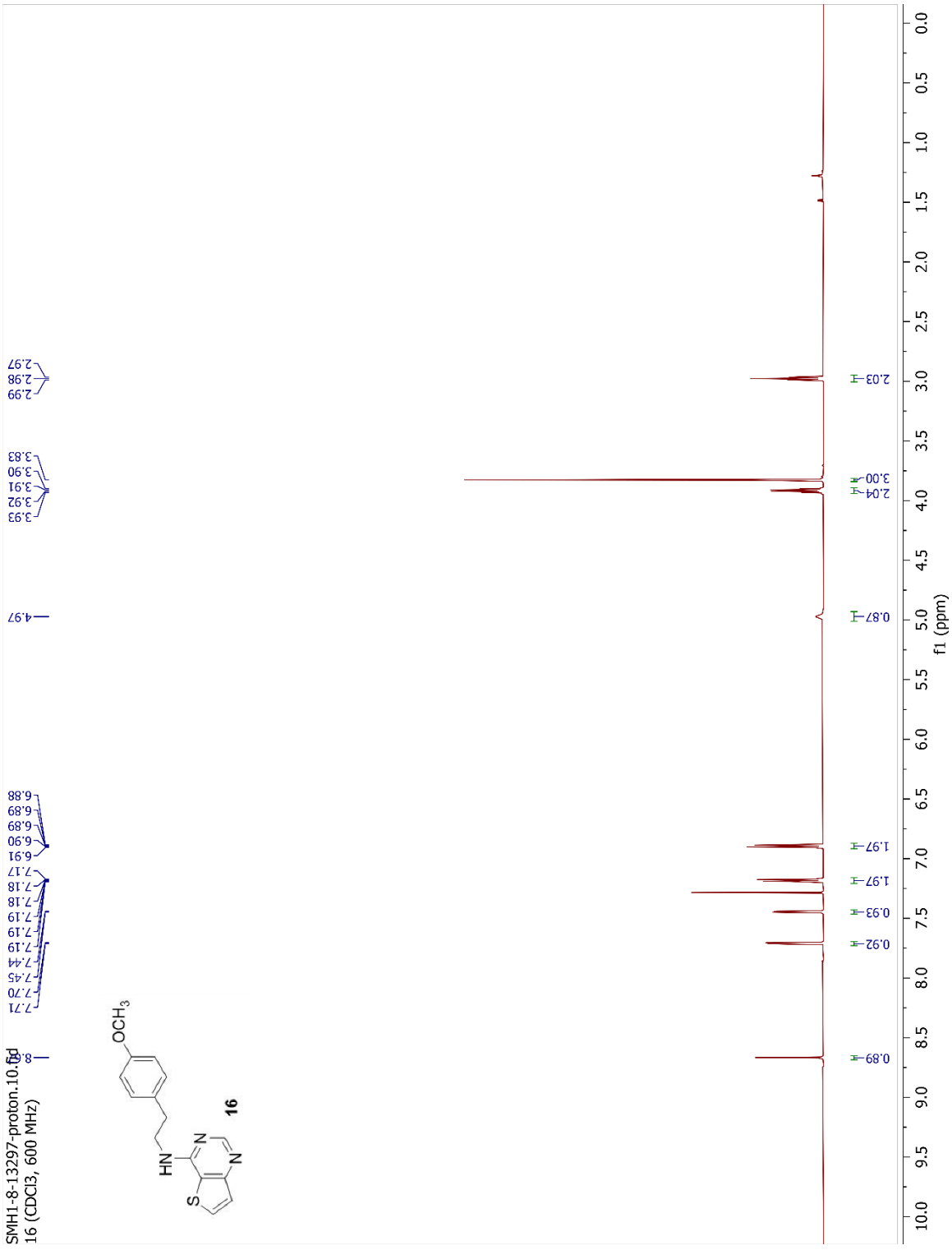

Figure A.35 ^{1}H NMR Spectrum ($CDCl_3$, 600 MHz) of **16**

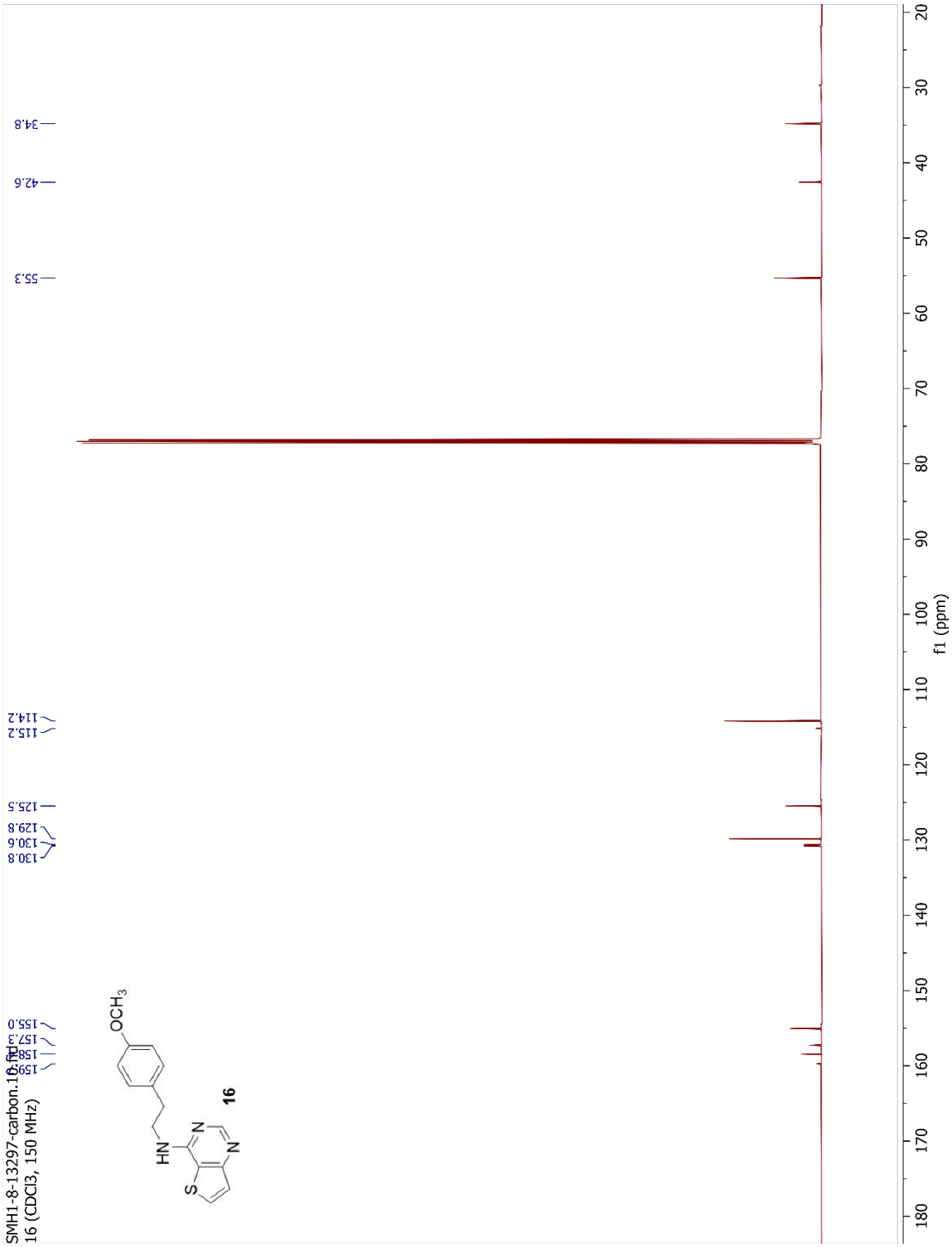

Figure A.36 ^{13}C NMR Spectrum ($CDCl_3$, 150 MHz) of **16**

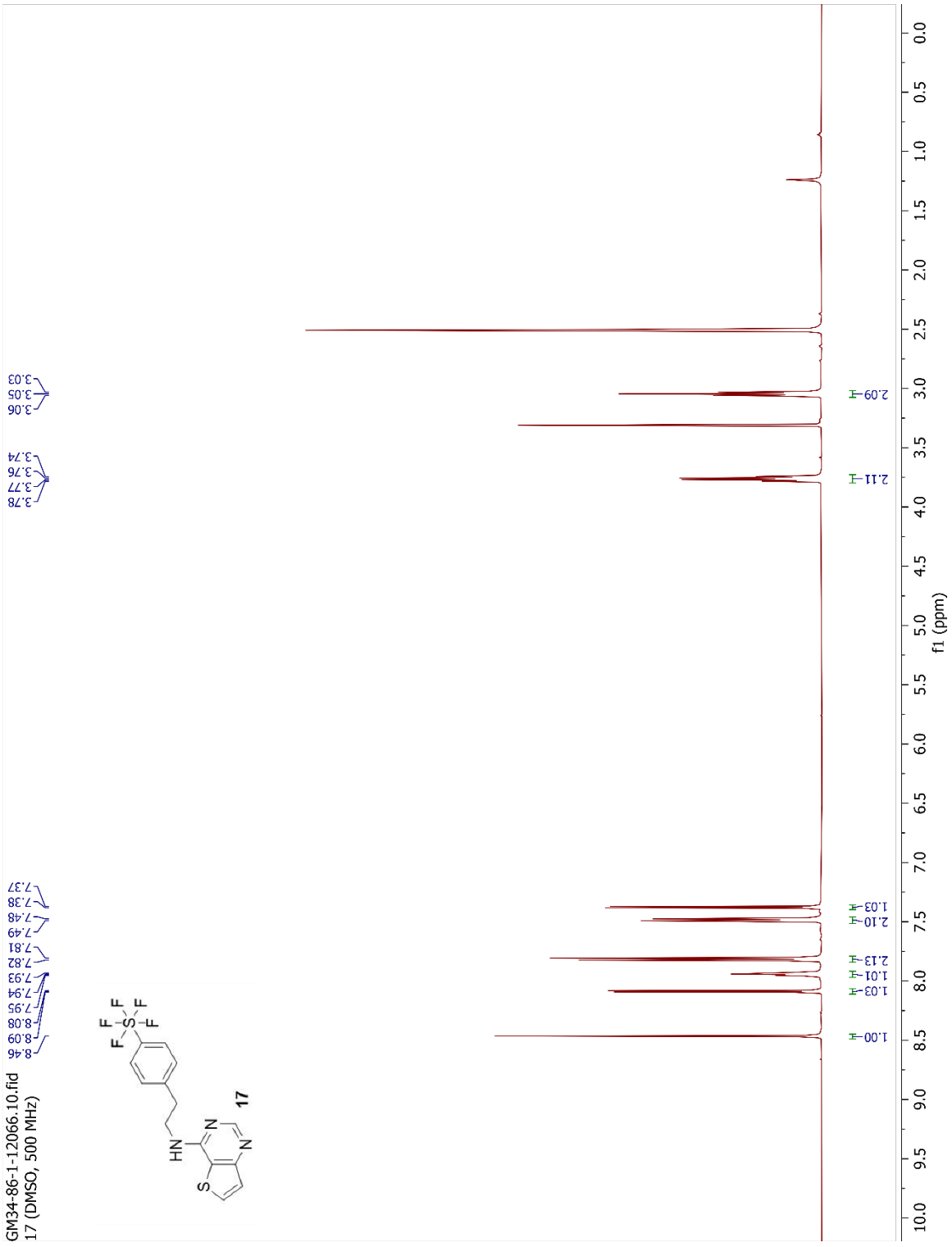

Figure A.37 ^{1}H NMR Spectrum (DMSO, 500 MHz) of **17**

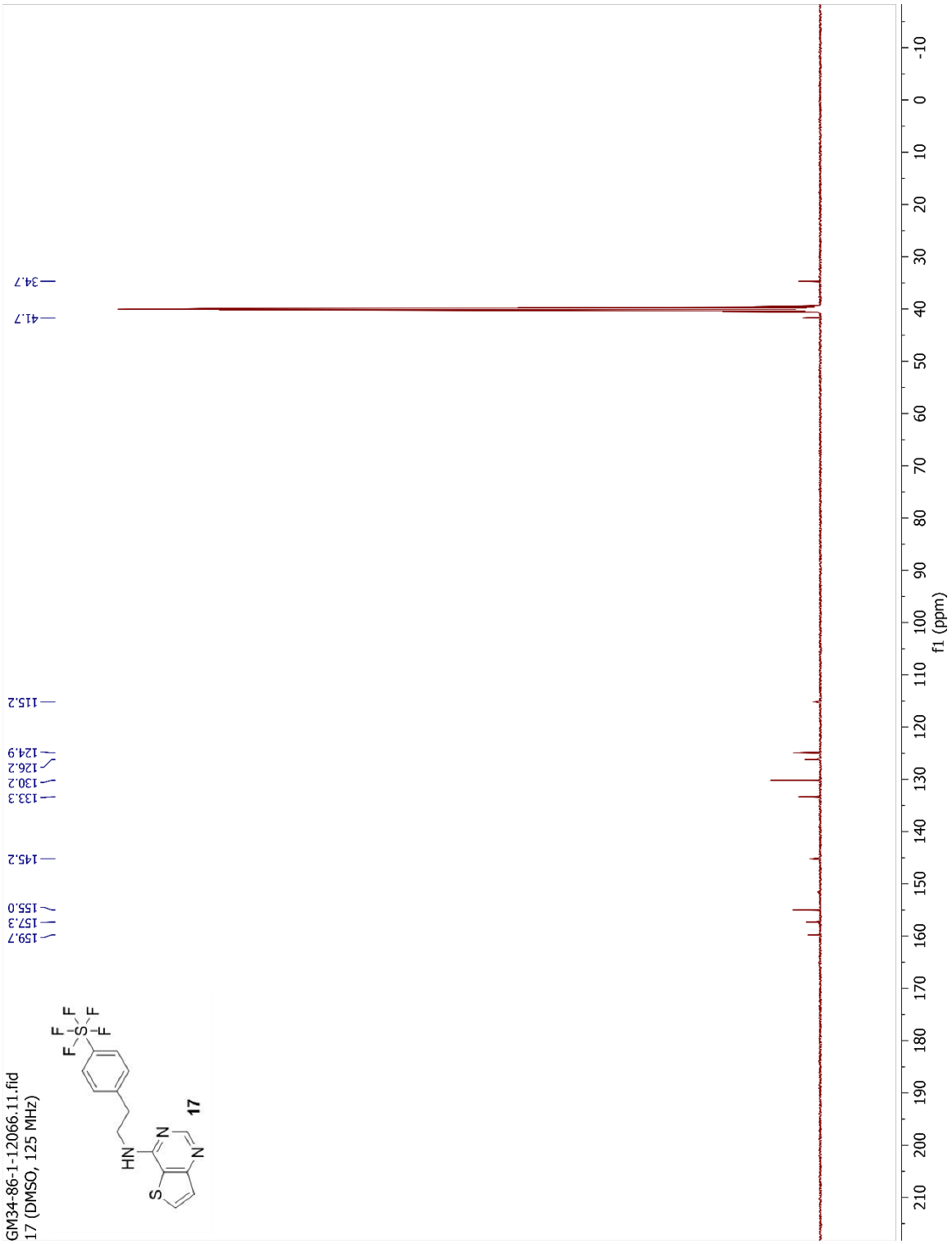

Figure A.38 ^{13}C NMR Spectrum (DMSO, 125 MHz) of **17**

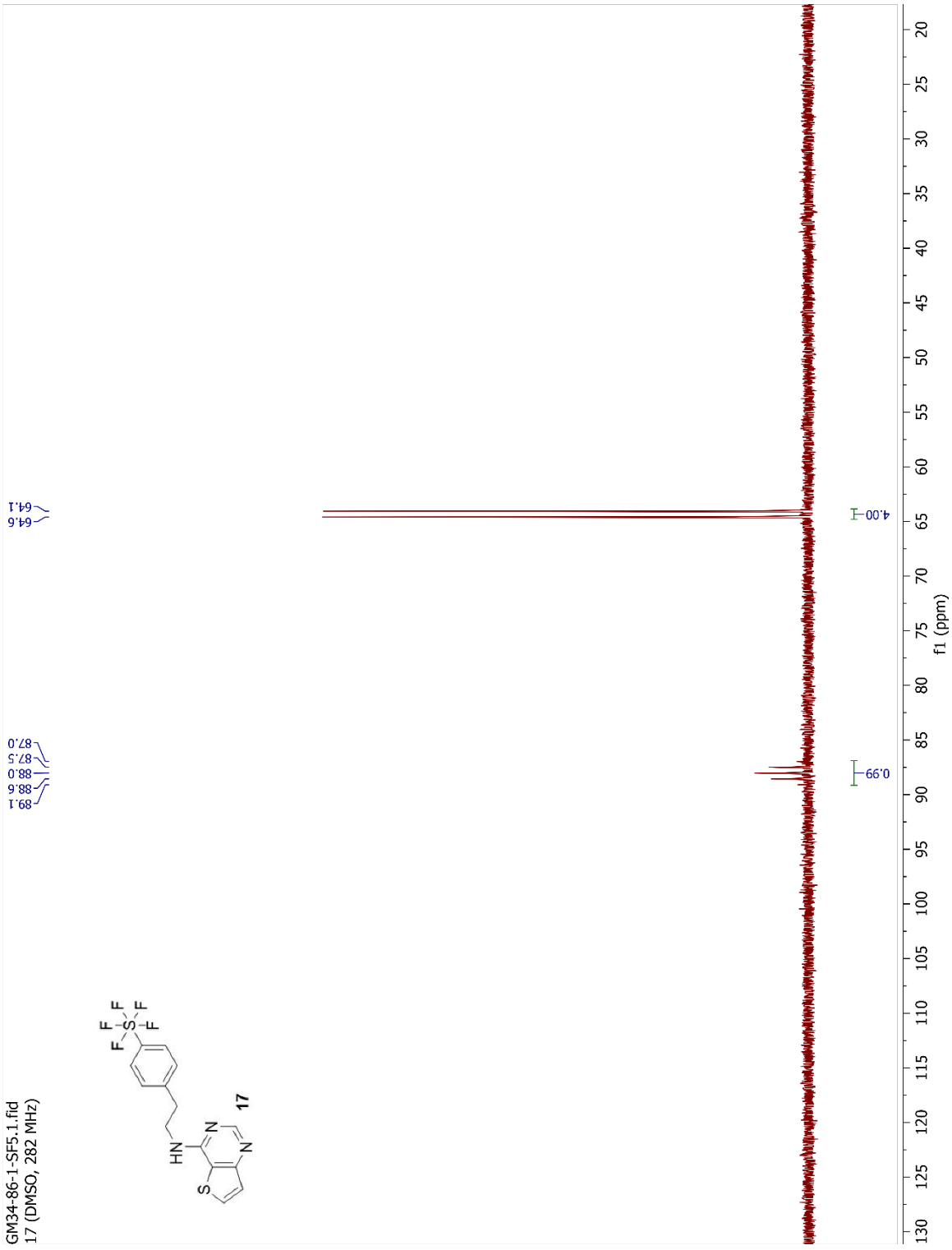
GM34-86-1-SF5.1.fid
17 (DMSO, 282 MHz)
17
64.6
64.1
89.1
88.6
88.0
87.5
87.0
4.00
0.99
f1 (ppm)

Figure A.39 ^{19}F NMR Spectrum (DMSO, 282 MHz) of **17**

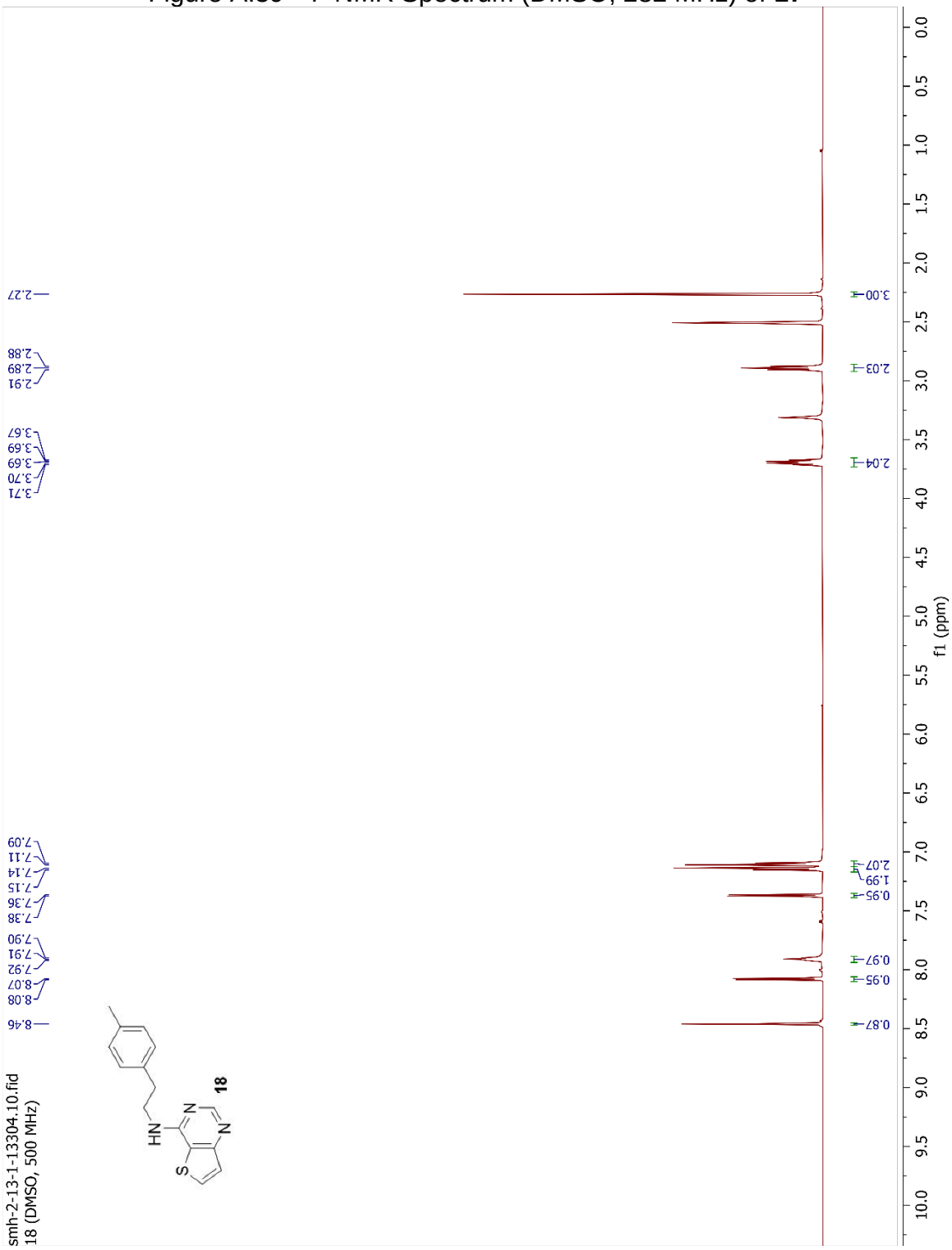

Figure A.40 ^{1}H NMR Spectrum (DMSO, 500 MHz) of **18**

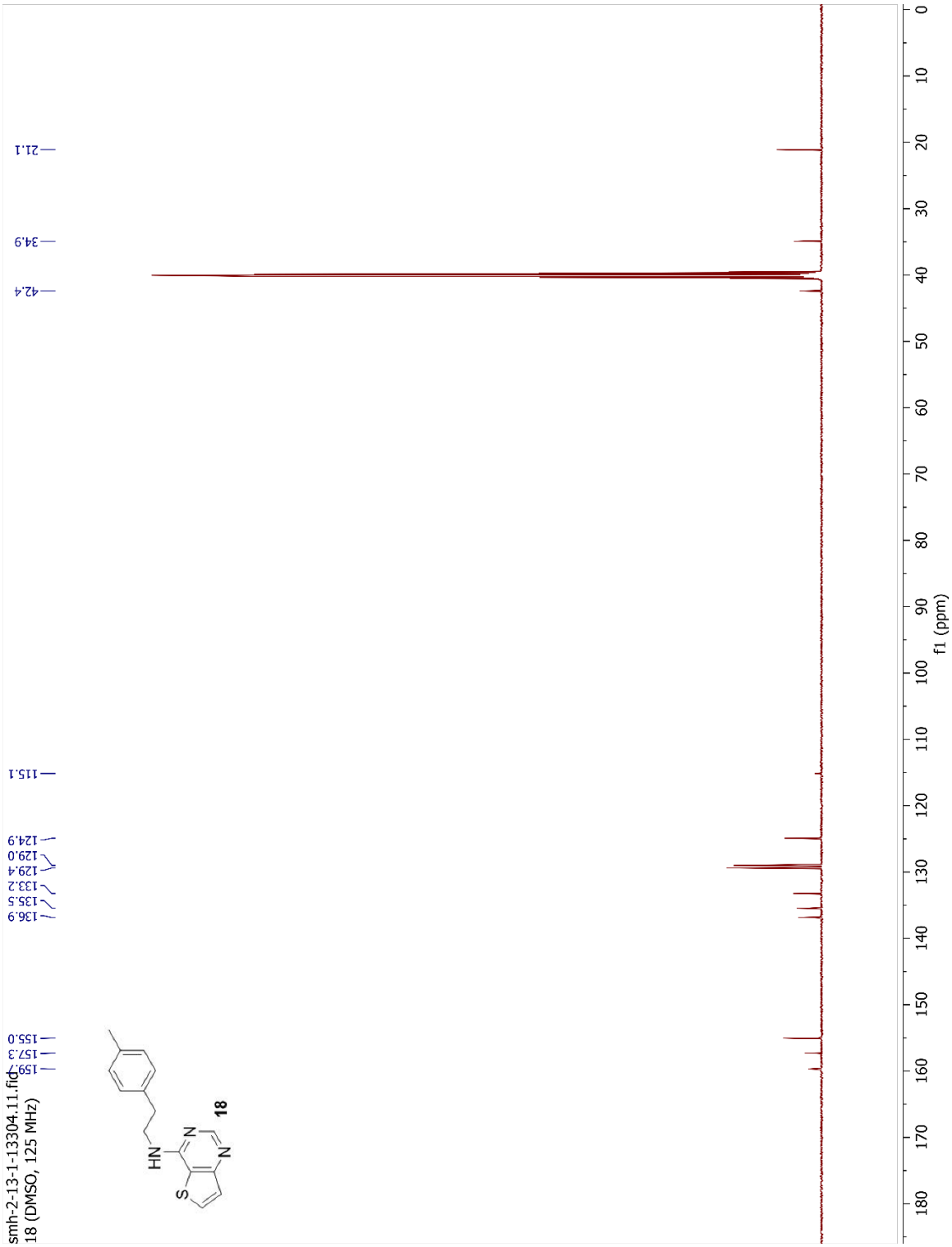

Figure A.41 ^{13}C NMR Spectrum (DMSO, 125 MHz) of **18**

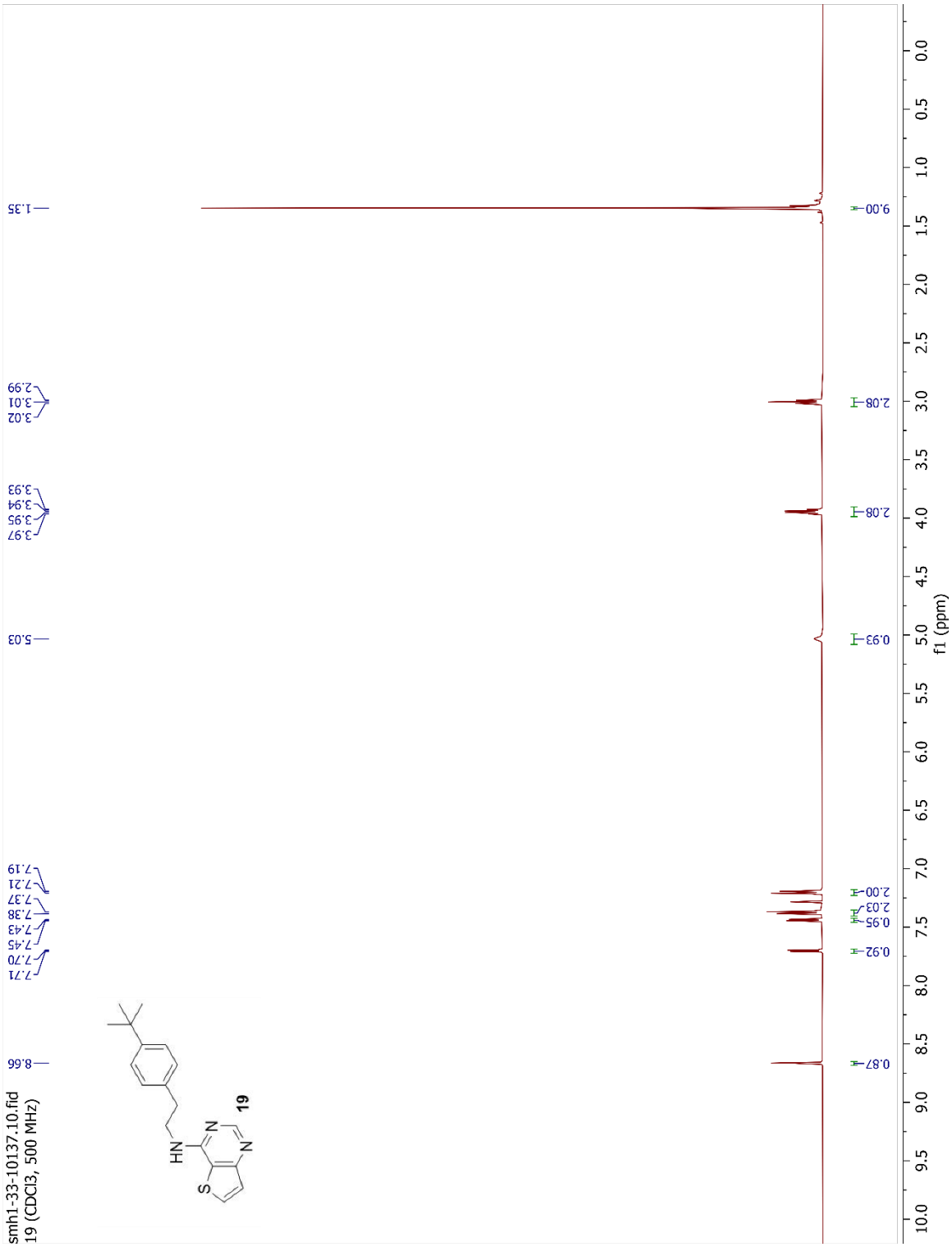

Figure A.42 ^{1}H NMR Spectrum ($CDCl_3$, 500 MHz) of **19**

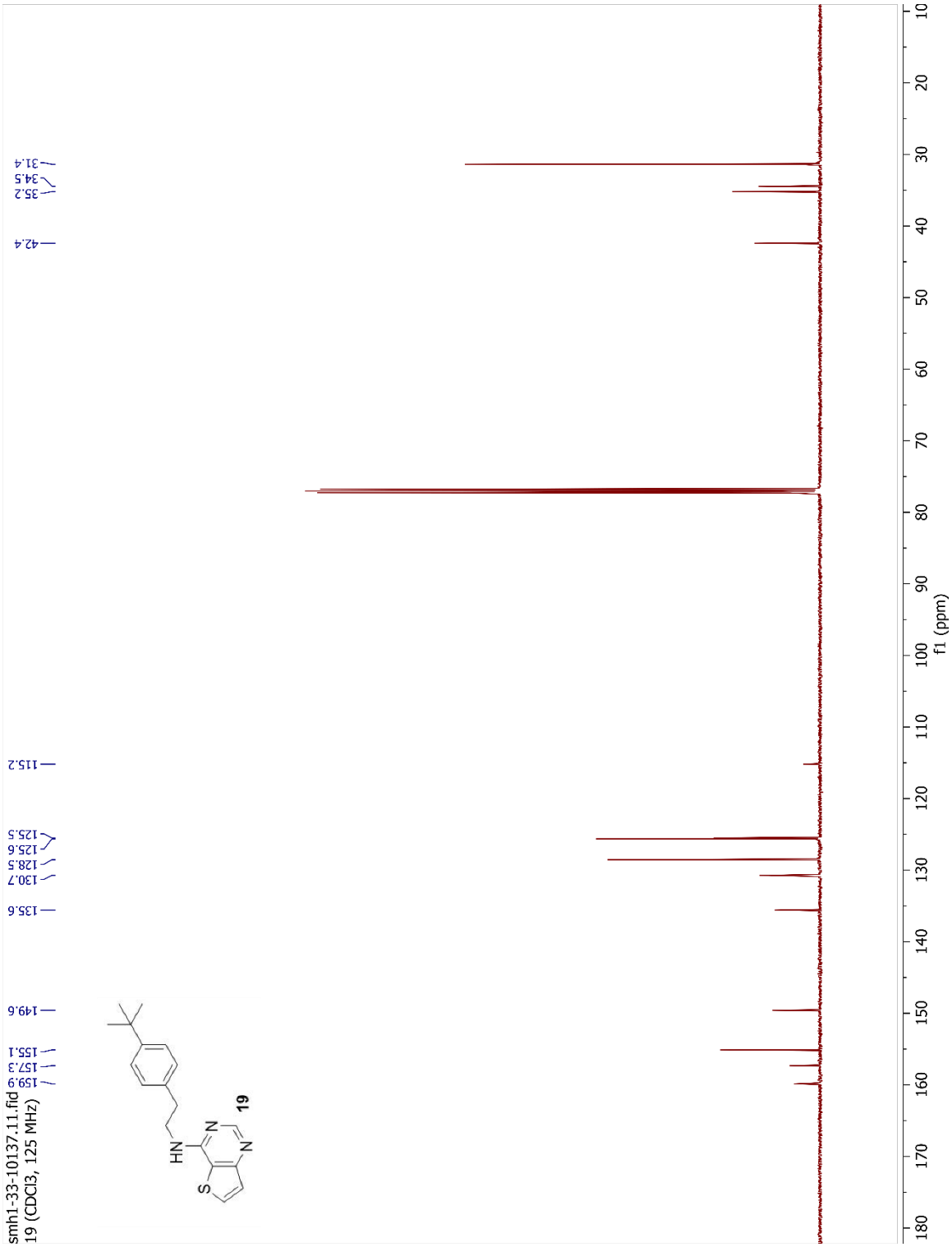

Figure A.43 ^{13}C NMR Spectrum ($CDCl_3$, 125 MHz) of **19**

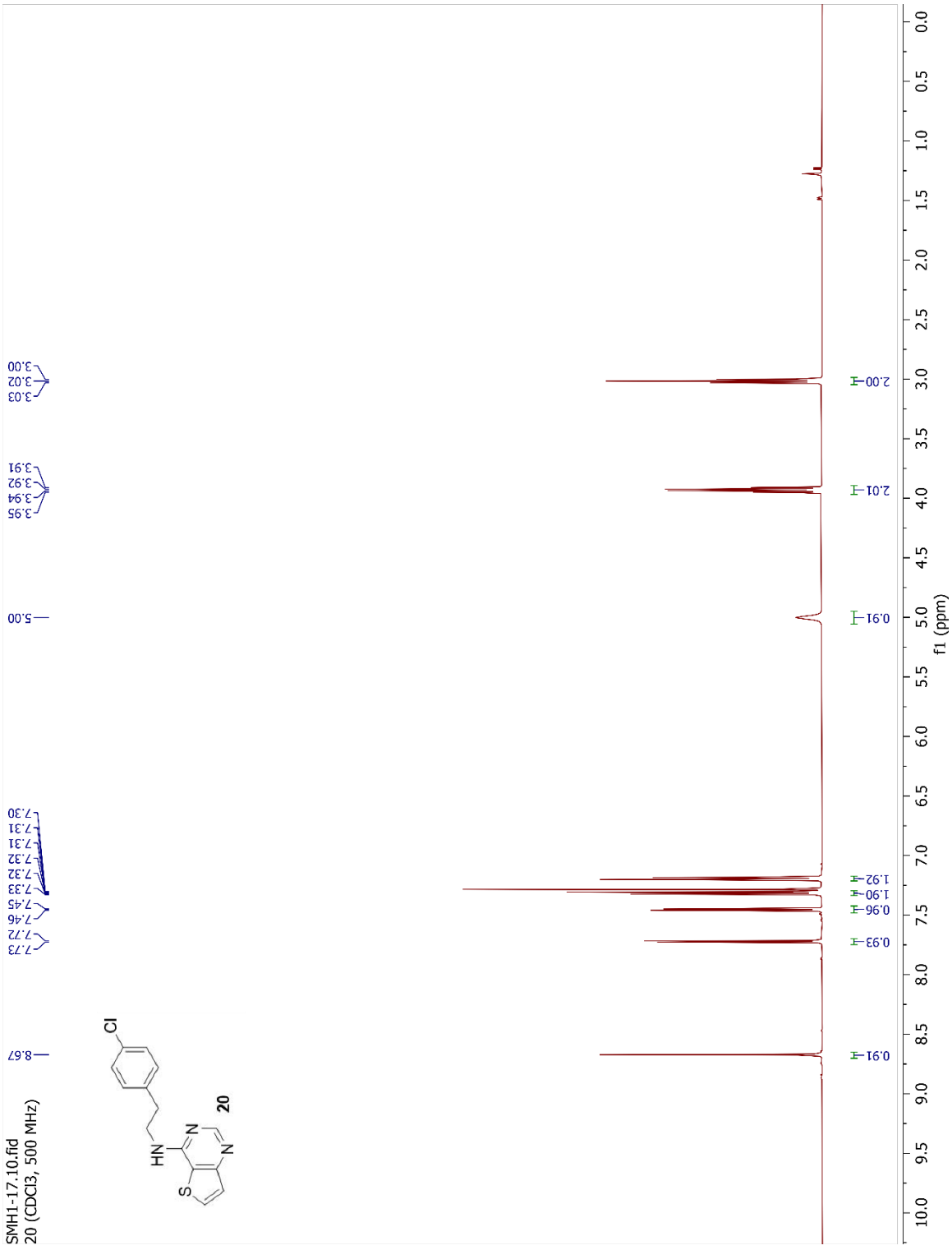

Figure A.44 ^{1}H NMR Spectrum ($CDCl_3$, 500 MHz) of **20**

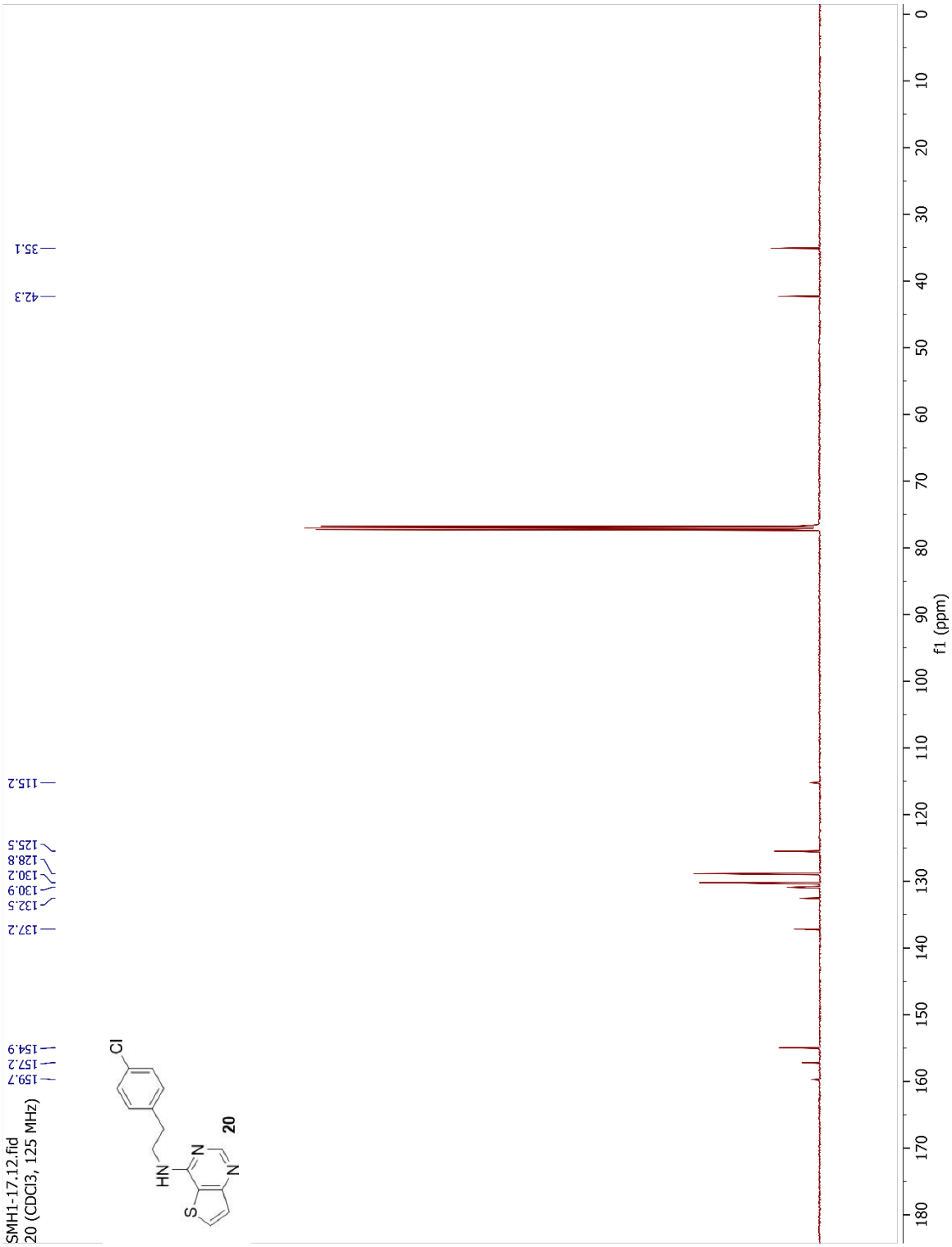

Figure A.45 ^{13}C NMR Spectrum ($CDCl_3$, 125 MHz) of **20**

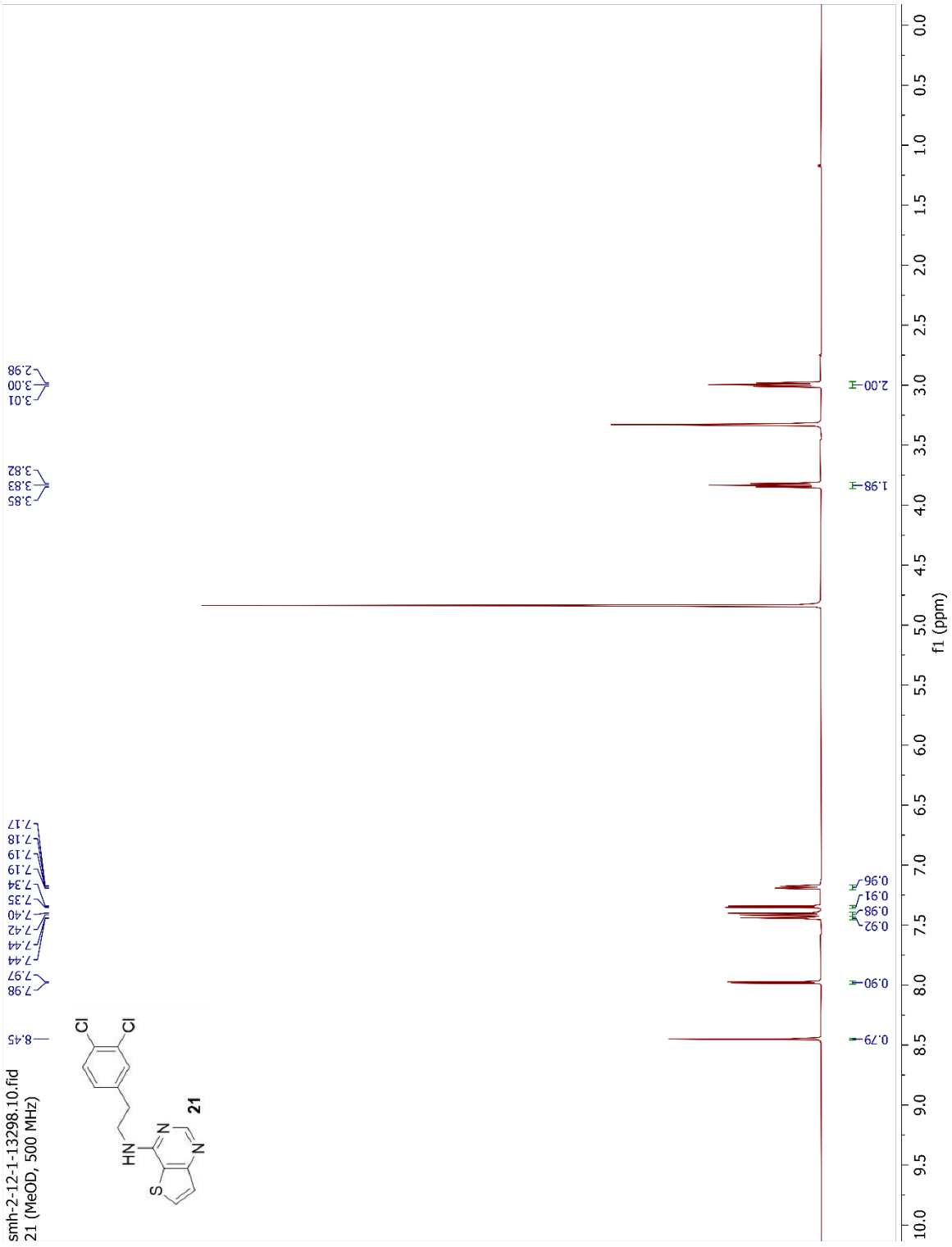

Figure A.46 ^{1}H NMR Spectrum (MeOD, 500 MHz) of **21**

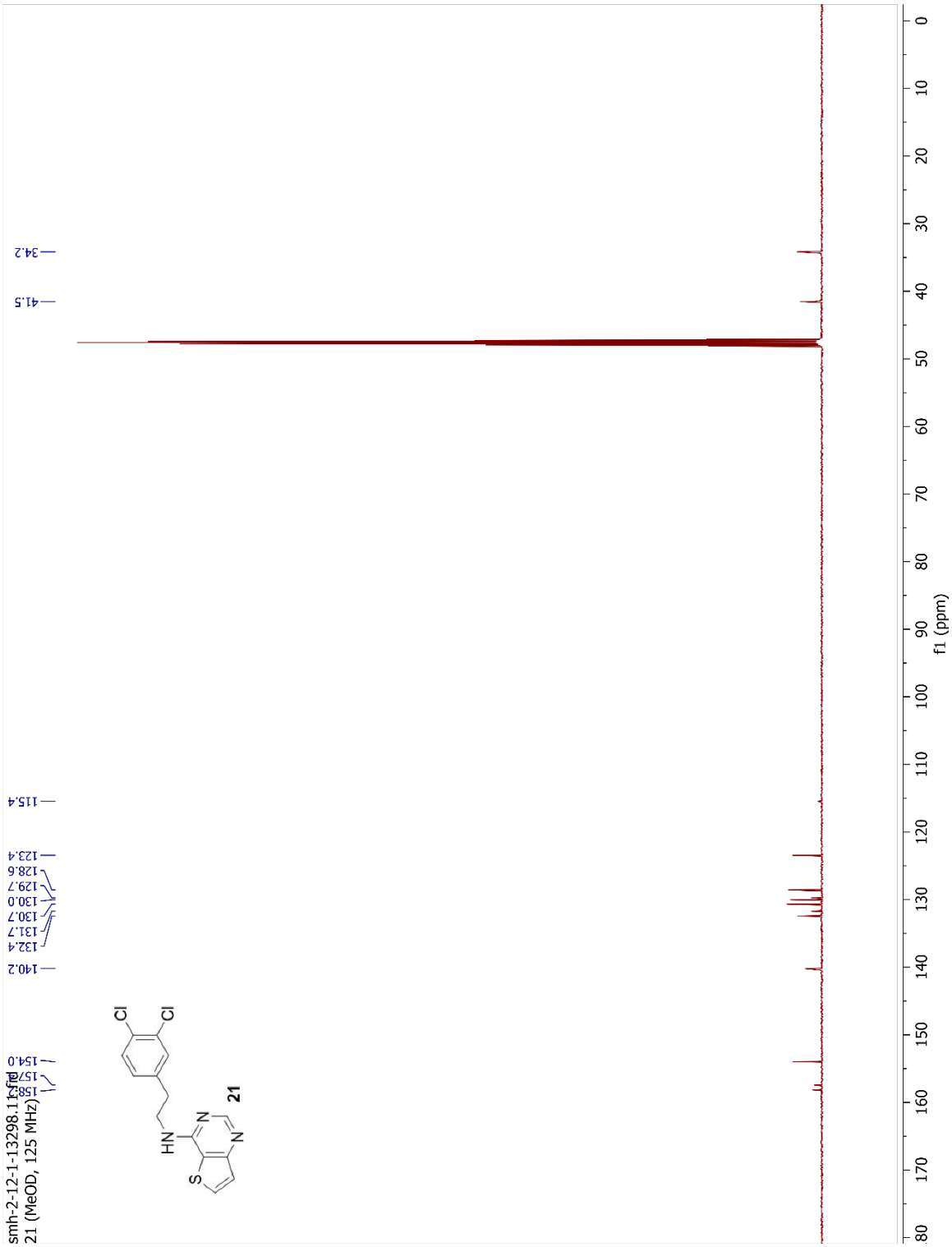

Figure A.47 ^{13}C NMR Spectrum (MeOD, 125 MHz) of **21**

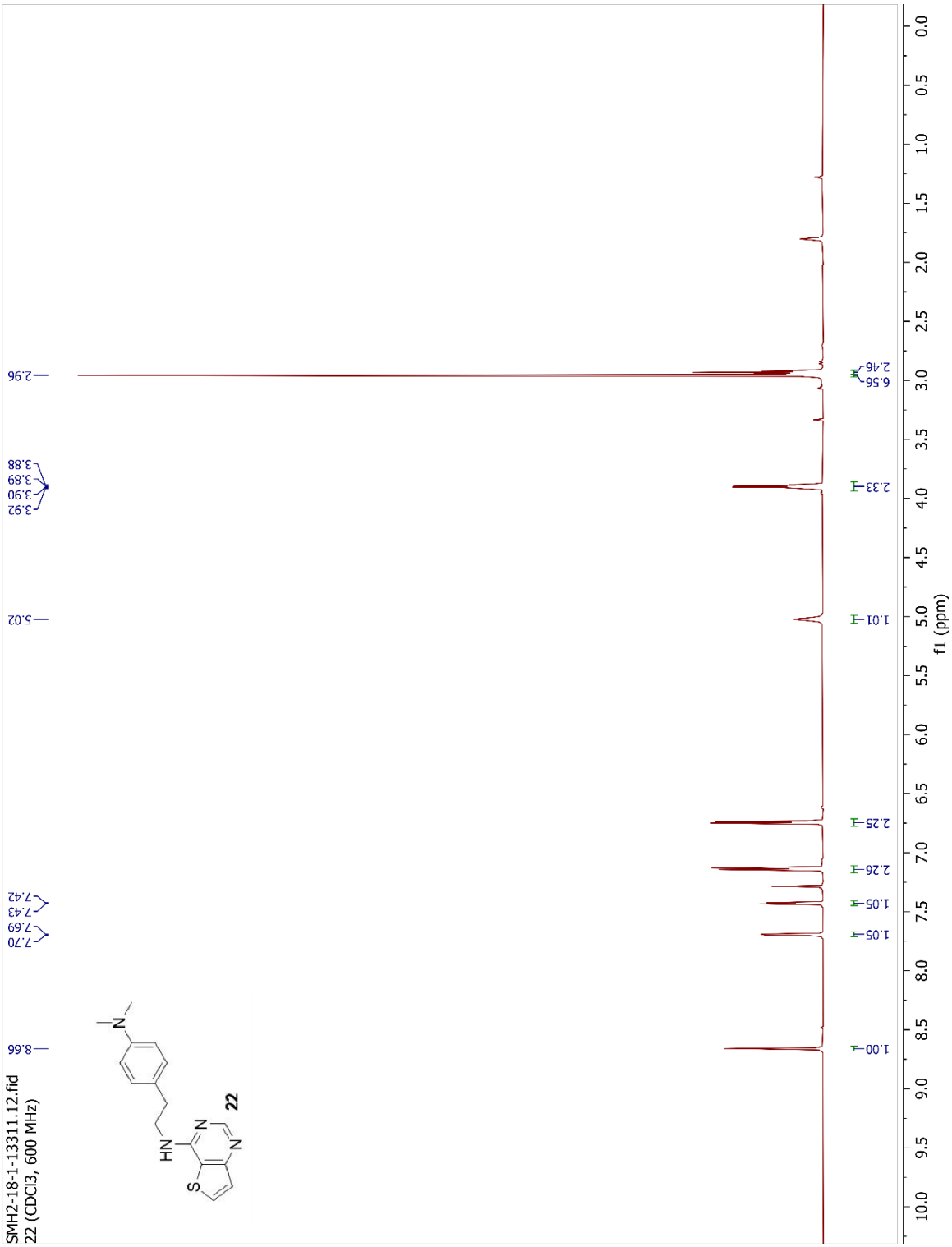

Figure A.48 ^{1}H NMR Spectrum ($CDCl_3$, 600 MHz) of **22**

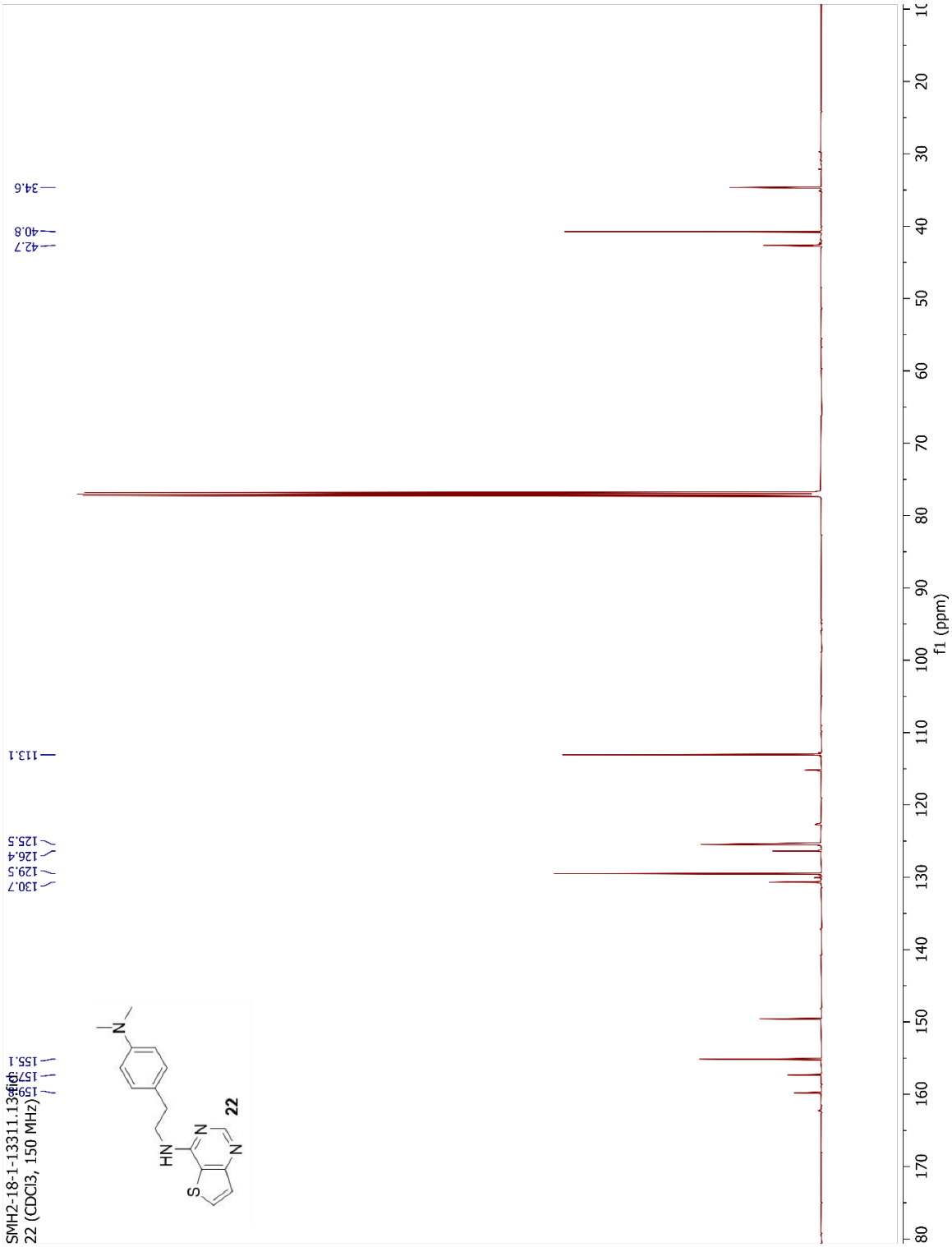

Figure A.49 ^{13}C NMR Spectrum ($CDCl_3$, 150 MHz) of **22**

Experimental section, Biology

Screening assay

Mycobacterium bovis BCG and *Mycobacterium tuberculosis* strains were cultured in Middlebrook 7H9 medium (Becton Dickson and Company Limited, USA) supplemented with 0.05% tween 80, 0.5% glycerol, Bovine Serum Albumin Fraction V, D-glucose, and NaCl. *M. tuberculosis* clinical isolate N0145 was a gift from Sebastien Gagneux. Prior to use, bacteria cells were pelleted and resuspended in medium without glycerol and adjusted to an approximated cell density of 10^7 CFU/mL. 1 µL of test compounds of varying concentrations were added to each well of 96-well white plates, and 100 µL of bacterial culture was subsequently added to each well. The assay plates were incubated at 37ºC for 15 hours, after which the BacTiter-Glo™ (Promega, USA) reagent was added. Following a 12-minute delay, the luminescence of each plate was measured using a BioTek Cytation 3 Cell Imaging Multiple-mode reader.

IC_{50} values were determined using GraphPad Prism 9. The values reflected in the table represent the average and standard deviation, which were calculated from the IC_{50} values of replicates from two experimental repeats.

APPENDIX B

SUPPORTING INFORMATION FOR CHAPTER 3

pKa Measurements

Preparation of solutions.

The pH of the solutions was measured with a PASCO Scientific pH probe connected to a Model 270 Denver Instrument pH meter at 20 °C. All solutions were prepared with degassed Aquafina water. The 0.01 M aqueous NaOH was standardized with potassium hydrogen phthalate (KHP). The 0.01 M aqueous HCl was standardized with sodium hydroxide. Compounds were dissolved in 2 mL of DMSO, diluted with water, sonicated, heated, and allowed to stir for 1 week.

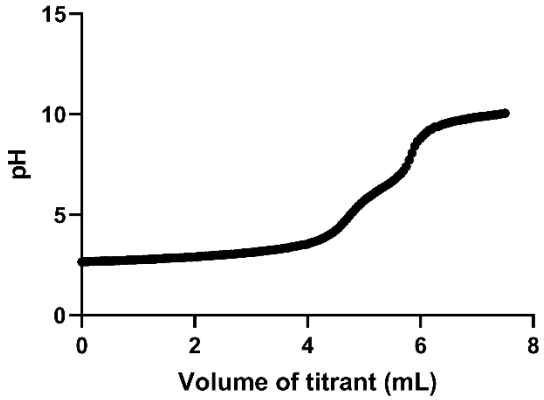

Figure B.1 Trial 1: Potentiometric titration curve of *N*-Phenethylthieno[3,2-*d*]pyrimidin-4-amine **1** with NaOH.

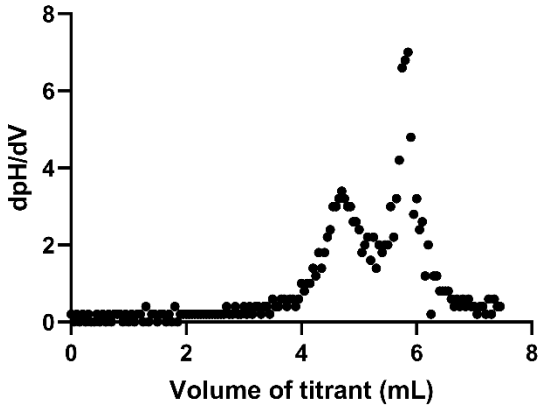

Figure B.2 Trial 1: First derivative curve of potentiometric titration of *N*-Phenethylthieno[3,2-*d*]pyrimidin-4-amine **1** with NaOH.

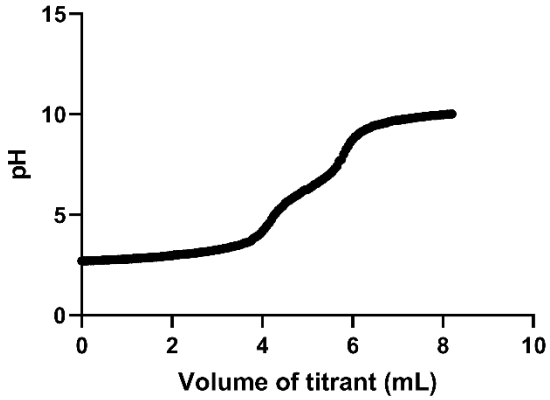

Figure B.3 Trial 2: Potentiometric titration curve of *N*-Phenethylthieno[3,2-*d*]pyrimidin-4-amine **1** with NaOH.

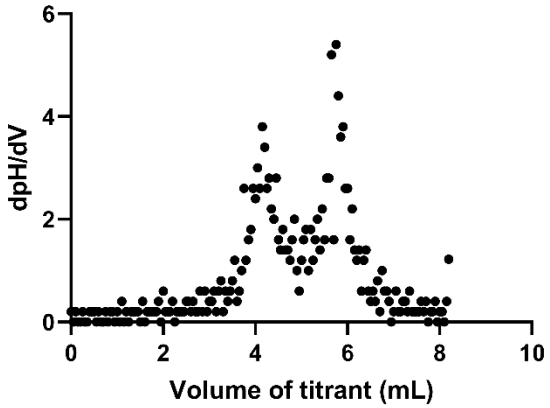

Figure B.4 Trial 2: First derivative curve of potentiometric titration of *N*-Phenethylthieno[3,2-*d*]pyrimidin-4-amine **1** with NaOH.

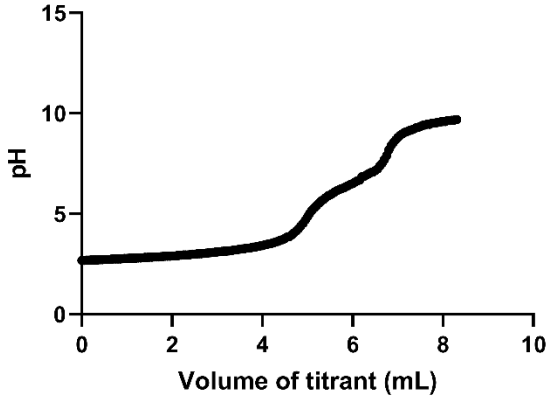

Figure B.5 Trial 3: Potentiometric titration curve of *N*-Phenethylthieno[3,2-*d*]pyrimidin-4-amine **1** with NaOH.

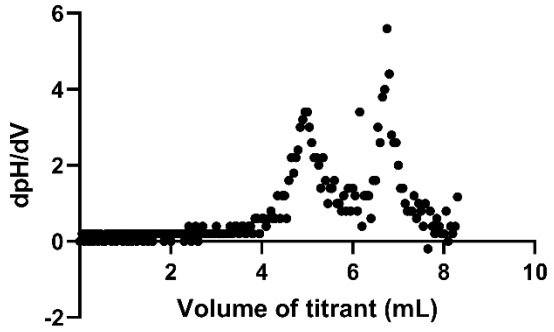

Figure B.6 Trial 3: First derivative curve of potentiometric titration of *N*-Phenethylthieno[3,2-*d*]pyrimidin-4-amine **1** with NaOH.

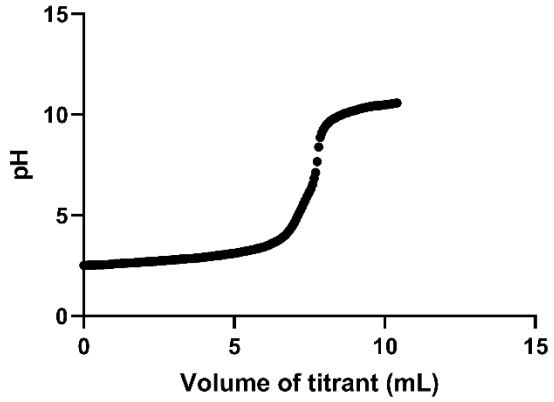

Figure B.7 Trial 1: Potentiometric titration curve of *N*-(4-Methylphenethyl)thieno[3,2-*d*]pyrimidin-4-amine **2** with NaOH.

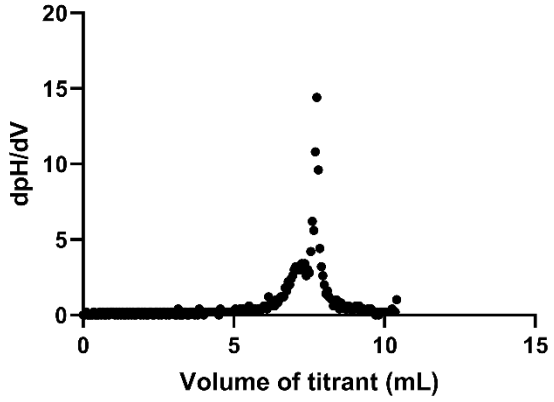

Figure B.8 Trial 1: First derivative curve of potentiometric titration of *N*-(4-Methylphenethyl)thieno[3,2-*d*]pyrimidin-4-amine **2** with NaOH.

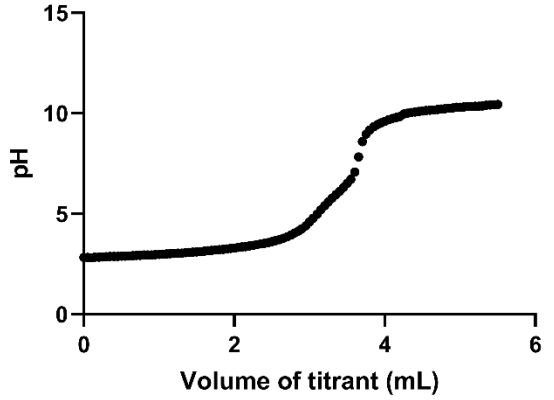

Figure B.9 Trial 2: Potentiometric titration curve of *N*-(4-Methylphenethyl)thieno[3,2-*d*]pyrimidin-4-amine **2** with NaOH.

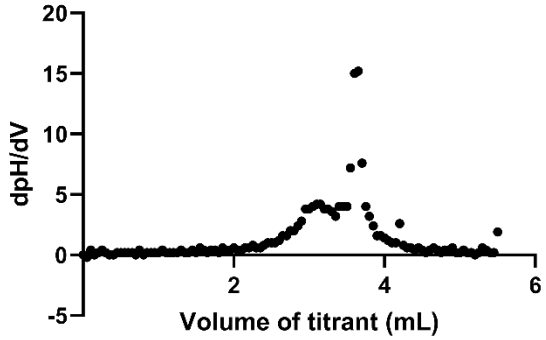

Figure B.10 Trial 2: First derivative curve of potentiometric titration of *N*-(4-Methylphenethyl)thieno[3,2-*d*]pyrimidin-4-amine **2** with NaOH.

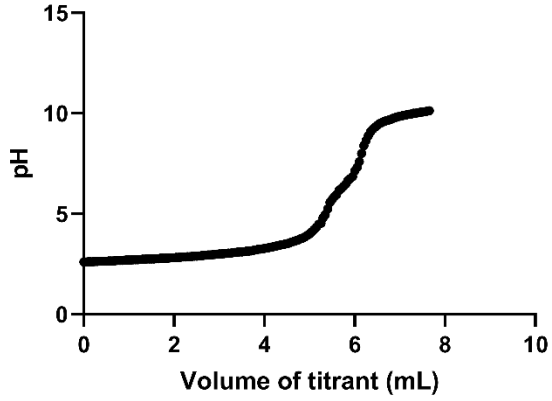

Figure B.11 Trial 2: Potentiometric titration curve of *N*-(4-Methylphenethyl)thieno[3,2-*d*]pyrimidin-4-amine **2** with NaOH.

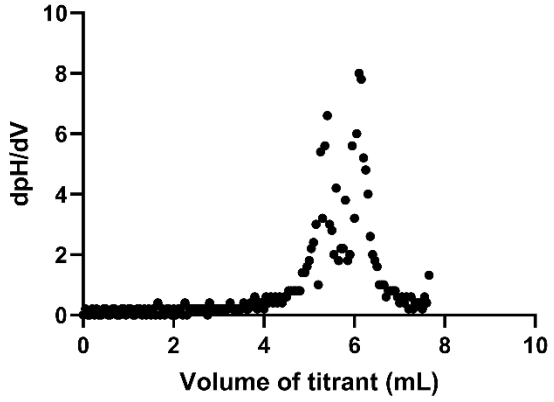

Figure B.12 Trial 3: First derivative curve of potentiometric titration of *N*-(4-Methylphenethyl)thieno[3,2-*d*]pyrimidin-4-amine **2** with NaOH.

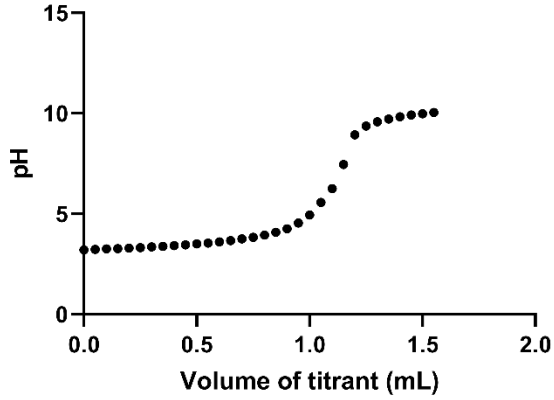

Figure B.13 Trial 1: Potentiometric titration curve of *N*-(4-(*tert*Butyl)phenethyl)thieno[3,2-*d*]pyrimidin-4-amine **3** with NaOH.

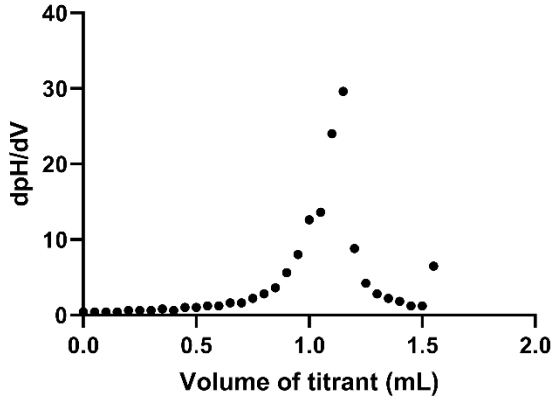

Figure B.14 Trial 1: First derivative curve of potentiometric titration of *N*-(4-(*tert*-Butyl)phenethyl)thieno[3,2-*d*]pyrimidin-4-amine **3** with NaOH.

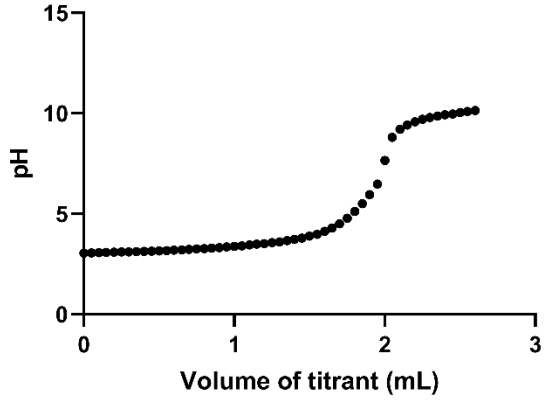

Figure B.15 Trial 2: Potentiometric titration curve of *N*-(4-(*tert*-Butyl)phenethyl)thieno[3,2-*d*]pyrimidin-4-amine **3** with NaOH.

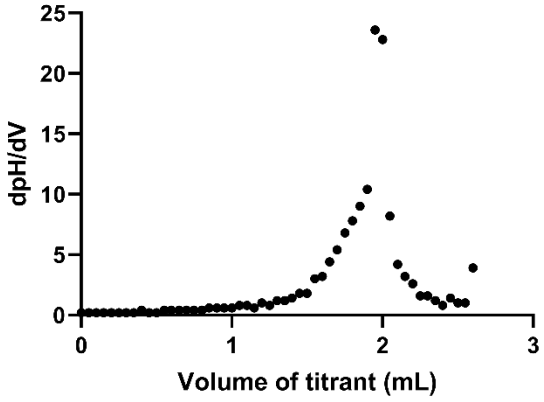

Figure B.16 Trial 2: First derivative curve of potentiometric titration of *N*-(4-(*tert*-Butyl)phenethyl)thieno[3,2-*d*]pyrimidin-4-amine **3** with NaOH.

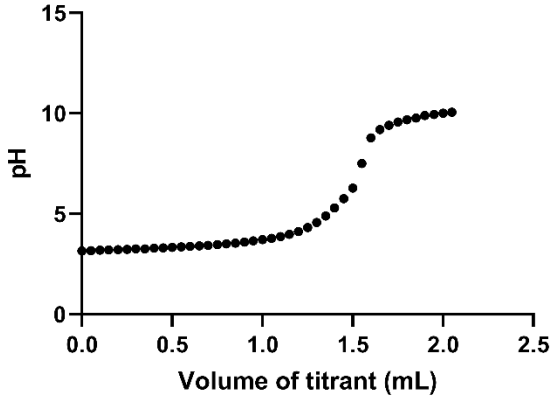

Figure B.17 Trial 3: Potentiometric titration curve of *N*-(4-(*tert*-Butyl)phenethyl)thieno[3,2-*d*]pyrimidin-4-amine **3** with NaOH.

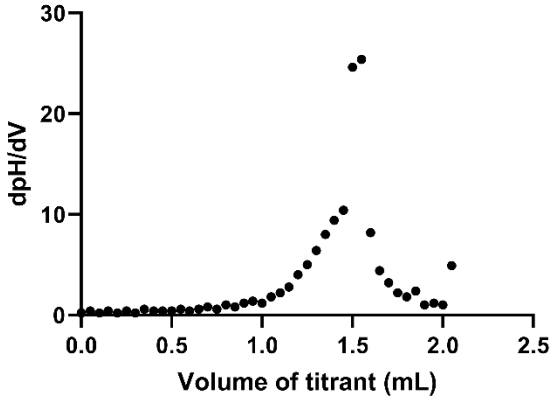

Figure B.18 **.** Trial 3: First derivative curve of potentiometric titration of *N*-(4-(*tert*-Butyl)phenethyl)thieno[3,2-*d*]pyrimidin-4-amine **3** with NaOH.

In order to determine the state of charge on compounds **1**-**3** at physiological pH, pKa measurements were taken. The results of those experiments are summarized below in Table B.1. These results indicate that at physiological pH compounds **1**-**3** are neutral.

pKa	**Compound 1**	**Compound 2**	**Compound 3**
pKa_1	2.99	2.99	3.50
pKa_2	3.18	3.05	

Table B.1 pKa values of compounds **1**-**3**

Steady-state fluorescence spectra of compounds 1, 2, and 3 in bulk solvents.

Excitation and emission wavelengths for Compounds **1**–**3** was selected based on each solute's steady state excitation and fluorescence emission spectrum. These data were used to determine the excitation and emission wavelengths used in the TCSPC experiments. While all three solutes were weakly solvatochromic, the excitation and emission wavelengths used in TCSPC measurements were chosen

to access all relevant solvation environments. All time-resolved fluorescence spectra were excited at 260 nm and emission was collected at 370 nm.

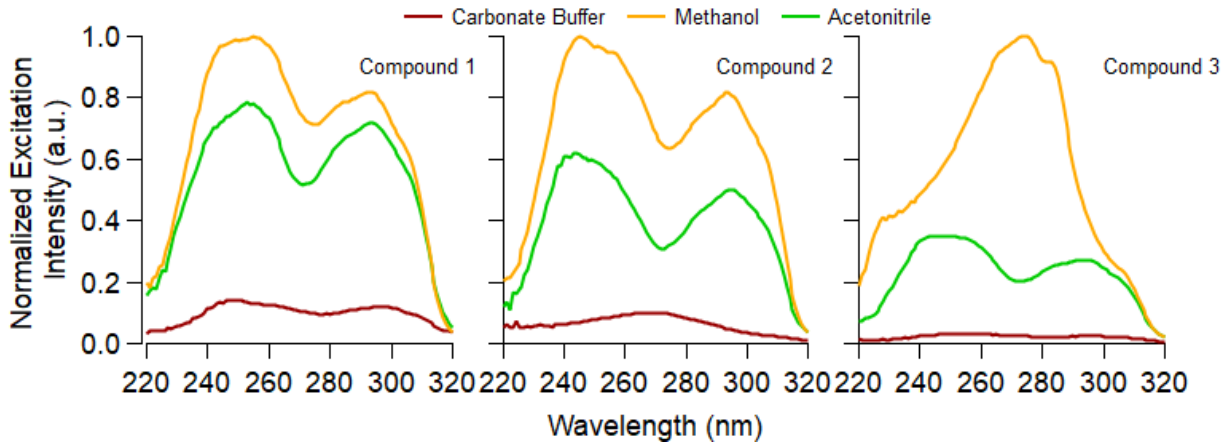

Figure B.19 Excitation spectra of Compounds **1**, **2**, and **3** in each of the bulk solvents.

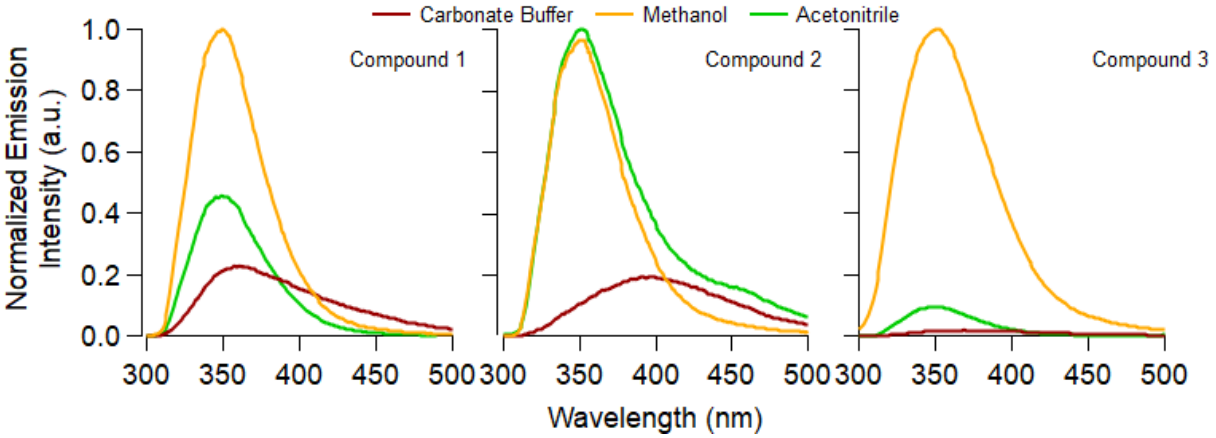

Figure B.20 Emission spectra of Compounds **1**, **2**, and **3** in each of the bulk solvents.

Fluorescence lifetime and amplitudes of compounds in a DPPC lipid vesicle solution from as function of temperature.

	Compound 1		**Compound 2**				**Compound 3**		
temp. (°C)	buffer τ_1 (A_1)	buffer τ_2 (A_2)	buffer τ_1 (A_1)	buffer τ_2 (A_2)	new K_{nr} τ_3 (A_3)	conf. restricted τ_4 (A_4)	buffer τ_1 (A_1)	buffer τ_2 (A_2)	new K_{nr} τ_3 (A_3)
10	0.25 (0.89)	1.71 (0.11)	0.31 (0.38)	1.40 (0.19)	3.89 (0.04)	0.06 (0.39)	0.19 (0.93)	0.84 (0.05)	3.60 (0.02)
20	0.26 (0.91)	1.70 (0.09)	0.29 (0.39)	1.36 (0.19)	3.98 (0.04)	0.05 (0.37)	0.19 (0.93)	0.78 (0.05)	3.42 (0.02)
30	0.23 (0.92)	1.69 (0.08)	0.28 (0.44)	1.35 (0.21)	3.94 (0.04)	0.05 (0.32)	0.18 (0.92)	0.70 (0.06)	3.22 (0.02)
40	0.25 (0.92)	1.67 (0.08)	0.28 (0.46)	1.01 (0.22)	3.57 (0.03)	0.07 (0.29)	0.18 (0.92)	0.74 (0.06)	3.26 (0.02)
50	0.23 (0.92)	1.63 (0.08)	0.25 (0.48)	1.37 (0.19)	4.22 (0.03)	0.08 (0.30)	0.17 (0.93)	0.80 (0.05)	3.49 (0.02)
60	0.23 (0.93)	1.62 (0.07)	0.23 (0.52)	1.27 (0.19)	3.59 (0.03)	0.14 (0.26)	0.17 (0.90)	0.71 (0.08)	3.15 (0.02)
70	0.22 (0.93)	1.61 (0.07)	0.24 (0.54)	1.39 (0.22)	5.05 (0.02)	0.10 (0.22)	0.17 (0.91)	0.68 (0.08)	3.03 (0.02)
60	0.23 (0.93)	1.62 (0.07)	0.24 (0.51)	1.37 (0.22)	4.58 (0.02)	0.09 (0.25)	0.17 (0.90)	0.74 (0.08)	3.17 (0.02)
50	0.23 (0.92)	1.64 (0.08)	0.24 (0.41)	1.30 (0.20)	3.96 (0.03)	0.09 (0.36)	0.17 (0.91)	0.81 (0.07)	3.23 (0.03)
40	0.24 (0.92)	1.65 (0.08)	0.25 (0.50)	1.29 (0.22)	3.59 (0.04)	0.06 (0.24)	0.18 (0.90)	0.80 (0.07)	3.19 (0.03)
30	0.25 (0.90)	1.67 (0.10)	0.27 (0.42)	1.30 (0.26)	3.36 (0.05)	0.07 (0.28)	0.18 (0.87)	0.79 (0.09)	3.06 (0.04)
20	0.25 (0.89)	1.70 (0.11)	0.28 (0.36)	1.31 (0.25)	3.63 (0.05)	0.07 (0.33)	0.18 (0.85)	0.79 (0.11)	3.10 (0.05)
10	0.25 (0.89)	1.70 (0.11)	0.31 (0.34)	1.36 (0.23)	3.58 (0.06)	0.09 (0.37)	0.18 (0.85)	0.90 (0.10)	3.22 (0.05)

Table B.2 Full list of fluorescent lifetimes (in ns) and amplitudes (in parentheses) of compounds in DPPC at a temperature ramp from 10 – 70 °C at 10 °C increments and back down again to 10 °C.

1D Selective Gradient NOESY spectra

1D Selective Gradient Nuclear Overhauser Effect (NOE) spectra were recorded at 300 K on a Bruker 600 MHz Avance III NMR Spectrometer. Generally used acquisition parameters: spectral width 12,019 Hz, acquisition time 2.73 seconds, pulse width 8 µs, relaxation delay 2 seconds, mixing time 0.3 seconds, number of scans 128. Peaks were selected to be excited for each experiment.

NOESY experiments were carried out to determine if through space proton interactions were occurring as a result of constrained or contorted special conformations. No such interactions were measured, therefore, if such a conformation exists, it was not captured by these experiments. This suggests then that such a constrained conformation is not likely in bulk solvent and only appears when the compounds are physically constrained either when interacting with vesicles or in frozen solution.

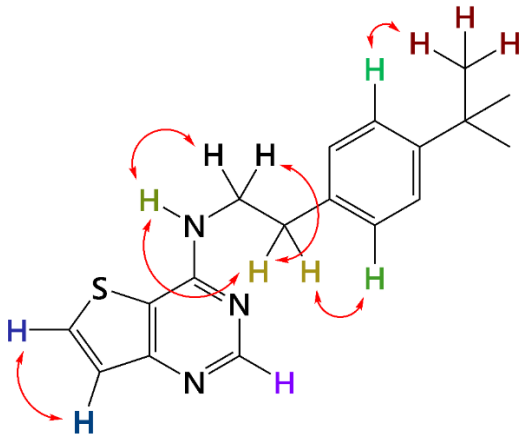

Figure B.21 NOE correlations of **3**. Red double-headed arrows indicate NOE.

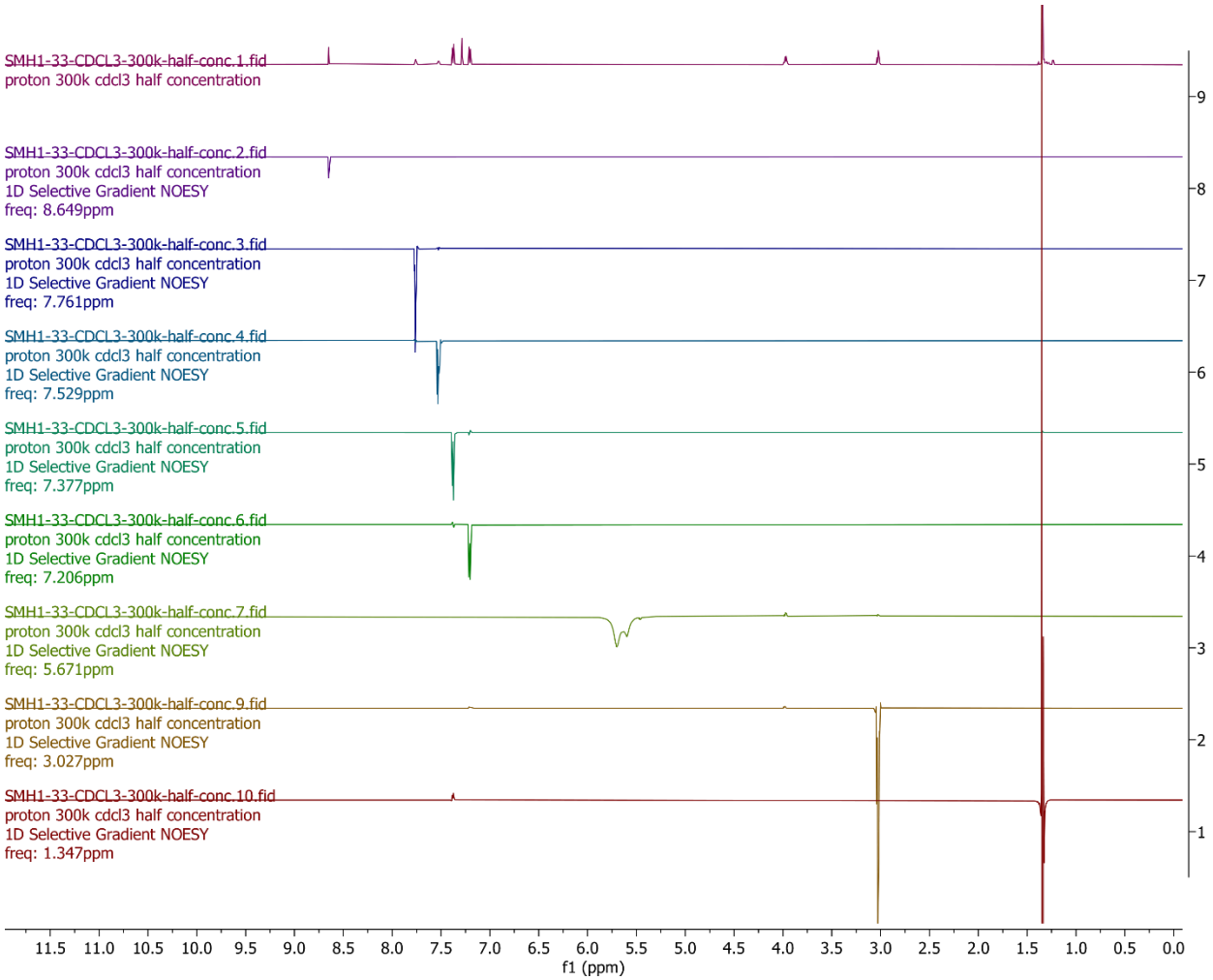

Figure B.22 Stacked NOE correlations of **3**.

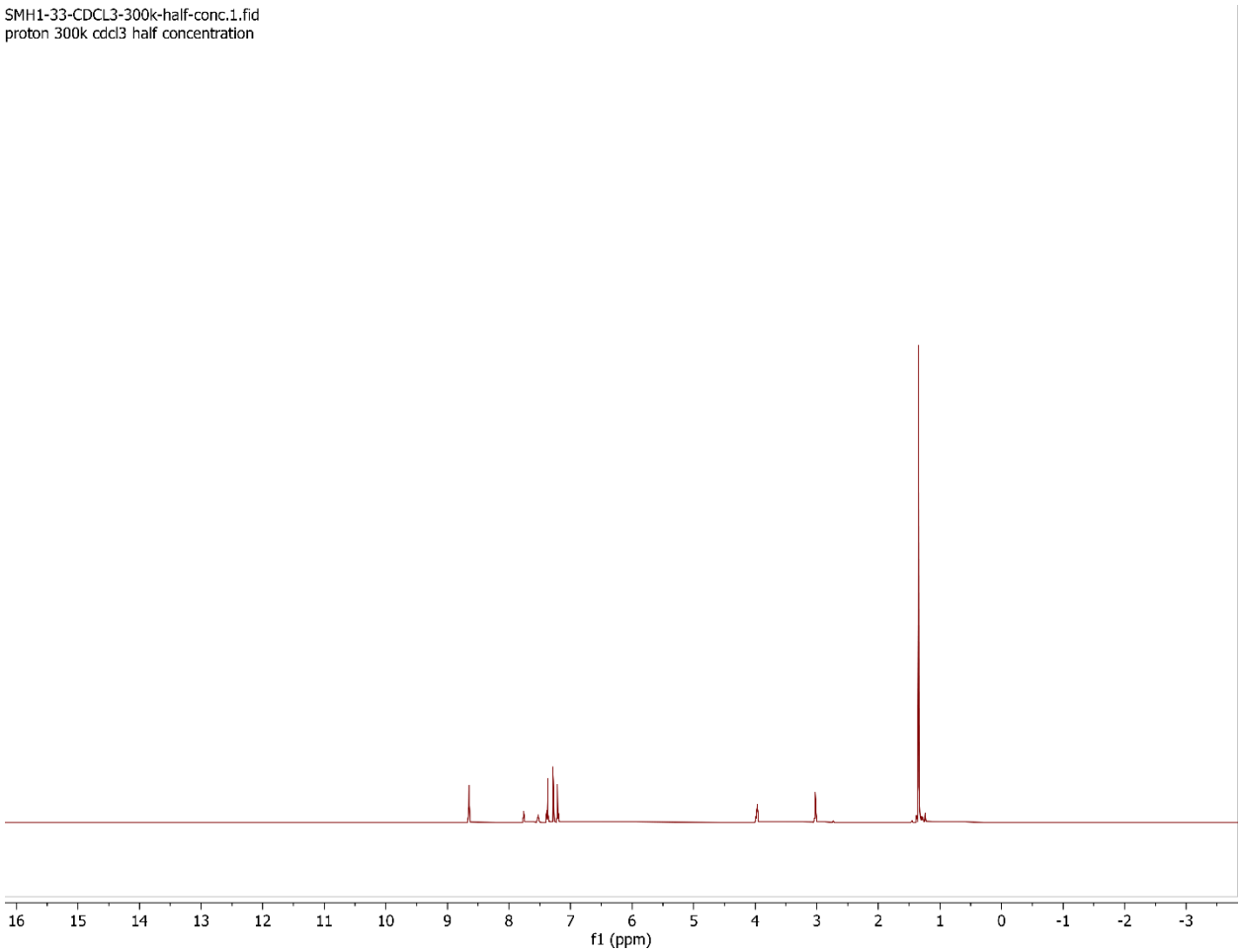

Figure B.23 ^{1}H NMR spectrum of **3** (600 MHz, $CDCl_3$)

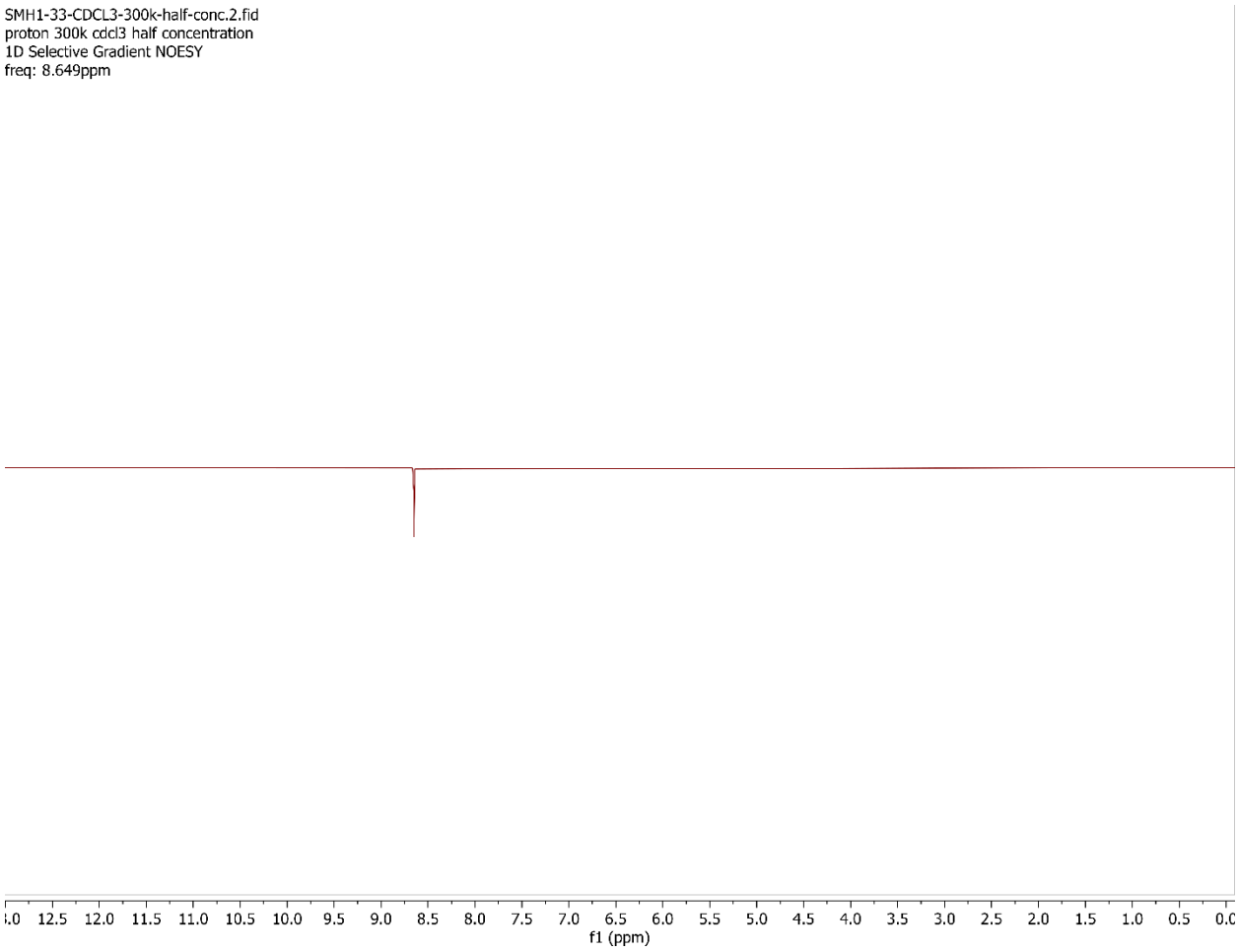

Figure B.24 Signal observed when 8.649 ppm peak probed

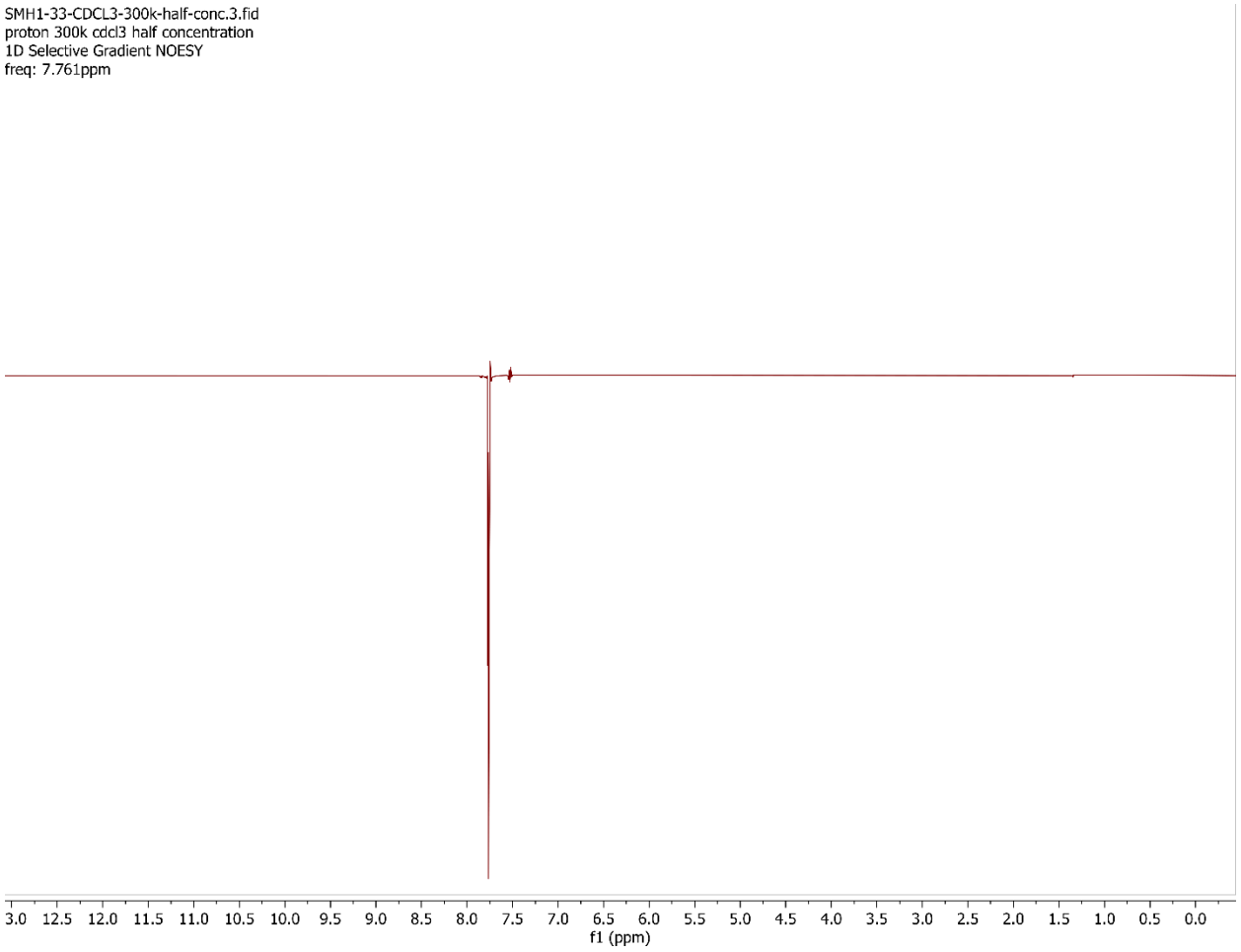

Figure B.25 Signal observed when 7.761 ppm peak probed

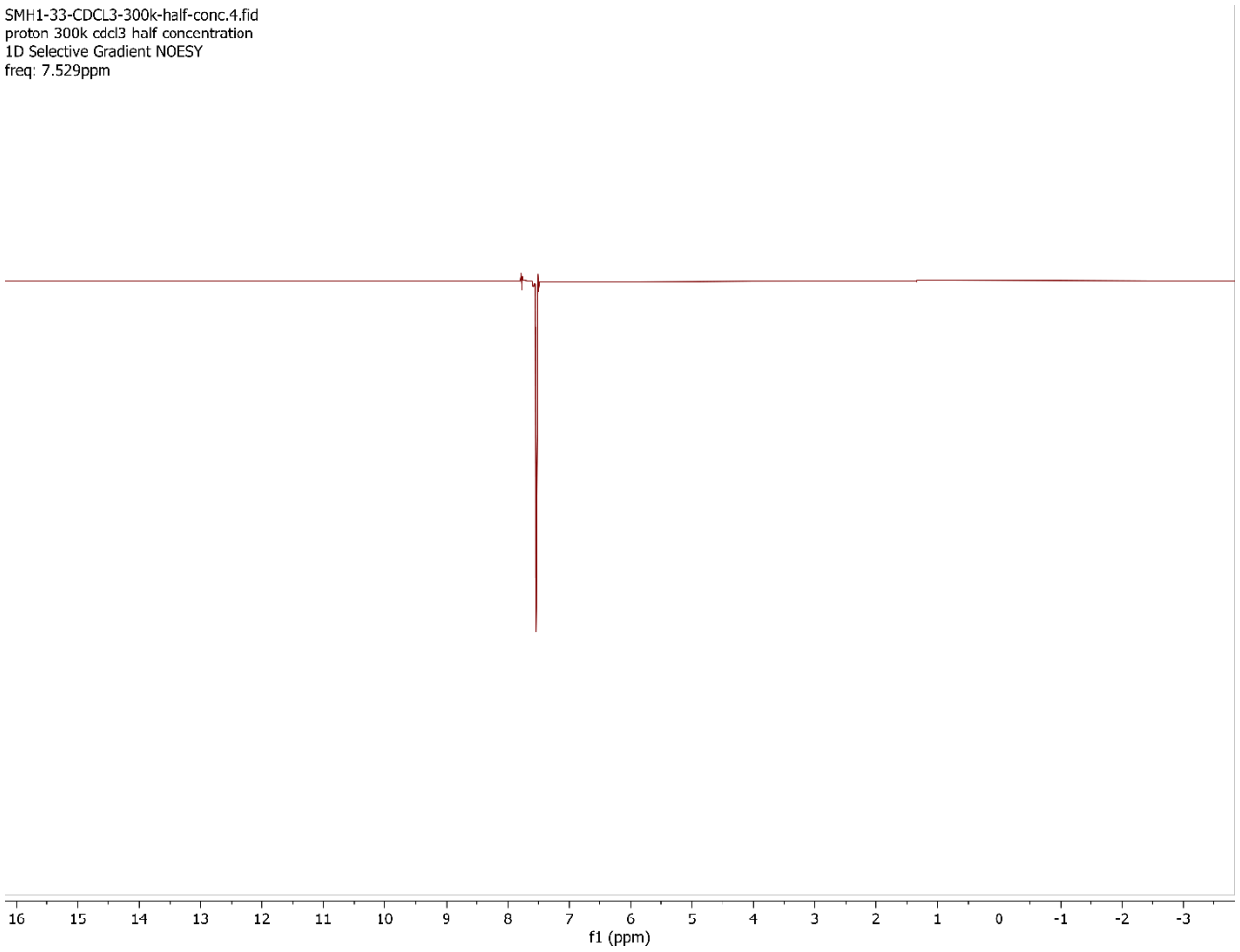

Figure B.26 Signal observed when 7.529 ppm peak probed

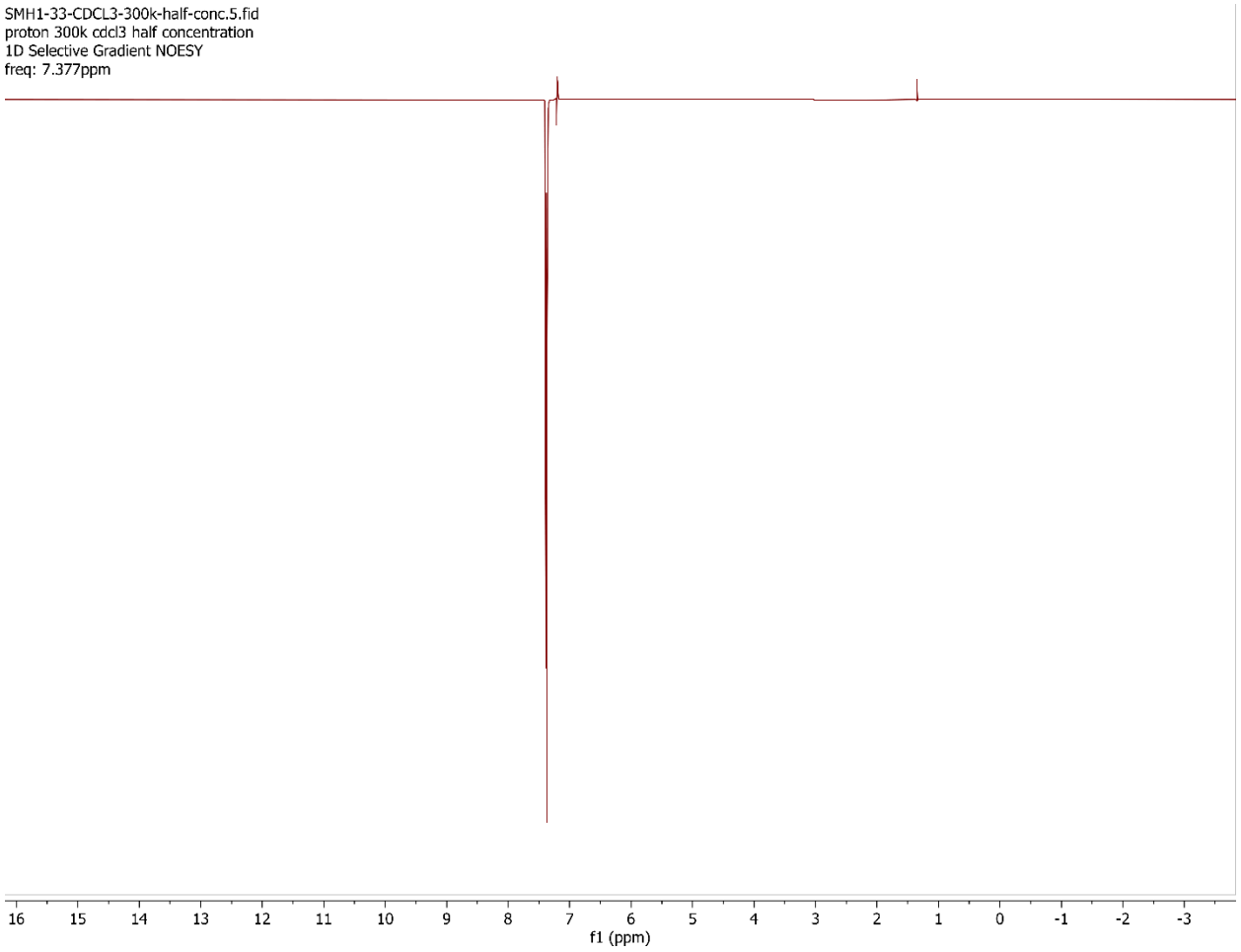

Figure B.27 Signal observed when 7.377 ppm peak probed

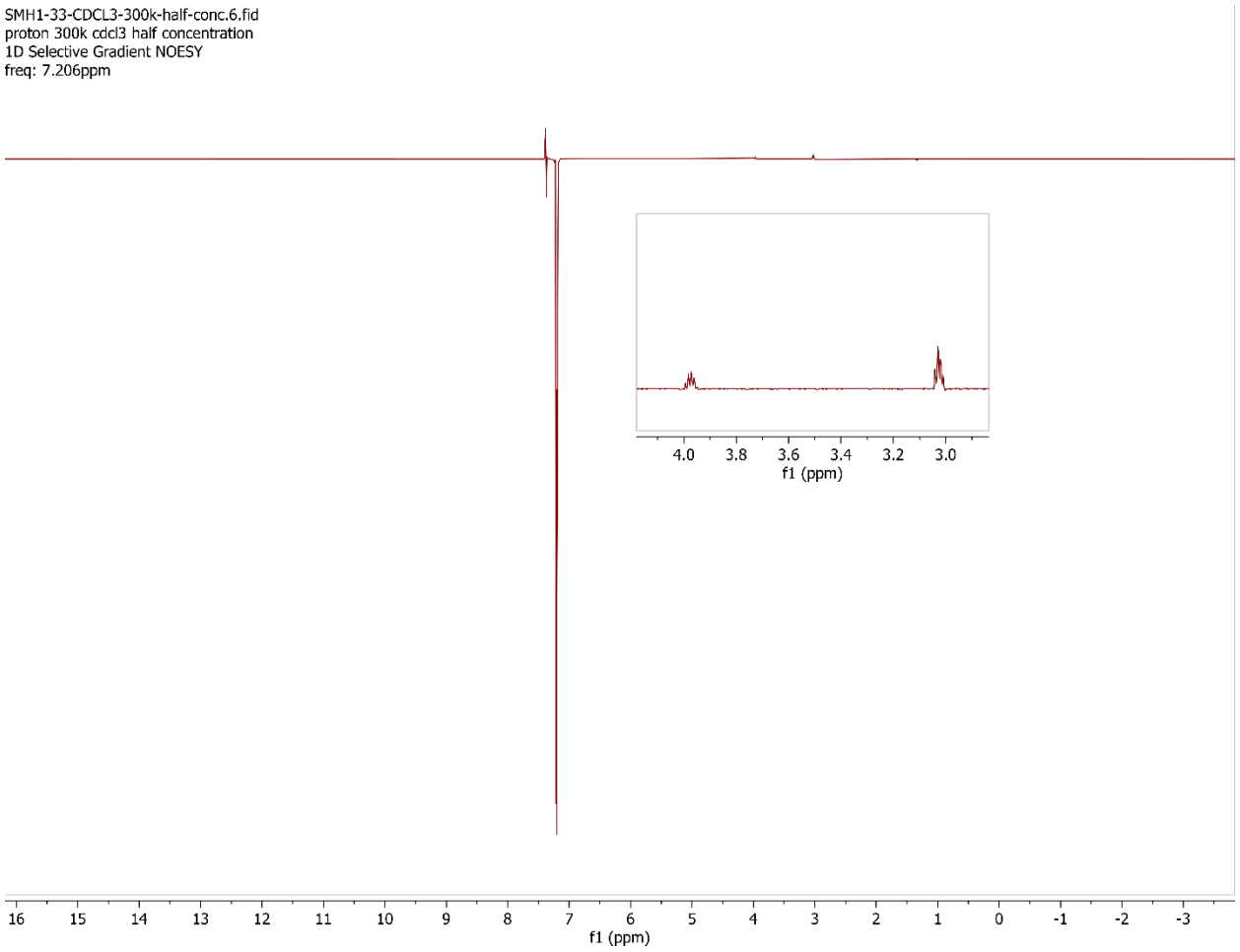

Figure B.28 Signal observed when 7.206 ppm peak probed

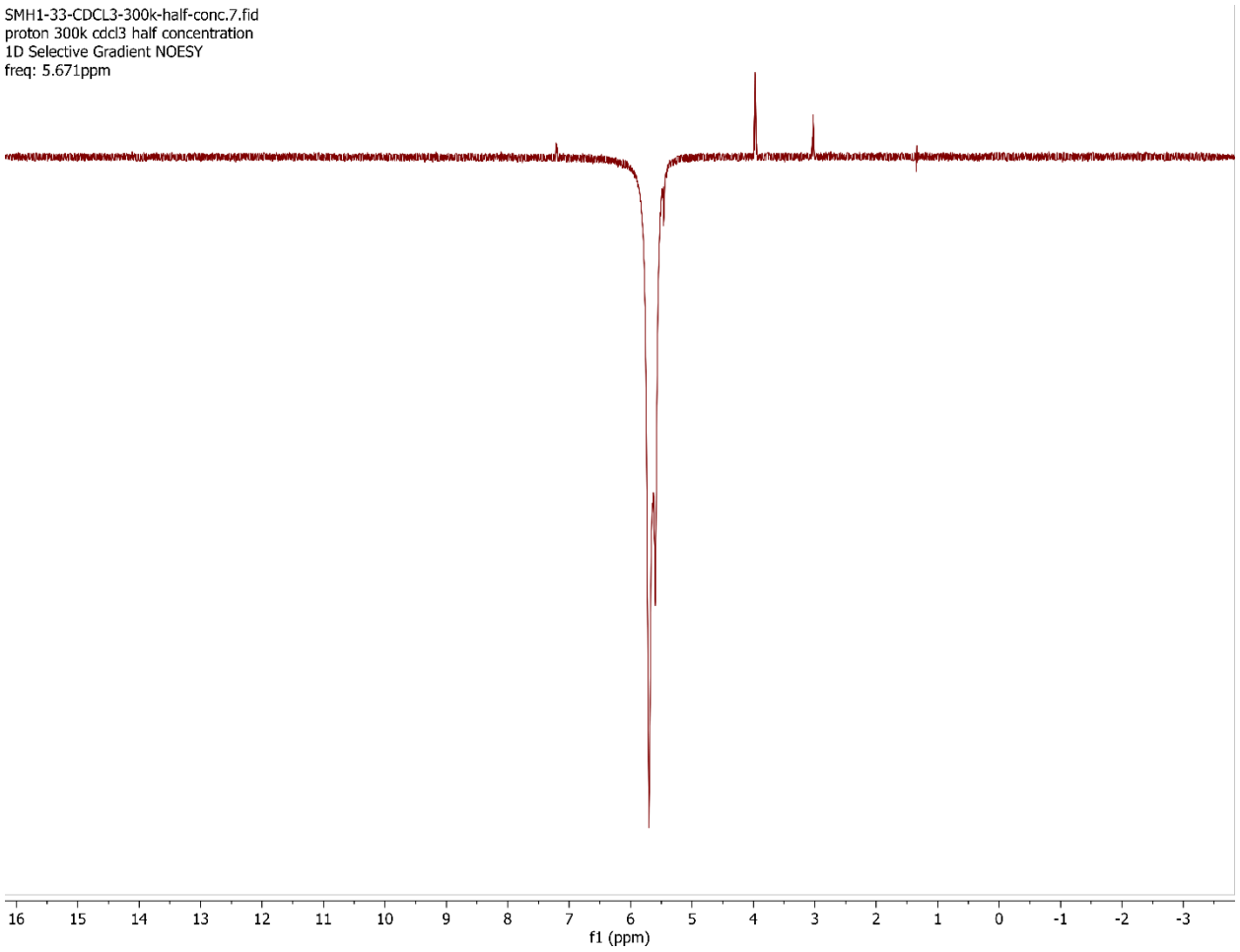

Figure B.29 Signal observed when 5.671 ppm peak probed

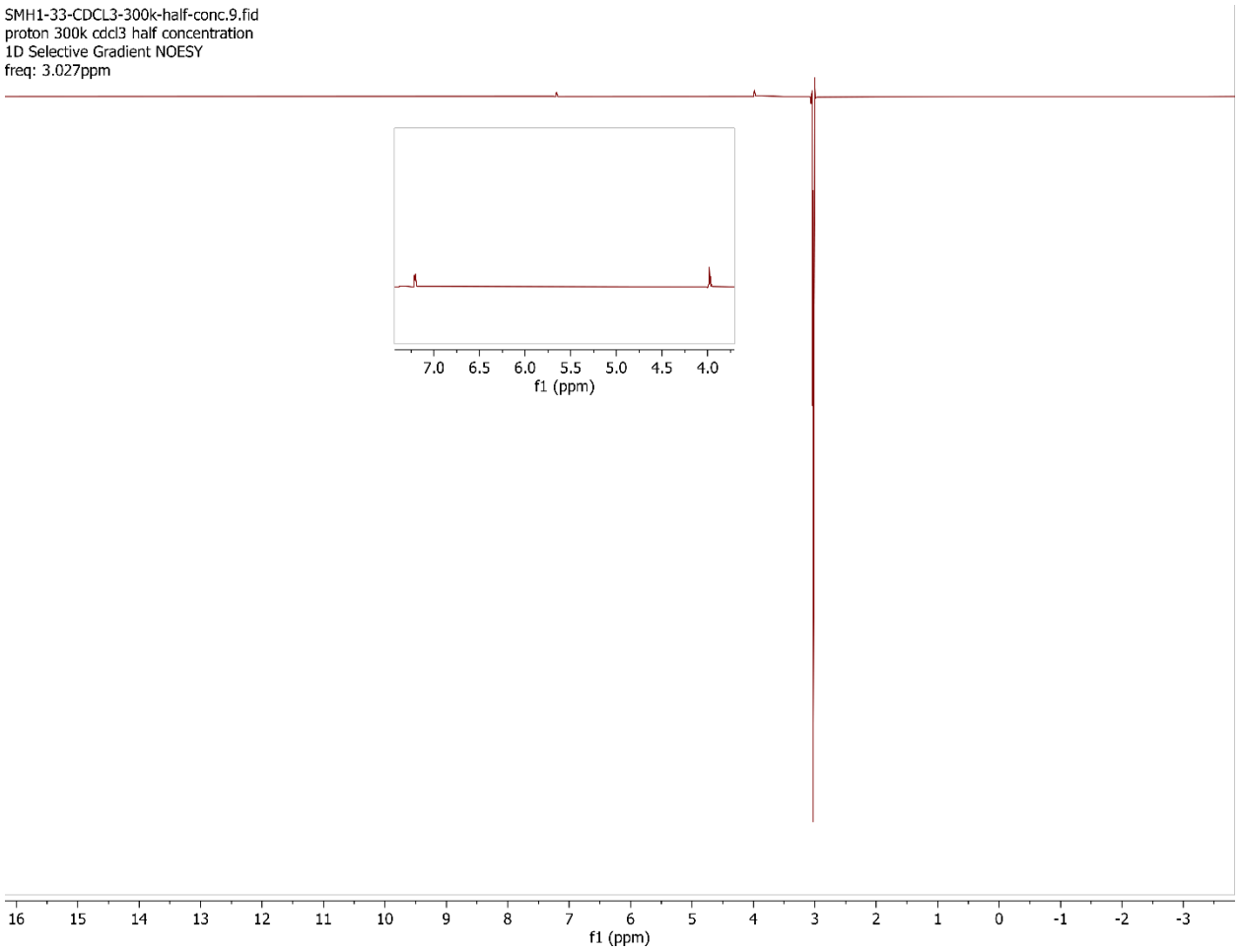

Figure B.30 Signal observed when 3.027 ppm peak probed

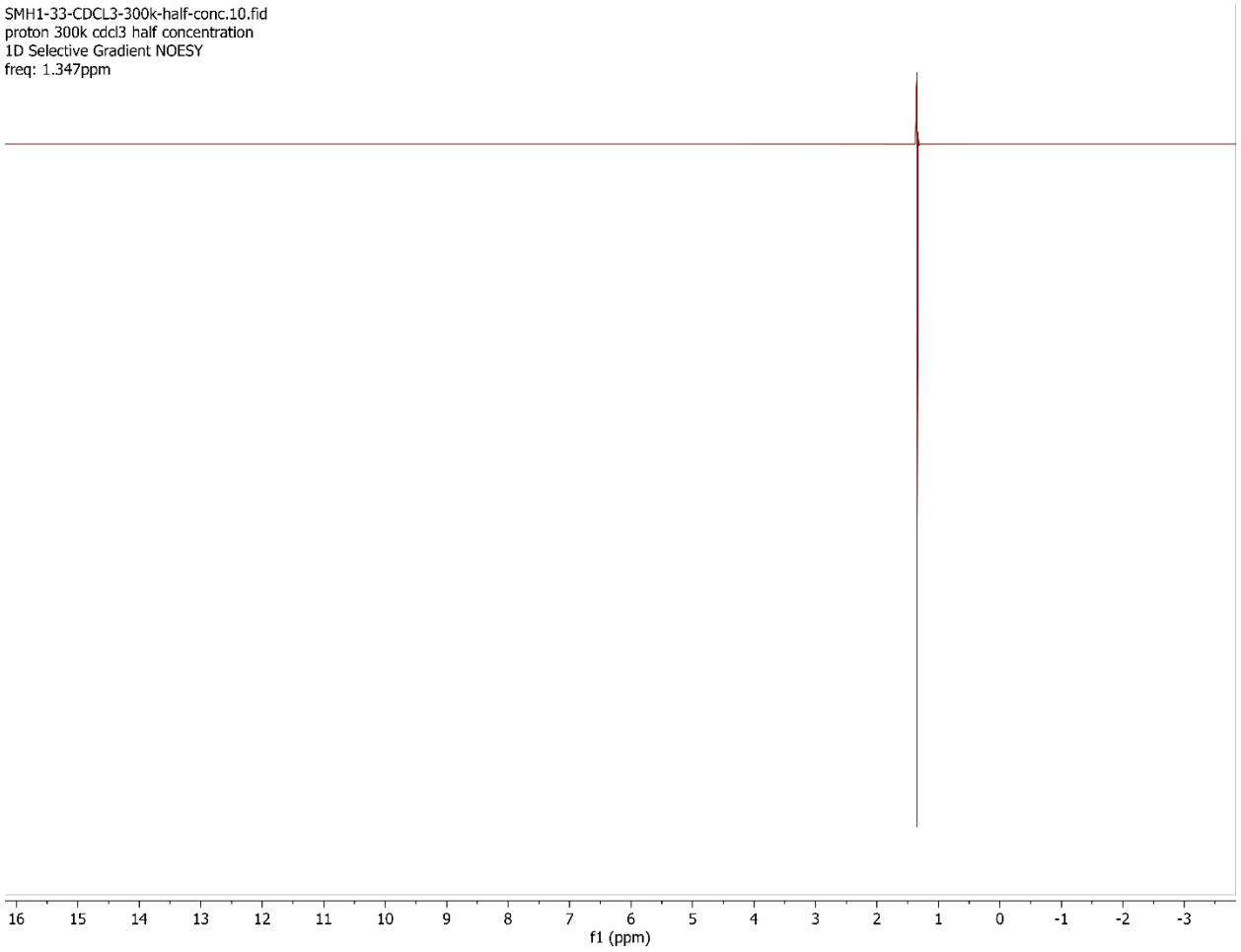

Figure B.31 Signal observed when 1.347 ppm peak probed

APPENDIX C

SUPPORTING INFORMATION FOR CHAPTER 4

^{1}H NMR, ^{13}C NMR and ^{19}F NMR Spectrum of all compounds

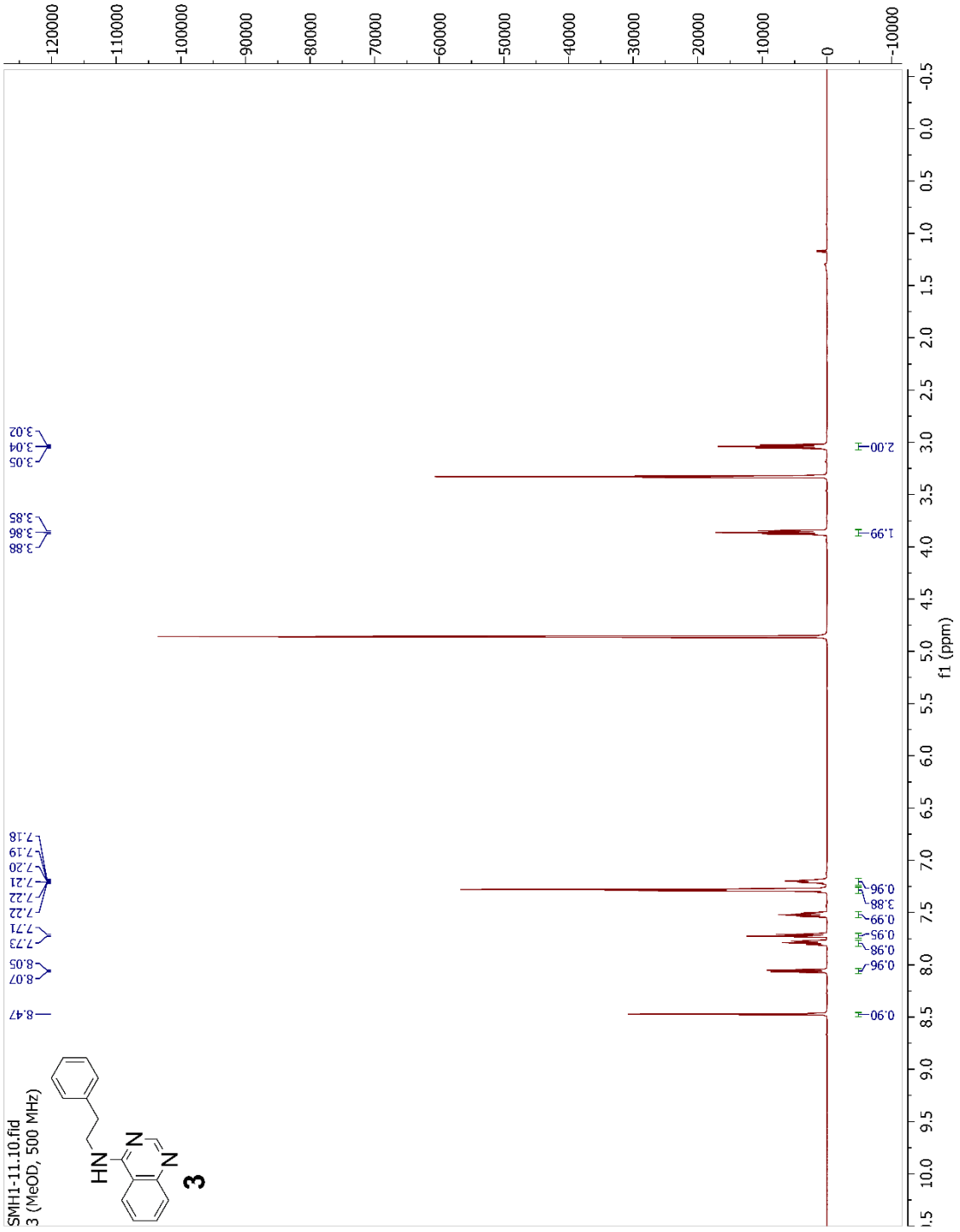

Figure C.1 ^{1}H NMR Spectrum (MeOD, 500 MHz) of **3**

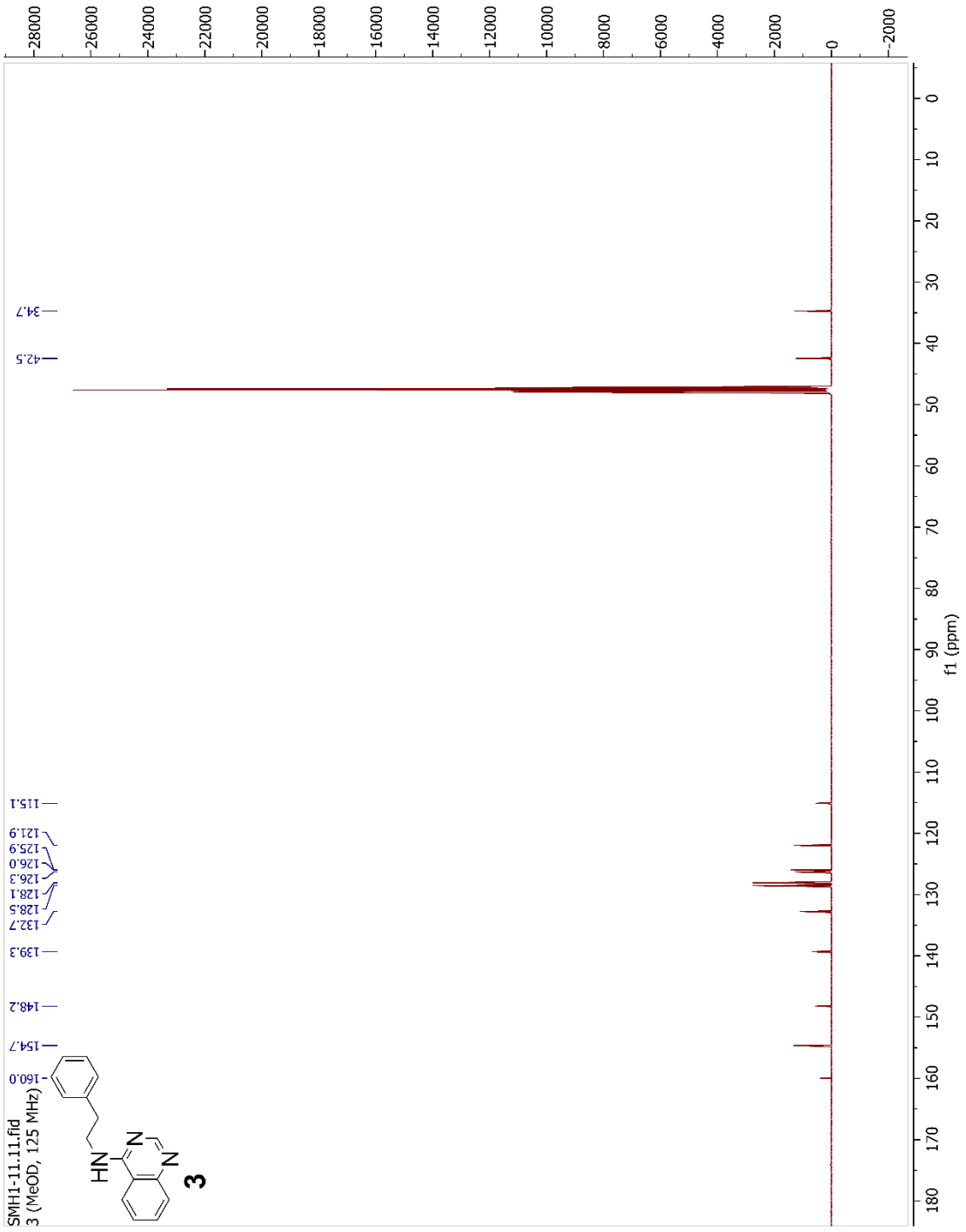

Figure C.2 ^{13}C NMR Spectrum (MeOD, 125 MHz) of **3**

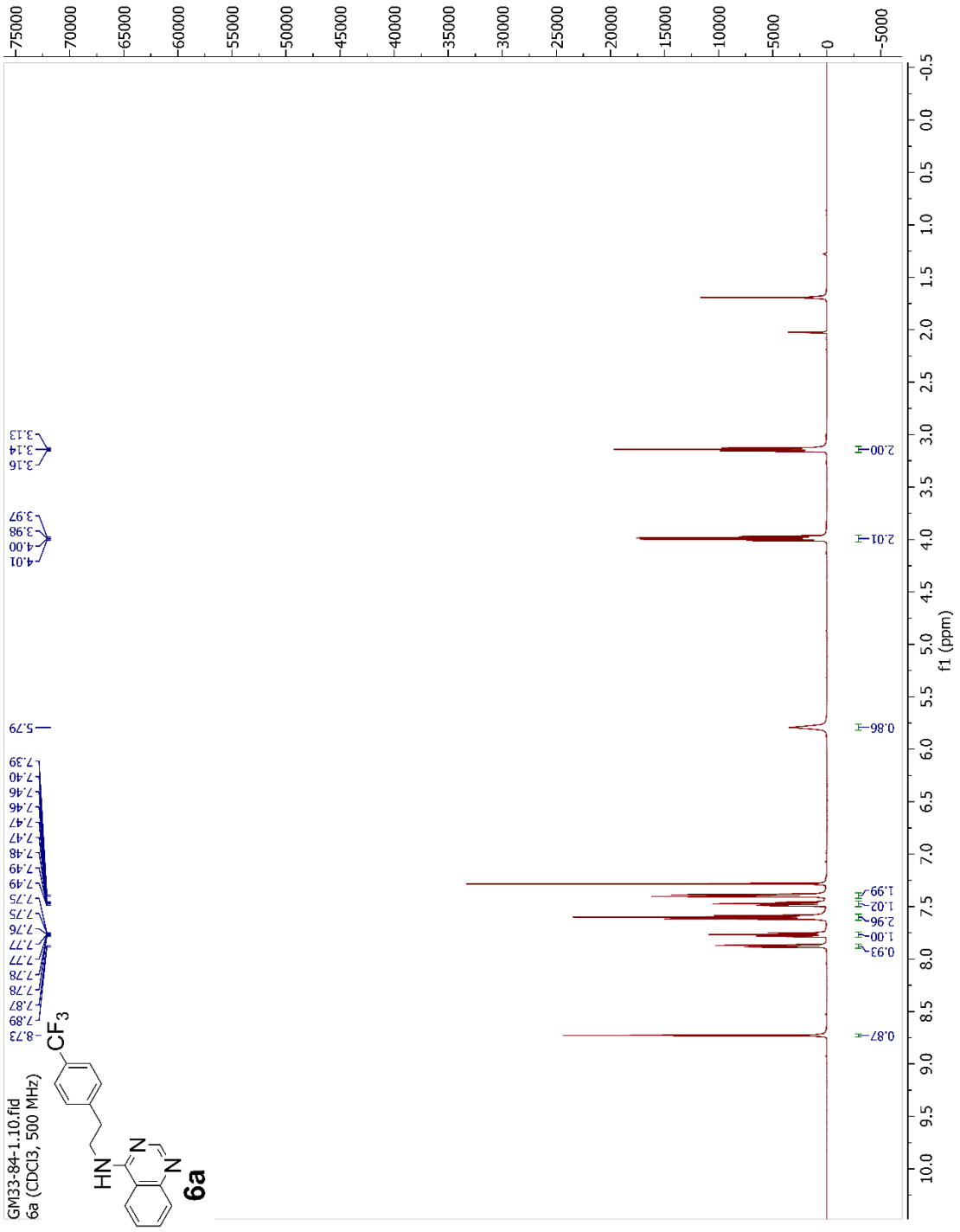

Figure C.3 ^{1}H NMR Spectrum ($CDCl_3$, 500 MHz) of **6a**

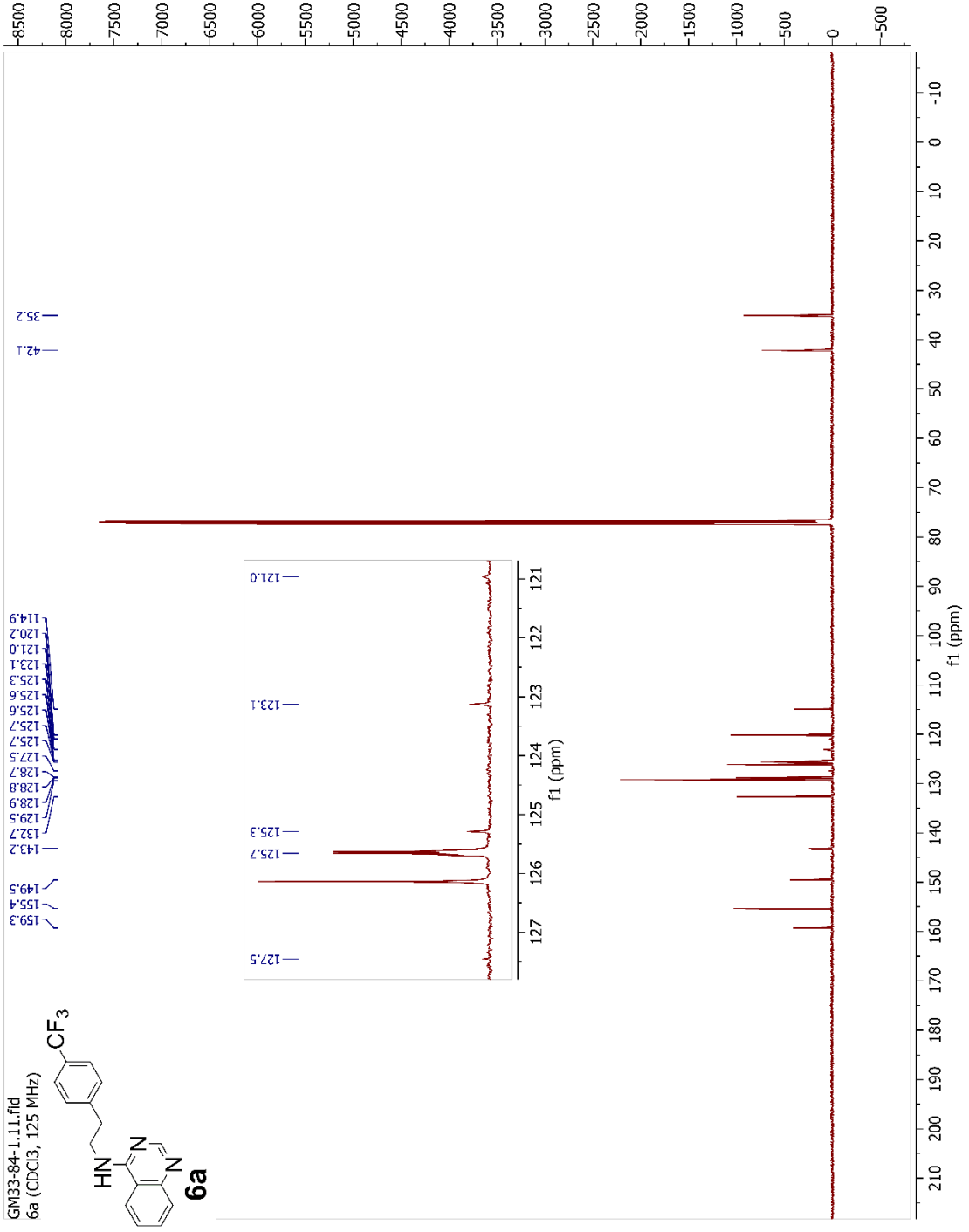

Figure C.4 ^{13}C NMR Spectrum ($CDCl_3$, 125 MHz) of **6a**

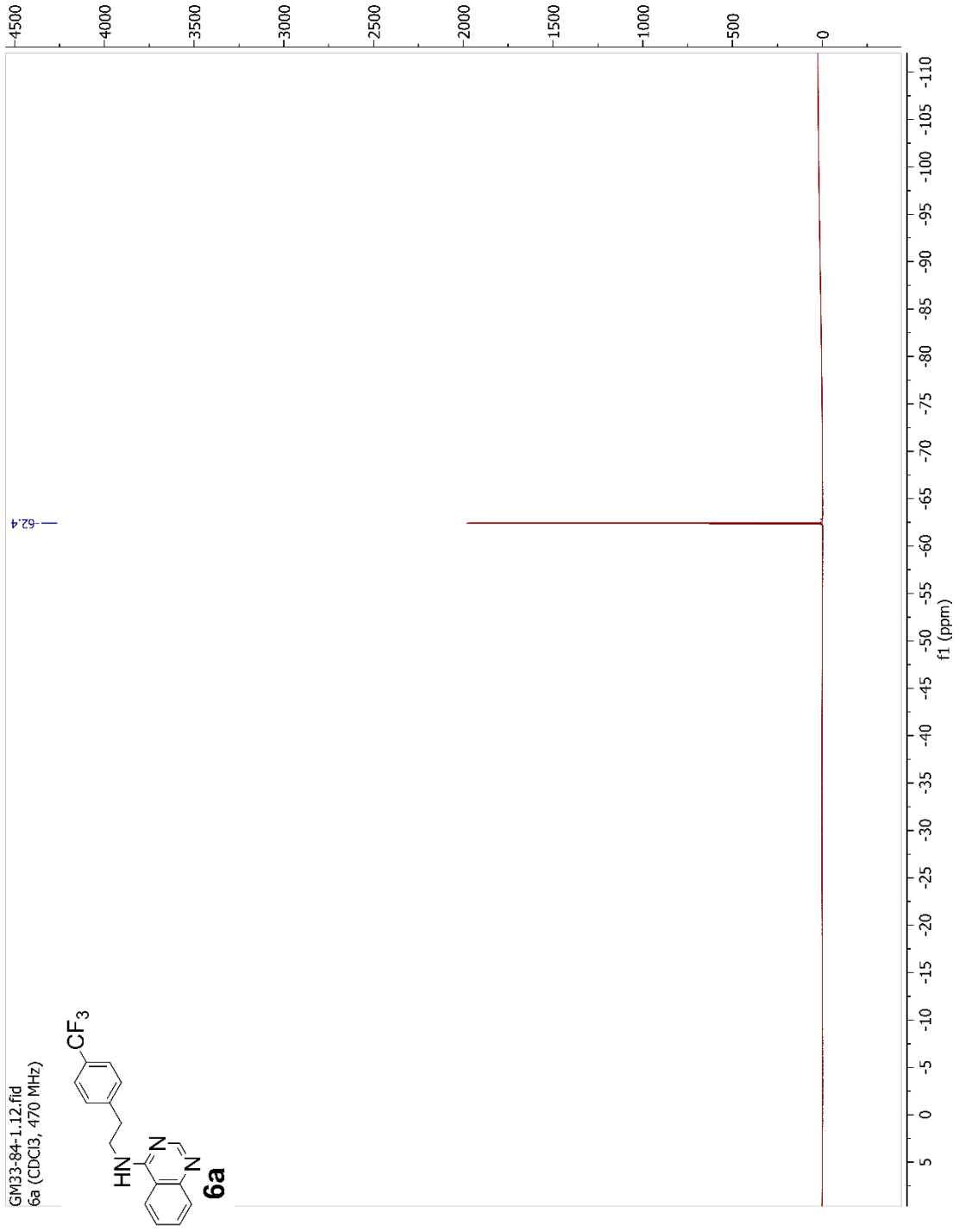

Figure C.5 ^{19}F NMR Spectrum ($CDCl_3$, 470 MHz) of **6a**

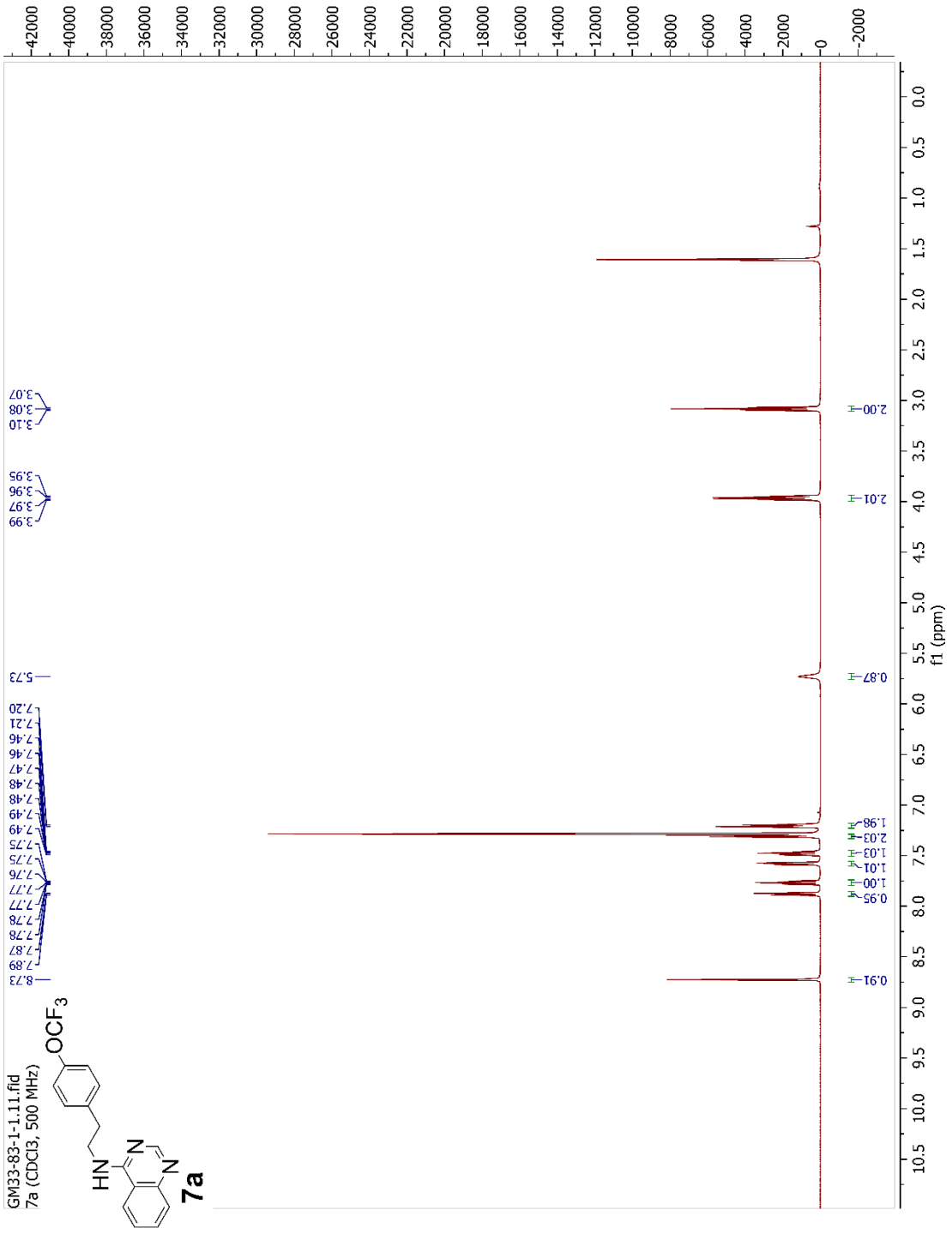

Figure C.6 ^{1}H NMR Spectrum ($CDCl_3$, 500 MHz) of **7a**

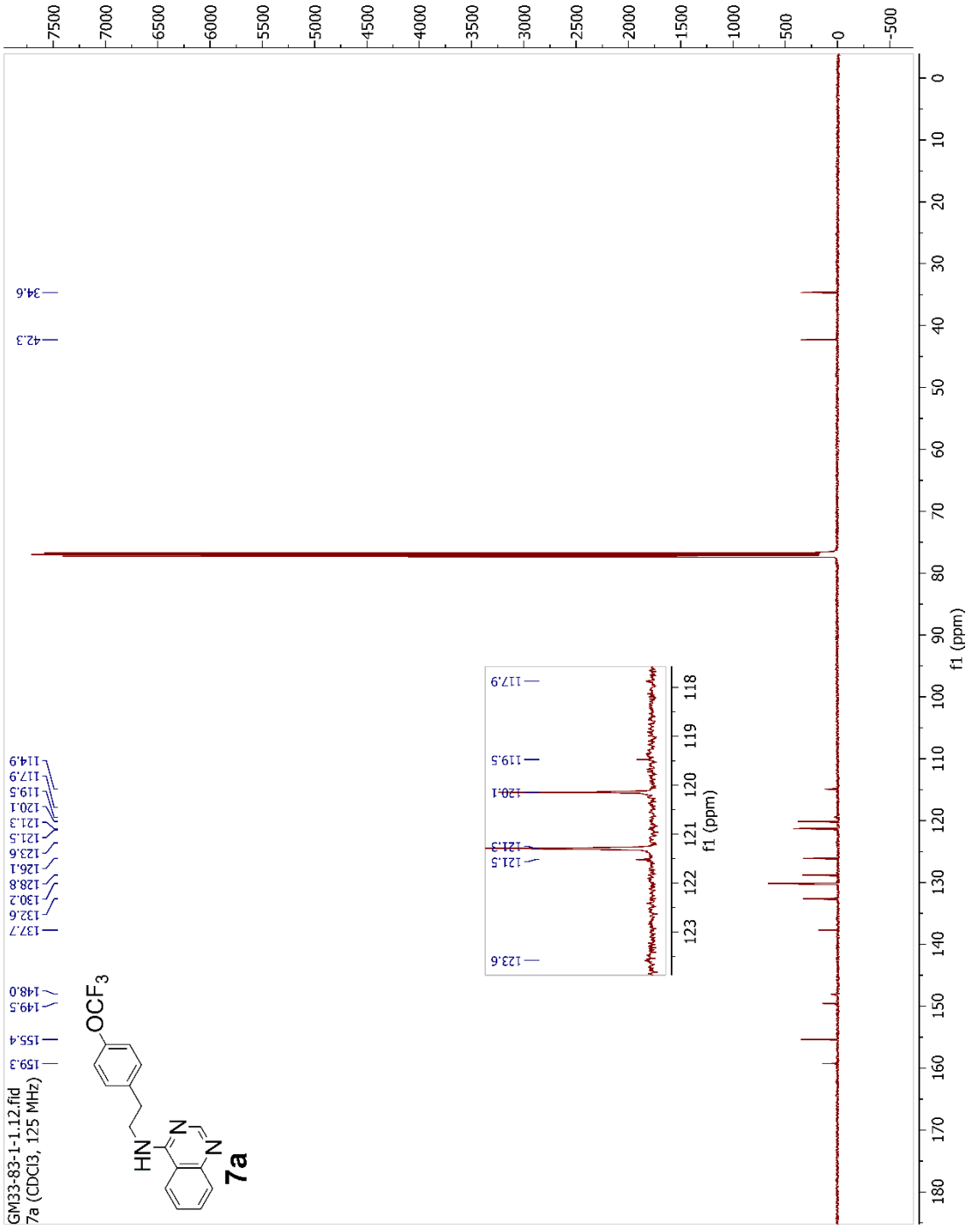

Figure C.7 ^{13}C NMR Spectrum ($CDCl_3$, 125 MHz) of **7a**

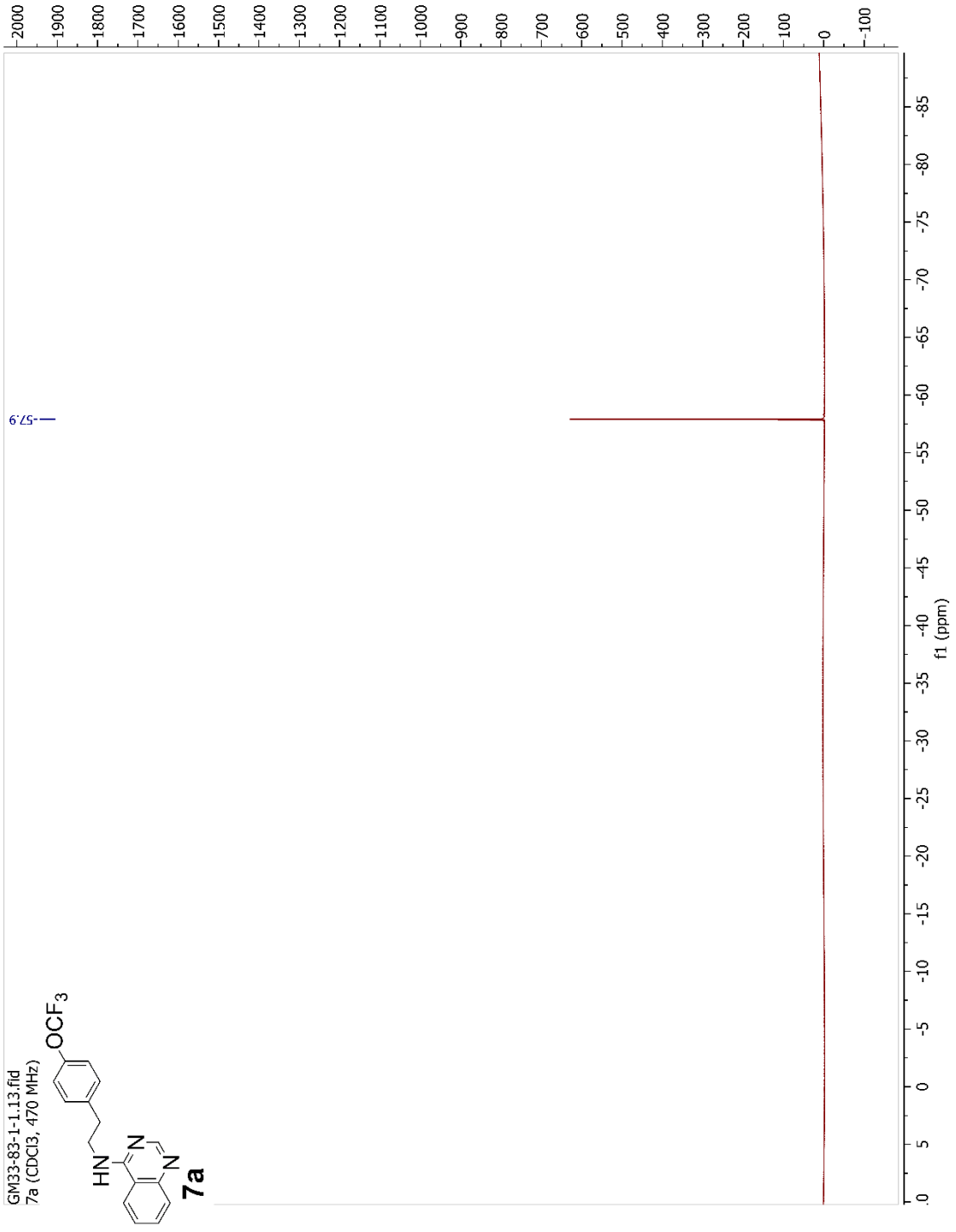

Figure C.8 ^{19}F NMR Spectrum ($CDCl_3$, 470 MHz) of **7a**

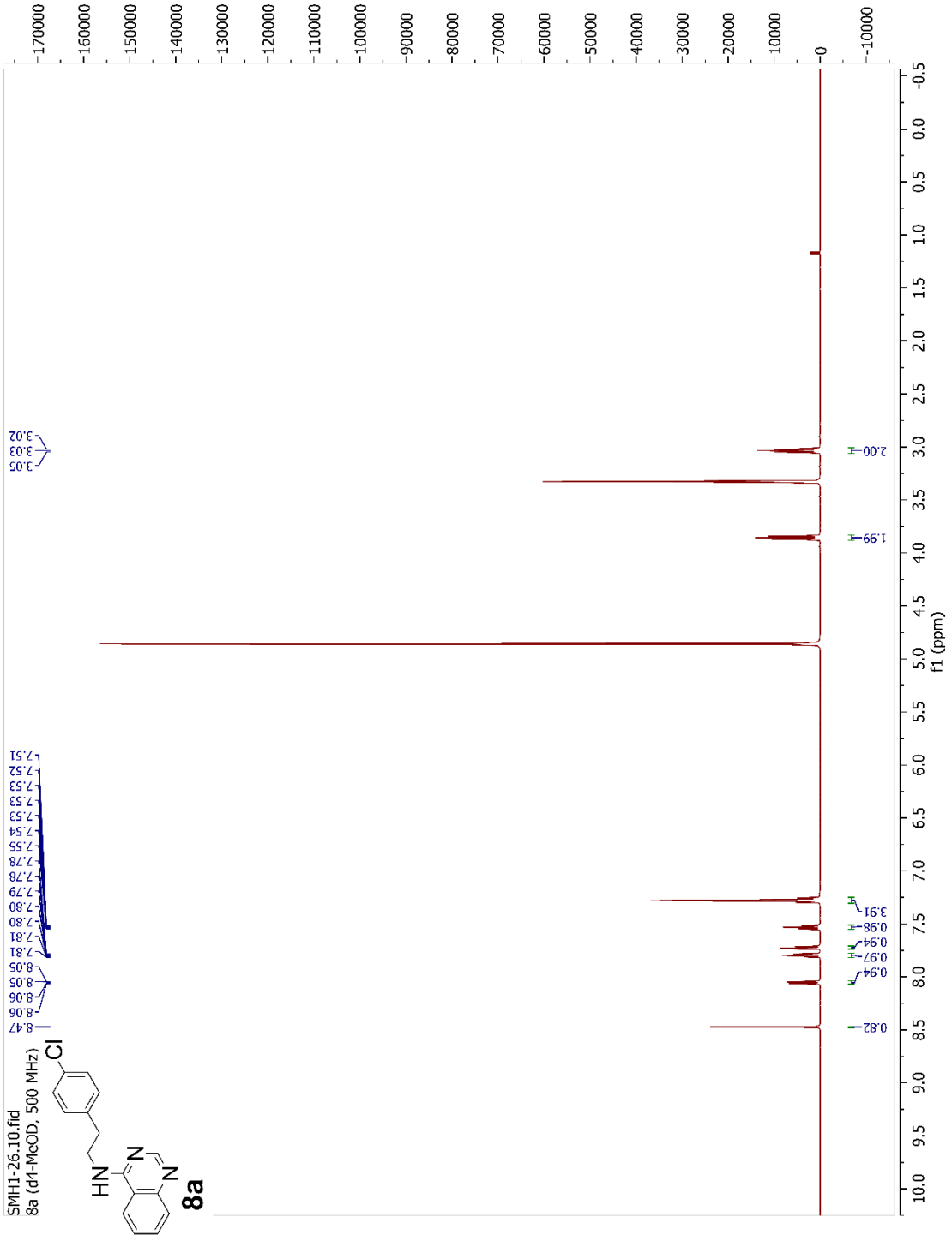

Figure C.9 ^{1}H NMR Spectrum (MeOD, 500 MHz) of **8a**

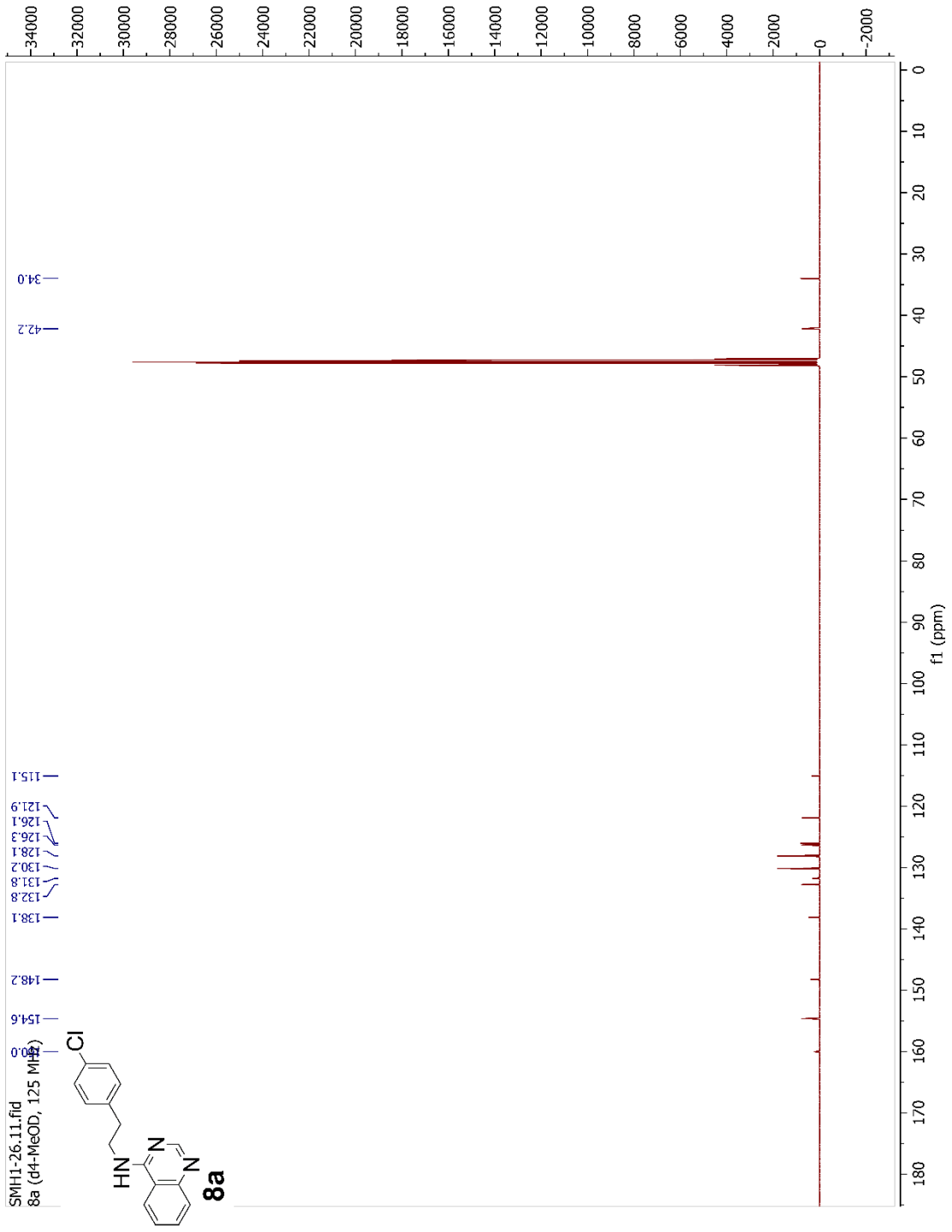

Figure C.10 ^{13}C NMR Spectrum (MeOD, 125 MHz) of **8a**

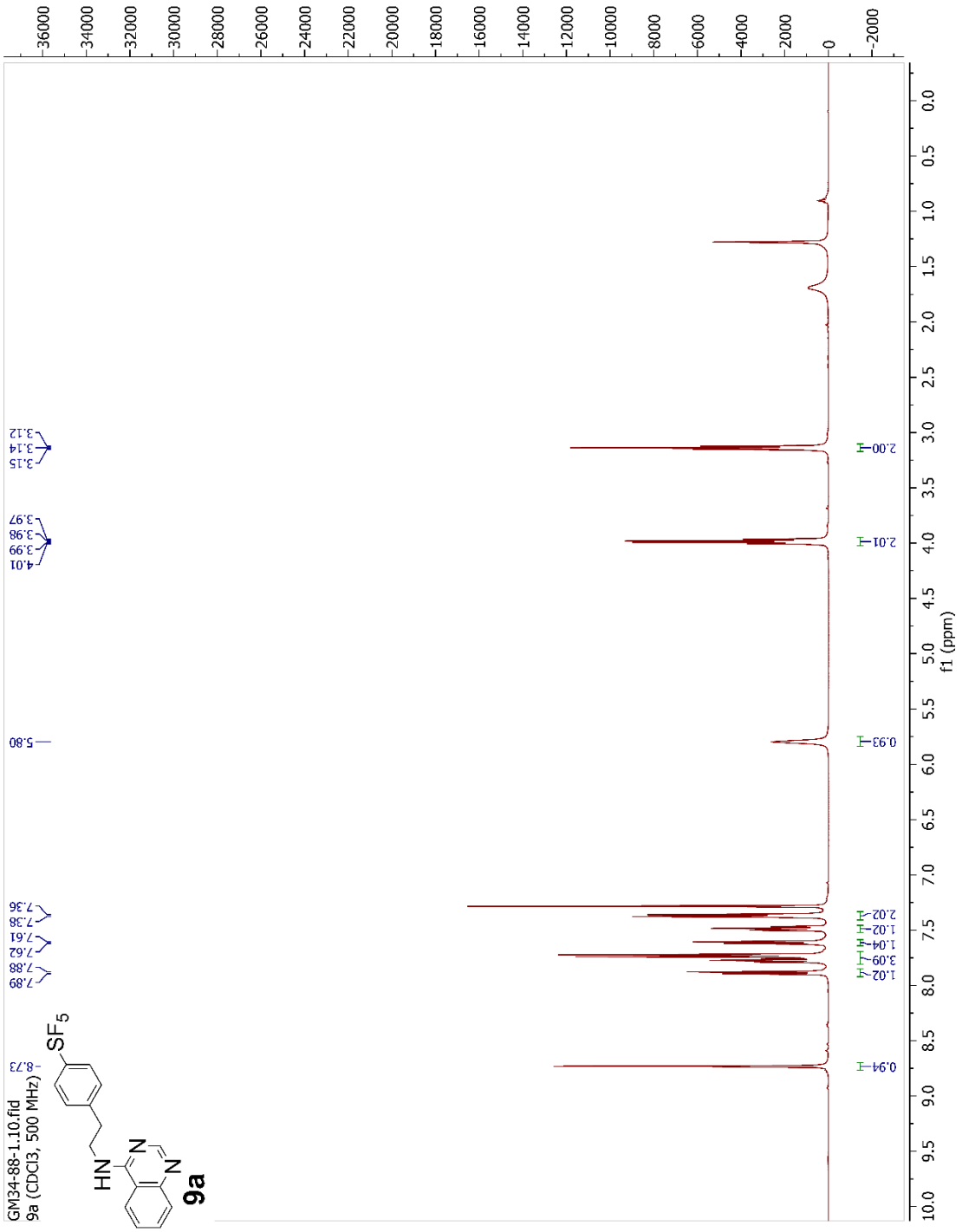

Figure C.11 ^{1}H NMR Spectrum ($CDCl_3$, 500 MHz) of **9a**

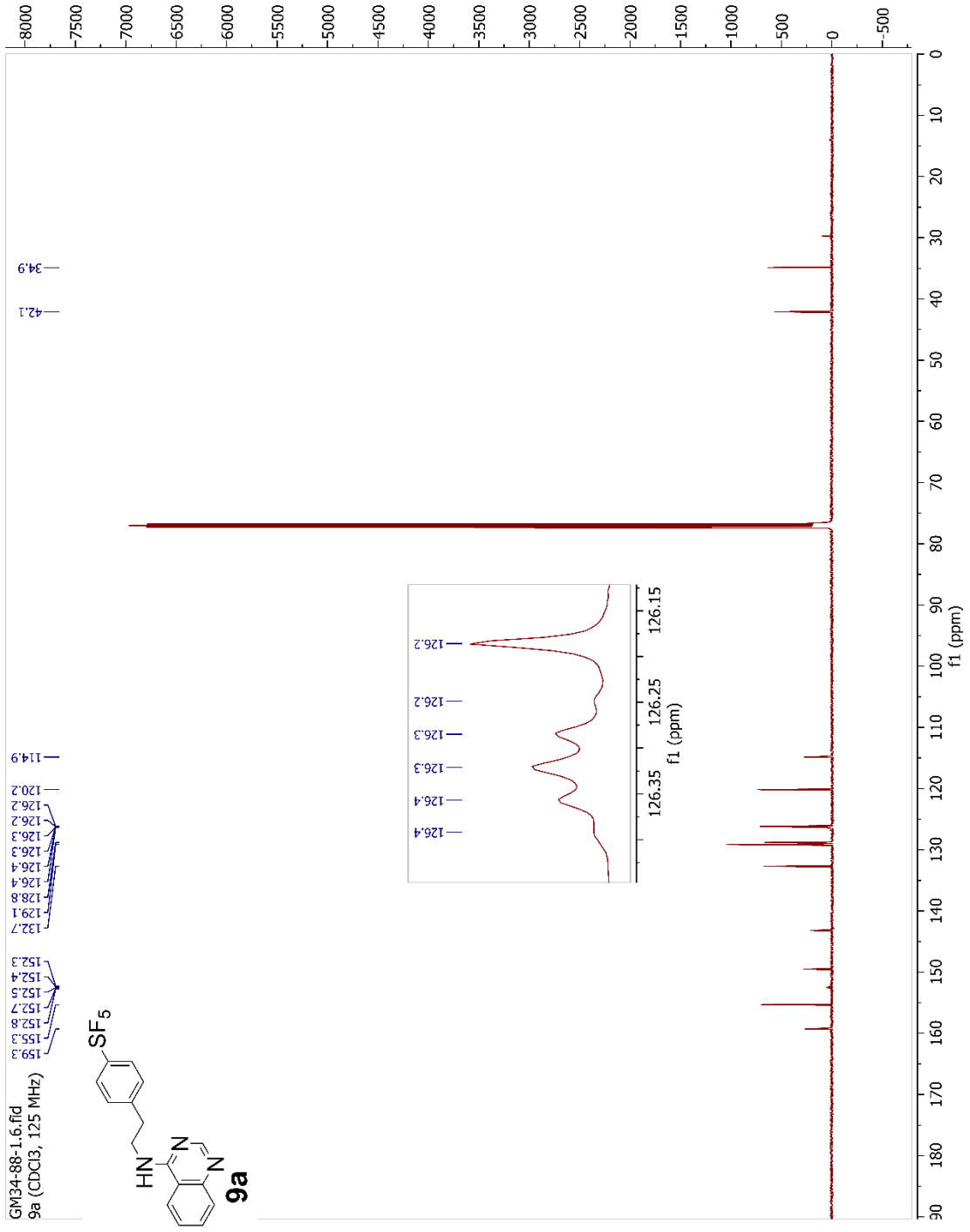

Figure C.12 ^{13}C NMR Spectrum ($CDCl_3$, 125 MHz) of **9a**

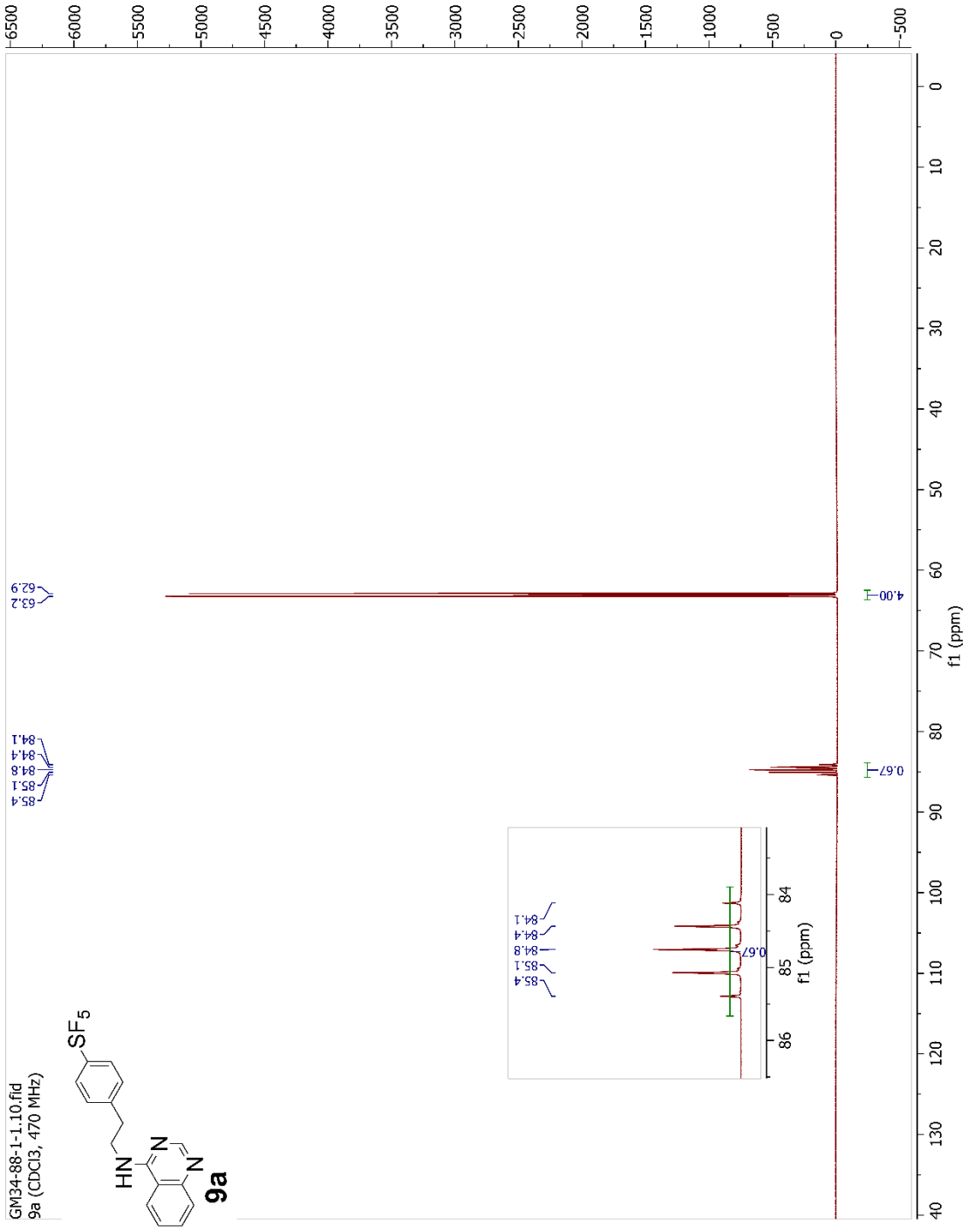

Figure C.13 ^{19}F NMR Spectrum ($CDCl_3$, 470 MHz) of **9a**

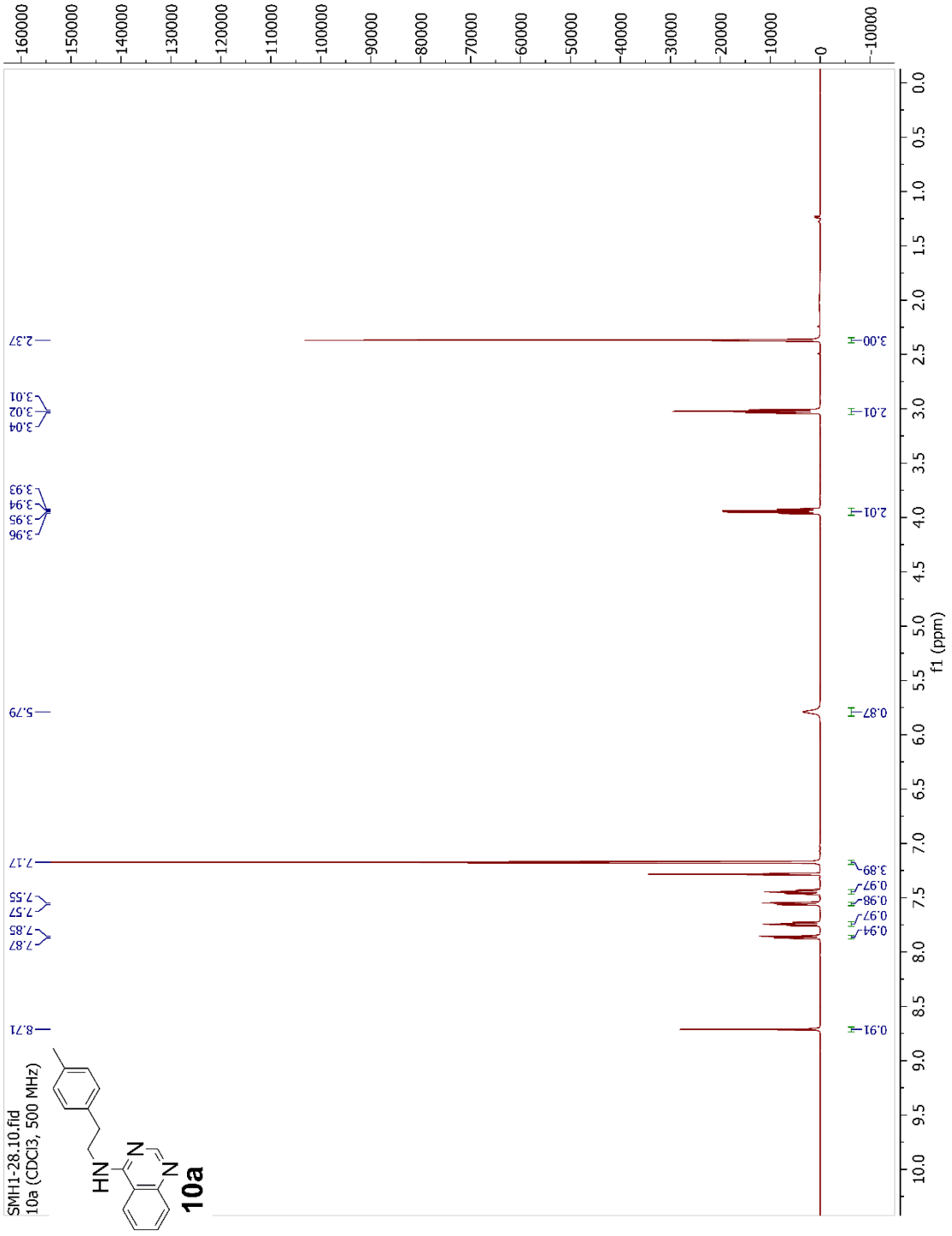

Figure C.14 ^{1}H NMR Spectrum ($CDCl_3$, 500 MHz) of **10a**

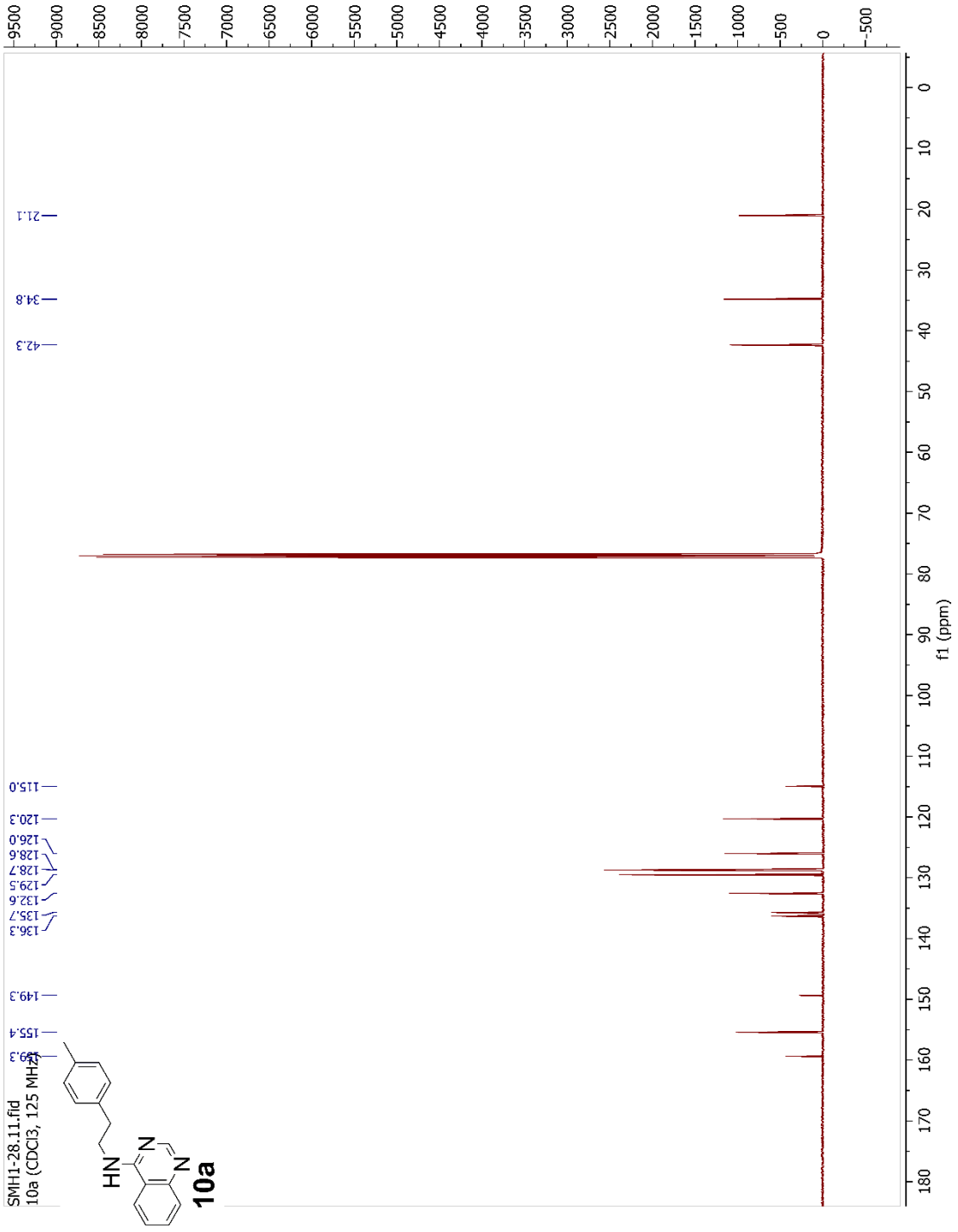

Figure C.15 ^{13}C NMR Spectrum ($CDCl_3$, 125 MHz) of **10a**

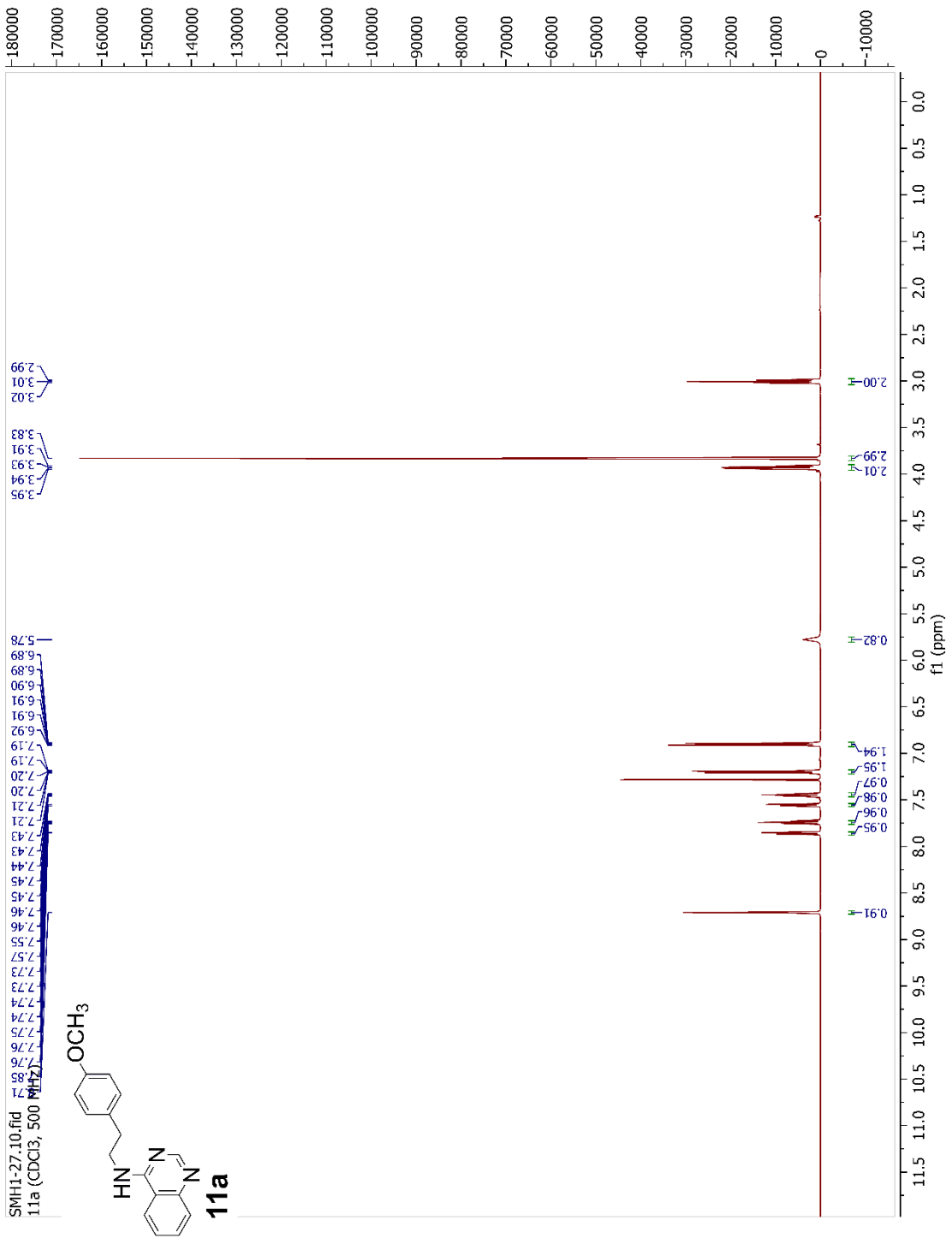

Figure C.16 ^{1}H NMR Spectrum ($CDCl_3$, 500 MHz) of **11a**

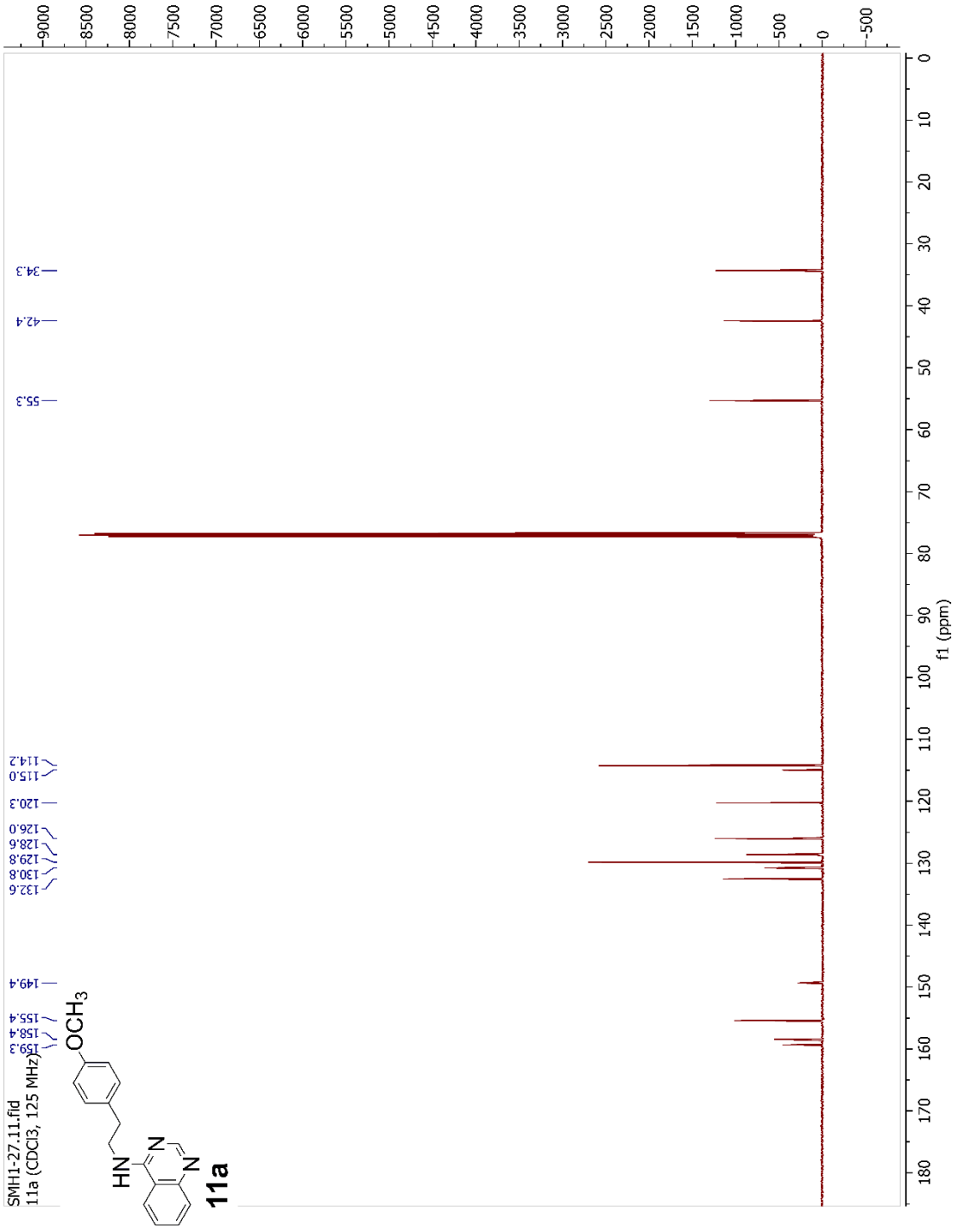

Figure C.17 ^{13}C NMR Spectrum ($CDCl_3$, 125 MHz) of **11a**

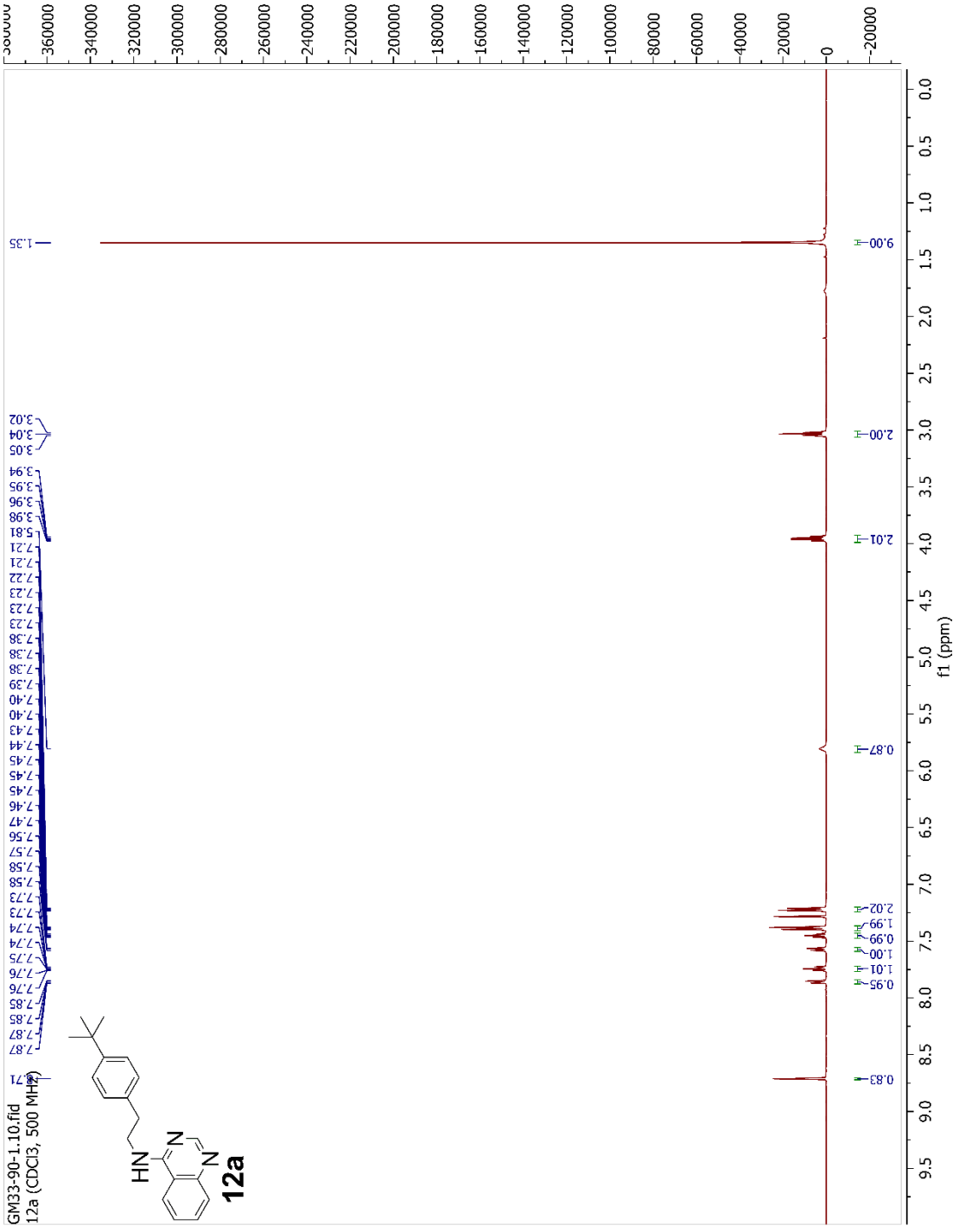

Figure C.18 ^{1}H NMR Spectrum ($CDCl_3$, 500 MHz) of **12a**

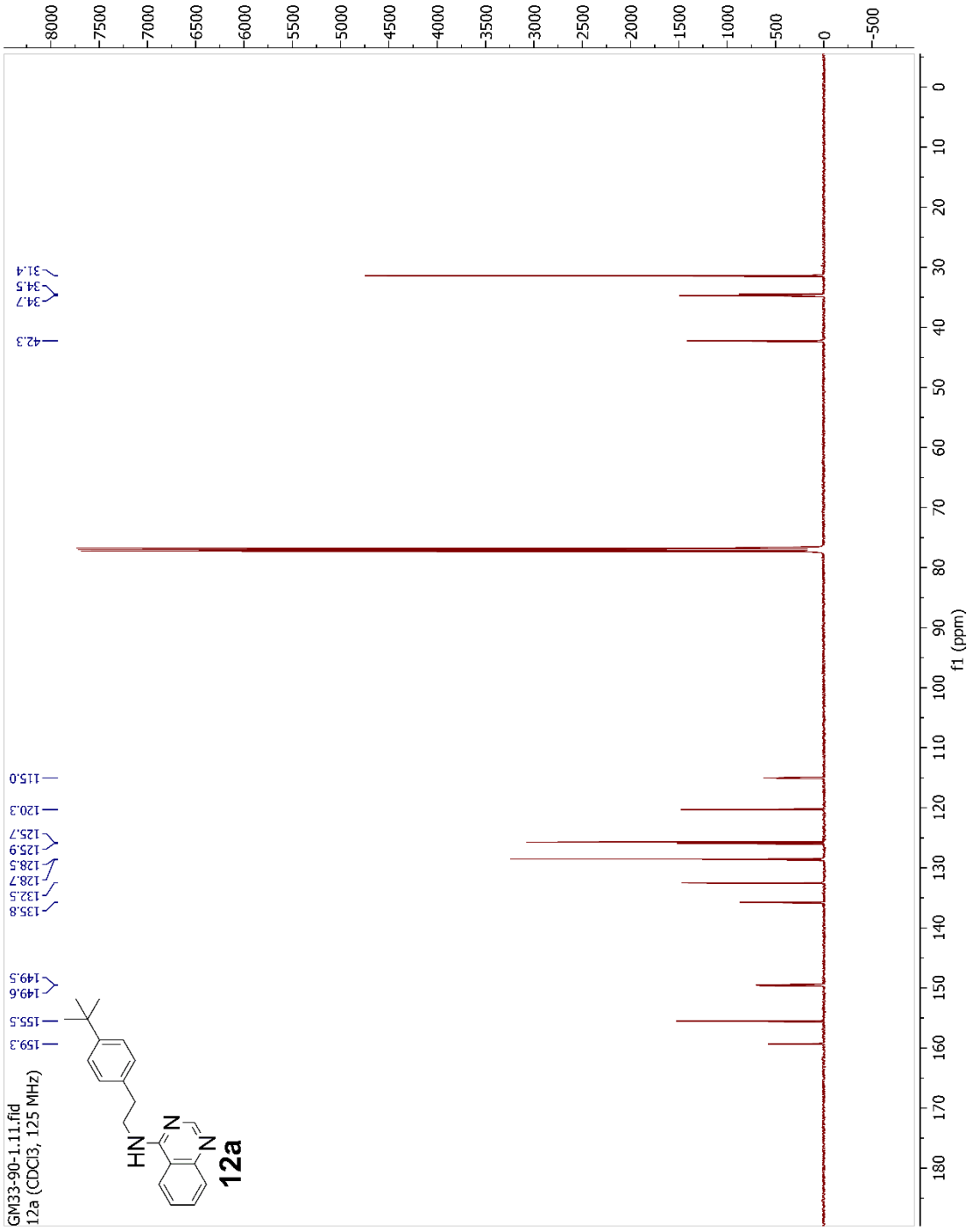

Figure C.19 ^{13}C NMR Spectrum ($CDCl_3$, 125 MHz) of **12a**

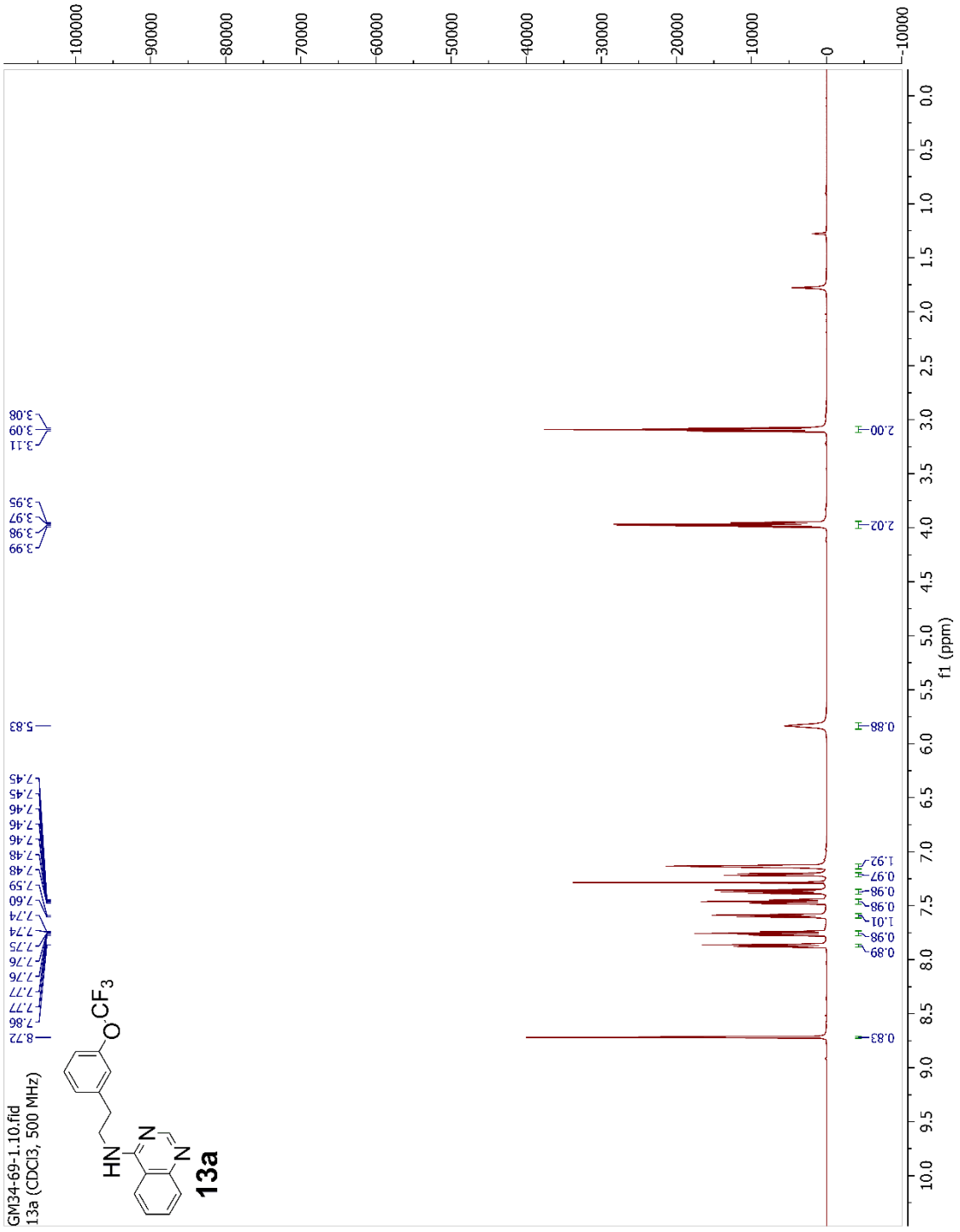

Figure C.20 ^{1}H NMR Spectrum ($CDCl_3$, 500 MHz) of **13a**

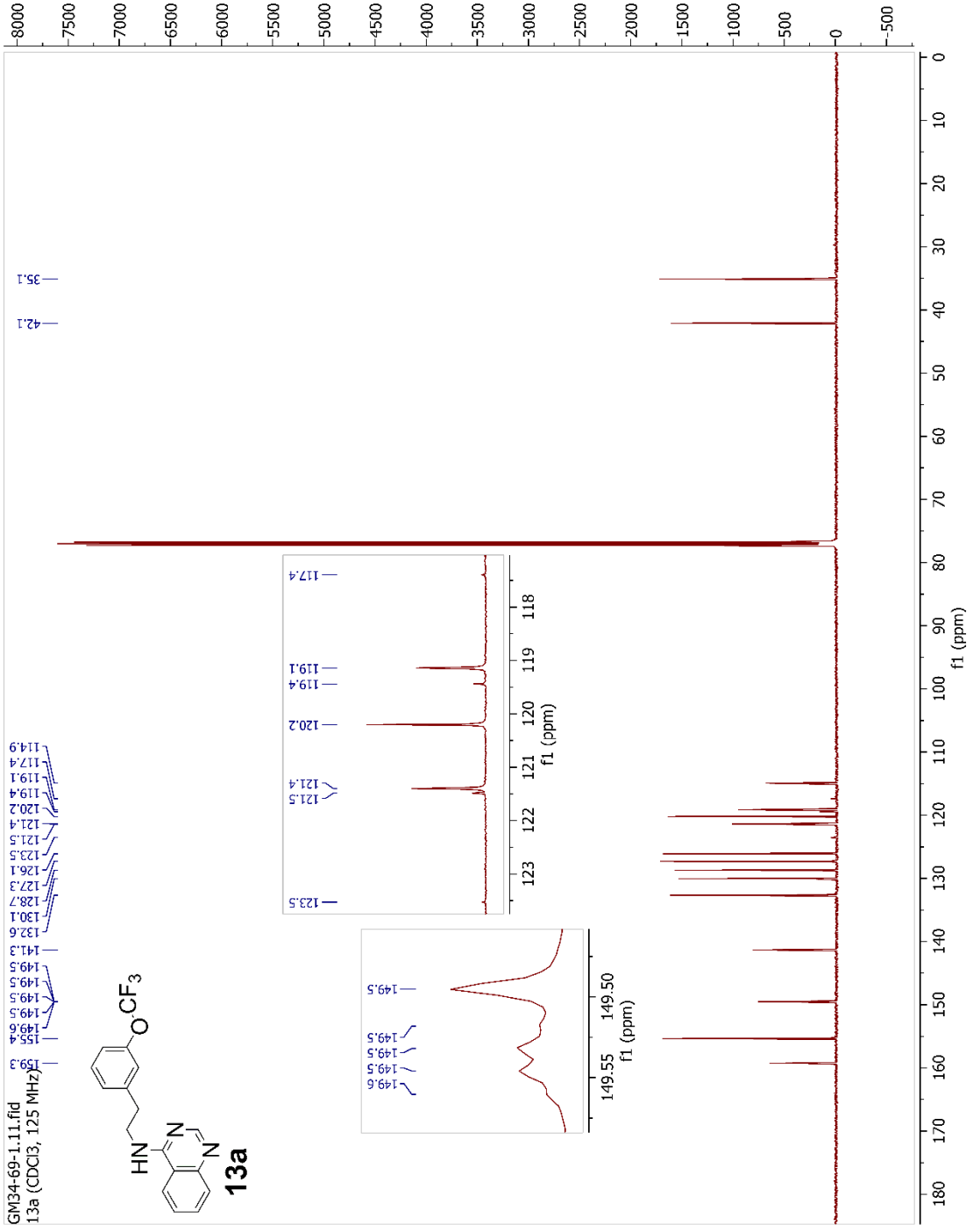

Figure C.21 ^{13}C NMR Spectrum ($CDCl_3$, 125 MHz) of **13a**

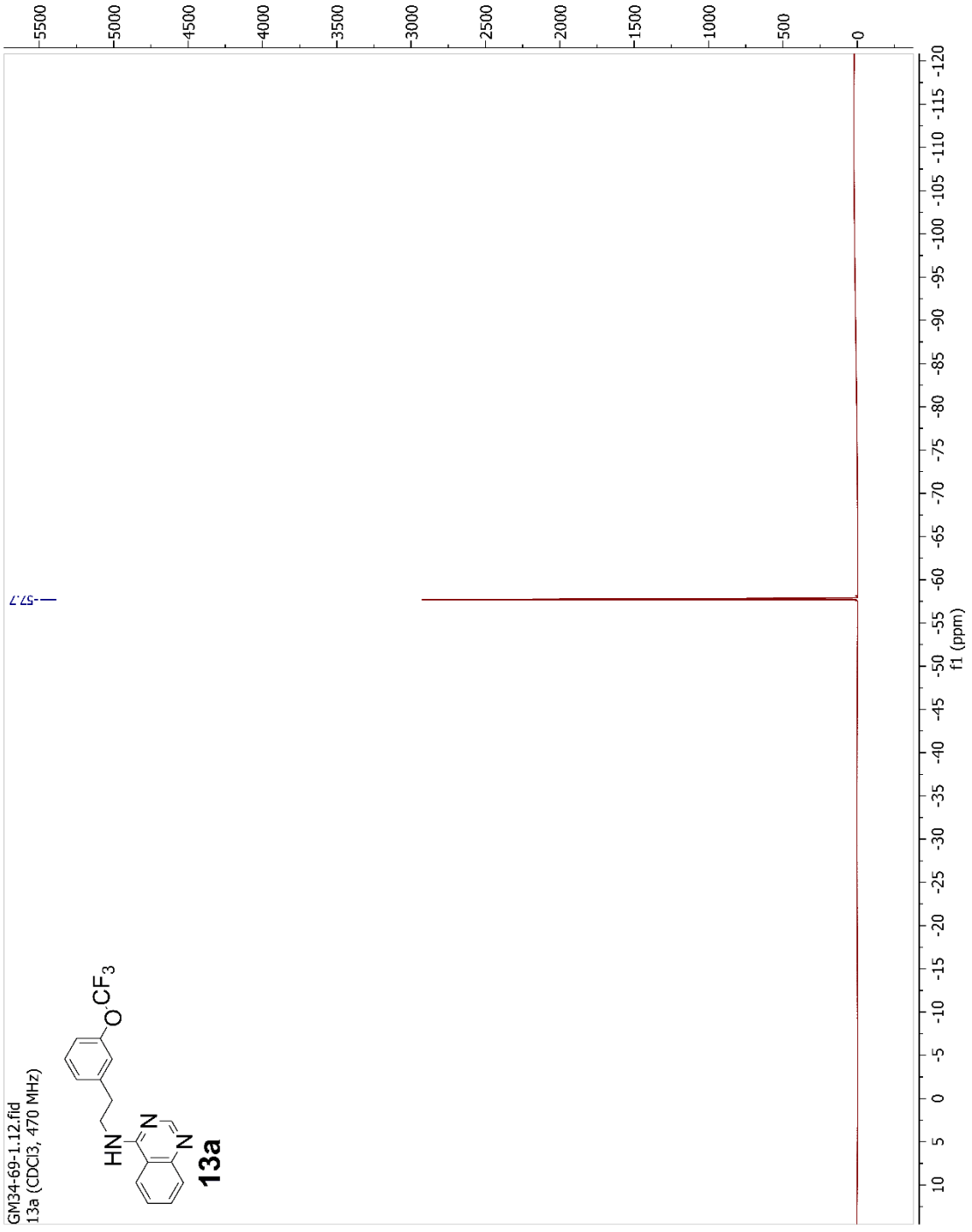

Figure C.22 ^{19}F NMR Spectrum ($CDCl_3$, 470 MHz) of **13a**

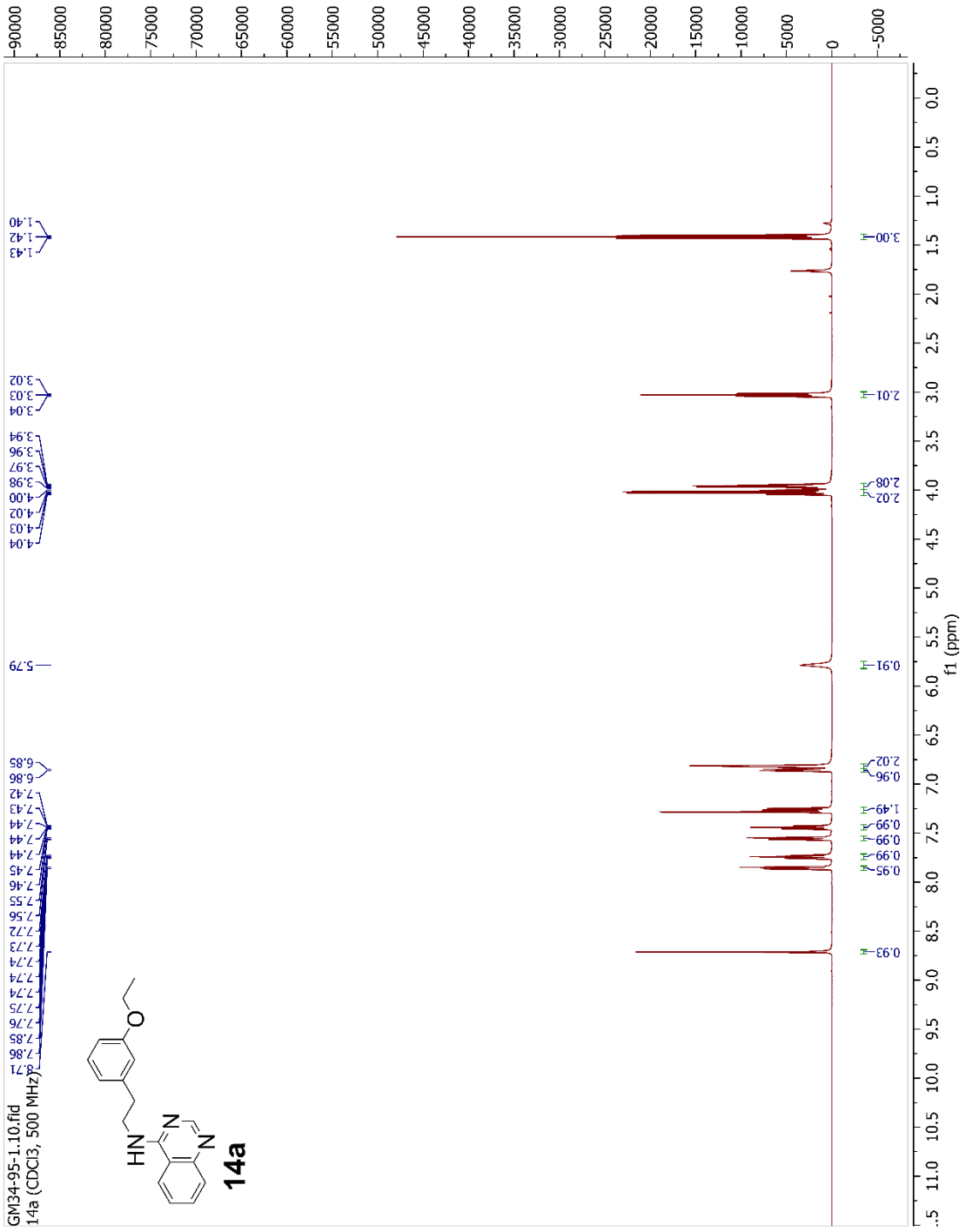

Figure C.23 ^{1}H NMR Spectrum ($CDCl_3$, 500 MHz) of **14a**

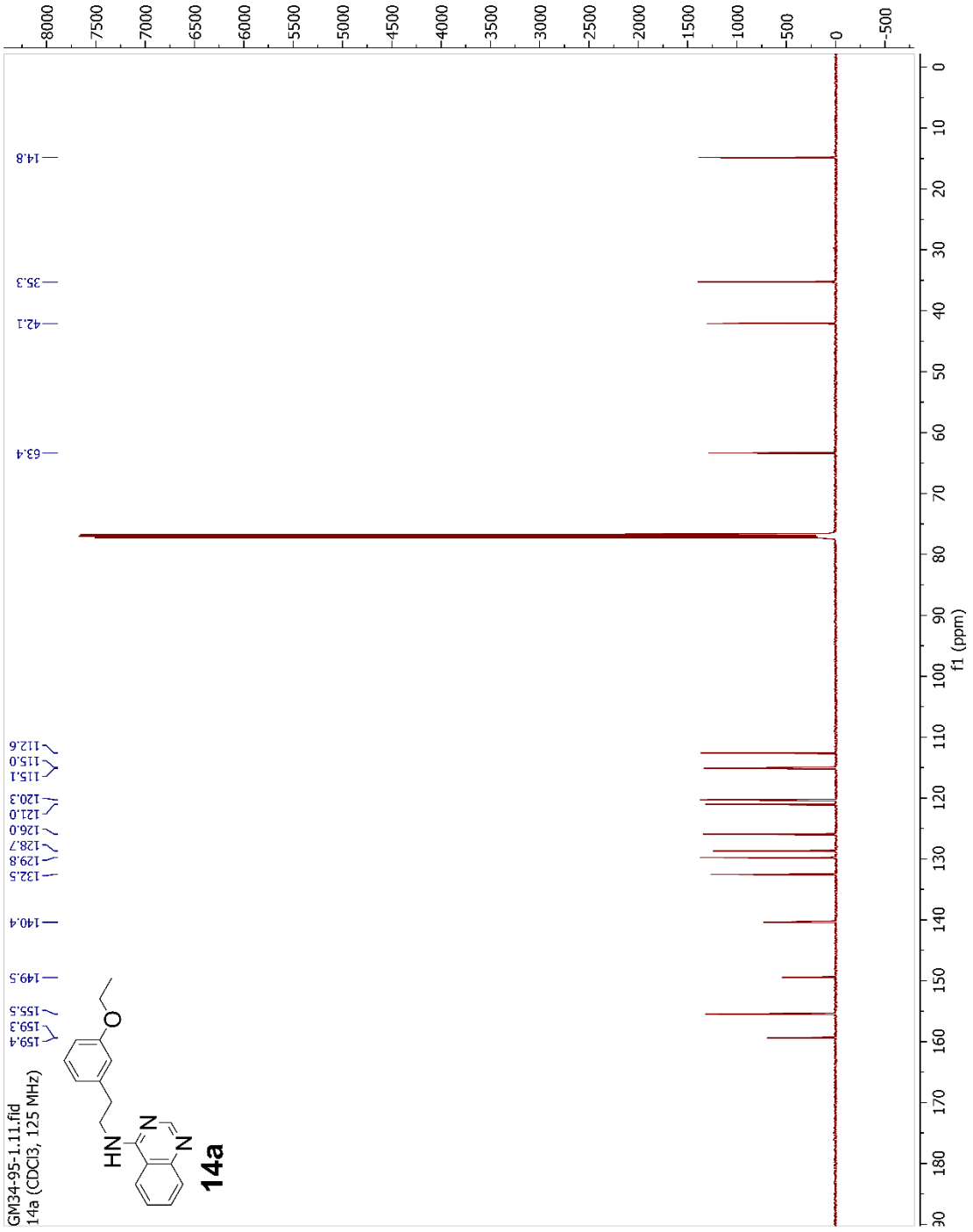

Figure C.24 ^{13}C NMR Spectrum ($CDCl_3$, 125 MHz) of **14a**

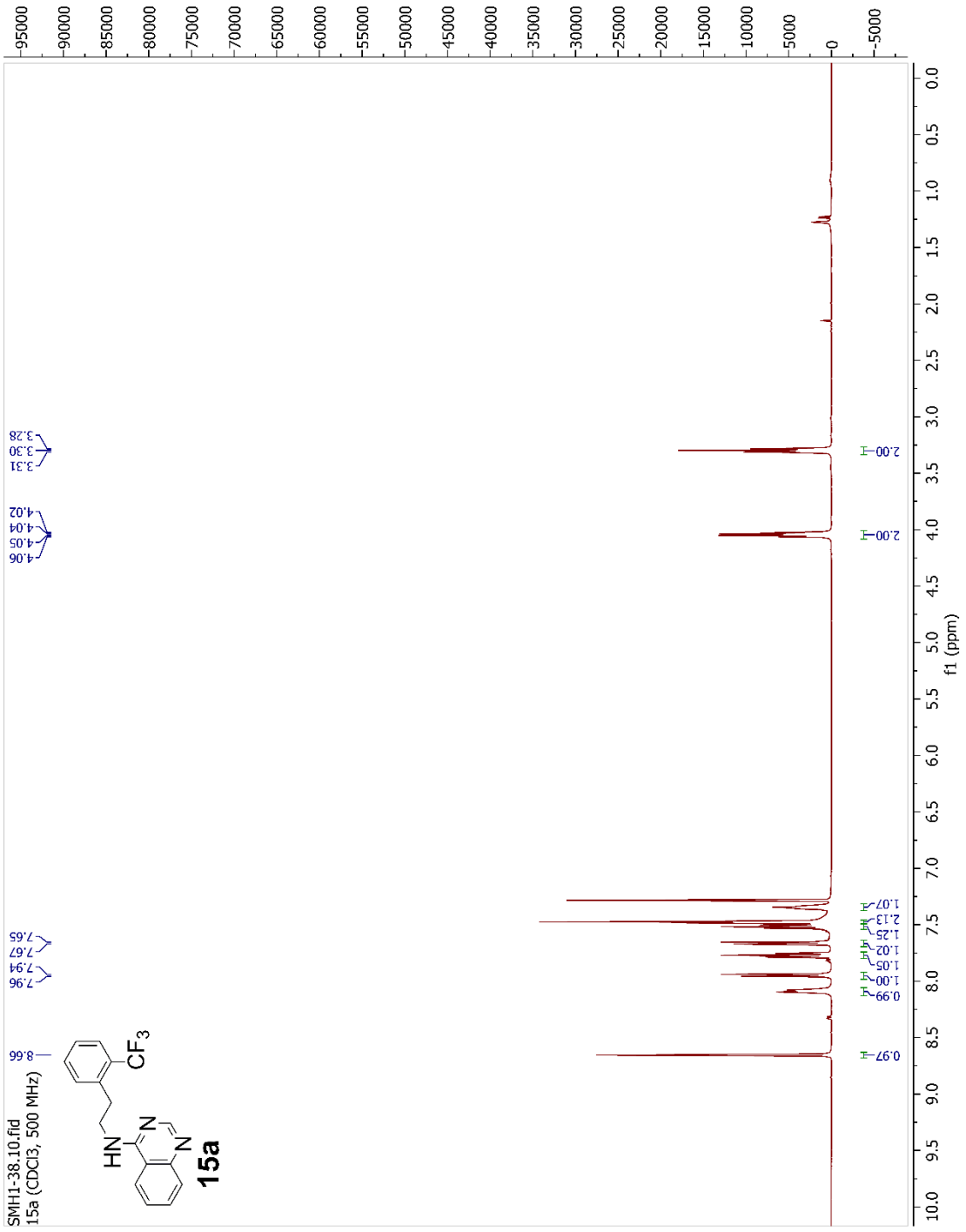

Figure C.25 ^{1}H NMR Spectrum ($CDCl_3$, 500 MHz) of **15a**

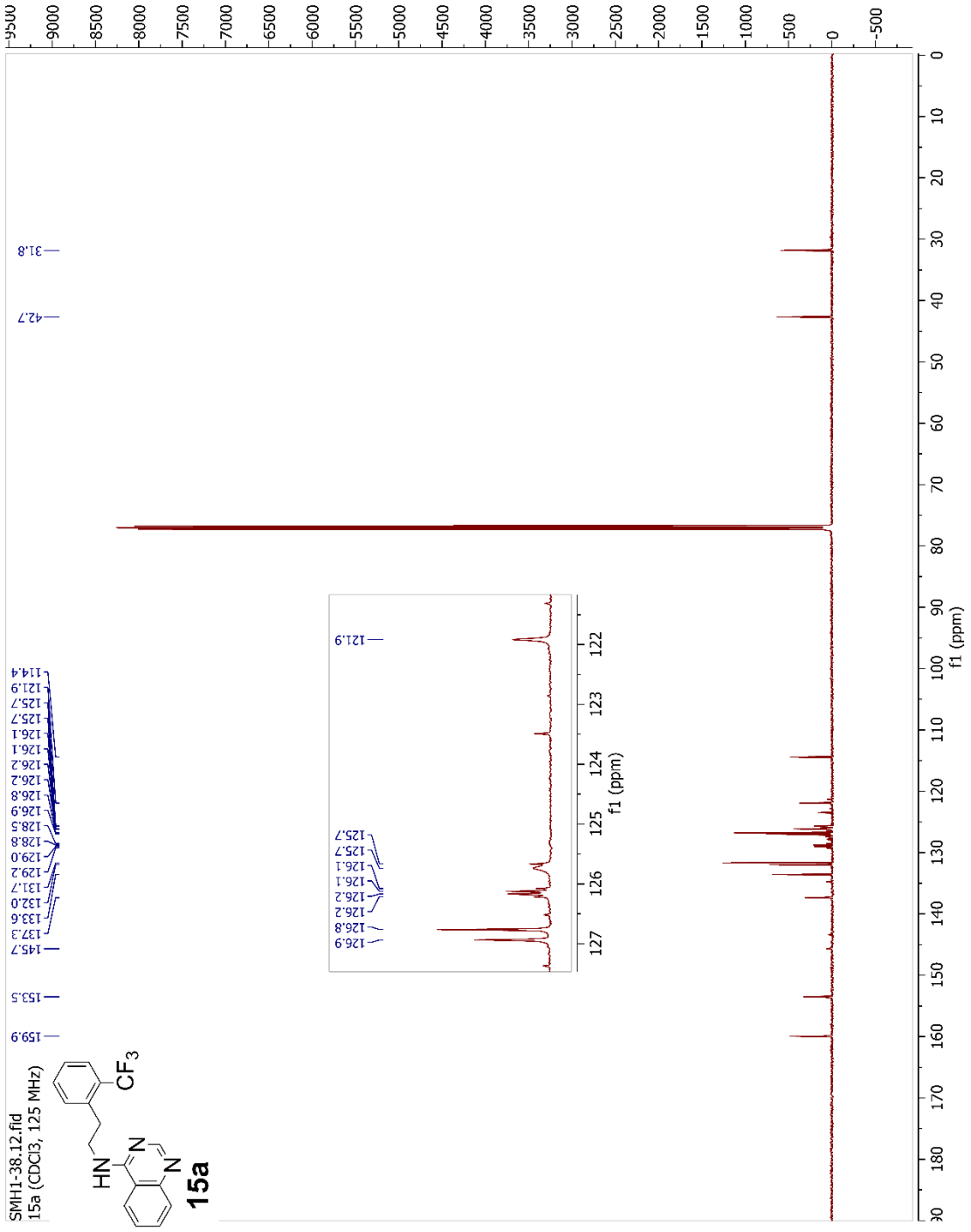

Figure C.26 ^{13}C NMR Spectrum ($CDCl_3$, 125 MHz) of **15a**

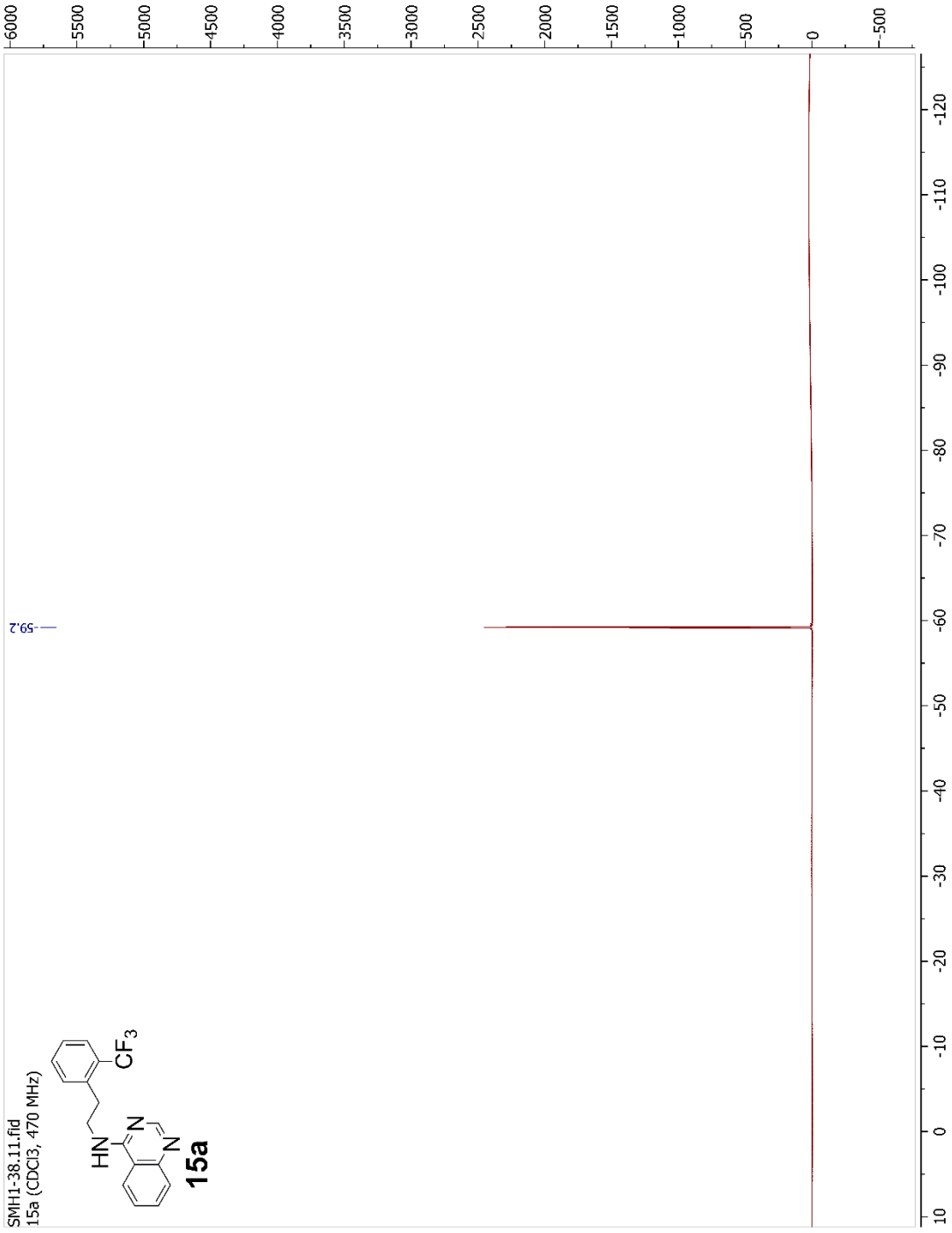

Figure C.27 ^{19}F NMR Spectrum ($CDCl_3$, 470 MHz) of **15a**

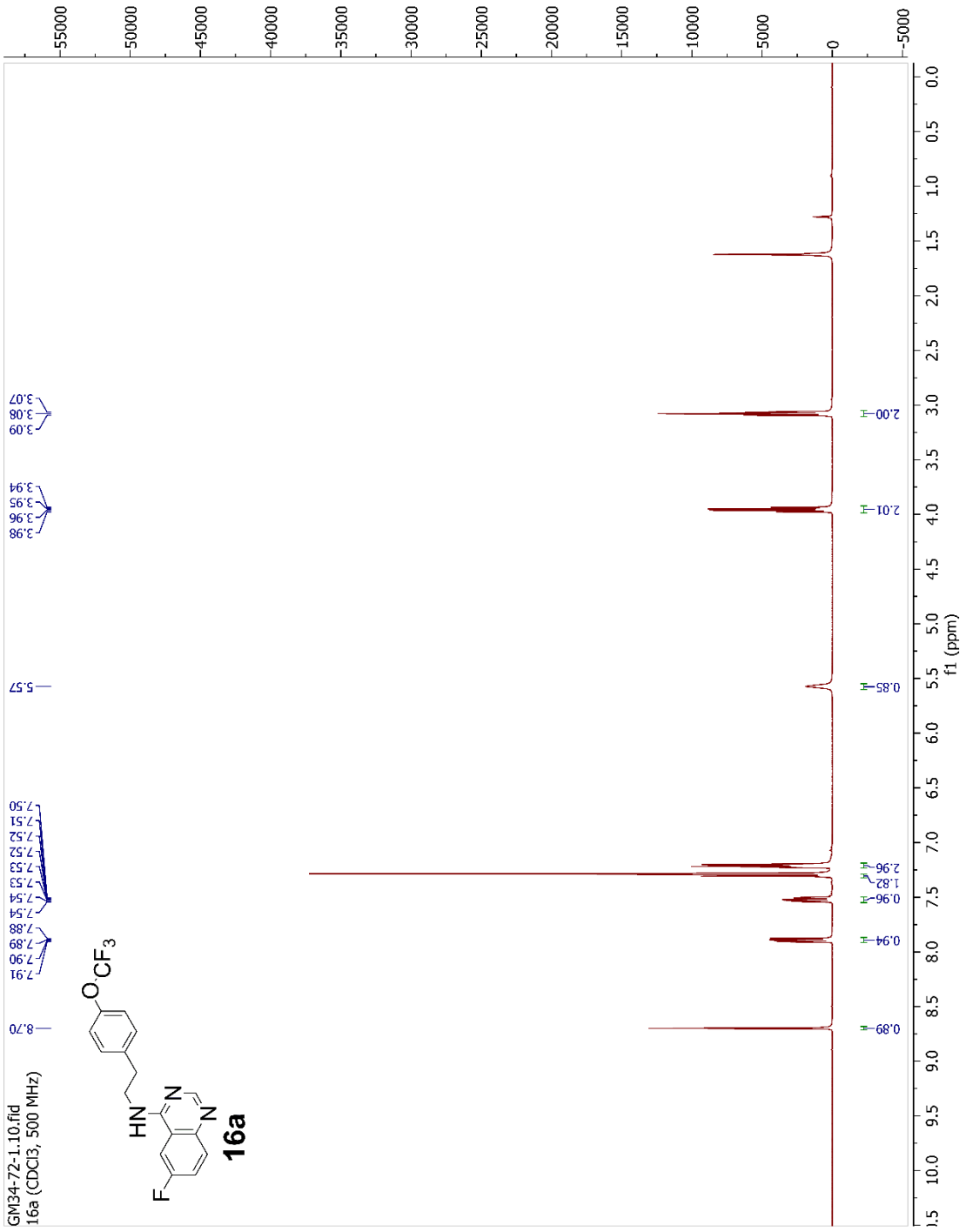

Figure C.28 ^{1}H NMR Spectrum ($CDCl_3$, 500 MHz) of **16a**

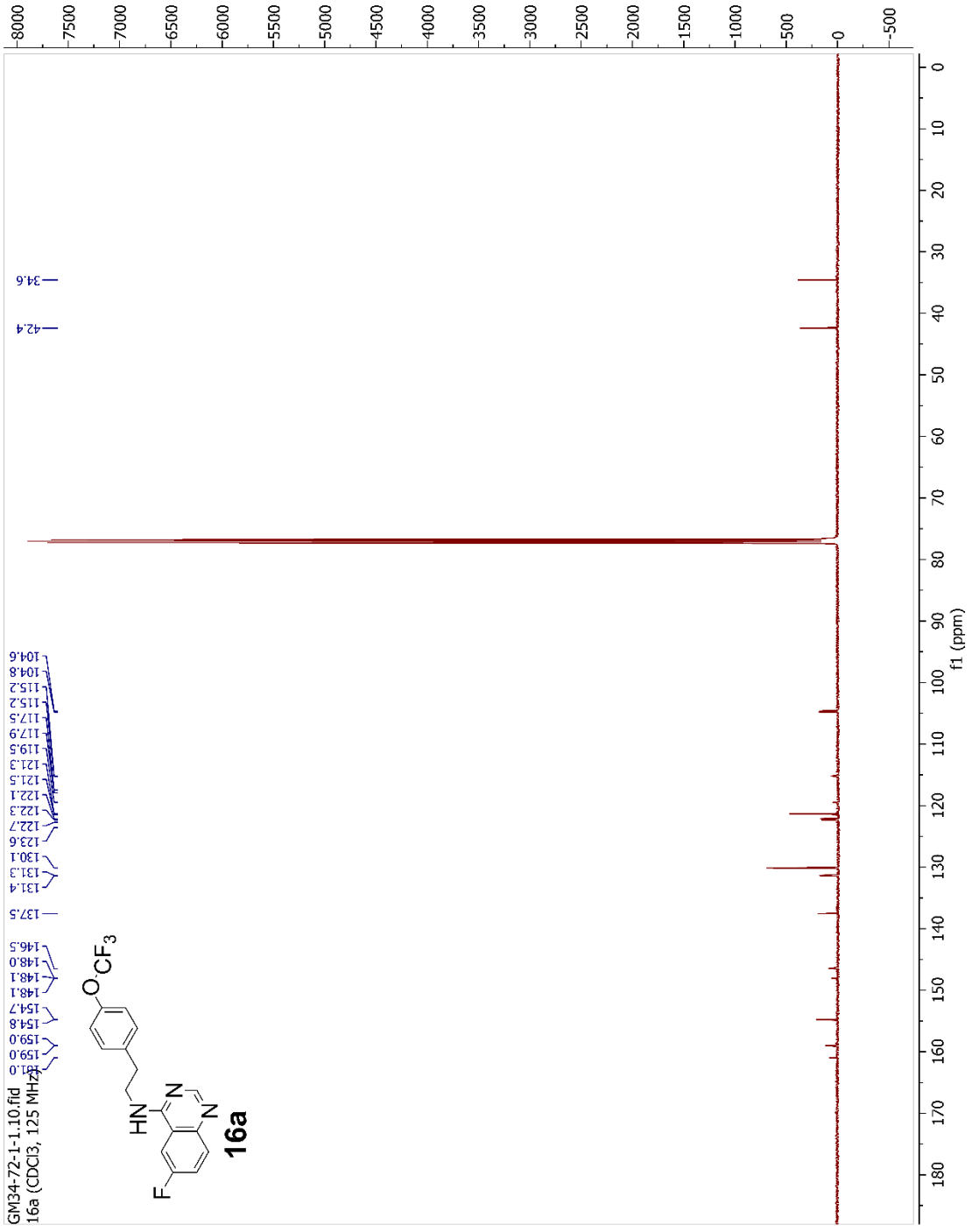

Figure C.29 ^{13}C NMR Spectrum ($CDCl_3$, 125 MHz) of **16a**

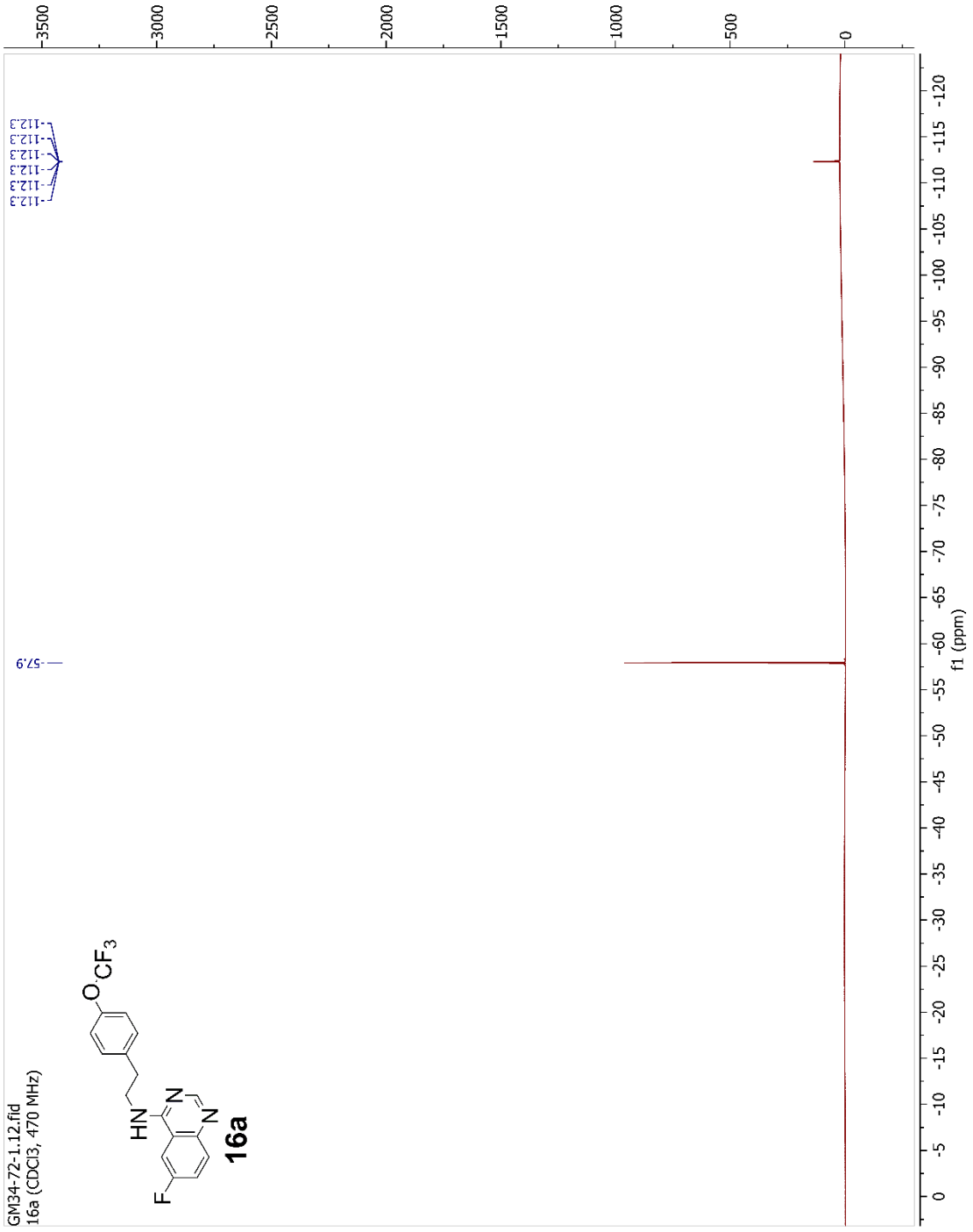

Figure C.30 ^{19}F NMR Spectrum ($CDCl_3$, 470 MHz) of **16a**

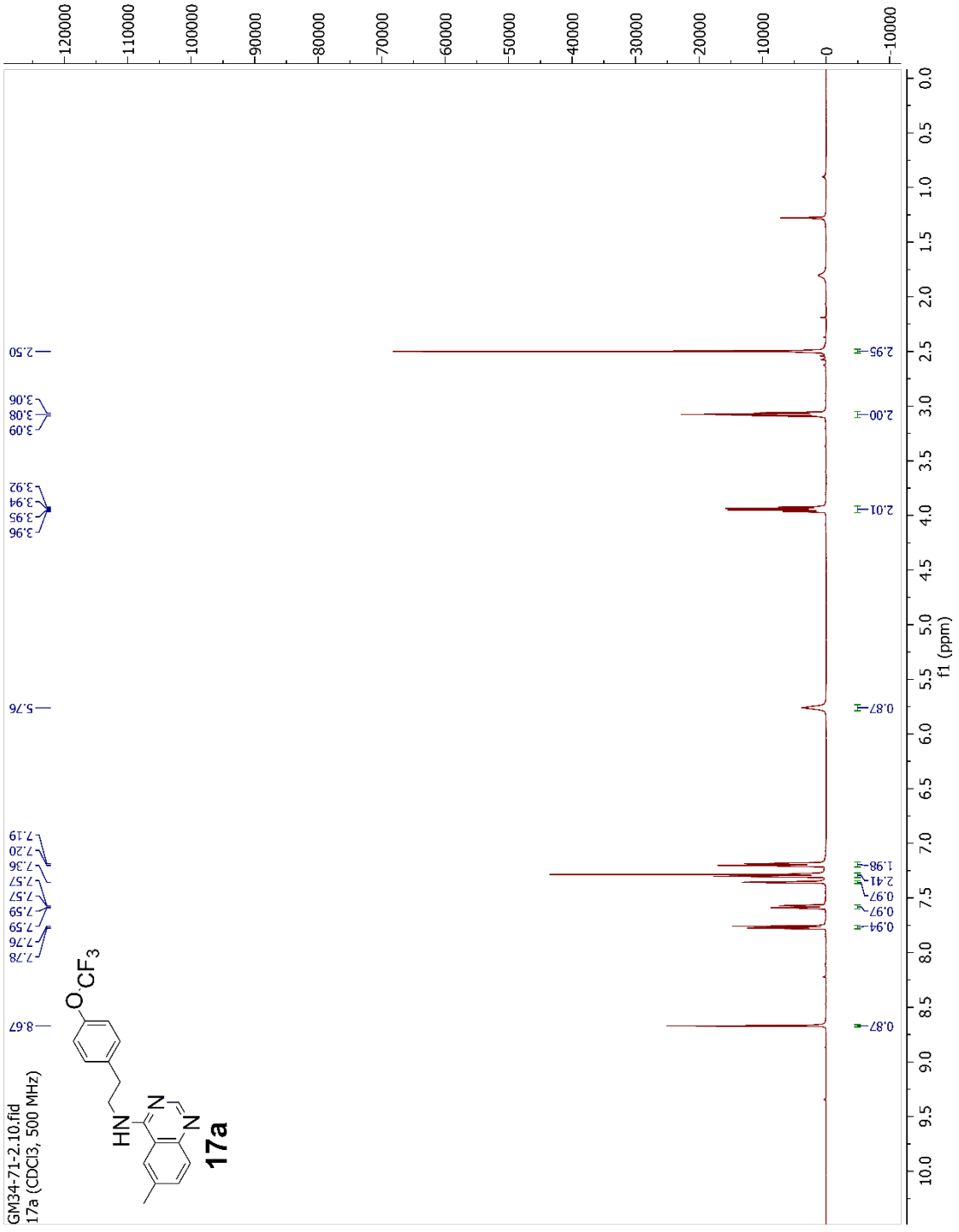

Figure C.31 ^{1}H NMR Spectrum ($CDCl_3$, 500 MHz) of **17a**

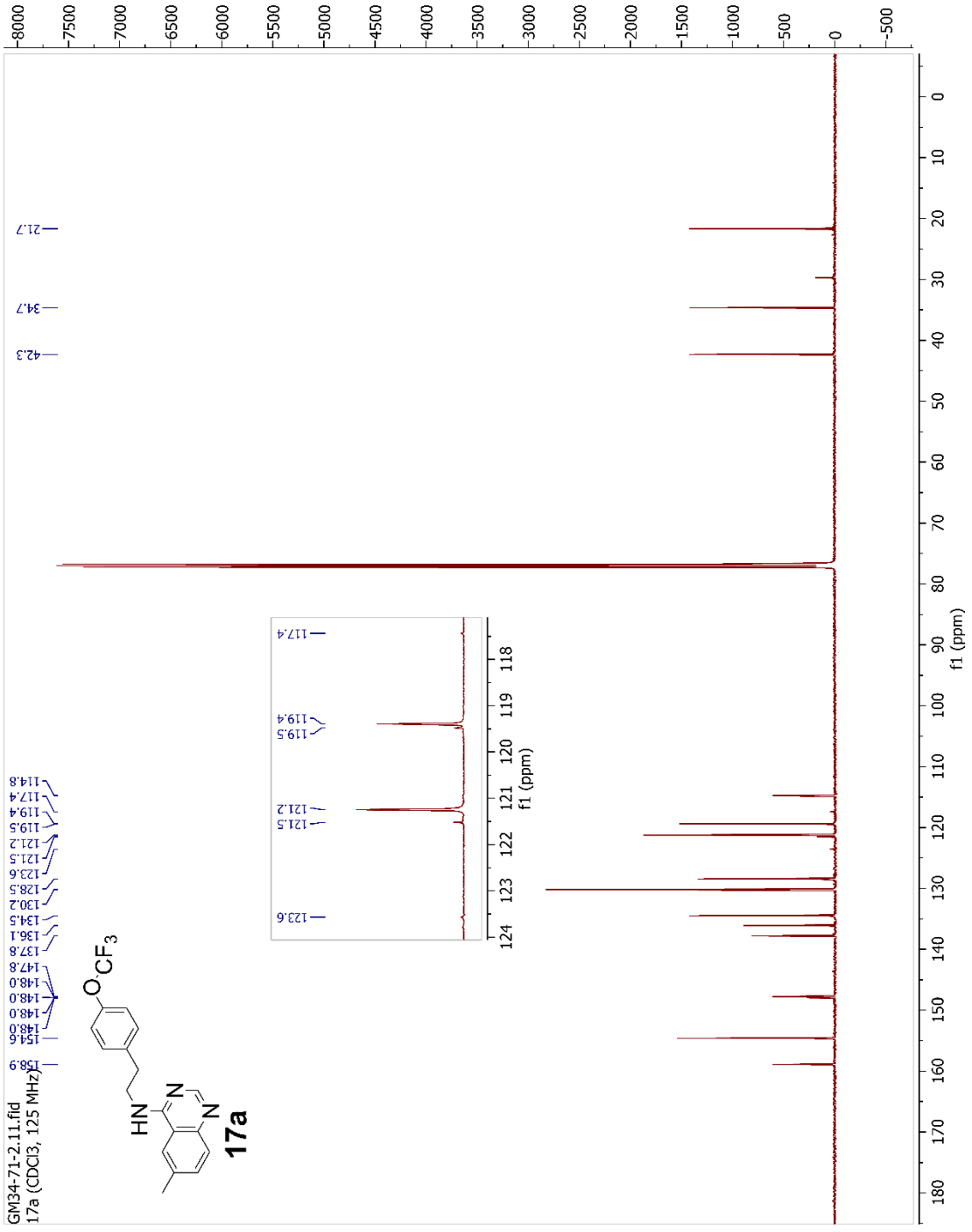

Figure C.32 ^{13}C NMR Spectrum ($CDCl_3$, 125 MHz) of **17a**

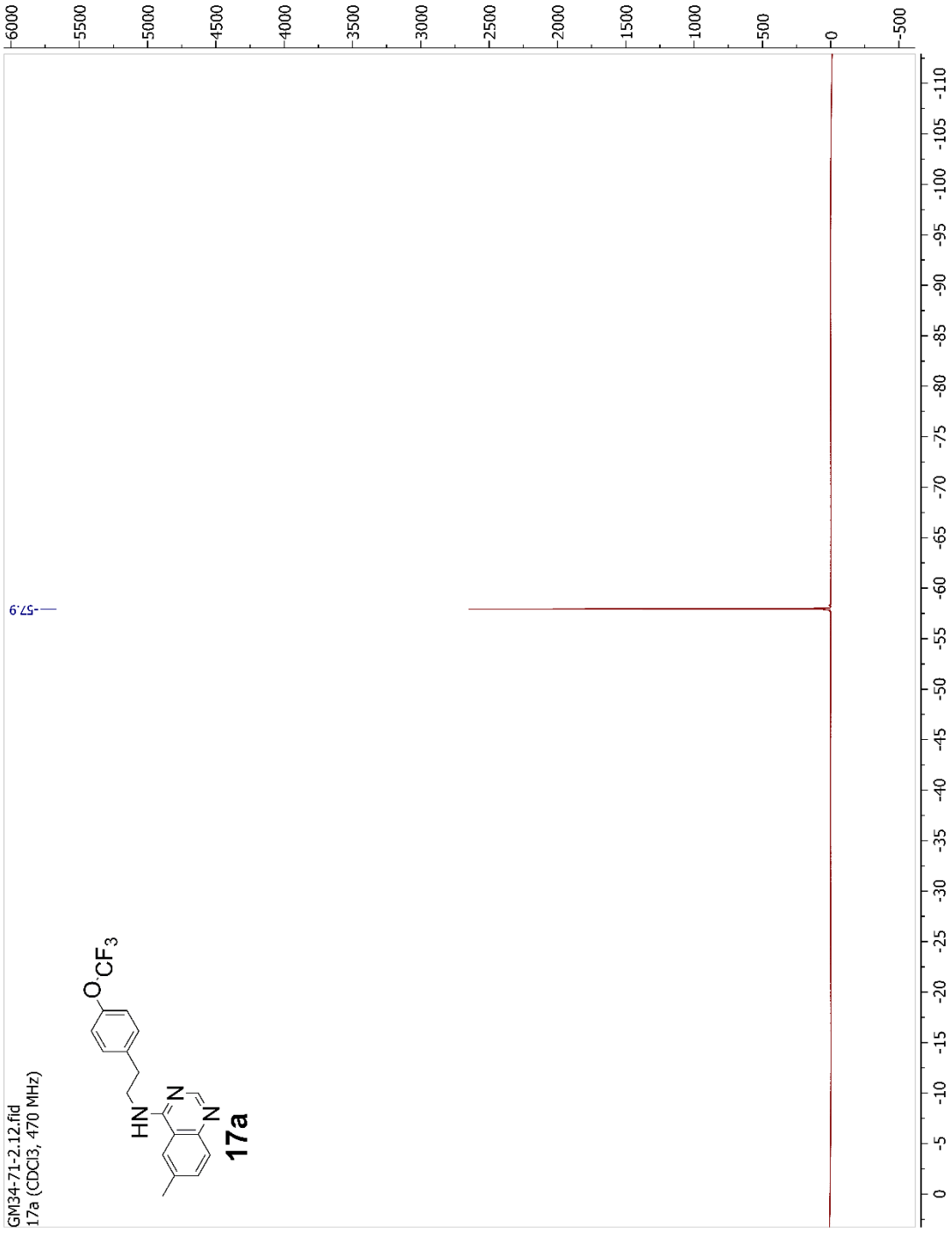

Figure C.33 ^{19}F NMR Spectrum ($CDCl_3$, 470 MHz) of **17a**

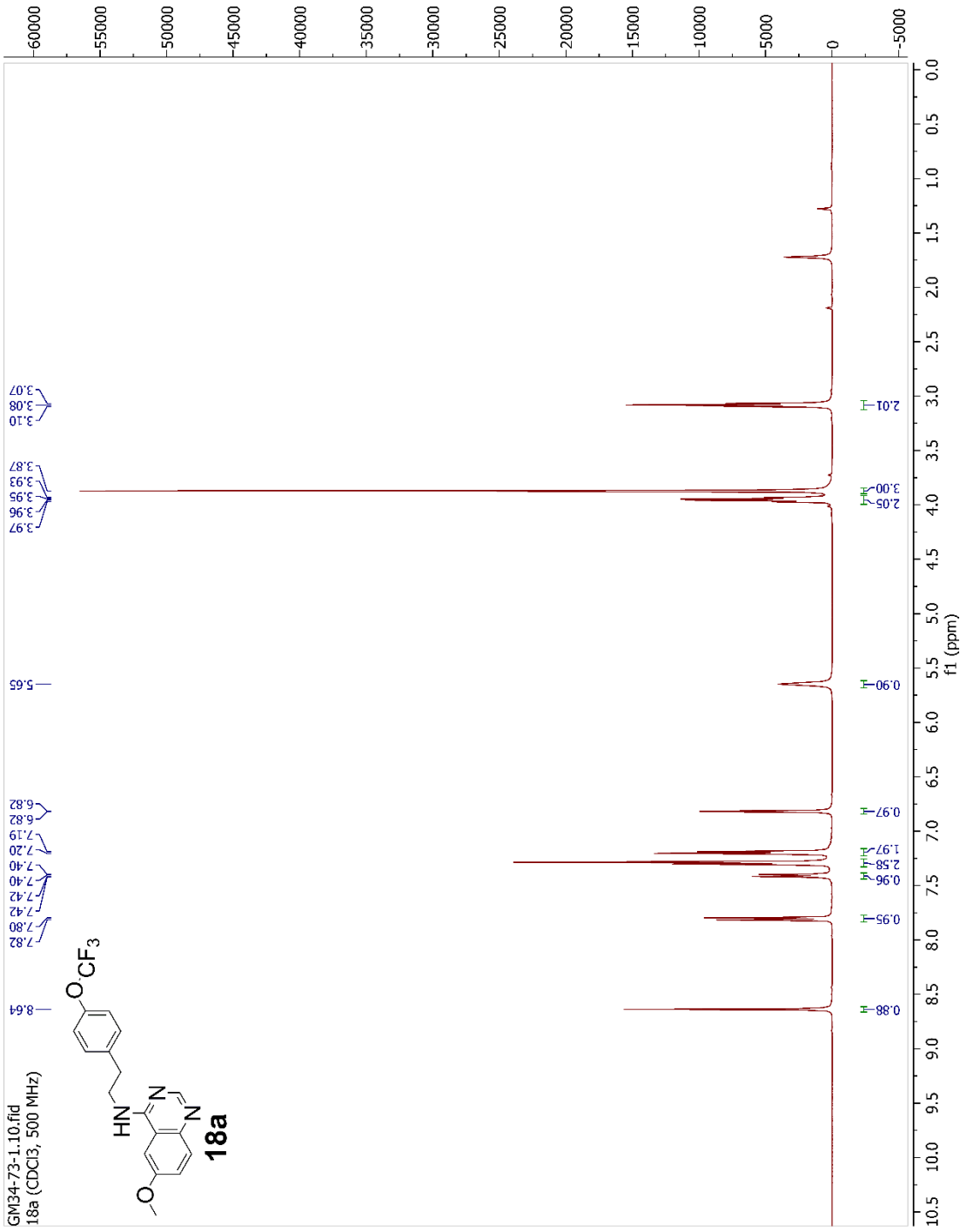

Figure C.34 ^{1}H NMR Spectrum ($CDCl_3$, 500 MHz) of **18a**

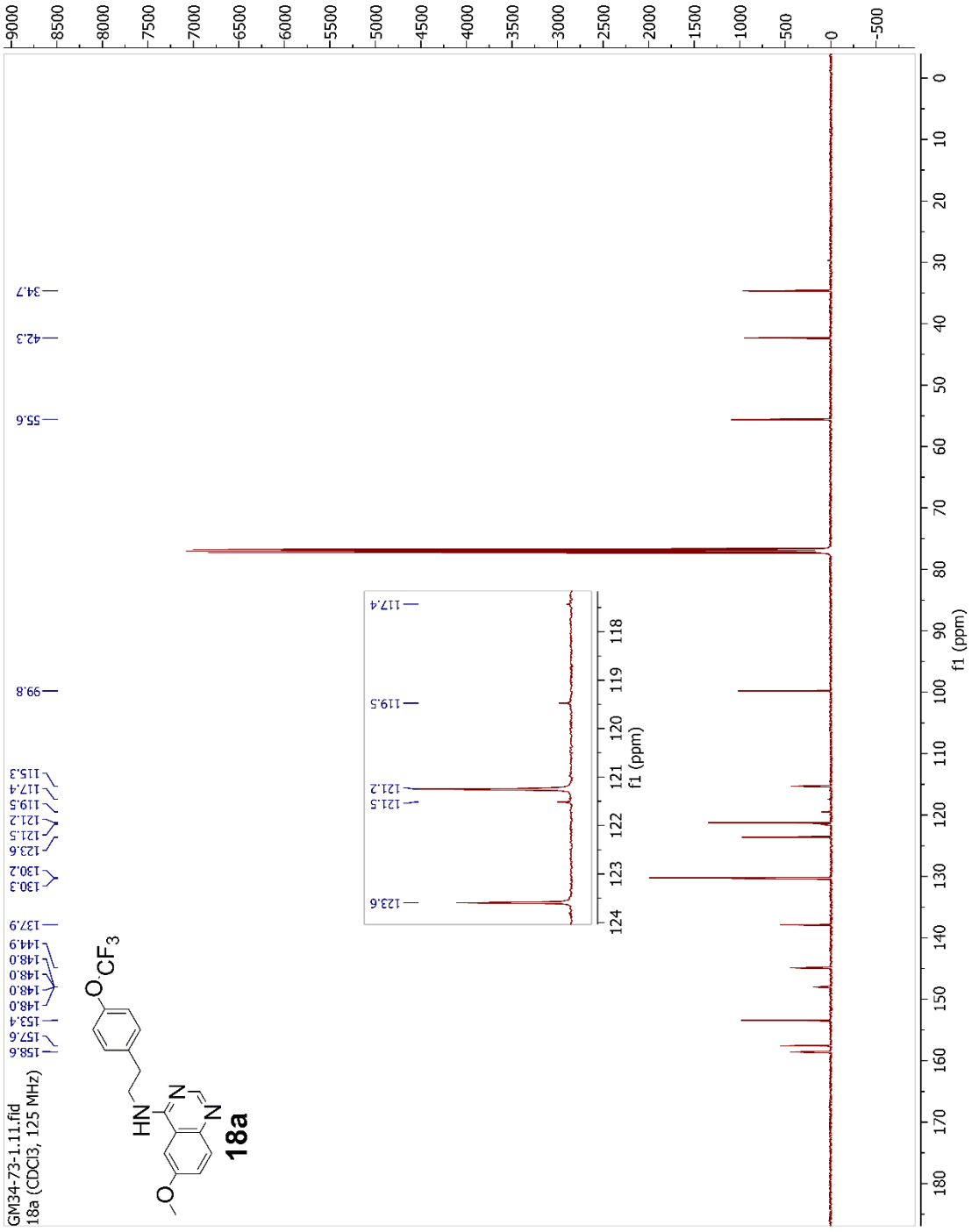

Figure C.35 ^{13}C NMR Spectrum ($CDCl_3$, 125 MHz) of **18a**

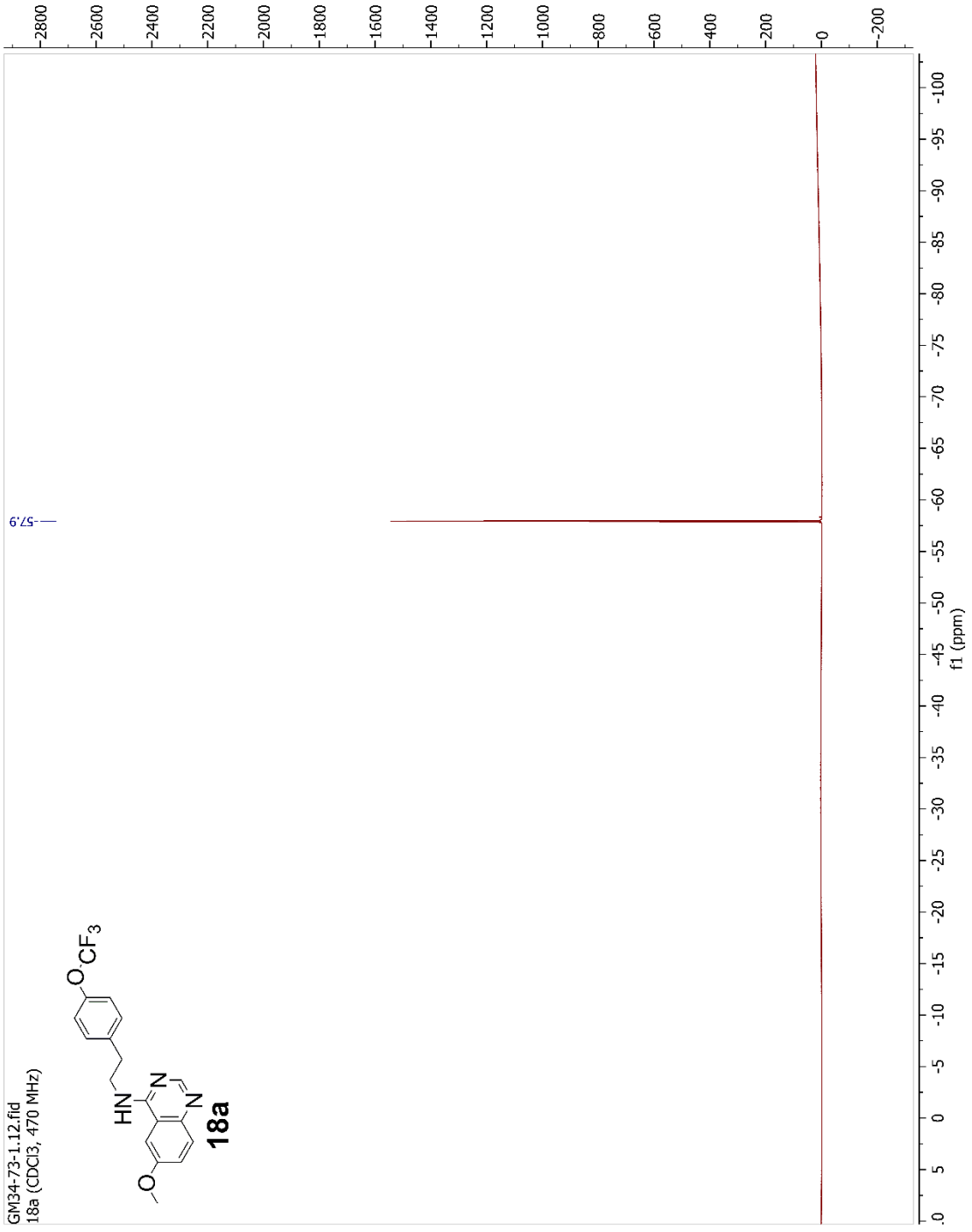

Figure C.36 ^{19}F NMR Spectrum ($CDCl_3$, 470 MHz) of **18a**

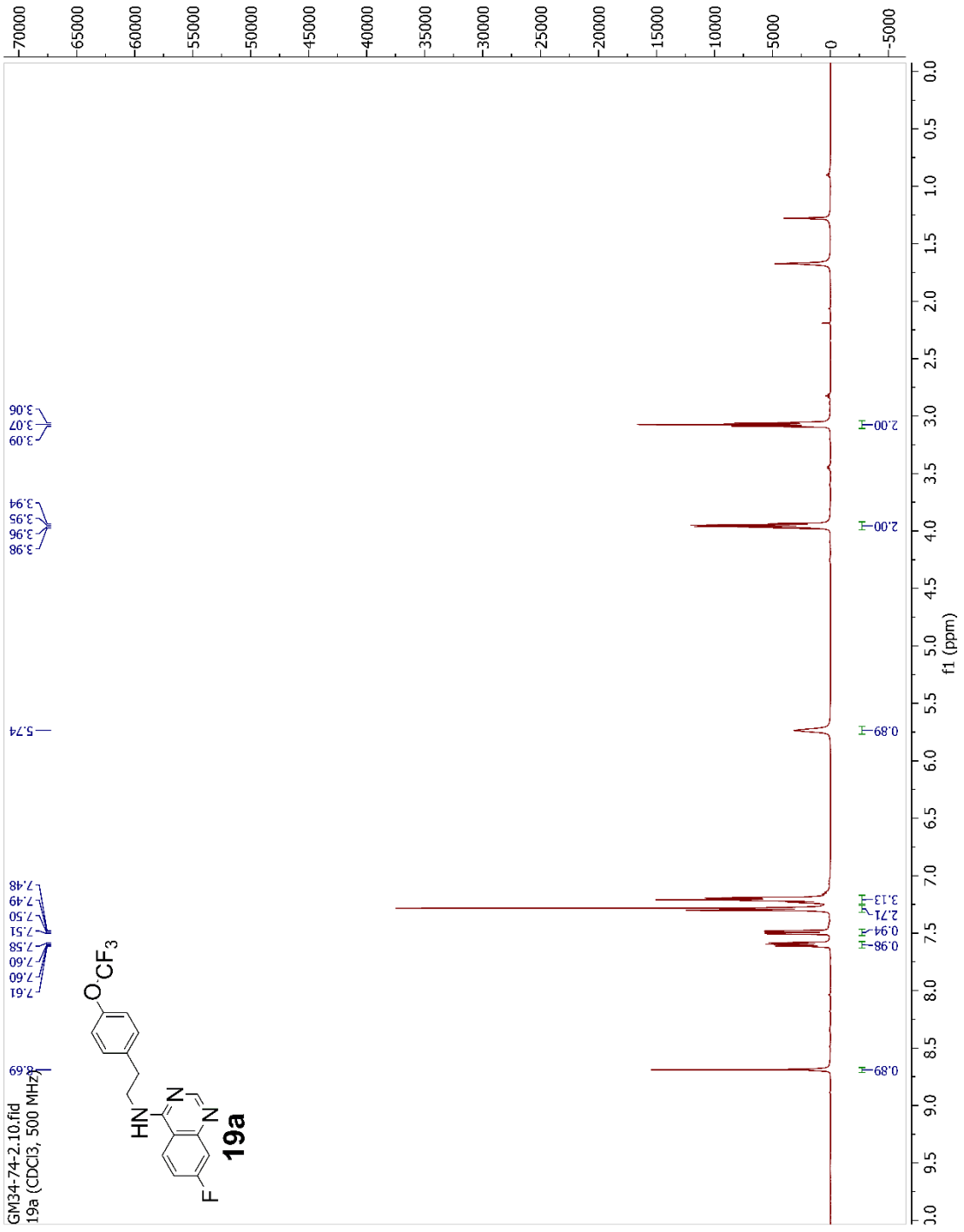

Figure C.37 ^{1}H NMR Spectrum ($CDCl_3$, 500 MHz) of **19a**

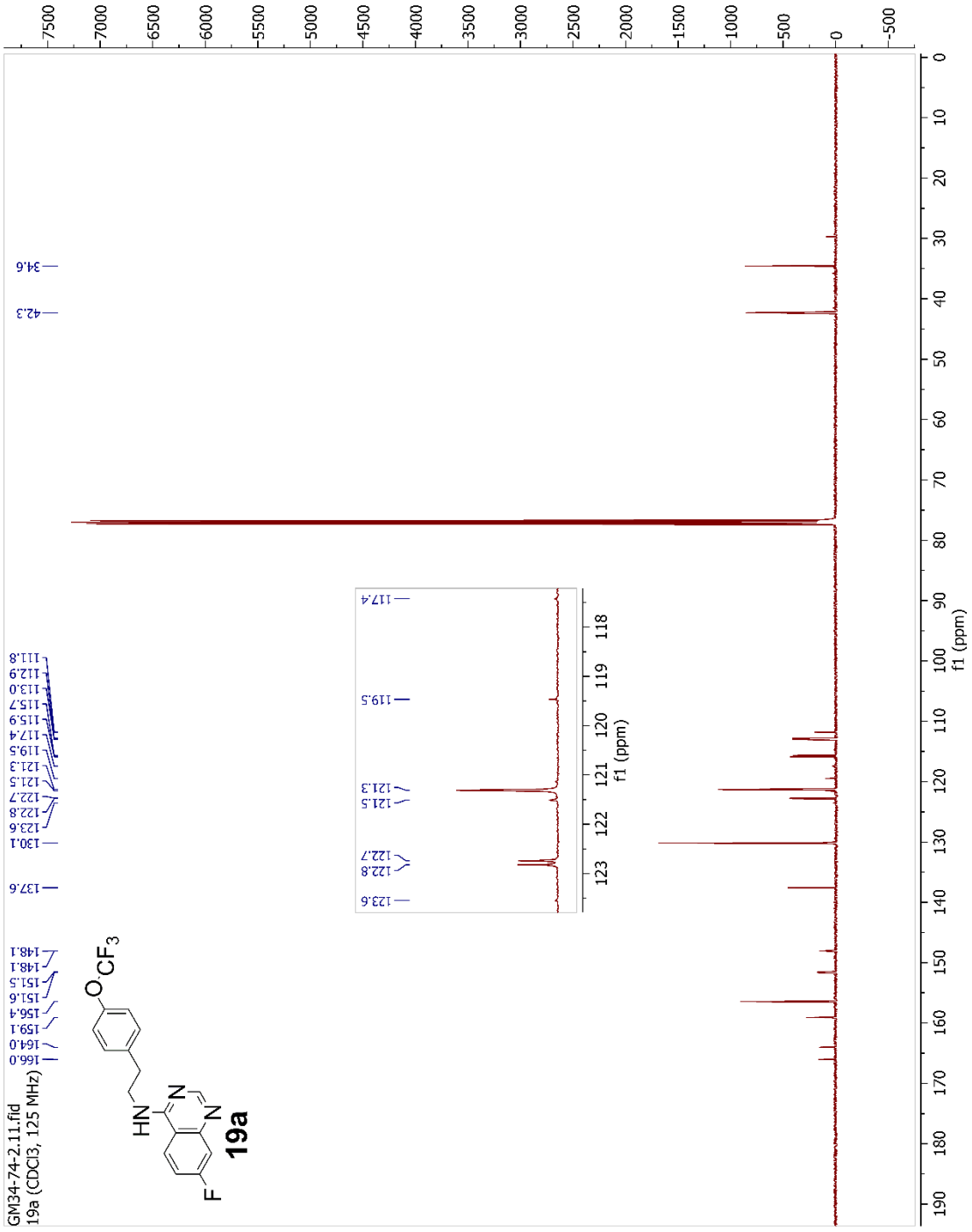

Figure C.38 ^{13}C NMR Spectrum ($CDCl_3$, 125 MHz) of **19a**

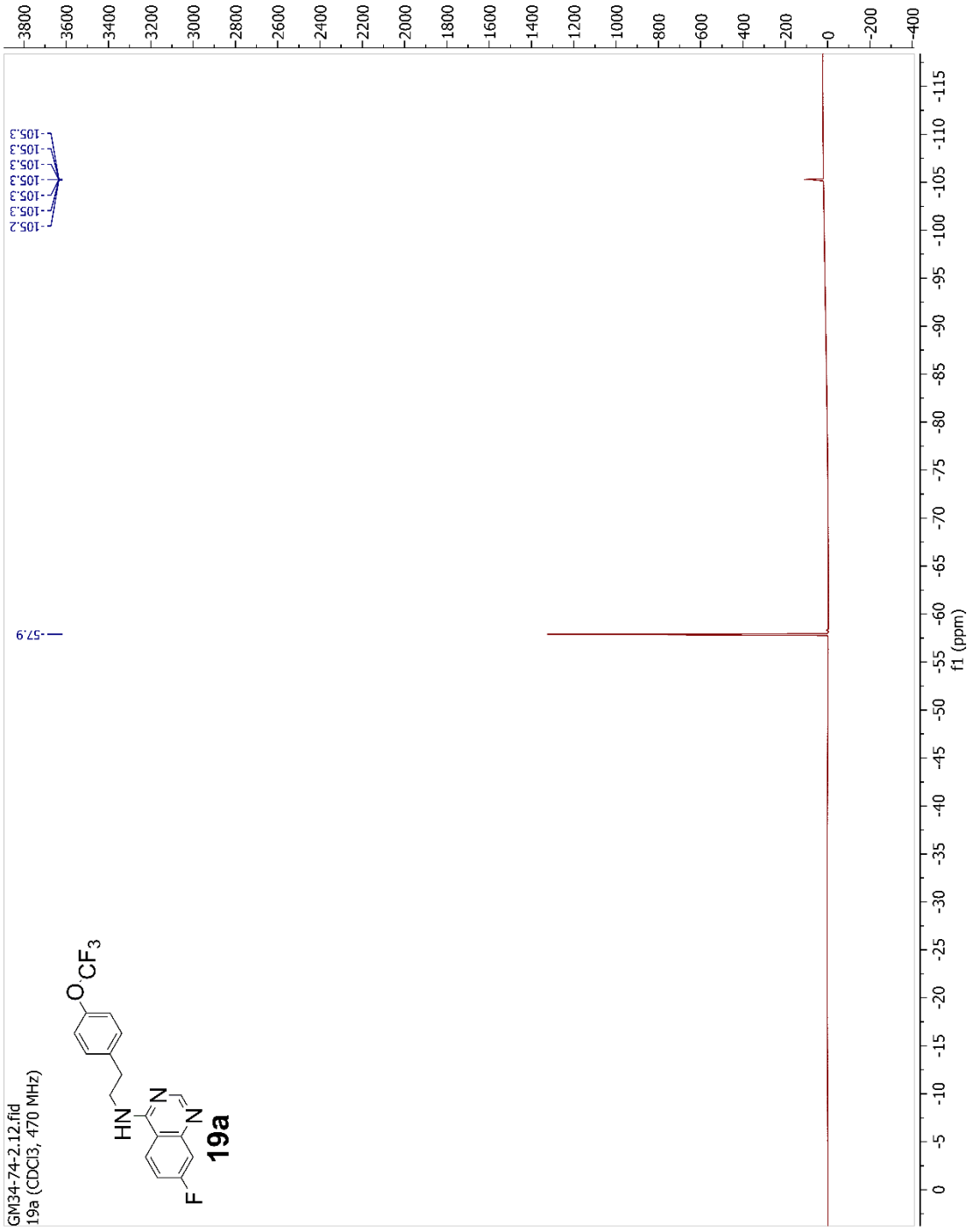

Figure C.39 ^{19}F NMR Spectrum ($CDCl_3$, 470 MHz) of **19a**

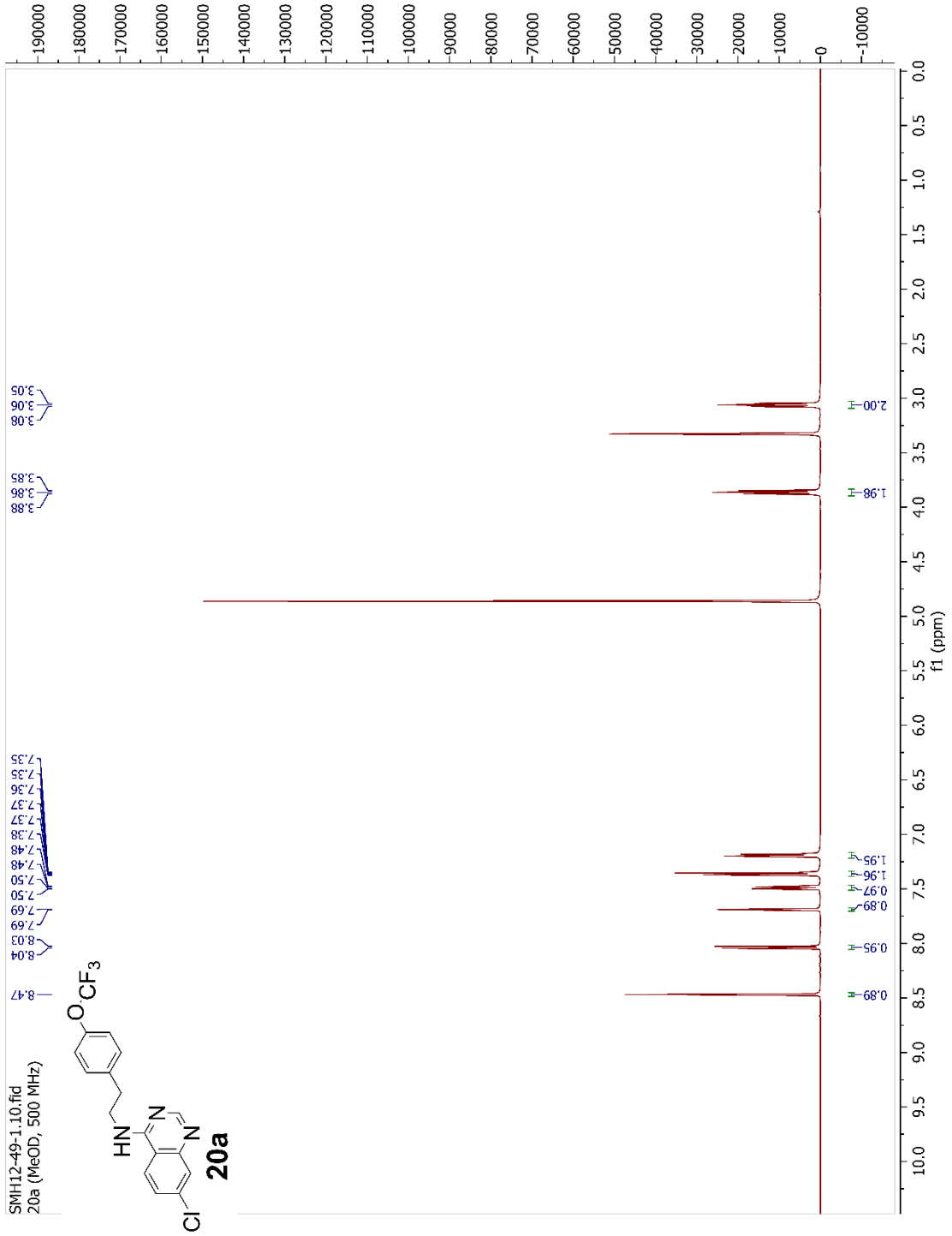

Figure C.40 ^{1}H NMR Spectrum (MeOD, 500 MHz) of **20a**

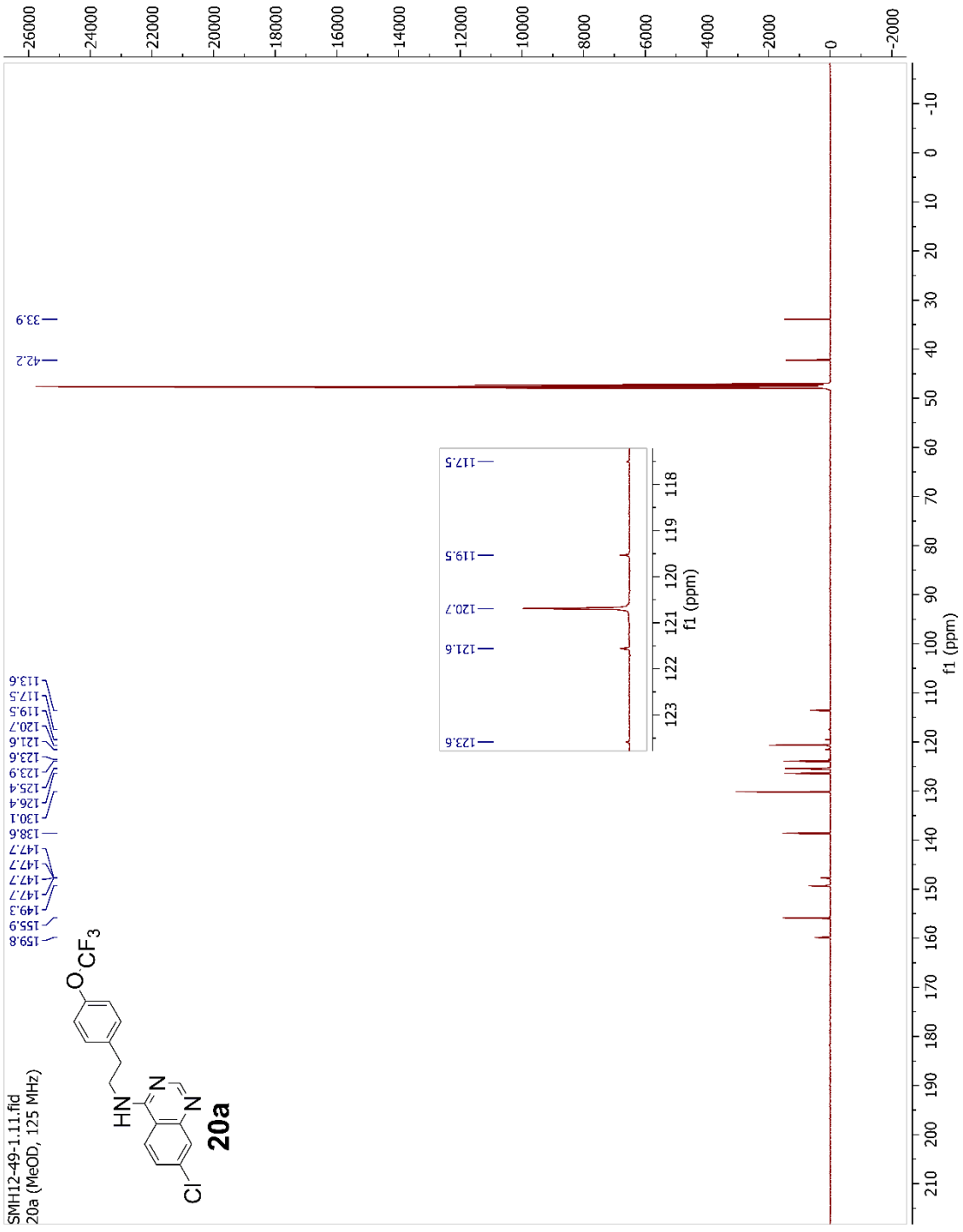

Figure C.41 ^{13}C NMR Spectrum (MeOD, 125 MHz) of **20a**

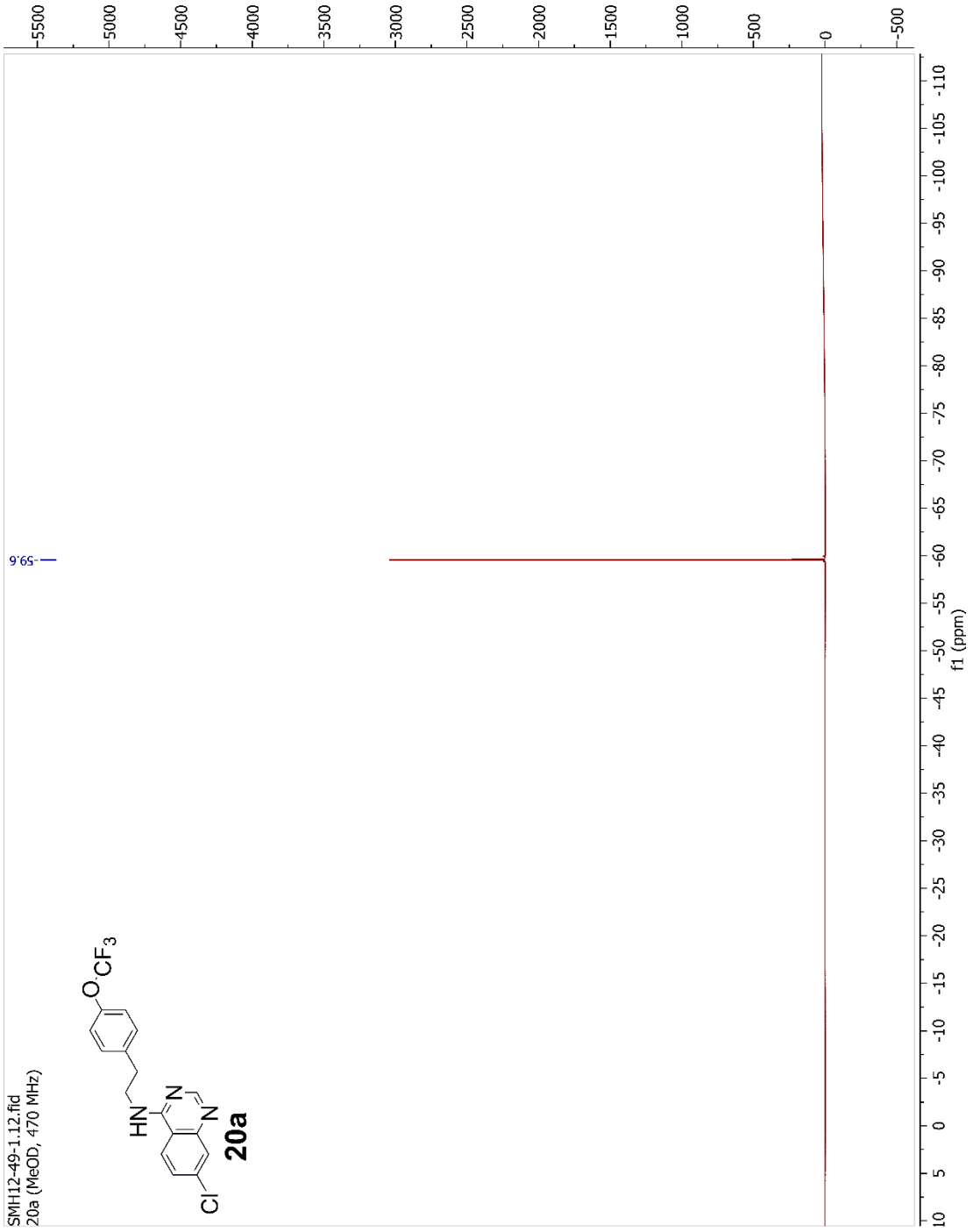

Figure C.42 ^{19}F NMR Spectrum (MeOD, 470 MHz) of **20a**

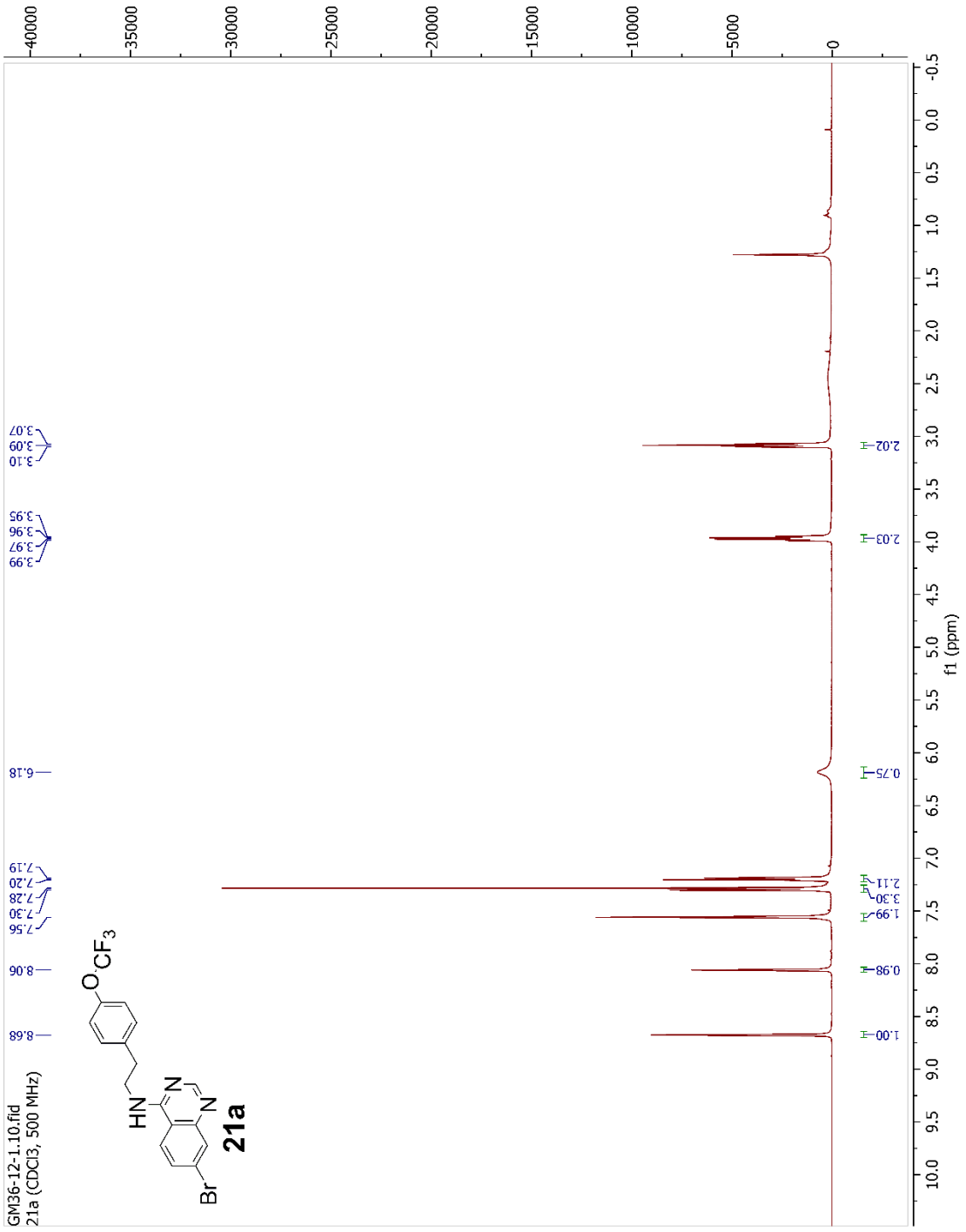

Figure C.43 ^{1}H NMR Spectrum ($CDCl_3$, 500 MHz) of **21a**

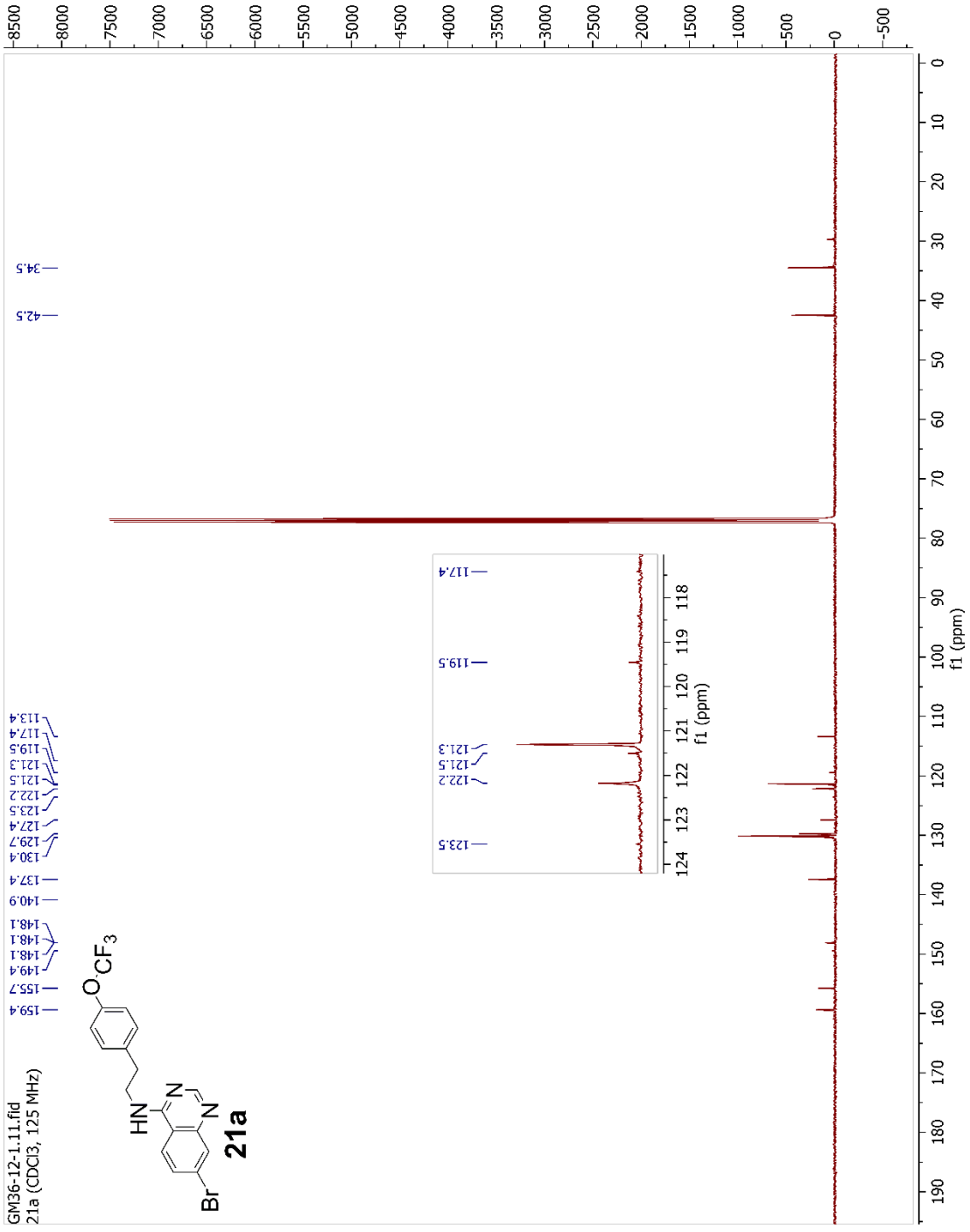

Figure C.44 ^{13}C NMR Spectrum ($CDCl_3$, 125 MHz) of **21a**

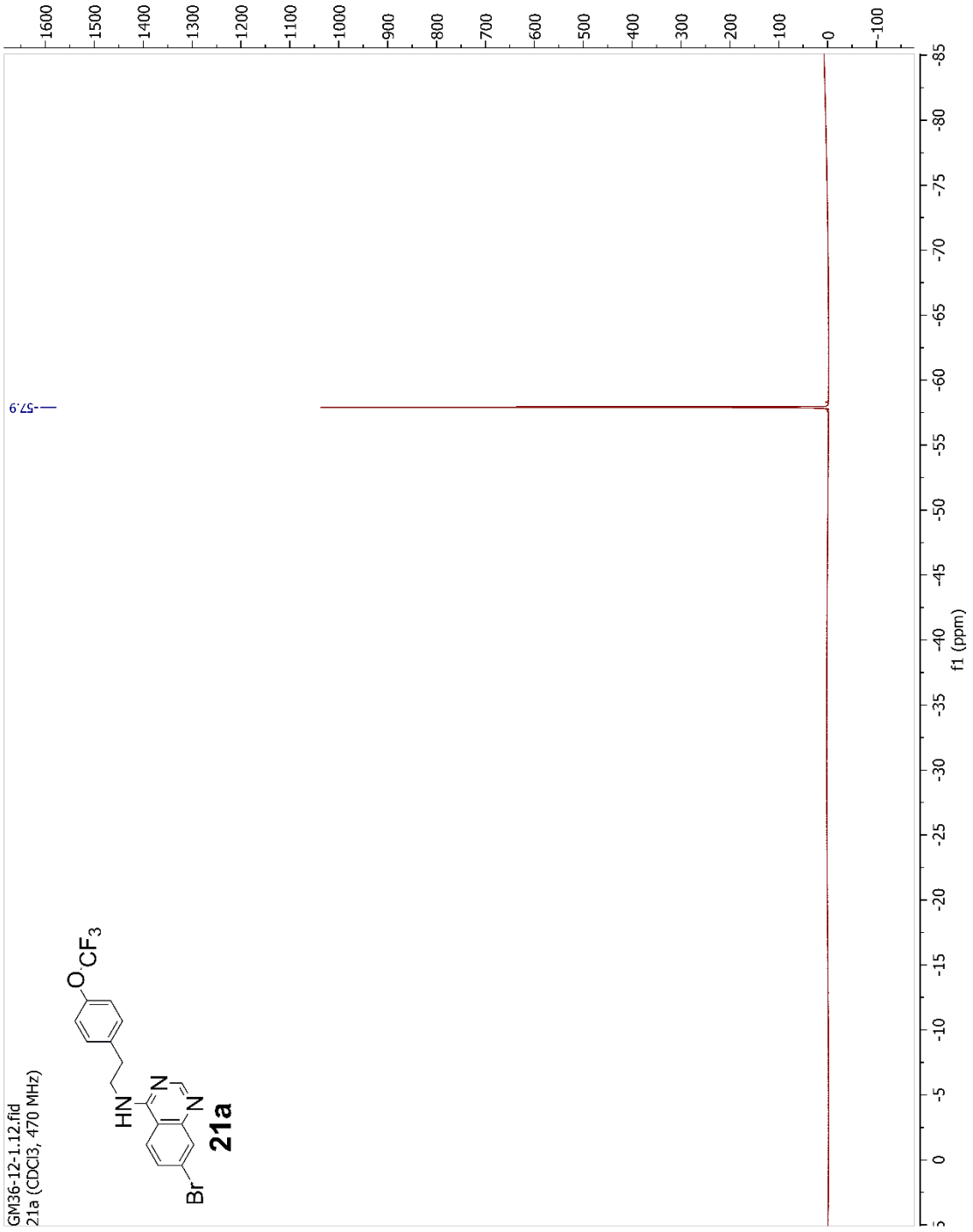

Figure C.45 ^{19}F NMR Spectrum ($CDCl_3$, 470 MHz) of **21a**

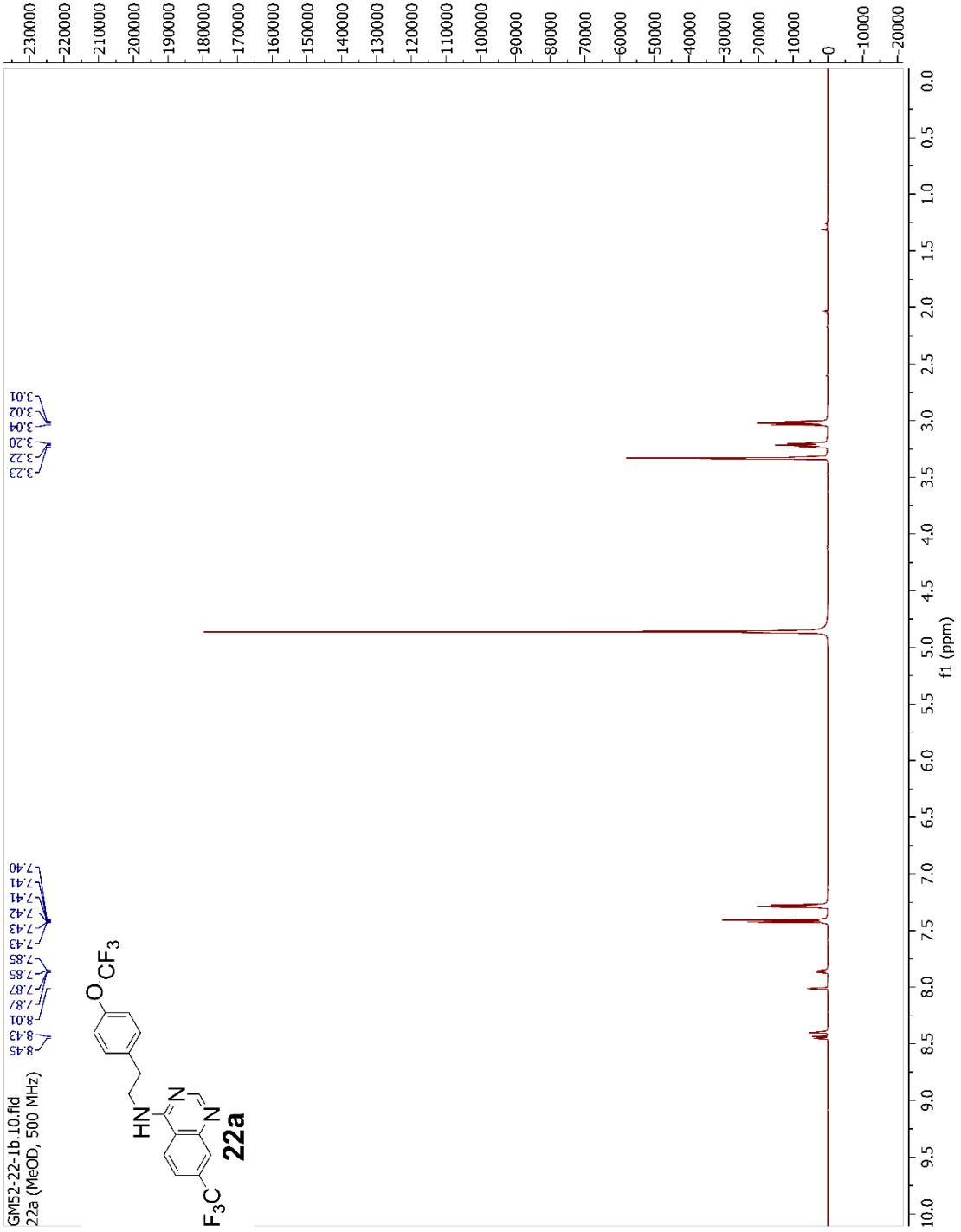

Figure C.46 ^{1}H NMR Spectrum (MeOD, 500 MHz) of **22a**

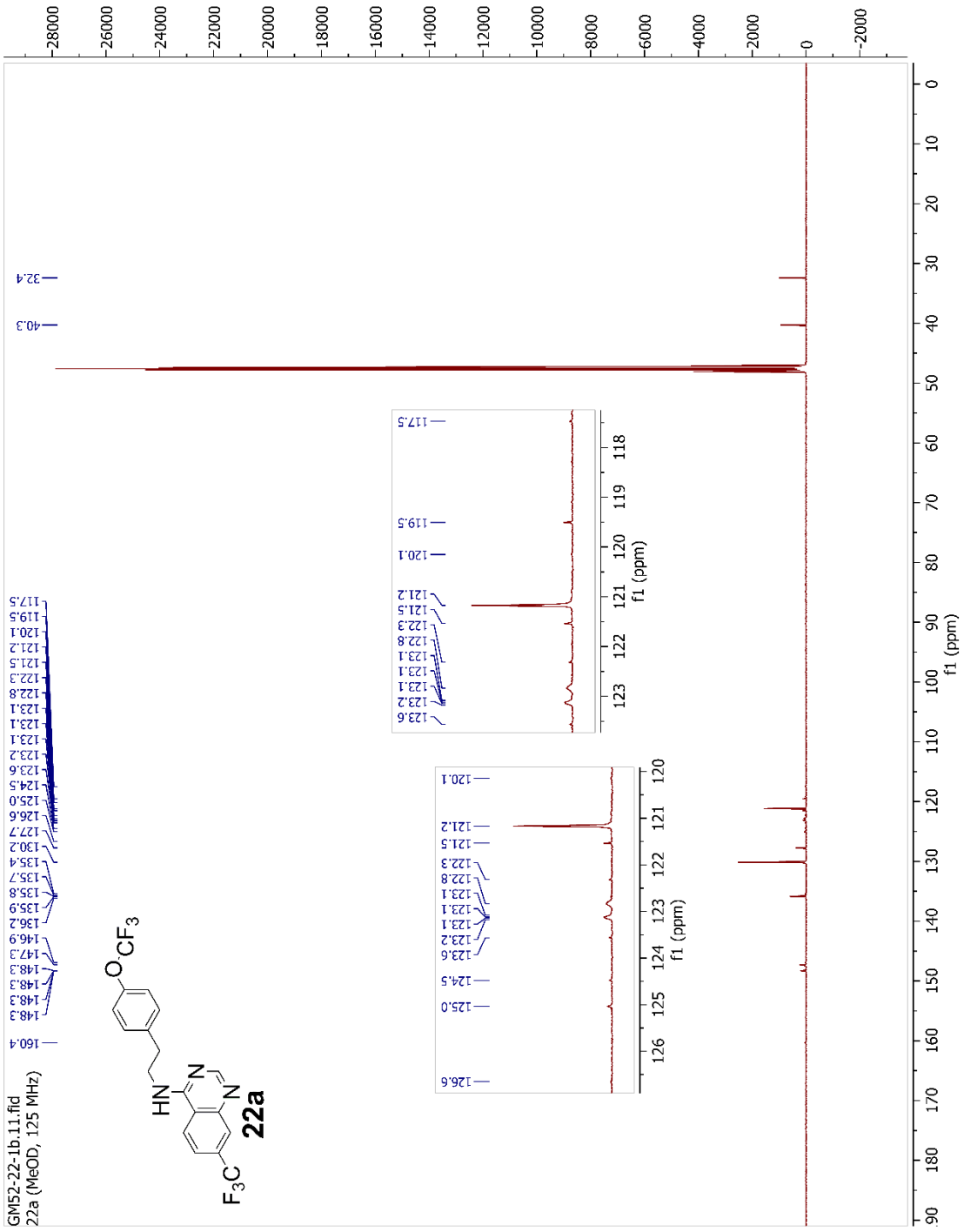

Figure C.47 ^{13}C NMR Spectrum (MeOD, 125 MHz) of **22a**

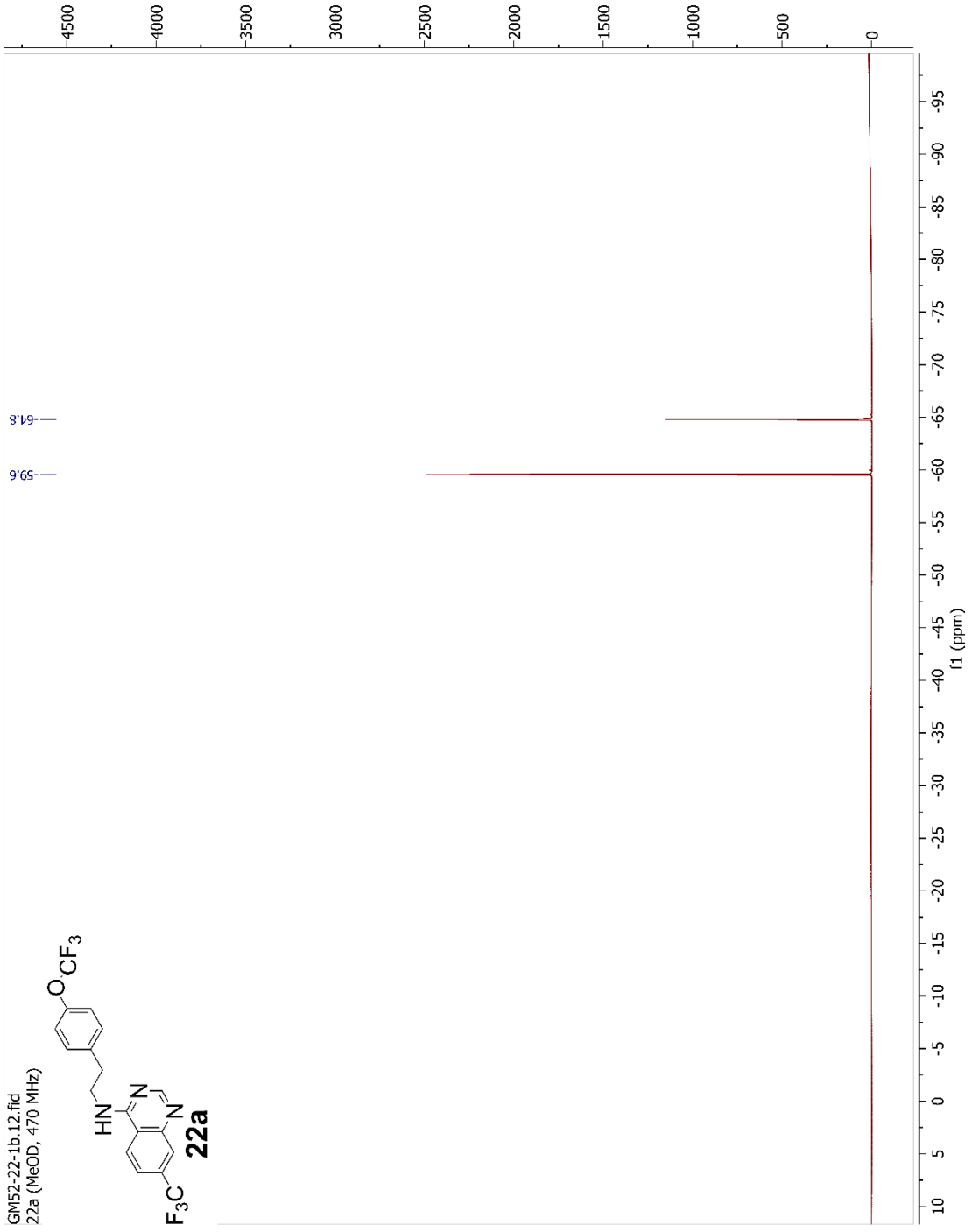

Figure C.48 ^{19}F NMR Spectrum (MeOD, 470 MHz) of **22a**

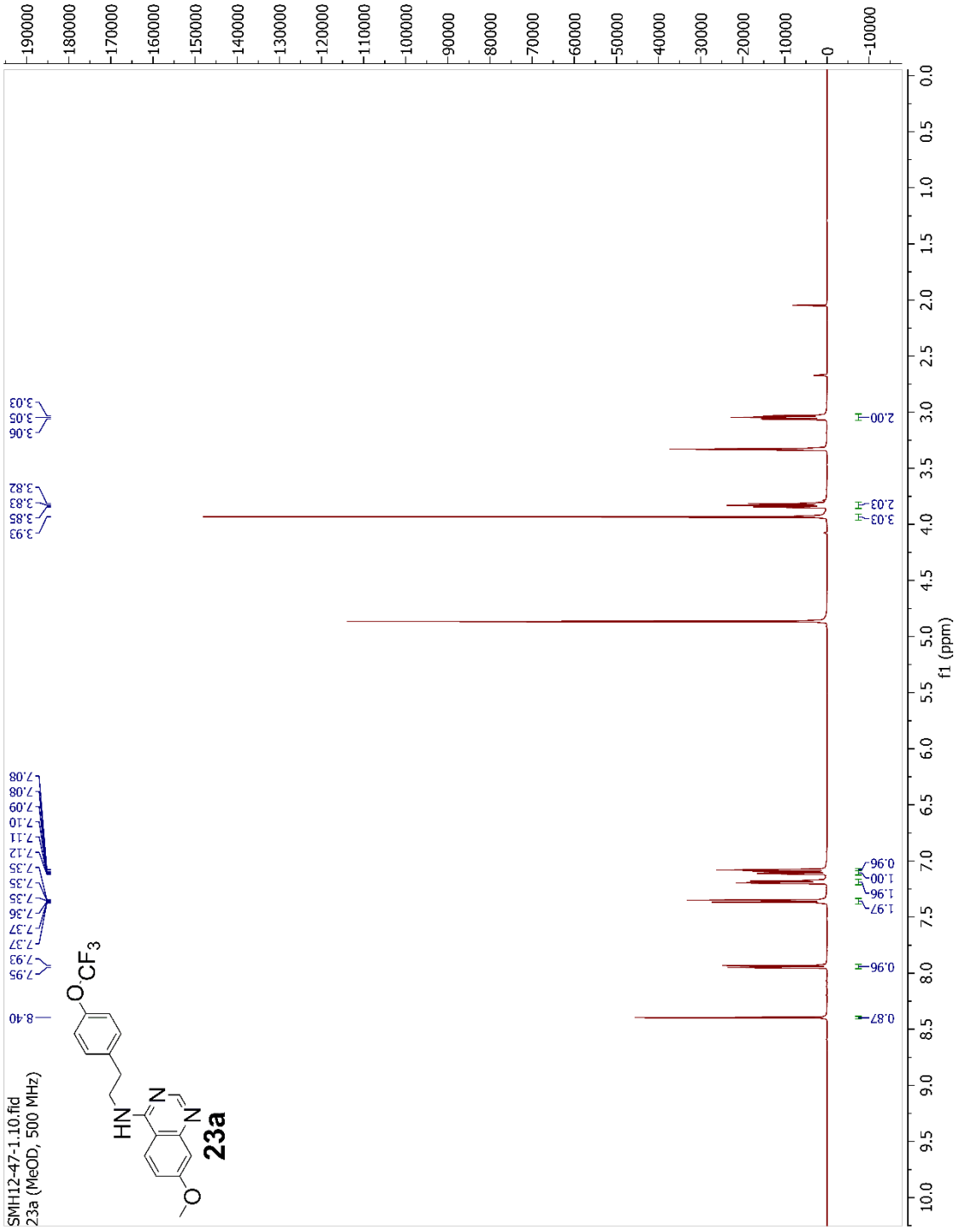

Figure C.49 ^{1}H NMR Spectrum (MeOD, 500 MHz) of **23a**

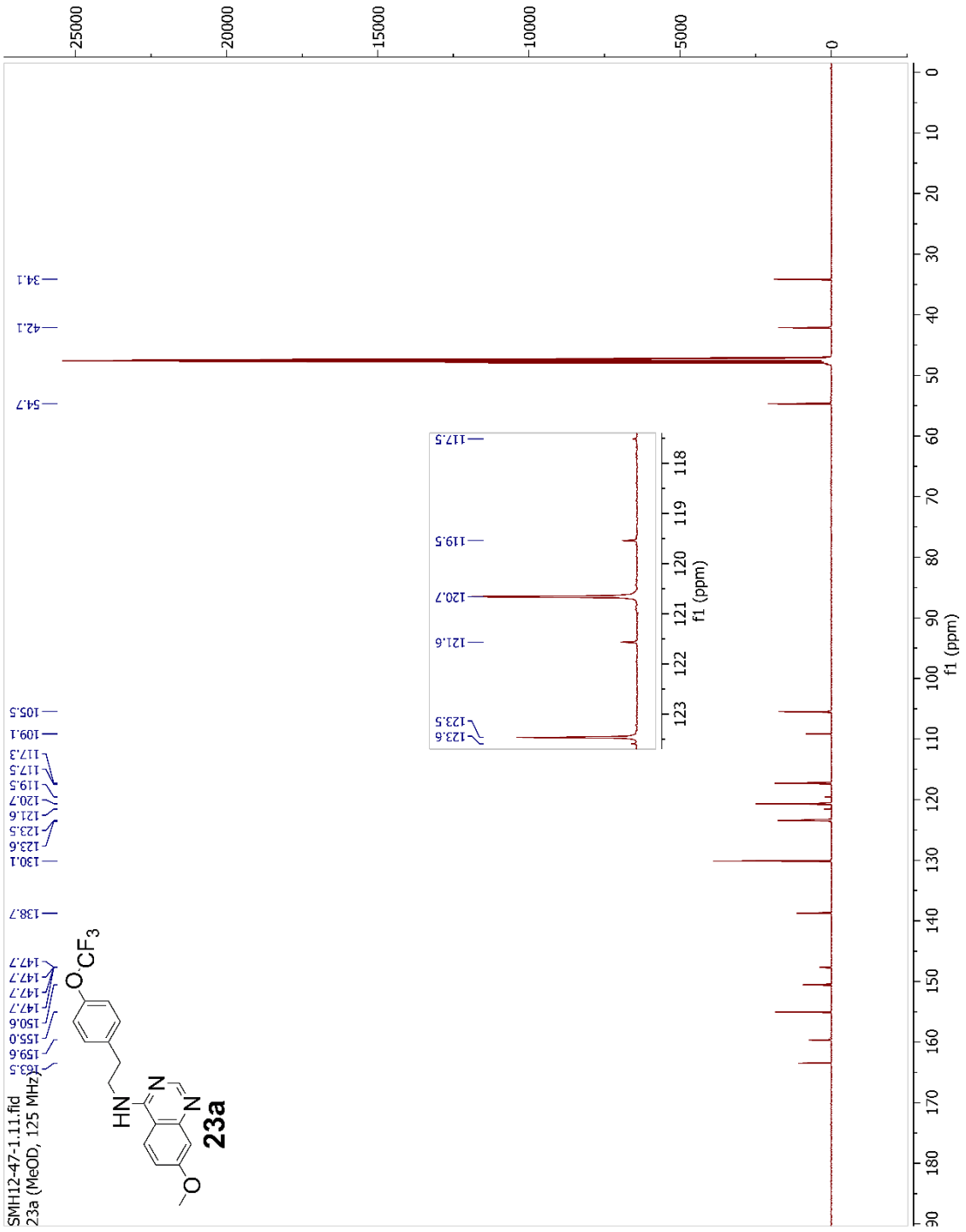

Figure C.50 ^{13}C NMR Spectrum (MeOD, 125 MHz) of **23a**

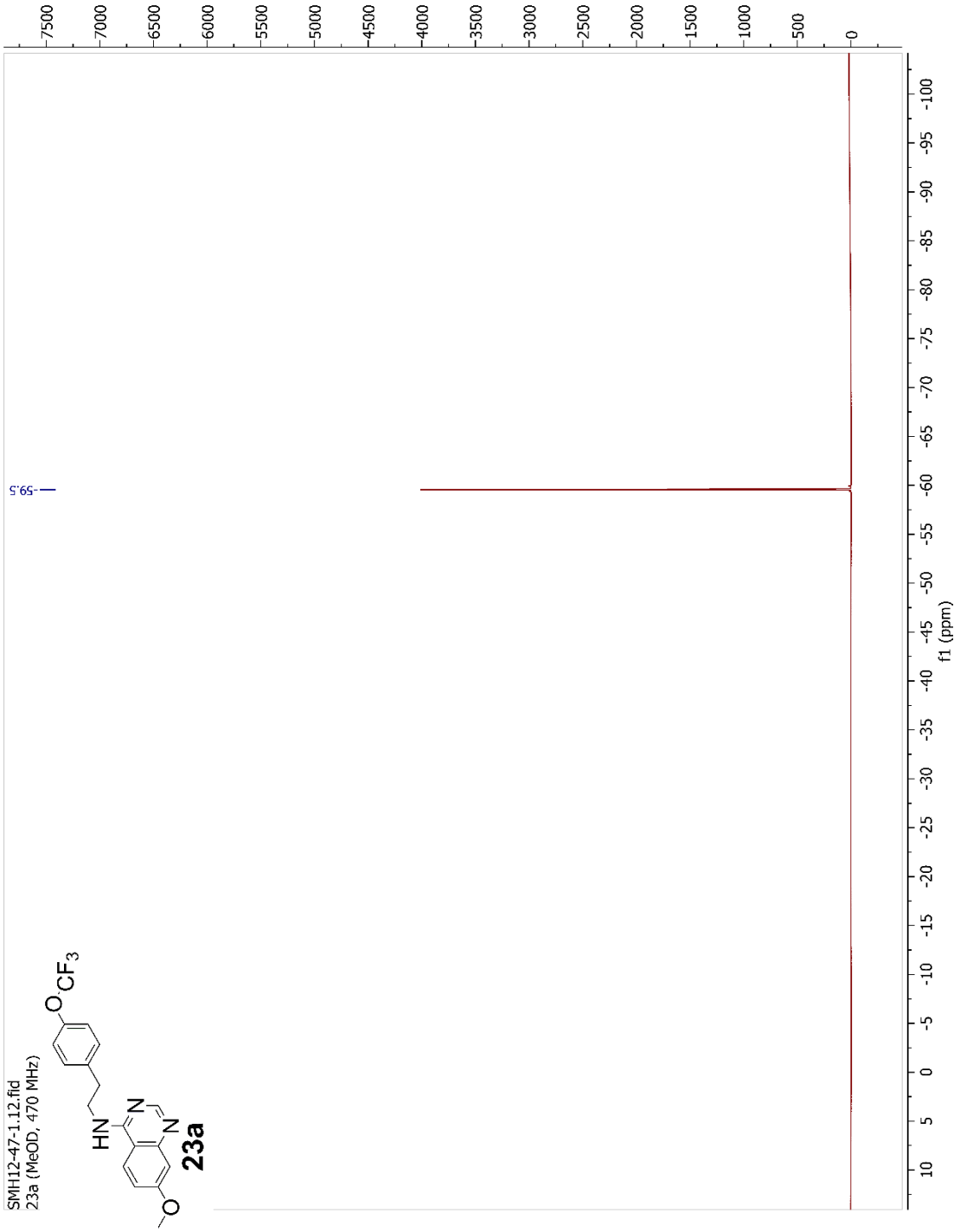

Figure C.51 ^{19}F NMR Spectrum (MeOD, 470 MHz) of **23a**

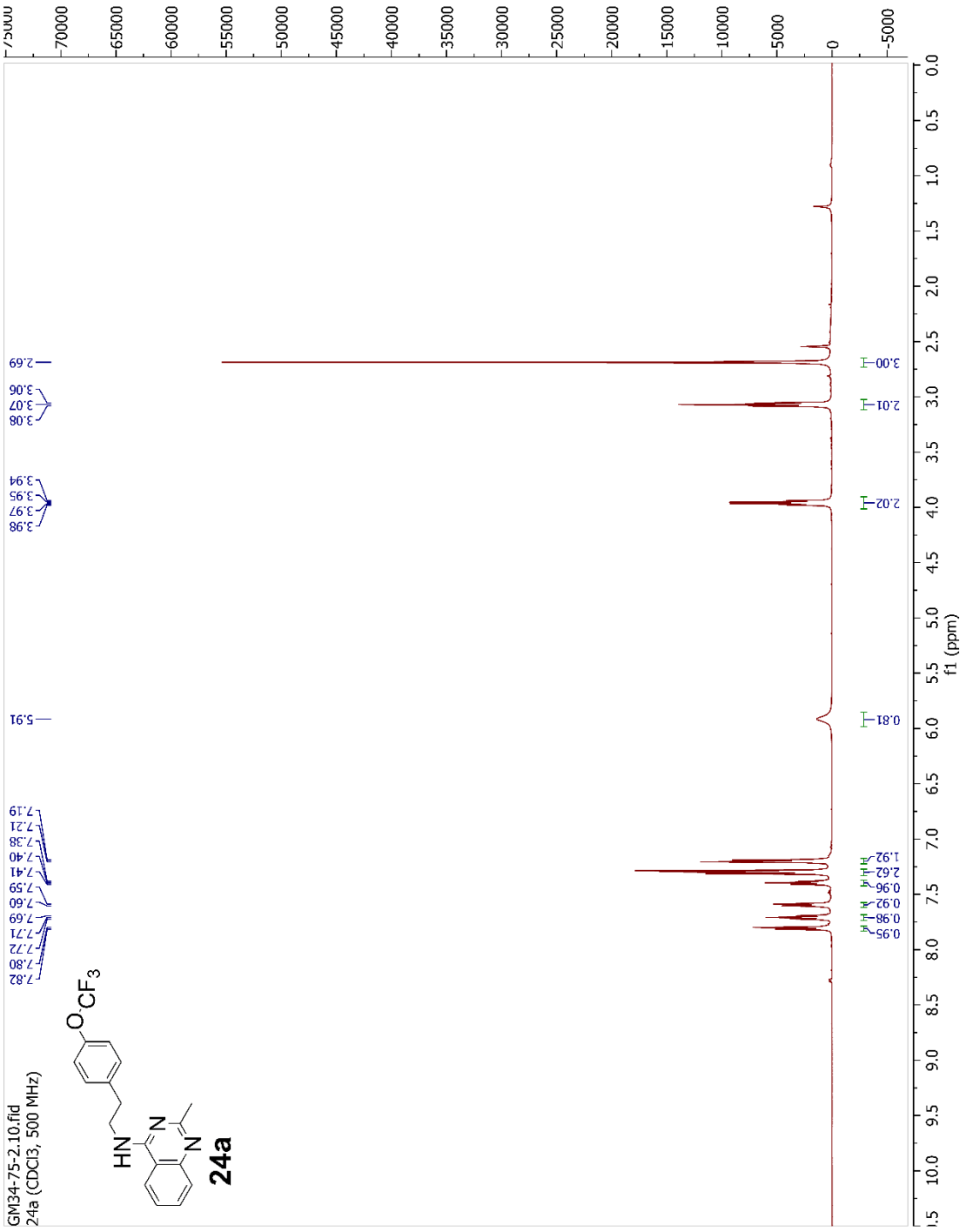

Figure C.52 ^{1}H NMR Spectrum ($CDCl_3$, 500 MHz) of **24a**

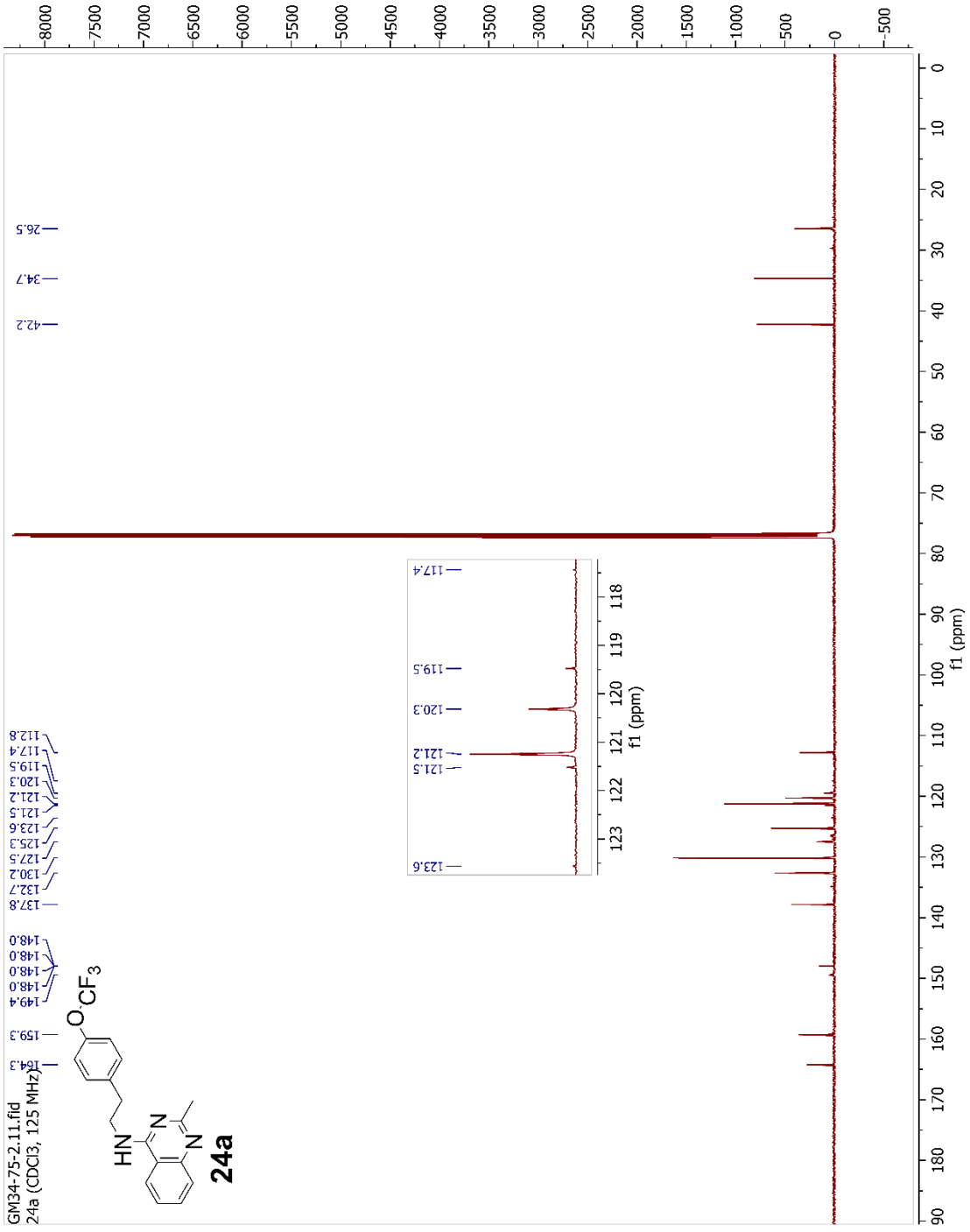

Figure C.53 ^{13}C NMR Spectrum ($CDCl_3$, 125 MHz) of **24a**

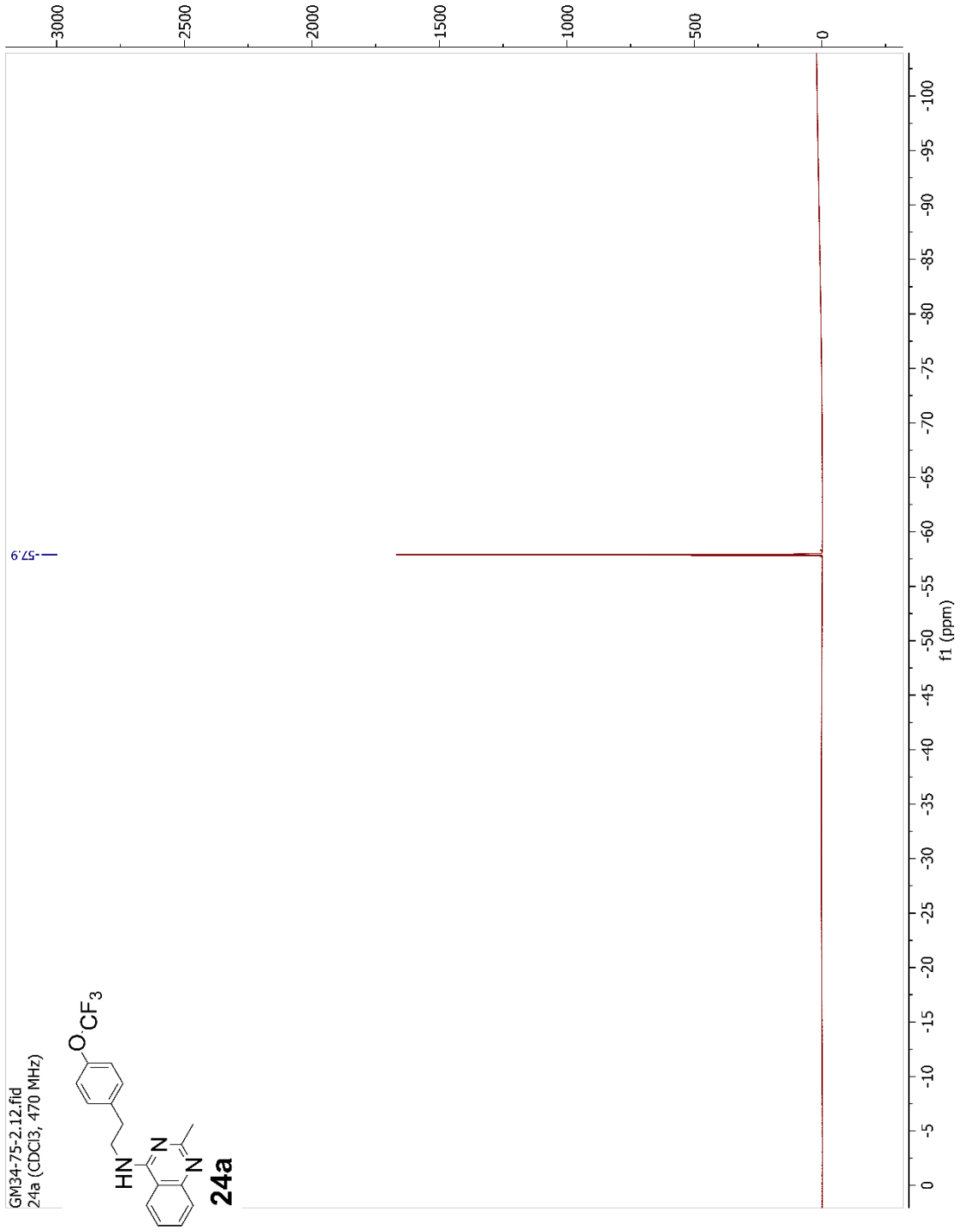

Figure C.54 ^{19}F NMR Spectrum ($CDCl_3$, 470 MHz) of **24a**

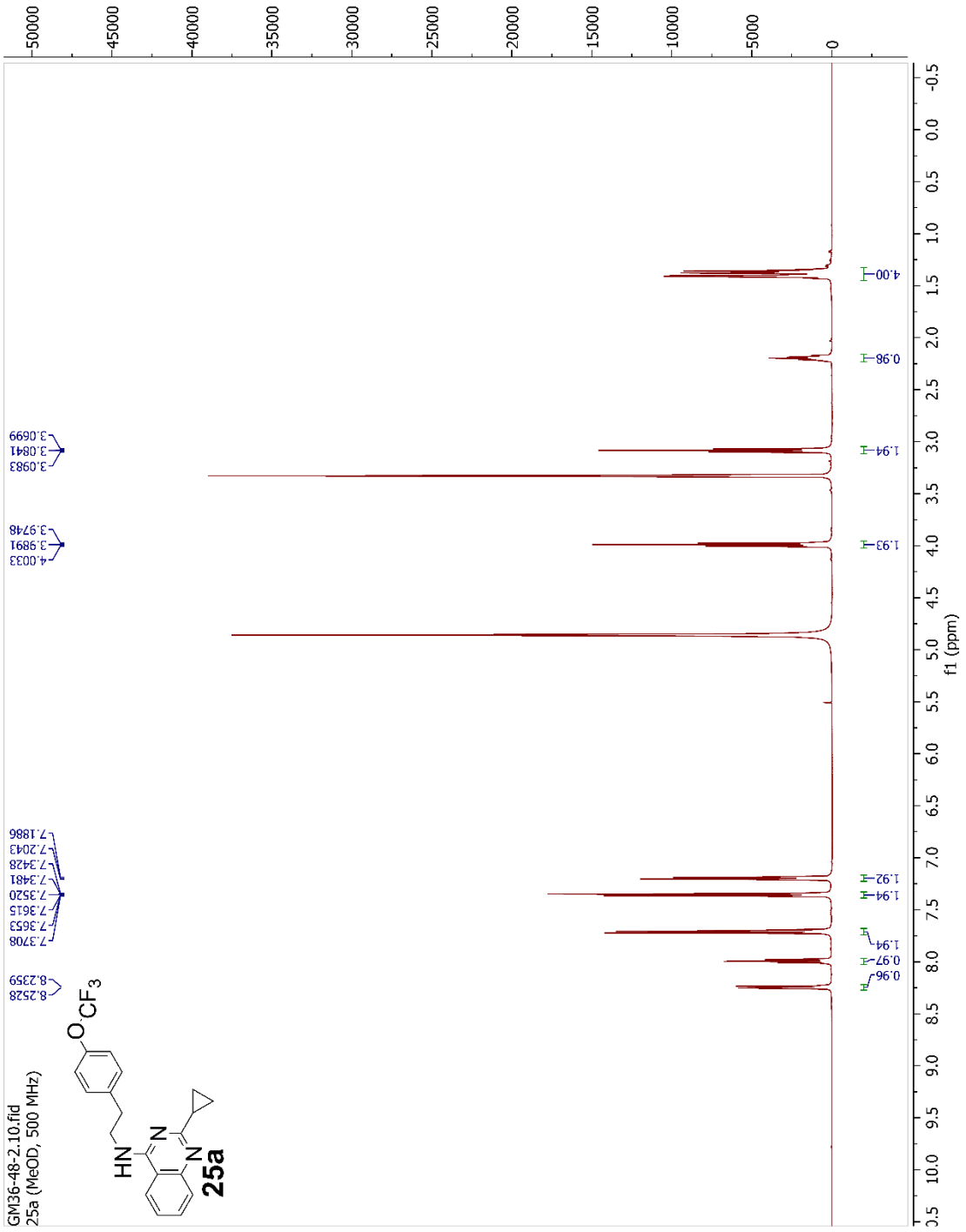

Figure C.55 ^{1}H NMR Spectrum (MeOD, 500 MHz) of **25a**

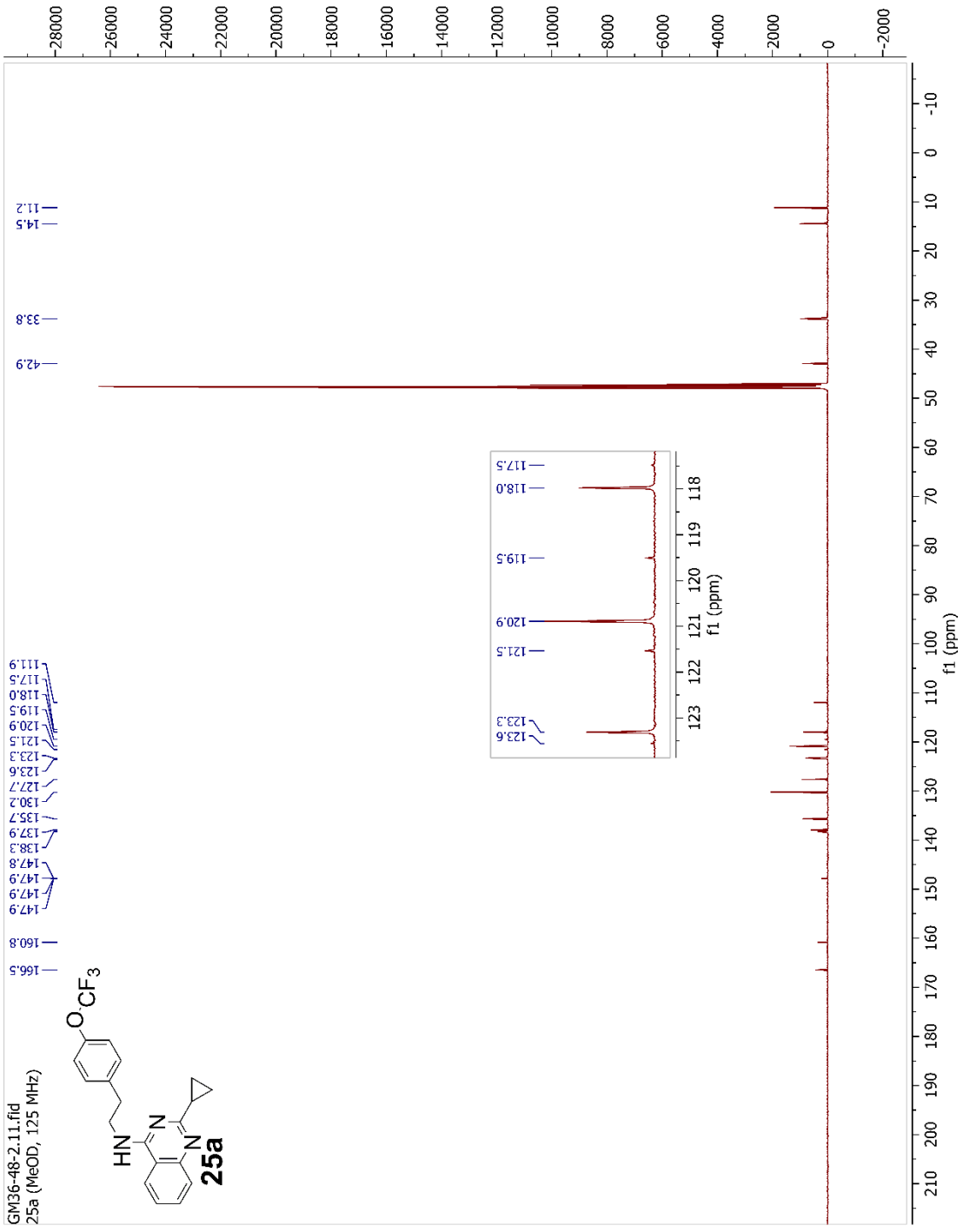

Figure C.56 ^{13}C NMR Spectrum (MeOD, 125 MHz) of **25a**

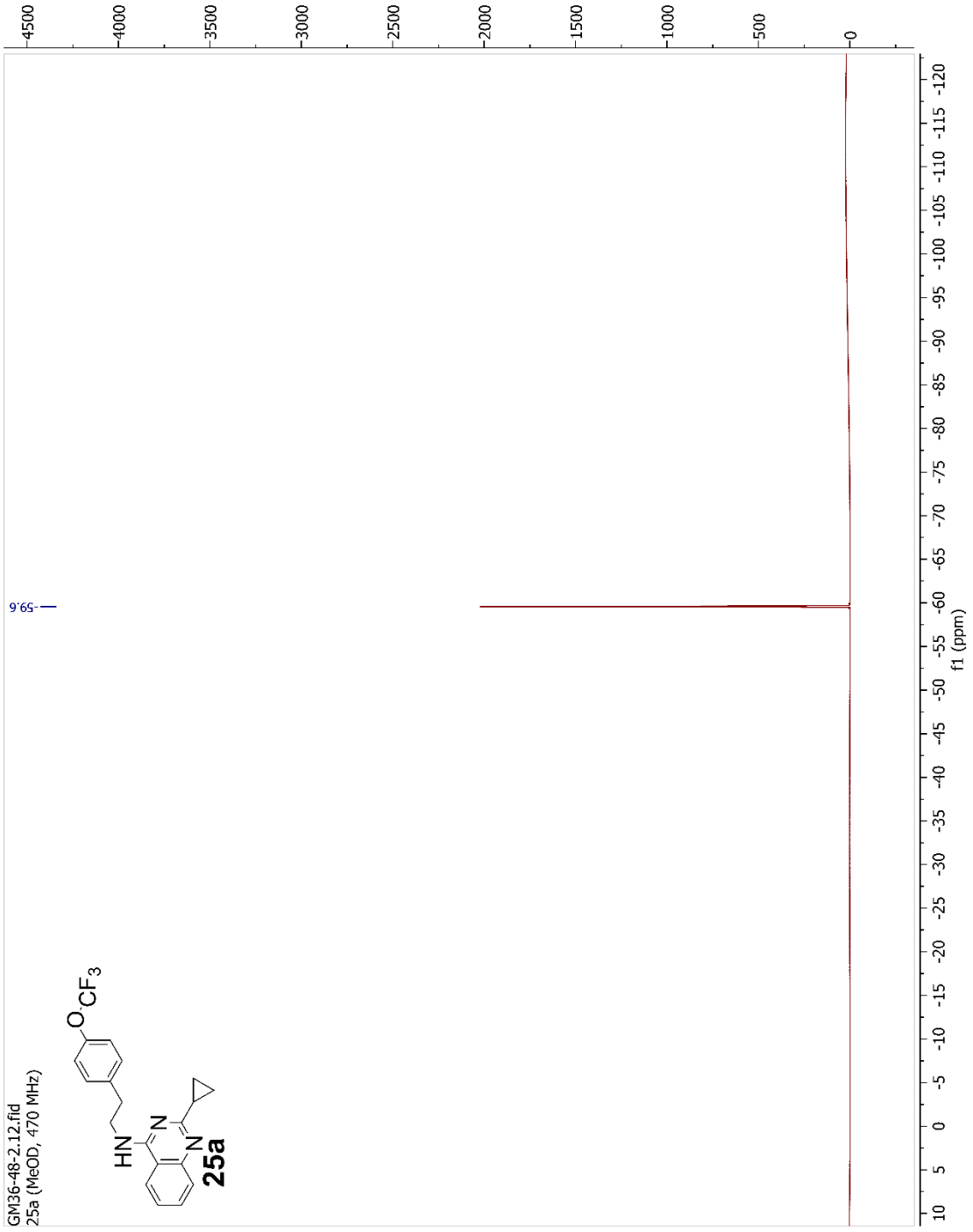

Figure C.57 ^{19}F NMR Spectrum (MeOD, 470 MHz) of **25a**

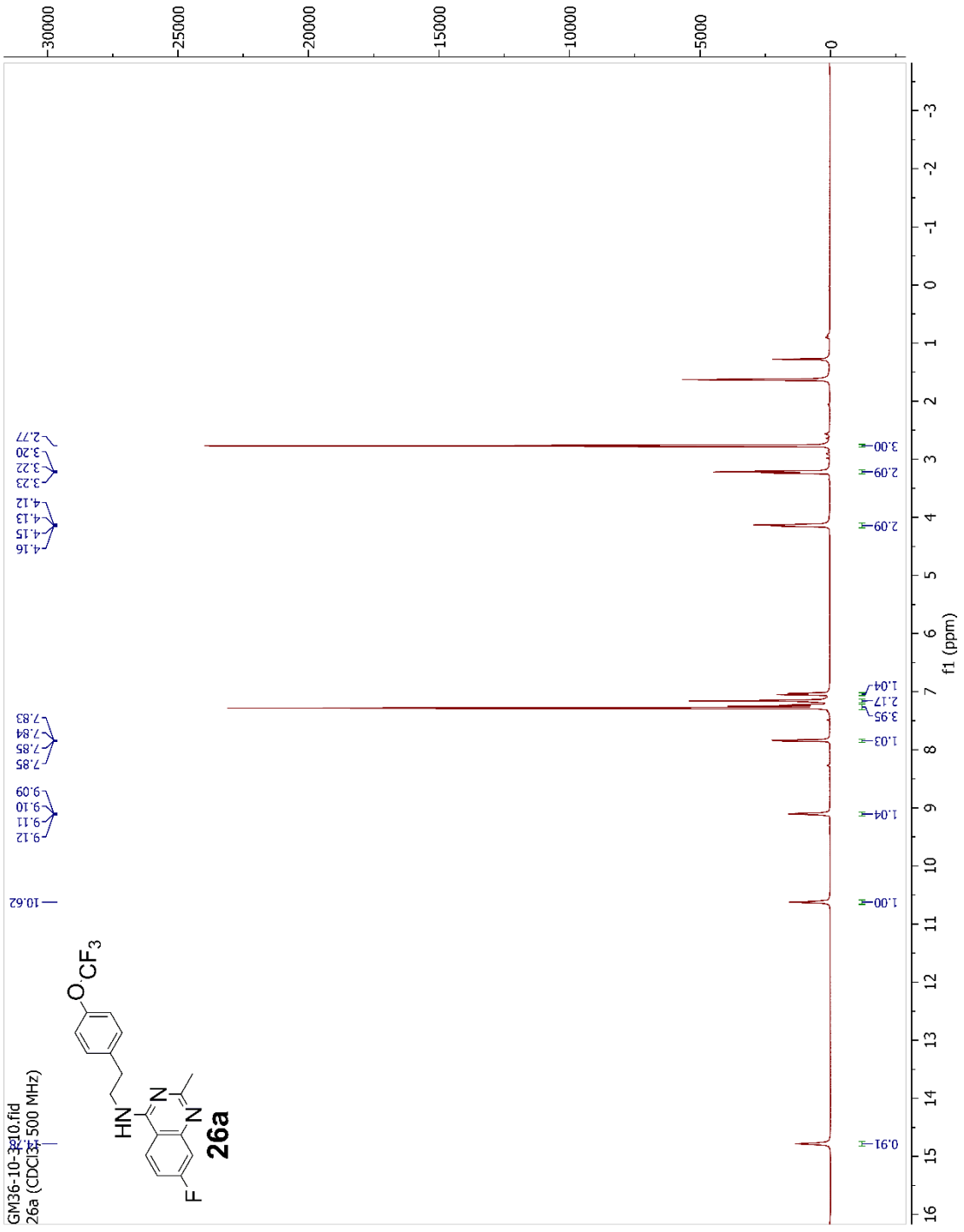

Figure C.58 ^{1}H NMR Spectrum ($CDCl_3$, 500 MHz) of **26a**

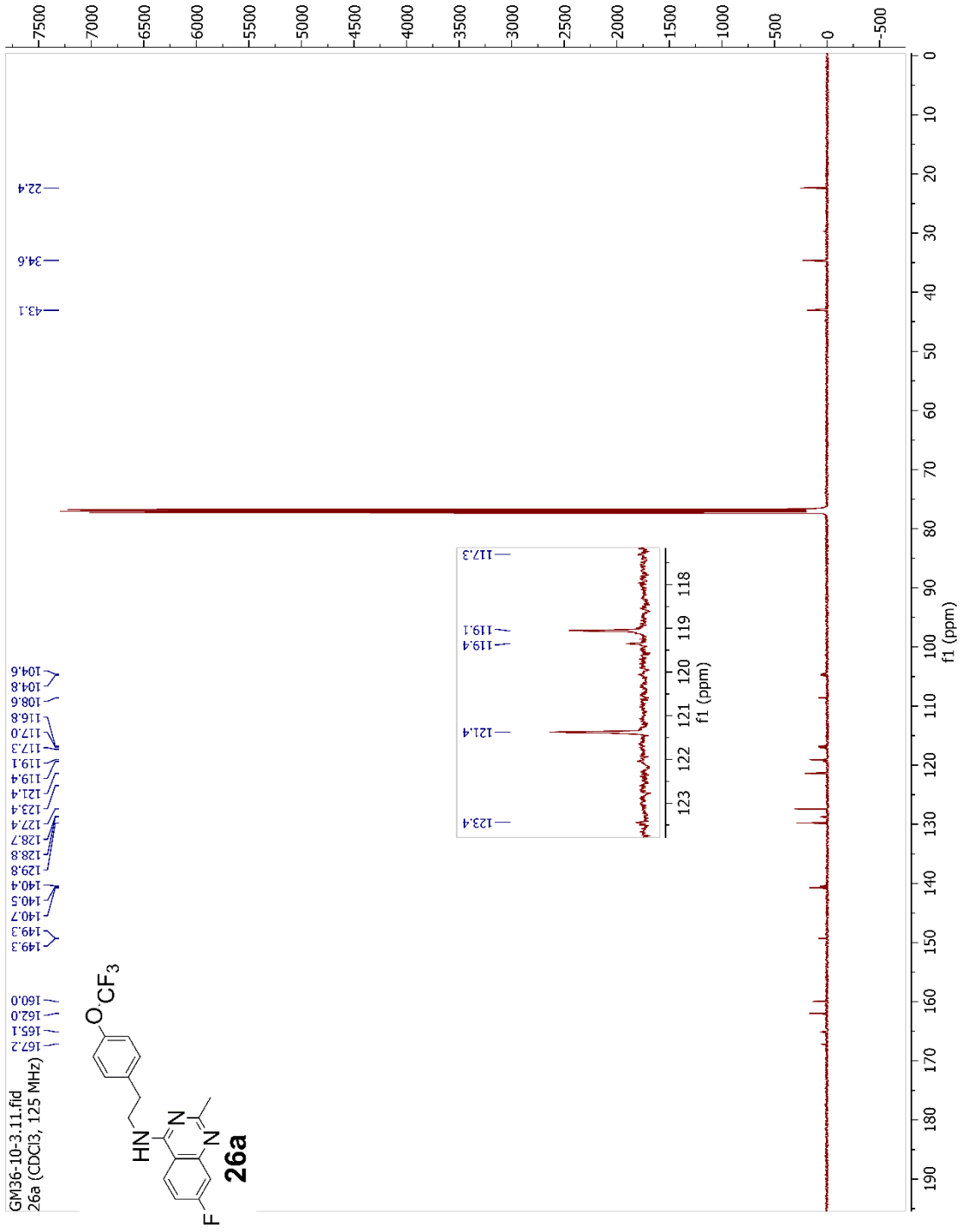

Figure C.59 ^{13}C NMR Spectrum ($CDCl_3$, 125 MHz) of **26a**

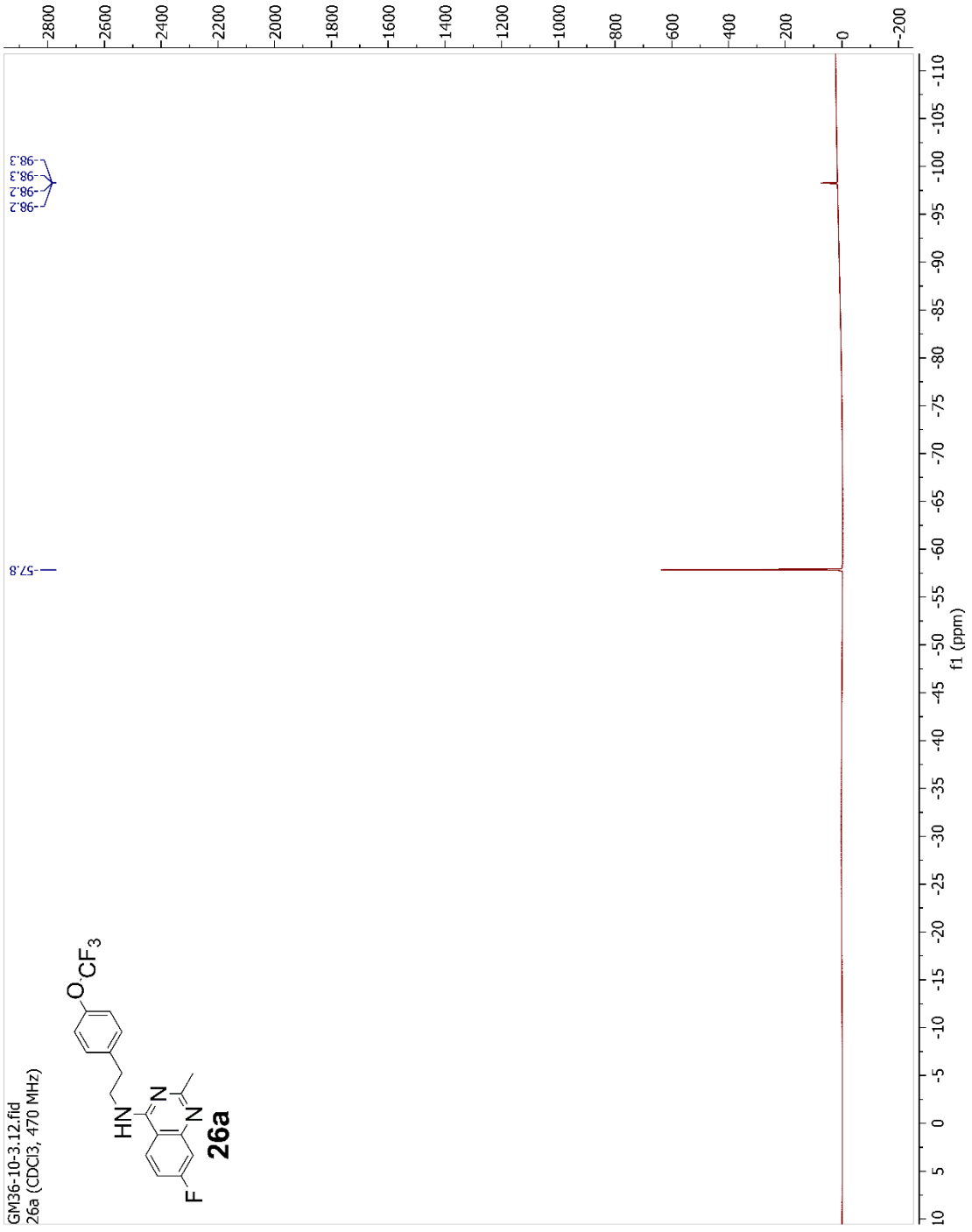

Figure C.60 ^{19}F NMR Spectrum ($CDCl_3$, 470 MHz) of **26a**

ATP Dose Response Curves of Q203

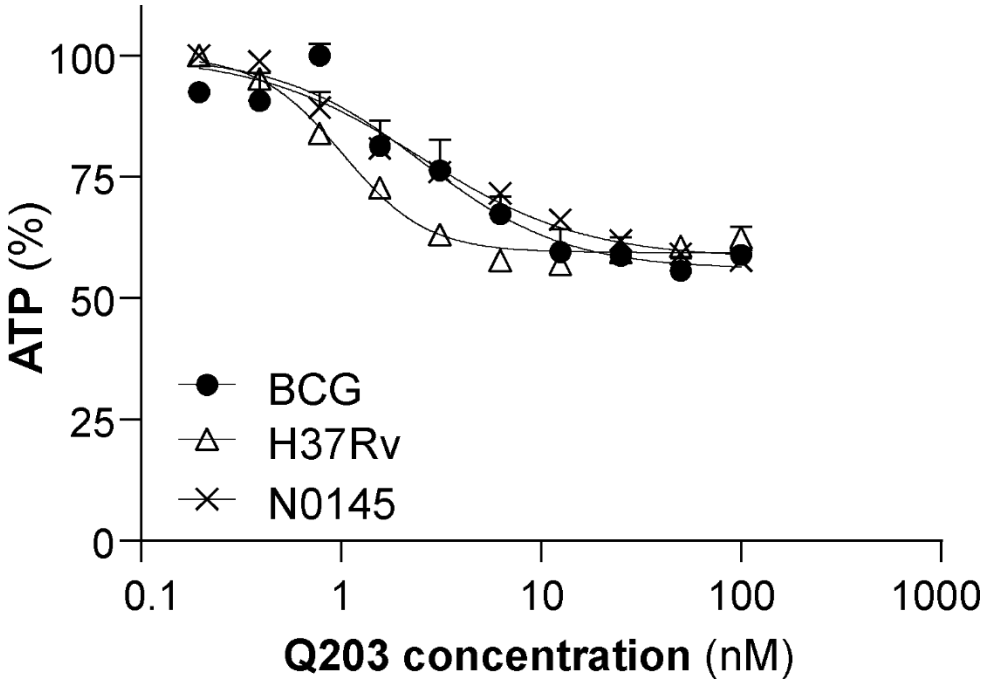

Figure C.61 ATP dose response curves of Q203 in *M. bovis* BCG, *M. tuberculosis* H37Rv, and *M. tuberculosis* N0145

REFERENCES CITED

REFERENCES

1. Organization, W. H., Global Tuberculosis Report 2020. **2020**.

2. Organization, W. H., Global Tuberculosis Report 2021. **2021**.

3. Cambau, E.; Drancourt, M., Steps Towards the Discovery of Mycobacterium Tuberculosis by Robert Koch, 1882. *Clin. Microbiol. Infect.* **2014**, *20*, 196-201.

4. Hershkovitz, I.; Donoghue, H. D.; Minnikin, D. E.; May, H.; Lee, O. Y. C.; Feldman, M.; Galili, E.; Spigelman, M.; Rothschild, B. M.; Bar-Gal, G. K., Tuberculosis Origin: The Neolithic Scenario. *Tuberculosis* **2015**, *95*, S122-S126.

5. Sakula, A., Koch, Robert - Centenary of the Discovery of the Tubercle Bacillus, 1882. *Thorax* **1982**, *37*, 246-251.

6. Barberis, I.; Bragazzi, N. L.; Galluzzo, L.; Martini, M., The History of Tuberculosis: From the First Historical Records to the Isolation of Koch's Bacillus. *Journal of Preventative Medicine and Hygiene* **2017**, *1*, E9-E12.

7. Wong, Y. J.; Noordin, N. M.; Keshavjee, S.; Lee, S. W. H., Impact of Latent Tuberculosis Infection on Health and Wellbeing: A Systematic Review and Meta-Analysis. *Eur. Respir. Rev.* **2021**, *30*, 11.

8. Oxlade, O.; Murray, M., Tuberculosis and Poverty: Why Are the Poor at Greater Risk in India? *PLoS One* **2012**, *7*, 8.

9. Erlinger, S., et al., Tuberculosis Patients with Higher Levels of Poverty Face Equal or Greater Costs of Illness. *Int. J. Tuberc. Lung Dis.* **2019**, *23*, 1205-1212.

10. Ravimohan, S.; Kornfeld, H.; Weissman, D.; Bisson, G. P., Tuberculosis and Lung Damage: From Epidemiology to Pathophysiology. *Eur. Respir. Rev.* **2018**, *27*, 20.

11. Consunji-Araneta, R.; Higgins, R.; Qing, G. F.; Bouhasan, L., Tuberculous Damaged Lung in a Child. *Pediatr. Pulmonol.* **2011**, *46*, 1247-1250.

12. Fennelly, K. P.; Jones-Lopez, E. C., Quantity and Quality of Inhaled Dose Predicts Immunopathology in Tuberculosis. *Front. Immunol.* **2015**, *6*, 13.

13. Eum, S. Y.; Kong, J. H.; Hong, M. S.; Lee, Y. J.; Kim, J. H.; Hwang, S. H.; Cho, S. N.; Via, L. E.; Barry, C. E., Neutrophils Are the Predominant Infected Phagocytic Cells in the Airways of Patients with Active Pulmonary Tb. *Chest* **2010**, *137*, 122-128.

14. Tena, A. F.; Clara, P. C., Deposition of Inhaled Particles in the Lungs. *Arch. Bronconeumol.* **2012**, *48*, 240-246.

15. Awuh, J. A.; Flo, T. H., Molecular Basis of Mycobacterial Survival in Macrophages. *Cell. Mol. Life Sci.* **2017**, *74*, 1625-1648.

16. Schnappinger, D., et al., Transcriptional Adaptation of Mycobacterium Tuberculosis within Macrophages: Insights into the Phagosomal Environment. *J. Exp. Med.* **2003**, *198*, 693-704.

17. Fontan, P.; Aris, V.; Ghanny, S.; Soteropoulos, P.; Smith, I., Global Transcriptional Profile of Mycobacterium Tuberculosis During Thp-1 Human Macrophage Infection. *Infect. Immun.* **2008**, *76*, 717-725.

18. Devi, P.; Khan, A.; Chattopadhyay, P.; Mehta, P.; Sahni, S.; Sharma, S.; Pandey, R., Co-Infections as Modulators of Disease Outcome: Minor Players or Major Players? *Front. Microbiol.* **2021**, *12*, 13.

19. Resende, L. S. O.; dos Santos-Neto, E. T., Risk Factors Associated with Adverse Reactions to Antituberculosis Drugs. *J. Bras. Pneumol.* **2015**, *41*, 77-89.

20. Amelio, P., et al., Hiv Infection Functionally Impairs Mycobacterium Tuberculosis-Specific Cd4 and Cd8 T-Cell Responses. *J. Virol.* **2019**, *93*, 18.

21. Cantini, F.; Nannini, C.; Niccoli, L.; Petrone, L.; Ippolito, G.; Goletti, D., Risk of Tuberculosis Reactivation in Patients with Rheumatoid Arthritis, Ankylosing Spondylitis, and Psoriatic Arthritis Receiving Non-Anti-Tnf-Targeted Biologics. *Mediat. Inflamm.* **2017**, *2017*, 15.

22. Vilcheze, C.; Kremer, L., Acid-Fast Positive and Acid-Fast Negative Mycobacterium Tuberculosis: The Koch Paradox. *Microbiol. Spectr.* **2017**, *5*, 14.

23. Batt, S. M.; Minnikin, D. E.; Besra, G. S., The Thick Waxy Coat of Mycobacteria, a Protective Layer against Antibiotics and the Host's Immune System. *Biochem. J.* **2020**, *477*, 1983-2006.

24. Guenin-Mace, L.; Simeone, R.; Demangel, C., Lipids of Pathogenic Mycobacteria: Contributions to Virulence and Host Immune Suppression. *Transbound. Emerg. Dis.* **2009**, *56*, 255-268.

25. Franco, A. R.; Peri, F., Developing New Anti-Tuberculosis Vaccines: Focus on Adjuvants. *Cells* **2021**, *10*, 17.

26. Cho, T.; Khatchadourian, C.; Nguyen, H.; Dara, Y.; Jung, S. N.; Venketaraman, V., A Review of the Bcg Vaccine and Other Approaches toward Tuberculosis Eradication. *Human Vaccines Immunother.* **2021**, *17*, 2454-2470.

27. Mangtani, P., et al., Protection by Bcg Vaccine against Tuberculosis: A Systematic Review of Randomized Controlled Trials. *Clin. Infect. Dis.* **2014**, *58*, 470-480.

28. Davenne, T.; McShane, H., Why Don't We Have an Effective Tuberculosis Vaccine Yet? *Expert Rev. Vaccines* **2016**, *15*, 1009-1013.

29. Anastasopoulou, A.; Ziogas, D. C.; Samarkos, M.; Kirkwood, J. M.; Gogas, H., Reactivation of Tuberculosis in Cancer Patients Following Administration of Immune Checkpoint Inhibitors: Current Evidence and Clinical Practice Recommendations. *J. Immunother. Cancer* **2019**, *7*, 13.

30. Cheng, M. P.; Chakra, C. N. A.; Yansouni, C. P.; Cnossen, S.; Shrier, I.; Menzies, D.; Greenaway, C., Risk of Active Tuberculosis in Patients with Cancer: A Systematic Review and Metaanalysis. *Clin. Infect. Dis.* **2017**, *64*, 635-644.

31. Lau, K. S., et al., Tuberculosis Reactivation at Ileum Following Immune Checkpoint Inhibition with Pembrolizumab for Metastatic Nasopharyngeal Carcinoma: A Case Report. *BMC Infect. Dis.* **2021**, *21*, 5.

32. Lee, H. Y.; Kim, J. W.; Yeo, C. D., A Case of Tuberculosis Reactivation Suspected of Cancer Progression During Oral Tyrosine Kinase Inhibitor Treatment in a Patient Diagnosed as Non-Small Cell Lung Cancer. *J. Thorac. Dis.* **2017**, *9*, E709-E713.

33. Hashimoto, M., et al., Reactivation of Latent Tuberculosis Infection Induced by Cabazitaxel in a Patient with Prostate Cancer a Case Report. *Medicine (Baltimore)* **2019**, *98*, 4.

34. Jacobs, R. E. A.; Gu, P.; Chachoua, A., Reactivation of Pulmonary Tuberculosis During Cancer Treatment. *Int. J. Mycobact.* **2015**, *4*, 337-340.

35. Martin, C., The Dream of a Vaccine against Tuberculosis; New Vaccines Improving or Replacing Bcg? *Eur. Resp. J.* **2005**, *26*, 162-167.

36. Stewart, E.; Triccas, J. A.; Petrovsky, N., Adjuvant Strategies for More Effective Tuberculosis Vaccine Immunity. *Microorganisms* **2019**, *7*, 16.

37. Tameris, M. D., et al., Safety and Efficacy of Mva85a, a New Tuberculosis Vaccine, in Infants Previously Vaccinated with Bcg: A Randomised, Placebo-Controlled Phase 2b Trial. *Lancet* **2013**, *381*, 1021-1028.

38. Schrager, L. K.; Vekemens, J.; Drager, N.; Lewinsohn, D. M.; Olesen, O. F., The Status of Tuberculosis Vaccine Development. *Lancet Infect. Dis.* **2020**, *20*, E28-E37.

39. Sable, S. B.; Posey, J. E.; Scriba, T. J., Tuberculosis Vaccine Development: Progress in Clinical Evaluation. *Clin. Microbiol. Rev.* **2020**, *33*, 30.

40. Lobue, P.; Menzies, D., Treatment of Latent Tuberculosis Infection: An Update. *Respirology* **2010**, *15*, 603-622.

41. Cerrone, M.; Bracchi, M.; Wasserman, S.; Pozniak, A.; Meintjes, G.; Cohen, K.; Wilkinson, R. J., Safety Implications of Combined Antiretroviral and Anti-Tuberculosis Drugs. *Expert Opin. Drug Saf.* **2020**, *19*, 23-41.

42. Wang, P. C.; Pradhan, K.; Zhong, X. B.; Ma, X. C., Isoniazid Metabolism and Hepatotoxicity. *Acta Pharm. Sin. B* **2016**, *6*, 384-392.

43. Saraf, G.; Akshata, J. S.; Kuruthukulangara, S.; Thippeswamy, H.; Reddy, S. K.; Buggi, S.; Chaturvedi, S. K., Cycloserine Induced Delirium During Treatment of Multi-Drug Resistant Tuberculosis (Mdr-Tb). *Egypt. J. Chest Dis. Tuberc.* **2015**, *64*, 449-451.

44. Chan, R. Y. C.; Kwok, A. K. H., Ocular Toxicity of Ethambutol. *Hong Kong Medical Journal* **2006**, *12*, 56-60.

45. Yee, D.; Valiquette, C.; Pelletier, M.; Parisien, I.; Rocher, I.; Menzies, D., Incidence of Serious Side Effects from First-Line Antituberculosis Drugs among Patients Treated for Active Tuberculosis. *Am. J. Respir. Crit. Care Med.* **2003**, *167*, 1472-1477.

46. Schaberg, T.; Rebhan, K.; Lode, H., Risk Factors for Side-Effects of Isoniazid, Rifampin and Pyrazinamide in Patients Hospitalized for Pulmonary Tuberculosis. *Eur. Resp. J.* **1996**, *9*, 2026-2030.

47. Gholami, K.; Kamali, E.; Hajiabdolbaghi, M.; Shalviri, G., Evaluation of Anti-Tuberculosis Induced Adverse Reactions in Hospitalized Patients. *Pharm Pract (Granada)* **2006**, *4*, 134-8.

48. Javadi, M. R.; Shalviri, G.; Gholami, K.; Salamzadeh, J.; Maghooli, G.; Mirsaeedi, S. M., Adverse Reactions of Anti Tuberculosis Drugs in Hospitalized Patients: Incidence, Severity and Risk Factors. *Pharmacoepidemiol. Drug Saf.* **2007**, *16*, 1104-1110.

49. Citron, K. M.; Thomas, G. O., Ocular Toxicity from Ethambutol. *Thorax* **1986**, *41*, 737-739.

50. Arbex, M. A.; Varella, M. D. L.; de Siqueira, H. R.; de Mello, F. A. F., Antituberculosis Drugs: Drug Interactions, Adverse Effects, and Use in Special Situations. Part 1: First-Line Drugs. *J. Bras. Pneumol.* **2010**, *36*, 626-640.

51. Cox, H. S.; Furin, J. J.; Mitnick, C. D.; Daniels, C.; Cox, V.; Goemaere, E., The Need to Accelerate Access to New Drugs for Multidrug-Resistant Tuberculosis. *Bull. World Health Organ.* **2015**, *93*, 491-497.

52. Belard, S.; Janssen, S.; Osbak, K. K.; Adegnika, A. A.; Ondounda, M.; Grobusch, M. P., Limited Access to Drugs for Resistant Tuberculosis: A Call to Action. *J. Public Health* **2015**, *37*, 691-693.

53. Ramma, L.; Cox, H.; Wilkinson, L.; Foster, N.; Cunnama, L.; Vassall, A.; Sinanovic, E., Patients' Costs Associated with Seeking and Accessing Treatment for Drug-Resistant Tuberculosis in South Africa. *Int. J. Tuberc. Lung Dis.* **2015**, *19*, 1513-1519.

54. Marais, B. J., Improving Access to Tuberculosis Preventive Therapy and Treatment for Children. *Int. J. Infect. Dis.* **2017**, *56*, 122-125.

55. Byun, J. Y.; Kim, H. L.; Lee, E. K.; Kwon, S. H., A Systematic Review of Economic Evaluations of Active Tuberculosis Treatments. *Front. Pharmacol.* **2021**, *12*, 14.

56. Sotgiu, G., et al., Faster for Less: The New "Shorter" Regimen for Multidrug-Resistant Tuberculosis. *Eur. Resp. J.* **2016**, *48*, 1503-1507.

57. Organization, W. H., *Companion Handbook to the Who Guidelines for the Programmatic Management of Drug-Resistant Tuberculosis*: Geneva, Switzerland, 2014.

58. *Who Consolidated Guidelines on Drug-Resistant Tuberculosis Treatment*; World Health Organization: Geneva, 2019.

59. Organization, W. H., Global Tuberculosis Report 2018. 2018; Vol. Licence: CC BY-NCSA 3.0 IGO.

60. Iacobino, A.; Fattorini, L.; Giannoni, F., Drug-Resistant Tuberculosis 2020: Where We Stand. *Appl. Sci.-Basel* **2020**, *10*, 17.

61. Bloemberg; Keller; Stucki, Acquired Resistance to Bedaquiline and Delamanid in Therapy for Tuberculosis (Vol 373, Pg 1986, 2015). *N. Engl. J. Med.* **2015**, *373*, 1.

62. Hasenoehrl, E. J.; Wiggins, T. J.; Berney, M., Bioenergetic Inhibitors: Antibiotic Efficacy and Mechanisms of Action in Mycobacterium Tuberculosis. *Front. Cell. Infect. Microbiol.* **2021**, *10*, 26.

63. Nobre, A.; Alarico, S.; Maranha, A.; Mendes, V.; Empadinhas, N., The Molecular Biology of Mycobacterial Trehalose in the Quest for Advanced Tuberculosis Therapies. *Microbiology-(UK)* **2014**, *160*, 1547-1570.

64. Sacksteder, K. A.; Protopopova, M.; Barry, C. E.; Andries, K.; Nacy, C. A., Discovery and Development of Sq109: A New Antitubercular Drug with a Novel Mechanism of Action. *Future Microbiol.* **2012**, *7*, 823-837.

65. Yendapally, R.; Lee, R. E., Design, Synthesis, and Evaluation of Novel Ethambutol Analogues. *Bioorg. Med. Chem. Lett.* **2008**, *18*, 1607-1611.

66. Zhang, Y.; Shi, W. L.; Zhang, W. H.; Mitchison, D., Mechanisms of Pyrazinamide Action and Resistance. *Microbiol. Spectr.* **2014**, *2*, 12.

67. Zhang, Y.; Wade, M. M.; Scorpio, A.; Zhang, H.; Sun, Z. H., Mode of Action of Pyrazinamide: Disruption of Mycobacterium Tuberculosis Membrane Transport and Energetics by Pyrazinoic Acid. *J. Antimicrob. Chemother.* **2003**, *52*, 790-795.

68. Stehr, M.; Elamin, A. A.; Singh, M., Pyrazinamide: The Importance of Uncovering the Mechanisms of Action in Mycobacteria. *Expert Rev. Anti-Infect. Ther.* **2015**, *13*, 593-603.

69. Barros, I. L. E., et al., Panb over-Representation as Part of Pyrazinamide Action: A Proteomic Insight. *Future Microbiol.* **2021**, *16*, 1303-1308.

70. Jelinska, A.; Zajac, M.; Dadej, A.; Tomczak, S.; Geszke-Moritz, M.; Muszalska-Kolos, I., Tuberculosis - Present Medication and Therapeutic Prospects. *Curr. Med. Chem.* **2020**, *27*, 630-656.

71. Druszczynska, M.; Kowalski, K.; Wawrocki, S.; Fol, M., Diversity and Functionality of Mycobacterial Mycolic Acids in Relation to Host-Pathogen Interactions. *Curr. Med. Chem.* **2017**, *24*, 4267-4278.

72. Glickman, M. S.; Jacobs, W. R., Microbial Pathogenesis of Mycobacterium Tuberculosis: Dawn of a Discipline. *Cell* **2001**, *104*, 477-485.

73. Bansal-Mutalik, R.; Nikaido, H., Mycobacterial Outer Membrane Is a Lipid Bilayer and the Inner Membrane Is Unusually Rich in Diacyl Phosphatidylinositol Dimannosides. *Proc. Natl. Acad. Sci. U. S. A.* **2014**, *111*, 4958-4963.

74. Cambier, C. J.; Takaki, K. K.; Larson, R. P.; Hernandez, R. E.; Tobin, D. M.; Urdahl, K. B.; Cosma, C. L.; Ramakrishnan, L., Mycobacteria Manipulate Macrophage Recruitment through Coordinated Use of Membrane Lipids. *Nature* **2014**, *505*, 218-+.

75. Lerner, T. R.; Borel, S.; Gutierrez, M. G., The Innate Immune Response in Human Tuberculosis. *Cell Microbiol.* **2015**, *17*, 1277-1285.

76. Philips, J. A.; Ernst, J. D., Tuberculosis Pathogenesis and Immunity. In *Annual Review of Pathology: Mechanisms of Disease, Vol 7*, Abbas, A. K.; Galli, S. J.; Howley, P. M., Eds. Annual Reviews: Palo Alto, 2012; Vol. 7, pp 353-384.

77. Lerner, T. R.; Borel, S.; Greenwood, D. J.; Repnik, U.; Russell, M. R. G.; Herbst, S.; Jones, M. L.; Collinson, L. M.; Griffiths, G.; Gutierrez, M. G., Mycobacterium Tuberculosis Replicates within Necrotic Human Macrophages. *J. Cell Biol.* **2017**, *216*, 583-594.

78. Lerner, T. R., et al., Lymphatic Endothelial Cells Are a Replicative Niche for Mycobacterium Tuberculosis. *J. Clin. Invest.* **2016**, *126*, 1093-1108.

79. Tornack, J.; Reece, S. T.; Bauer, W. M.; Vogelzang, A.; Bandermann, S.; Zedler, U.; Stingl, G.; Kaufmann, S. H. E.; Melchers, F., Human and Mouse Hematopoietic Stem Cells Are a Depot for Dormant Mycobacterium Tuberculosis. *PLoS One* **2017**, *12*, 18.

80. Das, B.; Kashino, S. S.; Pulu, I.; Kalita, D.; Swami, V.; Yeger, H.; Felsher, D. W.; Campos-Neto, A., Cd271(+) Bone Marrow Mesenchymal Stem Cells May Provide a Niche for Dormant Mycobacterium Tuberculosis. *Sci. Transl. Med.* **2013**, *5*, 10.

81. Neyrolles, O., et al., Is Adipose Tissue a Place for Mycobacterium Tuberculosis Persistence? *PLoS One* **2006**, *1*, 9.

82. North, E. J.; Jackson, M.; Lee, R. E., New Approaches to Target the Mycolic Acid Biosynthesis Pathway for the Development of Tuberculosis Therapeutics. *Curr. Pharm. Design* **2014**, *20*, 4357-4378.

83. Banerjee, A.; Dubnau, E.; Quemard, A.; Balasubramanian, V.; Um, K. S.; Wilson, T.; Collins, D.; Delisle, G.; Jacobs, W. R., Inha, a Gene Encoding a Target for Isoniazid and Ethionamide in Mycobacterium Tuberculosis. *Science* **1994**, *263*, 227-230.

84. Larsen, M. H., et al., Overexpression of Inha, but Not Kasa, Confers Resistance to Isoniazid and Ethionamide in Mycobacterium Smegmatis, M-Bovis Bcg and M-Tuberculosis. *Mol. Microbiol.* **2002**, *46*, 453-466.

85. Stehr, M.; Elamin, A. A.; Singh, M., Filling the Pipeline - New Drugs for an Old Disease. *Curr. Top. Med. Chem.* **2014**, *14*, 110-129.

86. Bruning, J. B.; Murillo, A. C.; Chacon, O.; Barletta, R. G.; Sacchettini, J. C., Structure of the Mycobacterium Tuberculosis D-Alanine:D-Alanine Ligase, a Target of the Antituberculosis Drug D-Cycloserine. *Antimicrob. Agents Chemother.* **2011**, *55*, 291-301.

87. Prosser, G. A.; de Carvalho, L. P. S., Kinetic Mechanism and Inhibition of Mycobacterium Tuberculosis D-Alanine:D-Alanine Ligase by the Antibiotic D-Cycloserine. *Febs J.* **2013**, *280*, 1150-1166.

88. Kurosu, M.; Mahapatra, S.; Narayanasamy, P.; Crick, D. C., Chemoenzymatic Synthesis of Park's Nucleotide: Toward the Development of High-Throughput Screening for Mray Inhibitors. *Tetrahedron Lett.* **2007**, *48*, 799-803.

89. Dini, C., Mray Inhibitors as Novel Antibacterial Agents. *Curr. Top. Med. Chem.* **2005**, *5*, 1221-1236.

90. Singh, P.; Rameshwaram, N. R.; Ghosh, S.; Mukhopadhyay, S., Cell Envelope Lipids in the Pathophysiology of Mycobacterium Tuberculosis. *Future Microbiol.* **2018**, *13*, 689-710.

91. Reynolds, P. E., Structure, Biochemistry and Mechanism of Action of Glycopeptide Antibiotics. *Eur. J. Clin. Microbiol. Infect. Dis.* **1989**, *8*, 943-950.

92. Wiedemann, I.; Breukink, E.; van Kraaij, C.; Kuipers, O. P.; Bierbaum, G.; de Kruijff, B.; Sahl, H. G., Specific Binding of Nisin to the Peptidoglycan Precursor Lipid Ii Combines Pore Formation and Inhibition of Cell Wall Biosynthesis for Potent Antibiotic Activity. *J. Biol. Chem.* **2001**, *276*, 1772-1779.

93. Lo, M. C.; Men, H.; Branstrom, A.; Helm, J.; Yao, N.; Goldman, R.; Walker, S., A New Mechanism of Action Proposed for Ramoplanin. *J. Am. Chem. Soc.* **2000**, *122*, 3540-3541.

94. Banerjee, D. K.; Scher, M. G.; Waechter, C. J., Amphomycin - Effect of the Lipopeptide Antibiotic on the Glycosylation and Extraction of Dolichyl Monophosphate in Calf Brain Membranes. *Biochemistry* **1981**, *20*, 1561-1568.

95. Wilson, R., et al., Antituberculosis Thiophenes Define a Requirement for Pks13 in Mycolic Acid Biosynthesis. *Nat. Chem. Biol.* **2013**, *9*, 499-U60.

96. Stanley, S. A., et al., Diarylcoumarins Inhibit Mycolic Acid Biosynthesis and Kill Mycobacterium Tuberculosis by Targeting Fadd32. *Proc. Natl. Acad. Sci. U. S. A.* **2013**, *110*, 11565-11570.

97. Zhang, Q.; Liu, Y. D.; Tang, S. J.; Sha, W.; Xiao, H. P., Clinical Benefit of Delamanid (Opc-67683) in the Treatment of Multidrug-Resistant Tuberculosis Patients in China. *Cell Biochem. Biophys.* **2013**, *67*, 957-963.

98. Stover, C. K., et al., A Small-Molecule Nitroimidazopyran Drug Candidate for the Treatment of Tuberculosis. *Nature* **2000**, *405*, 962-966.

99. Mdluli, K.; Kaneko, T.; Upton, A., The Tuberculosis Drug Discovery and Development Pipeline and Emerging Drug Targets. *Cold Spring Harb. Perspect. Med.* **2015**, *5*, 24.

100. La Rosa, V., et al., Mmpl3 Is the Cellular Target of the Antitubercular Pyrrole Derivative Bm212. *Antimicrob. Agents Chemother.* **2012**, *56*, 324-331.

101. Grzegorzewicz, A. E., et al., Inhibition of Mycolic Acid Transport across the Mycobacterium Tuberculosis Plasma Membrane. *Nat. Chem. Biol.* **2012**, *8*, 334-341.

102. Stanley, S. A., et al., Identification of Novel Inhibitors of M. Tuberculosis Growth Using Whole Cell Based High-Throughput Screening. *ACS Chem. Biol.* **2012**, *7*, 1377-1384.

103. Li, W.; Sanchez-Hidalgo, A.; Jones, V.; de Moura, V. C. N.; North, E. J.; Jackson, M., Synergistic Interactions of Mmpl3 Inhibitors with Antitubercular Compounds in Vitro. *Antimicrob. Agents Chemother.* **2017**, *61*, 6.

104. Warrier, T., et al., Antigen 85c Inhibition Restricts Mycobacterium Tuberculosis Growth through Disruption of Cord Factor Biosynthesis. *Antimicrob. Agents Chemother.* **2012**, *56*, 1735-1743.

105. Favrot, L.; Ronning, D. R., Targeting the Mycobacterial Envelope for Tuberculosis Drug Development. *Expert Rev. Anti-Infect. Ther.* **2012**, *10*, 1023-1036.

106. Lechartier, B.; Hartkoorn, R. C.; Cole, S. T., In Vitro Combination Studies of Benzothiazinone Lead Compound Btz043 against Mycobacterium Tuberculosis. *Antimicrob. Agents Chemother.* **2012**, *56*, 5790-5793.

107. Wolf, J. E., High Altitude in the Treatment of Tuberculosis. *Schweiz. Med. Wochenschr.* **1946**, *76*, 870-873.

108. Amrein, O., The High Altitude Treatment of Pulmonary Tuberculosis. *Br. Med. J.* **1929**, *1929*, 1188-1191.

109. Shi, L. B.; Sohaskey, C. D.; Kana, B. D.; Dawes, S.; North, R. J.; Mizrahi, V.; Gennaro, M. L., Changes in Energy Metabolism of Mycobacterium Tuberculosis in Mouse Lung and under in Vitro Conditions Affecting Aerobic Respiration. *Proc. Natl. Acad. Sci. U. S. A.* **2005**, *102*, 15629-15634.

110. Gomez, J. E.; McKinney, J. D., M-Tuberculosis Persistence, Latency, and Drug Tolerance. *Tuberculosis* **2004**, *84*, 29-44.

111. Berney, M.; Cook, G. M., Respiration and Oxidative Phosphorylation in Mycobacteria. In *Structural Basis of Biological Energy Generation*, HohmannMarriott, M. F., Ed. Springer: Dordrecht, 2014; Vol. 39, pp 277-293.

112. Bald, D.; Villellas, C.; Lu, P.; Koul, A., Targeting Energy Metabolism in Mycobacterium Tuberculosis, a New Paradigm in Antimycobacterial Drug Discovery. *mBio* **2017**, *8*, 11.

113. Wayne, L. G.; Sohaskey, C. D., Nonreplicating Persistence of Mycobacterium Tuberculosis. *Annu. Rev. Microbiol.* **2001**, *55*, 139-163.

114. Yano, T.; Kassovska-Bratinova, S.; Teh, J. S.; Winkler, J.; Sullivan, K.; Isaacs, A.; Schechter, N. M.; Rubin, H., Reduction of Clofazimine by Mycobacterial Type 2 Nadh: Quinone Oxidoreductase a Pathway for the Generation of Bactericidal Levels of Reactive Oxygen Species. *J. Biol. Chem.* **2011**, *286*, 10276-10287.

115. Beites, T., et al., Plasticity of the Mycobacterium Tuberculosis Respiratory Chain and Its Impact on Tuberculosis Drug Development. *Nat. Commun.* **2019**, *10*, 12.

116. Arora, K., et al., Respiratory Flexibility in Response to Inhibition of Cytochrome C Oxidase in Mycobacterium Tuberculosis. *Antimicrob. Agents Chemother.* **2014**, *58*, 6962-6965.

117. Koul, A., et al., Diarylquinolines Target Subunit C of Mycobacterial Atp Synthase. *Nat. Chem. Biol.* **2007**, *3*, 323-324.

118. Kalia, N. P., et al., Exploiting the Synthetic Lethality between Terminal Respiratory Oxidases to Kill Mycobacterium Tuberculosis and Clear Host Infection. *Proc. Natl. Acad. Sci. U. S. A.* **2017**, *114*, 7426-7431.

119. Pethe, K., et al., Discovery of Q203, a Potent Clinical Candidate for the Treatment of Tuberculosis. *Nat. Med.* **2013**, *19*, 1157-1160.

120. de Jager, V. R.; Dawson, R.; van Niekerk, C.; Hutchings, J.; Kim, J.; Vanker, N.; van der Merwe, L.; Choi, J.; Nam, K.; Diacon, A. H., Telacebec (Q203), a New Antituberculosis Agent. *N. Engl. J. Med.* **2020**, *382*, 1280-1281.

121. Lu, P.; Asseri, A. H.; Kremer, M.; Maaskant, J.; Ummels, R.; Lill, H.; Bald, D., The Anti-Mycobacterial Activity of the Cytochrome Bcc Inhibitor Q203 Can Be Enhanced by Small-Molecule Inhibition of Cytochrome Bd. *Sci Rep* **2018**, *8*, 7.

122. Matsoso, L. G.; Kana, B. D.; Crellin, P. K.; Lea-Smith, D. J.; Pelosi, A.; Powell, D.; Dawes, S. S.; Rubin, H.; Coppel, R. L.; Mizrahi, V., Function of the Cytochrome Bc(1)-Aa(3) Branch of the Respiratory Network in Mycobacteria and Network Adaptation Occurring in Response to Its Disruption. *J. Bacteriol.* **2005**, *187*, 6300-6308.

123. Mascolo, L.; Bald, D., Cytochrome Bd in Mycobacterium Tuberculosis: A Respiratory Chain Protein Involved in the Defense against Antibacterials. *Prog. Biophys. Mol. Biol.* **2020**, *152*, 55-63.

124. Lee, B. S., et al., Dual Inhibition of the Terminal Oxidases Eradicates Antibiotic-Tolerant Mycobacterium Tuberculosis. *Embo Molecular Medicine* **2021**, *13*, 16.

125. Topliss, J. G., Utilization of Operational Schemes for Analog Synthesis in Drug Design. *J. Med. Chem.* **1972**, *15*, 1006-1011.

126. Bunally, S. B.; Luscombe, C. N.; Young, R. J., Using Physicochemical Measurements to Influence Better Compound Design. *SLAS Discov.* **2019**, *24*, 791-801.

127. Meanwell, N. A., Improving Drug Candidates by Design: A Focus on Physicochemical Properties as a Means of Improving Compound Disposition and Safety. *Chem. Res. Toxicol.* **2011**, *24*, 1420-1456.

128. Safarian, S., et al., The Cryo-Em Structure of the Bd Oxidase from M. Tuberculosis Reveals a Unique Structural Framework and Enables Rational Drug Design to Combat Tb. *Nat. Commun.* **2021**, *12*, 10.

129. Singer, S. J.; Nicolson, G. L., The Fluid Mosaic Model of the Structure of Cell Membranes. *Science* **1972**, *175*, 720-+.

130. Nicolson, G. L., The Fluid-Mosaic Model of Membrane Structure: Still Relevant to Understanding the Structure, Function and Dynamics of Biological Membranes after More Than 40 Years. *Biochim. Biophys. Acta-Biomembr.* **2014**, *1838*, 1451-1466.

131. Lucio, M.; Lima, J.; Reis, S., Drug-Membrane Interactions: Significance for Medicinal Chemistry. *Curr. Med. Chem.* **2010**, *17*, 1795-1809.

132. Hafez, I. M.; Ansell, S.; Cullis, P. R., Tunable Ph-Sensitive Liposomes Composed of Mixtures of Cationic and Anionic Lipids. *Biophys. J.* **2000**, *79*, 1438-1446.

133. Leo, A. J., Calculating Logpoct from Structures. *Chem. Rev.* **1993**, *93*, 1281-1306.

134. Lipinski, C. A.; Lombardo, F.; Dominy, B. W.; Feeney, P. J., Experimental and Computational Approaches to Estimate Solubility and Permeability in Drug Discovery and Development Settings (Reprinted from Advanced Drug Delivery Reviews, Vol 23, Pg 3-25, 1997). *Adv. Drug Deliv. Rev.* **2001**, *46*, 3-26.

135. Chiou, C. T.; Freed, V. H.; Schmedding, D. W.; Kohnert, R. L., Partition-Coefficient and Bioaccumulation of Selected Organic Chemicals. *Environ. Sci. Technol.* **1977**, *11*, 475-478.

136. Leo, A.; Hansch, C.; Elkins, D., Partition Coefficients and Their Uses. *Chem. Rev.* **1971**, *71*, 525-+.

137. Keseru, G. M.; Makara, G. M., The Influence of Lead Discovery Strategies on the Properties of Drug Candidates. *Nat. Rev. Drug Discov.* **2009**, *8*, 203-212.

138. Young, R. J., Physical Properties in Drug Design. In *Tactics in Contemporary Drug Design*, Meanwell, N. A., Ed. Springer-Verlag Berlin: Berlin, 2015; Vol. 9, pp 1-68.

139. Panicker, L.; Sharma, V. K.; Datta, G.; Deniz, K. U.; Parvathanathan, P. S.; Ramanathan, K. V.; Khetrapal, C. L., Interaction of Aspirin with Dppc in the Lyotropic, Dppc-Aspirin-H2o/D2o Membrane. *Mol. Cryst. Liq. Cryst. Sci. Technol. Sect. A-Mol. Cryst. Liq. Cryst.* **1995**, *260*, 611-621.

140. Puglisi, G.; Fresta, M.; Ventura, C.; Mazzone, G.; Vandelli, M. A., Methotrexate Interaction with a Lipid-Membrane Model of Dppc. *J. Therm. Anal.* **1995**, *44*, 1287-1299.

141. Mady, M. M.; Shafaa, M. W.; Abbase, E. R.; Fahium, A. H., Interaction of Doxorubicin and Dipalmitoylphosphatidylcholine Liposomes. *Cell Biochem. Biophys.* **2012**, *62*, 481-486.

142. McDonald, A. E.; Vanlerberghe, G. C., Respiration and Oxidative Phosphorylation in Mycobacteria. In *Structural Basis of Biological Energy Generation*, Hohmann-Marriott, M. F., Ed. Springer: Dordrecht, 2014; Vol. 39, pp 277-293.

143. Lu, P.; Heineke, M. H.; Koul, A.; Andries, K.; Cook, G. M.; Lill, H.; van Spanning, R.; Bald, D., The Cytochrome Bd-Type Quinol Oxidase Is Important for Survival of Mycobacterium Smegmatis under Peroxide and Antibiotic-Induced Stress. *Sci Rep* **2015**, *5*, 10.

144. R.G. Edie, R. E. H., E.V. Krumkains Thienopyrimidine Derivatives. EP452002A2, 1991.

145. Munchhof, M. J., Sobolov-Jaynes, S. B. Thienopyrimidine and Thienopyridine Derivatives Useful as Anticancer Agents. WO9924440A1, 1999.

146. Baskaran, S., Lew, W., Oslob, J. D., Yoburn, J. C., Zhong, M. Thienopyrimidines Useful as Aurora Kinase Inhibitors and Their Preparation, Pharmaceutical Compositions, and Their Use for Treatment of Aurora Kinase-Mediated Diseases. 0216, 2006.

147. Ward, S. A., Taylor, M. J. O'Neill, P. M., Hong, W. D. Benayoud, F. Preparation of Compounds Useful in Treatment or Prevention of Filarial Worm Infections. US20190345157A1, 2018.

148. C. Beauregard, A. J. B., R. L. Davis, D. A. Gamache, J. M. Yanni Aminopyrimidine Inhibitors of Histamine Receptors for the Treatment of Disease. 2010.

149. Harrison, G. A., et al., Identification of 4-Amino-Thieno 2,3-D Pyrimidines as Qcrb Inhibitors in Mycobacterium Tuberculosis. *mSphere* **2019**, *4*, 14.

150. S. Arnett, M. M., M. Singh, C. Stallings, L. Weiss, S. Wildman Thieno[2,3-D]Pyrimidines and Benzofuro[3,2-D]Pyrimidines as Antimicrobial Agents. WO2019018359A1, 2019.

151. Neri, J. M.; Cavalcanti, L. N.; Araujo, R. M.; Menezes, F. G., 2,3-Dichloroquinoxaline as a Versatile Building Block for Heteroaromatic Nucleophilic Substitution: A Review of the Last Decade. *Arab. J. Chem.* **2020**, *13*, 721-739.

152. Savoie, P. R.; Welch, J. T., Preparation and Utility of Organic Pentafluorosulfanyl-Containing Compounds. *Chem. Rev.* **2015**, *115*, 1130-1190.

153. Peetla, C.; Stine, A.; Labhasetwar, V., Biophysical Interactions with Model Lipid Membranes: Applications in Drug Discovery and Drug Delivery. *Mol. Pharm.* **2009**, *6*, 1264-1276.

154. Perlovich, G. L., Thermodynamic Approaches to the Challenges of Solubility in Drug Discovery and Development. *Mol. Pharm.* **2014**, *11*, 1-11.

155. Cao, Y. C.; Xiang, T. X.; Anderson, B. D., Development of Structure-Lipid Bilayer Permeability Relationships for Peptide-Like Small Organic Molecules. *Mol. Pharm.* **2008**, *5*, 371-388.

156. Chamberlain, K.; Evans, A. A.; Bromilow, R. H., 1-Octanol/Water Partition Coefficient (K-Ow) and Pk(a) for Ionisable Pesticides Measured by a Ph-Metric Method. *Pestic. Sci.* **1996**, *47*, 265-271.

157. Hughes, J. D., et al., Physiochemical Drug Properties Associated with in Vivo Toxicological Outcomes. *Bioorg. Med. Chem. Lett.* **2008**, *18*, 4872-4875.

158. Goude, R.; Amin, A. G.; Chatterjee, D.; Parish, T., The Arabinosyltransferase Embc Is Inhibited by Ethambutol in Mycobacterium Tuberculosis. *Antimicrob. Agents Chemother.* **2009**, *53*, 4138-4146.

159. Aubry, A.; Fisher, L. M.; Jarlier, V.; Cambau, E., First Functional Characterization of a Singly Expressed Bacterial Type Ii Topoisomerase: The Enzyme from Mycohacterium Wherculosis. *Biochem. Biophys. Res. Commun.* **2006**, *348*, 158-165.

160. Aung, H. L.; Berney, M.; Cook, G. M., Hypoxia-Activated Cytochrome Bd Expression in Mycobacterium Smegmatis Is Cyclic Amp Receptor Protein Dependent. *J. Bacteriol.* **2014**, *196*, 3091-3097.

161. Malasala, S.; Polomoni, A.; Ahmad, M. N.; Shukla, M.; Kaul, G.; Dasgupta, A.; Chopra, S.; Nanduri, S., Structure Based Design, Synthesis and Evaluation of New Thienopyrimidine Derivatives as Anti-Bacterial Agents. *J. Mol. Struct.* **2021**, *1234*, 13.

162. Hopfner, S. M.; Lee, B. S.; Kalia, N. P.; Miller, M. J.; Pethe, K.; Moraski, G. C., Structure Guided Generation of Thieno [3,2-*D*] Pyrimidin-4-Amine *Mycobacterium Tuberculosis Bd* Oxidase Inhibitors. *RSC Med. Chem.* **2021**, *12*, 73-77.

163. Zhan, M.; Deng, Y. F.; Zhao, L. F.; Yan, G. Y.; Wang, F. Y.; Tian, Y.; Zhang, L. X.; Jiang, H. X.; Chen, Y. W., Design, Synthesis, and Biological Evaluation of Dimorpholine Substituted Thienopyrimidines as Potential Class I Pi3k/Mtor Dual Inhibitors. *J. Med. Chem.* **2017**, *60*, 4023-4035.

164. Zhang, Y. M.; Chen, Y. D.; Zhang, D. F.; Wang, L.; Lu, T.; Jiao, Y., Discovery of Novel Potent Vegfr-2 Inhibitors Exerting Significant Antiproliferative Activity against Cancer Cell Lines. *J. Med. Chem.* **2018**, *61*, 140-157.

165. Ghith, A.; Ismail, N. S. M.; Youssef, K.; Abouzid, K. A. M., Medicinal Attributes of Thienopyrimidine Based Scaffold Targeting Tyrosine Kinases and Their Potential Anticancer Activities. *Arch. Pharm.* **2017**, *350*, 24.

166. Pal, K.; Raza, M. K.; Legac, J.; Rahman, M. A.; Manzoor, S.; Rosenthal, P. J.; Hoda, N., Design, Synthesis, Crystal Structure and Anti-Plasmodial Evaluation of Tetrahydrobenzo 4,5 Thieno 2,3-D Pyrimidine Derivatives. *RSC Med. Chem.* **2021**, *12*, 970-981.

167. Thesseling, A.; Rasmussen, T.; Burschel, S.; Wohlwend, D.; Kagi, J.; Muller, R.; Bottcher, B.; Friedrich, T., Homologous Bd Oxidases Share the Same Architecture but Differ in Mechanism. *Nat. Commun.* **2019**, *10*, 7.

168. Safarian, S., et al., Active Site Rearrangement and Structural Divergence in Prokaryotic Respiratory Oxidases. *Science* **2019**, *366*, 100-+.

169. Safarian, S.; Rajendran, C.; Muller, H.; Preu, J.; Langer, J. D.; Ovchinnikov, S.; Hirose, T.; Kusumoto, T.; Sakamoto, J.; Michel, H., Structure of a Bd Oxidase Indicates Similar Mechanisms for Membrane-Integrated Oxygen Reductases. *Science* **2016**, *352*, 583-586.

170. Wang, W. W., et al., Cryo-Em Structure of Mycobacterial Cytochrome Bd Reveals Two Oxygen Access Channels. *Nat. Commun.* **2021**, *12*, 8.

171. Lipinski, C. A., Drug-Like Properties and the Causes of Poor Solubility and Poor Permeability. *J. Pharmacol. Toxicol. Methods* **2000**, *44*, 235-249.

172. Duncan, K. M.; Steel, W. H.; Walker, R. A., Amino Acids Change Solute Affinity for Lipid Bilayers. *Biophys. J.* **2021**, *120*, 3676-3687.

173. Alifrangis, L. H.; Christensen, I. T.; Berglund, A.; Sandberg, M.; Hovgaard, L.; Frokjaer, S., Structure-Property Model for Membrane Partitioning of Oligopeptides. *J. Med. Chem.* **2000**, *43*, 103-113.

174. Ma, B.; Zha, H. Y.; Li, N.; Yang, D.; Lin, G., Effect of Structural Modification of Alpha-Aminoxy Peptides on Their Intestinal Absorption and Transport Mechanism. *Mol. Pharm.* **2011**, *8*, 1073-1082.

175. Sharifian, G. M., Recent Experimental Developments in Studying Passive Membrane Transport of Drug Molecules. *Mol. Pharm.* **2021**, *18*, 2122-2141.

176. Chen, I. J.; Taneja, R.; Yin, D. X.; Seo, P. R.; Young, D.; MacKerell, A. D.; Polli, J. E., Chemical Substituent Effect on Pyridine Permeability and Mechanistic Insight from Computational Molecular Descriptors. *Mol. Pharm.* **2006**, *3*, 745-755.

177. Duncan, K. M.; Casey, A.; Gobrogge, C. A.; Trousdale, R. C.; Piontek, S. M.; Cook, M. J.; Steel, W. H.; Walker, R. A., Coumarin Partitioning in Model Biological Membranes: Limitations of Log P as a Predictor. *J. Phys. Chem. B* **2020**, *124*, 8299-8308.

178. Gobrogge, C. A.; Kong, V. A.; Walker, R. A., Temperature-Dependent Partitioning of C152 in Binary Phosphatidylcholine Membranes and Mixed Phosphatidylcholine/Phosphatidylethanolamine Membranes. *J. Phys. Chem. B* **2017**, *121*, 7889-7898.

179. Purnell, G. E.; Walker, R. A., Hindered Isomerization at the Silica/Aqueous Interface: Surface Polarity or Restricted Solvation? *Langmuir* **2018**, *34*, 9946-9949.

180. Purnell, G. E.; McNally, M. T.; Callis, P. R.; Walker, R. A., Buried Liquid Interfaces as a Form of Chemistry in Confinement: The Case of 4-Dimethylaminobenzonitrile at the Silica-Aqueous Interface. *J. Am. Chem. Soc.* **2020**, *142*, 2375-2385.

181. Nad, S.; Pal, H., Unusual Photophysical Properties of Coumarin-151. *J. Phys. Chem. A* **2001**, *105*, 1097-1106.

182. Nad, S.; Kumbhakar, M.; Pal, H., Photophysical Properties of Coumarin-152 and Coumarin-481 Dyes: Unusual Behavior in Nonpolar and in Higher Polarity Solvents. *J. Phys. Chem. A* **2003**, *107*, 4808-4816.

183. Roy, D.; Liu, S. L.; Woods, B. L.; Siler, A. R.; Fourkas, J. T.; Weeks, J. D.; Walker, R. A., Nonpolar Adsorption at the Silica/Methanol Interface: Surface Mediated Polarity and Solvent Density across a Strongly Associating Solid/Liquid Boundary. *J. Phys. Chem. C* **2013**, *117*, 27052-27061.

184. Ahmed, M.; Younis, O.; Orabi, E. A.; Sayed, A. M.; El-Dean, A. M. K.; Hassanien, R.; Davis, R. L.; Tsutsumi, O.; Tolba, M. S., Synthesis of Novel Biocompatible Thienopyrimidine Chromophores with Aggregation-Induced Emission Sensitive to Molecular Aggregation. *ACS Omega* **2020**, *5*, 29988-30000.

185. Sayed, M.; Younis, O.; Hassanien, R.; Ahmed, M.; Mohammed, A. A. K.; Kamal, A. M.; Tsutsumi, O., Design and Synthesis of Novel Indole Derivatives with Aggregation-Induced Emission and Antimicrobial Activity. *J. Photochem. Photobiol. A-Chem.* **2019**, *383*, 11.

186. Hu, R.; Leung, N. L. C.; Tang, B. Z., Aie Macromolecules: Syntheses, Structures and Functionalities. *Chem. Soc. Rev.* **2014**, *43*, 4494-4562.

187. Cook, G. M.; Hards, K.; Vilcheze, C.; Hartman, T.; Berney, M., Energetics of Respiration and Oxidative Phosphorylation in Mycobacteria. *Microbiol. Spectr.* **2014**, *2*, 20.

188. Mohamed, T.; Rao, P. P. N., 2,4-Disubstituted Quinazolines as Amyloid-Beta Aggregation Inhibitors with Dual Cholinesterase Inhibition and Antioxidant Properties: Development and Structure-Activity Relationship (Sar) Studies. *Eur. J. Med. Chem.* **2017**, *126*, 823-843.

189. Rewcastle, G. W.; Denny, W. A.; Bridges, A. J.; Zhou, H. R.; Cody, D. R.; McMichael, A.; Fry, D. W., Tyrosine Kinase Inhibitors. 5. Synthesis and Structure-Activity Relationships for 4-[(Phenylmethyl)Amino]- and 4-(Phenylamino)Quinazolines as Potent Adenosine 5'-Triphosphate Binding Site Inhibitors of the Tyrosine Kinase Domain of the Epidermal Growth Factor Receptor. *J. Med. Chem.* **1995**, *38*, 3482-3487.

190. Lee, C. C.; MacKay, J. A.; Frechet, J. M. J.; Szoka, F. C., Designing Dendrimers for Biological Applications. *Nat. Biotechnol.* **2005**, *23*, 1517-1526.

191. Dreikorn, B. A.; Jourdan, G. P.; Suhr, R. G. Quinazoline Derivatives. U.S. Patent No. 5,411,963, 1995.

192. Tobe, M.; Isobe, Y.; Tomizawa, H.; Matsumoto, M.; Obara, F.; Nagasaki, T.; Hayashi, H., Structure-Activity Relationships of Quinazoline Derivatives: Dual-Acting Compounds with Inhibitory Activities toward Both Tnf-Alpha

Production and T Cell Proliferation. *Bioorg. Med. Chem. Lett.* **2001**, *11*, 545-548.

193. Tobe, M.; Isobe, Y.; Tomizawa, H.; Nagasaki, T.; Takahashi, H.; Fukazawa, T.; Hayashi, H., Discovery of Quinazolines as a Novel Structural Class of Potent Inhibitors of Nf-Kappa B Activation. *Bioorg. Med. Chem.* **2003**, *11*, 383-391.

194. Tsai, K. C.; Teng, L. W.; Shao, Y. M.; Chen, Y. C.; Lee, Y. C.; Li, M. Y.; Hsiao, N. W., The First Pharmacophore Model for Potent Nf-Kappa B Inhibitors. *Bioorg. Med. Chem. Lett.* **2009**, *19*, 5665-5669.

195. Matsumoto, J., et al., Anaerobic Nadh-Fumarate Reductase System Is Predominant in the Respiratory Chain of Echinococcus Multilocularis, Providing a Novel Target for the Chemotherapy of Alveolar Echinococcosis. *Antimicrob. Agents Chemother.* **2008**, *52*, 164-170.

196. Yuan, J.; Ma, D.; Liu, J.; Zhang, L. Potent Small Molecule Inhibitors of Autophagy, and Methods of Use Thereof. 21 July 2009, 2011.

197. Mammen, M.; Choi, S. K.; Whitesides, G. M., Polyvalent Interactions in Biological Systems: Implications for Design and Use of Multivalent Ligands and Inhibitors. *Angew. Chem.-Int. Edit.* **1998**, *37*, 2755-2794.

198. Page, M. I.; Jencks, W. P., Entropic Contributions to Rate Accelerations in Enzymic and Intramolecular Reactions and Chelate Effect. *Proc. Natl. Acad. Sci. U. S. A.* **1971**, *68*, 1678-+.

199. Najlah, M.; Freeman, S.; Attwood, D.; D'Emanuele, A., In Vitro Evaluation of Dendrimer Prodrugs for Oral Drug Delivery. *Int. J. Pharm.* **2007**, *336*, 183-190.

200. Esfand, R.; Tomalia, D. A., Poly(Amidoamine) (Pamam) Dendrimers: From Biomimicry to Drug Delivery and Biomedical Applications. *Drug Discov. Today* **2001**, *6*, 427-436.

201. Caminade, A. M.; Turrin, C. O., Dendrimers for Drug Delivery. *J. Mat. Chem. B* **2014**, *2*, 4055-4066.

202. Jiang, Y. Y.; Tang, G. T.; Zhang, L. H.; Kong, S. Y.; Zhu, S. J.; Pei, Y. Y., Pegylated Pamam Dendrimers as a Potential Drug Delivery Carrier: In Vitro and in Vivo Comparative Evaluation of Covalently Conjugated Drug and Noncovalent Drug Inclusion Complex. *J. Drug Target.* **2010**, *18*, 389-403.

203. Paleos, C. M.; Tsiourvas, D.; Sideratou, Z.; Tziveleka, L. A., Drug Delivery Using Multifunctional Dendrimers and Hyperbranched Polymers. *Expert Opin. Drug Deliv.* **2010**, *7*, 1387-1398.

204. Kukowska-Latallo, J. F.; Candido, K. A.; Cao, Z. Y.; Nigavekar, S. S.; Majoros, I. J.; Thomas, T. P.; Balogh, L. P.; Khan, M. K.; Baker, J. R., Nanoparticle Targeting of Anticancer Drug Improves Therapeutic Response in Animal Model of Human Epithelial Cancer. *Cancer Res.* **2005**, *65*, 5317-5324.

205. Frechet, J. M. J.; Hawker, C. J.; Gitsov, I.; Leon, J. W., Dendrimers and Hyperbranched Polymers: Two Families of Three-Dimensional Macromolecules with Similar but Clearly Distinct Properties. *J. Macromol. Sci.-Pure Appl. Chem.* **1996**, *A33*, 1399-1425.

206. Johnson, B. M.; Shu, Y. Z.; Zhuo, X. L.; Meanwell, N. A., Metabolic and Pharmaceutical Aspects of Fluorinated Compounds. *J. Med. Chem.* **2020**, *63*, 6315-6386.